

**Alma Mater Studiorum – Università di Bologna**  
**in cotutela con Institut de Physique du Globe de Paris**

**DOTTORATO DI RICERCA IN**

**Geofisica**

**Ciclo XXVIII**

**Settore Concorsuale di afferenza: 04/A4**

**Settore Scientifico disciplinare: Geo/10**

**RUPTURE DYNAMICS ALONG SUBDUCTION ZONES: STRUCTURAL  
AND GEOMETRICAL COMPLEXITIES AND THE CASE OF TOHOKU-OKI  
EARTHQUAKE.**

**Presentata da: Antonio Scala**

**Coordinatore Dottorato**

**Nadia Pinardi**

**Relatore**

**Gaetano Festa**

**Relatore**

**Jean-Pierre Vilotte**

**Esame finale anno 2016**



<b>INTRODUCTION</b>	<b>4</b>
<b>1 NUMERICAL MODELLING FOR SEISMOLOGY</b>	<b>11</b>
<b>1.1 Elastodynamics</b>	<b>11</b>
1.1.1 Continuum mechanics: strain and stress tensors	11
1.1.2 Hooke's law and general problem of elastodynamics	13
1.1.3 Initial and Boundary conditions	14
<b>1.2 The extended source</b>	<b>15</b>
1.2.1 Fault boundary conditions	16
1.2.2 Signorini's contact condition	18
1.2.3 Coulomb's friction condition	18
1.2.4 Frictional laws	19
<b>1.3 Numerical models for seismological problems</b>	<b>21</b>
1.3.1 Variational formulation	22
<b>1.4 Spectral element method (SEM) for wave propagation</b>	<b>23</b>
1.4.1 Meshing and mapping over master element	23
1.4.2 Galerkin approximation	25
1.4.3 Numerical integration: the Gauss-Lobatto-Legendre formula	26
1.4.4 Time stepping evolution: the Newmark algorithm	28
<b>1.5 The extended source with SEM</b>	<b>30</b>
1.5.1 Domain decomposition and traction at split node method	30
1.5.2 Time resolution algorithm	32
<b>2 BIMATERIAL INTERFACES</b>	<b>37</b>
<b>2.1 Introduction</b>	<b>37</b>
<b>2.2 Stroh formalism for isotropic bimaterial interfaces</b>	<b>41</b>
2.2.1 Steady state crack propagation along bimaterial interface	42
2.2.2 Stroh formalism for isotropic homogeneous material	44
2.2.3 Matrix $\mathbf{H}$ for bimaterial crack	47
2.2.4 Crack tip fields	48
2.2.5 Real $\mathbf{H}$ -matrix	50
2.2.6 Complex $\mathbf{H}$ -matrix	52
2.2.7 Stroh formalism for Coulomb friction sliding rupture	57

<b>2.3</b>	<b>Bimaterial ill-posedness for Coulomb friction conditions</b>	<b>61</b>
2.3.1	Frictionless sliding	64
2.3.2	Friction sliding: the Coulomb conditions	64
2.3.3	Stability problem for regularized solutions	66
<b>2.4</b>	<b>Numerical modelling for bimaterial interfaces</b>	<b>68</b>
2.4.1	Prakash-Clifton regularization	68
2.4.2	Numerical discretization	70
2.4.3	Simulation setup	71
2.4.4	Regularization parametric study: dynamic time scale	75
2.4.5	Regularization parametric study: constant time scale	88
2.4.6	Alternative regularization	94
2.4.7	Stationary phase	100
2.4.8	Stationary phase: not existing $C_{gr}$	101
2.4.9	Stationary phase: existing $C_{gr}$	105
<b>2.5</b>	<b>Conclusions</b>	<b>115</b>
	<b>APPENDIX A</b>	<b>120</b>
<b>A.1</b>	<b>Eigenvalue problem for general homogeneous case</b>	<b>120</b>
<b>A.2</b>	<b>Eigenvalue problem for bimaterial case (general complex matrix <math>\mathbf{H}</math>)</b>	<b>123</b>
<b>A.3</b>	<b>Energy release rate for bimaterial case (general complex matrix <math>\mathbf{H}</math>)</b>	<b>124</b>
<b>A.4</b>	<b>Shear-displacement relationship in <math>p</math>-domain: matrix <math>\hat{\mathbf{K}}</math></b>	<b>126</b>
<b>3</b>	<b>FREE SURFACE INTERACTIONS</b>	<b>128</b>
<b>3.1</b>	<b>Introduction</b>	<b>128</b>
<b>3.2</b>	<b>Geometrical models and simulations setup</b>	<b>130</b>
<b>3.3</b>	<b>Results</b>	<b>134</b>
3.3.1	Vertical fault	134
3.3.2	Dipping fault with $\alpha = 45^\circ$	138
3.3.3	Dipping fault with $\alpha = 10^\circ$	145
3.3.4	Regularization of normal stress perturbations	148
<b>3.4</b>	<b>Conclusions</b>	<b>150</b>

<b>4 TOHOKU 2D DYNAMIC MODELS</b>	<b>153</b>
4.1 Introduction	153
4.2 Initial conditions and simulation setup	154
4.3 Uniform regional stress condition	157
4.4 Normal stress increasing with depth	162
4.4.1 Accretionary prism	165
4.5 Bimaterial regularization for Tohoku models	167
4.6 Small asperities in the deepest part	172
4.7 Dynamic models for tsunami hazard	175
4.8 Conclusions	183
<b>CONCLUSIONS</b>	<b>186</b>
<b>REFERENCES</b>	<b>186</b>

# Introduction

The development of dense digital networks in the last decades in several seismogenic areas, and in particular in Japan, allowed data to be recorded in the near source range, bringing additional constraints for the interpretation of the spectral content of the seismic source and for the time and space distribution of slip and slip rate during rupture process of large earthquakes. At the same time, it has opened new challenging questions about the fully understanding of source processes, such as the stress triggering, the frictional conditions along the various parts of the rupture and the coupling between the normal and shear stress. This latter is very relevant in presence of complex geometry and structures, including smooth and/or sharp slope variations, interaction between dipping faults and the free surface, and when the rupture propagates along interfaces between materials with different elastic parameters. These complexities can be introduced in the study of rupture processes through rock mechanics principles and, when the functional form of these complexities approaches realistic cases, analytic solutions have to give way to numerical techniques.

In this work of thesis, we are mainly interested to the dynamic rupture processes related to giant subduction events.

In geology, subduction is the process that takes place at convergent boundaries where one plate usually moves under the other one and it sinks into the mantle as the plates converge. Magnitude order of rate of subduction is typically of centimetres per year, with the average rate of convergence being approximately two to eight centimetres per year. Subduction zones are places of convective downwelling of Earth's lithosphere. The descending slab is over-ridden by the leading edge of the other plate. The slab sinks at variables angle from few degrees to forty-five degrees with respect to the Earth's surface. This sinking is driven by the temperature difference between the subducting oceanic lithosphere and the surrounding mantle asthenosphere, as the colder oceanic lithosphere is on average denser.

For what concerning the modern instrumental seismology, these areas are responsible for the most of biggest thrust events occurring on the Earth's surface. In

particular the 1960 Giant Chilean earthquake occurred off the west coast of South America, was the biggest seismic event ever recorded with moment magnitude  $M_w = 9.5$ . Recently the large 2004 Indian Ocean earthquake and the 2011 Tohoku-Oki earthquake have evidenced not only the destructive power of earthquakes but also their capability to originate huge tsunami waves increasing the related damage and the casualties. The seismicity at a subduction zone provides the key to the processes active there. The subducting plate pulls down the continental plate and, in the shallow part, the plates are locked storing elastic deformation with time. In the deep part the subduction of cold oceanic crust into the mantle depresses the local geothermal gradient and causes a larger portion of Earth to deform in a more brittle way than it would in a normal geothermal gradient setting, contributing to load the overlying regions.

Specifically, the Tohoku-Oki megathrust earthquake, occurred on, March 11, 2011 off the northeast coast of Honshu island in Japan and ruptured a vast region in the vicinity of the subduction trench in an unforeseen way both in terms of earthquake and tsunami risk scenarios (Satriano *et al.*, 2014). The big quantity of seismic, teleseismic, geodetic and tsunami data, recorded by the dense networks around the Japan coast and worldwide far from the source, revealed that this event originated in a crustal part of the subduction slab at shallower depth as compared to the recent smaller magnitude events ( $M < 8$ , e.g. Miyagi, 1978). It initially propagates bilaterally towards the shallow trench and the deep oceanic crust/continental mantle interface. This propagation remained confined for a pretty long time (about 100s) in a small stripe of the fault plane along the dip direction and extended for a length of  $\sim 260\text{km}$  as evidenced by several source inversion analyses (e.g. Maercklin *et al.*, 2012; Satriano *et al.*, 2014). Then it widely extended along the strike direction for about 500km producing a final moment magnitude of  $M_w = 9.0$  (JMA, Japan Meteorology Agency).

This event can be considered one of the most important for modern seismology not only because of its size but also because of the challenging aspects emerging from its features in terms of understanding of a megathrust rupture and of the seismic cycle in subduction zones (Satriano *et al.*, 2014). In particular along the dip direction it showed a very peculiar asymmetry with large slip values recorded in the shallow part, at the trench, where the huge tsunami waves were originated, associated with low

frequency content of the emitted radiation (Simons *et al.*, 2011; Ide *et al.*, 2011; Maercklin *et al.*, 2012). Conversely most of the seismic source inversions or back-projection analyses (Lee *et al.*, 2011; Honda *et al.*, 2011; Satriano *et al.*, 2014; and others, see Chapter 4) inferred a rupture composed by at least 3-4 sub-events eventually associated with deep asperities located in the areas which also generated the recent past events (Kurahashi & Irikura, 2013). The high-frequency content, recorded on coastal seismograms, can be associated to these sub-events, reinforcing the idea of the partitioning of the fault plane along the dip direction.

The above described asymmetry can be ascribed both to the expected along-dip segmentation of the fault deriving from changes in thermal and petrophysical structure (Satriano *et al.*, 2014) and to particular dynamic rupture processes directly connected to fault structure and geometry and to the initial stress state.

The geological structure around the fault plane, that can be specified through the elastic properties of the materials within which the fault is embedded, can strongly influence the dynamic rupture propagation and, in particular, the near-fault velocity field may drive the rupture velocity. If a homogeneous medium is considered the asymptotic rupture sub-shear speed is the Rayleigh speed of the medium as confirmed by the analysis of the rupture velocity of realistic earthquakes (Gutenberg, 1995) and by analytical results from fracture mechanics for brittle cracks (Freund, 1990; Broberg, 1999). For particular initial stress conditions the rupture can accelerate to a super-shear regime and, according to the study describing the admissible rupture velocities for propagating cracks (Burridge, 1973) in-plane fractures can accelerate towards the P-wave velocity. These features were also confirmed by several laboratory experiments (Xia *et al.*, 2004; 2005a) and numerical simulations (Festa & Vilotte, 2006).

Realistically, subduction zone cannot be modelled as faults embedded in a homogeneous medium and they should be rather considered as interfaces between materials with different elastic properties. In particular the characteristics of the oceanic lithosphere, continental crust, continental mantle, and slow regions in the shallow part of the subduction zone such as the accretionary prism are expected to drive the rupture dynamics. Even if planar faults are considered, the propagation of rupture along bimaterial interfaces rapidly leads to a break of symmetry due to the induced normal stress perturbations. Even for the simplest case of a planar fault

between two different materials the dynamics was widely shown to be driven by this break of symmetry and by the dissimilarity between materials (Cochard & Rice, 2000; Ranjith & Rice, 2001; Xia *et al.*, 2005b; Rubin & Ampuero, 2007, and many others, see Chapter 2) both in terms of kinematic fields on the fault and rupture speed. Therefore, when the rupture is expected to pass through fault portions with a weak or strong elastic contrast, as at the entrance in the mantle wedge for subduction zone, sharp rupture accelerations/decelerations and jumps are expected. Moreover when a classical Coulomb friction law is used in modelling an instantaneous shear/normal coupling, analytical and numerical solutions show instabilities due to the lack of a physical time/length scale associated with the coupling. The dynamic effects of a bimaterial interface as well as the shear/normal coupling have to be properly addressed in order to achieve physically reliable rupture models for the subduction zones.

The role of fault geometry was studied by numerical and theoretical investigations, (e.g. Harris & Day, 1993; Nielsen *et al.*, 2000; Tada & Yashamita, 1997) tomographic inversions and historical distributions of seismic events around the seismogenic areas. Branching of fault, strong slope variations and interaction with free surface can be considered as the most important geometrical factors. In particular in this work of thesis the break of symmetry deriving from free surface interactions with dipping faults (Nielsen, 1998; Oglesby *et al.*, 1998) will be investigated in detail and we will show how it can drive the rupture in the vicinity of the trench allowing large values of slip, associated with low frequency radiation. Even in this case the break of symmetry is due to the normal stress perturbations and thus the complex shear/normal coupling has to be investigated in detail as for bimaterial propagation.

Finally initial stress state can be inferred from the slip and rupture time maps obtained from waveform inversions or using intermediary kinematic description of the rupture processes. It is worth to highlight that due to the strong non-linearity of dynamic parameters the initial state is the most debated input for dynamic models and parametric studies are very often necessary to find the most reliable set up for complex realistic applications.

Once complex fault geometry, realistic velocity fields around the fault and reliable initial stress state around the fault are imposed and after properly describing the complex shear/normal coupling, the only way to model the rupture processes and the

associated radiation is to perform numerical simulations. In particular numerical simulations of rupture dynamics can provide synthetic seismograms, directly comparable with real data or can be used to evaluate the kinematic (slip, slip rate, rupture velocity) and dynamic fields (stress drop, normal stress perturbations, frictional conditions) at the source.

The most used numerical techniques in the context of seismology can be subdivided into three big families: the Finite Difference Methods (FD), The Boundary Integral (BIE) and the Finite Element Methods (FEM).

FD is the easiest technique to implement and it was the first to be widely used for seismological applications due to the simplicity in solving the velocity-stress formulation of elastodynamics equation through staggered grids, that are grids where stress and velocity are computed on nodes staggered both in time and space (Virieux, 1984, 1986). Velocity-stress formulation is furthermore easily included in efficient absorbing boundary conditions (e.g. Perfectly Matching Layers, PML, Festa & Nielsen, 2003) allowing to deal with local domains. Nevertheless the staggered scheme, albeit very performing for wave propagation, is less efficient to handle rupture problems due to the necessity to interpolate the quantities that do not lie on the fault itself. Moreover they cannot allow to properly follow the curvature of the fault since geometrical discontinuities are drawn on Cartesian grids.

The BIE are instead able to implement more realistic curvatures, but they can be used only to solve rupture processes without explicitly computing the contribution associated with the emitted radiation. This allows to discretize the fault problem more precisely, enabling to properly study high-frequency processes and to achieve very rapid convergence, but they cannot be used when we are interested in producing synthetic seismograms. Additionally their applicability is limited to almost homogeneous media.

Finally FEM is based upon a variational formulation of the elastodynamics similar to the classical principle of virtual work from analytical mechanics. It allows to deal with complex geometries, to naturally treat the classical seismological boundary conditions and after choosing a numerical integration technique it is based upon the solution of an algebraic problem. The Spectral Element Method (SEM), which is used for all the simulations presented in this work of thesis, is a particular FEM, from which it inherits the geometrical flexibility, and it couples it with the rapid

convergence of spectral methods (Patera, 1984; Maday and Patera, 1989). It was firstly used for seismological applications in the pioneering work by Komatitsch & Vilotte (1998) and it is based upon a particular decomposition of the domain which provides a diagonal mass matrix that can be inverted at the beginning of run significantly reducing the computational costs.

We can summarise the main objectives of this thesis in the characterization of the coupling between shear traction and normal stress when large normal stress perturbations are induced by the rupture propagation, and then in the use of these results to produce realistic rupture dynamics models for the case-study of the Tohoku earthquake. This will give an insight into the main dynamic features of the ruptures associated with mega-thrust events in subduction zones.

To this aim the results deriving from several dynamic numerical simulations will be shown in simple bi-dimensional planar cases both in the case of bimaterial ruptures and dipping fault reaching the free surface with different angles. In light of the results obtained from these numerical simulations some numerical models of the Tohoku earthquake along-dip rupture propagation will be shown, stressing the effects of this coupling on the macroscopic observations that emerged from that giant thrust event and evidencing how the normal/shear interaction may have also influenced the triggering of the huge tsunami waves that hit the east Japan coast as a consequence of that event.

The whole work can be summarized as follows:

- In Chapter 1, the physical model of seismic wave propagation will be presented in the classical framework of linear elasticity. Then the rupture process will be modelled in terms of a non-smooth contact-friction formulation along the fault surface. Finally the characteristics of Spectral Element Method will be illustrated in detail in order to demonstrate why this method is particularly useful for our purposes.
- In Chapter 2, we will provide a broad overview about the typical bimaterial processes both in the framework of the fracture mechanics and by the support of several numerical results. In particular the numerical models provided many interesting answers about the shear/normal coupling when a rupture propagates between dissimilar materials and they allow for the characterization of a typical length scale of the interaction. The expected

behaviour during the acceleration of a growing crack will be also provided and interpreted in the framework of a linear slip weakening constitutive law. Also the stationary phase will be discussed for different dissimilarities between the two sides of the interface.

- In Chapter 3, the interaction between a fault reaching the free surface and the free surface itself will be investigated still through Spectral Element models of rupture dynamics. The most relevant results for this topic concern the break of symmetry between the hanging-wall and the footwall when thrust faults are taken into account, the largest coseismic slip, and the low-frequency content of emitted radiation close to the surface (as an effect of this asymmetry coupled with initial normal stress increasing with depth). We will also demonstrate the amplification of these features when small angles between fault and surface are considered.
- Finally, in Chapter 4, exploiting the results deriving from Chapters 2 and 3 bi-dimensional dynamic models of the along-dip propagation for Tohoku rupture will be shown. We will demonstrate how the described shear/normal coupling can be, at first order, considered as responsible for the biggest macroscopic results observed during that event, even when simple initial conditions are imposed. In particular the large slip in the vicinity of the trench can be mainly ascribed to the fault/surface interaction. When the bimaterial interfaces are well-modelled, considering an appropriate dynamic shear/normal interaction length, the signals from the trench result are depleted in high-frequency. The deep radiators could be associated to an inhomogeneous initial stress distribution in the deepest part of the fault. In conclusion we will show how taking into account the above described dynamics features the tsunami scenarios for the Tohoku earthquake lead to larger estimates for tsunami hazard (Murphy *et al.*, 2016).

# 1 Numerical modelling for seismology

## 1.1 Elastodynamics

### 1.1.1 Continuum mechanics: strain and stress tensors

In mechanics when the deformations within a body can be neglected, the motion can be formally described by rigid body theory. It works with the assumption that the distance between the points is fixed and thus the entire motion can be described by studying the translation of one point and the rotation of the body around that point. To follow the whole motion of a rigid body just six time laws (generally the coordinates of the reference point and the Euler's angles which describe rotations) are needed.

When these assumptions are no longer valid and the deformation of a body, in terms of variability of mutual distance among points, cannot be neglected the rigid body theory fails and we need to define a mathematical instrument to properly describe the deformation itself.

Let us consider a solid body  $S$  at a reference initial time  $t_0$  and a point of  $S$ , which lies at coordinates  $\xi$  at initial time. The motion of that point can be expressed by an invertible relation:

$$\mathbf{x} = \mathbf{x}(\xi, t) \quad (1.1)$$

The motion of whole body in turn can be described by the same equation referred to all initial position  $\xi$  according to the classical Lagrangian formalism.

$$\mathbf{u}(\xi, t) = \mathbf{x}(\xi, t) - \xi \quad (1.2)$$

Deriving the equation (1.2) with respect to  $\partial \xi_j$  we get the following system of equations:

$$F_{ij} = H_{ij} + \delta_{ij} \quad (1.3)$$

Where  $F_{ij} = \partial x_i / \partial \xi_j$  and  $H_{ij} = \partial u_i / \partial \xi_j$ , whereas  $\delta_{ij}$  is the Kronecker delta. Let us now consider the coordinates of two nearby points  $\boldsymbol{\xi}$  and  $\boldsymbol{\xi} + d\boldsymbol{\xi}$  when the body is at rest. When the body is in motion, the new coordinates of the labelled points can be indicated as  $\mathbf{x}$  and  $\mathbf{x} + d\mathbf{x}$  and the deformation can be described in terms of variation between the squared distances:

$$dl^2 = dx^2 - d\xi^2 = (F_{ij}F_{im} - \delta_{jm})d\xi_j d\xi_m \quad (1.4)$$

Now exploiting the equation (1.3) we get:

$$(H_{ij}H_{im} + H_{jm} + H_{mj})d\xi_j d\xi_m \quad (1.5)$$

Assuming infinitesimal deformations, the second order derivatives of  $\mathbf{u}$  can be neglected leading to the following approximated representation of the deformation:

$$dl^2 \approx \left( \frac{\partial u_i}{\partial \xi_j} + \frac{\partial u_j}{\partial \xi_i} \right) d\xi_i d\xi_j \quad (1.6)$$

Since the deformations are infinitesimal, the derivatives of  $\mathbf{u}$  with respect to  $\xi_i$  and to  $x_i$  are practically indistinguishable and we can define the strain tensor as:

$$\varepsilon_{ij} = \frac{1}{2} \left( \frac{\partial u_i}{\partial x_j} + \frac{\partial u_j}{\partial x_i} \right) \quad (1.7)$$

Its diagonal components represent the contractions or the dilatations of the considered solid along the directions of reference frame, whereas the off-diagonal components give information about the angle between the normals to the faces of deformed and original volume. Since strain tensor is symmetric, it can be diagonalized and the obtained eigenvectors represent the directions of main compressive and extensional deformations.

In continuum mechanics the interaction between nearby points influences the dynamics in the same way the external forces do. These internal stresses are forces, which nearby volumes exert on each other due to their mutual contact. The Euler–Cauchy principle states that on any surface internal to the body, the action of one part of the body on the other is equivalent to a system of distributed forces on the surface dividing the body, and it is represented by a field  $\mathbf{T}(\mathbf{x}, t, \mathbf{n})$ , called the traction vector, defined on that surface and continuously varying as a function of the surface unit

normal vector  $\mathbf{n}$  (Chadwick, 1999, Romano, 1996). In terms of the above-defined stress vector the momentum balance can be expressed as:

$$\int_C (\rho \dot{\mathbf{v}} - \mathbf{f}) dV = \int_{\partial C} \mathbf{T}(\mathbf{x}, t, \mathbf{n}) dS \quad (1.8)$$

Where  $\partial C$  represents the boundary of volume  $C$ , which is a fraction of the body, whereas  $\mathbf{v}$  and  $\mathbf{f}$  are respectively the velocity of a point within  $C$  and the external forces by volume unit. According to Cauchy's postulate the stress tensor is equivalent for all surfaces passing for the same point  $P$  and having the same normal vector and thus the Cauchy's fundamental lemma claims that:

$$\mathbf{T}(\mathbf{x}, t, \mathbf{n}) = -\mathbf{T}(\mathbf{x}, t, -\mathbf{n}) \quad (1.9)$$

The Cauchy's stress theorem also states that a second order tensor field exists, independent of  $\mathbf{n}$ , such that  $\mathbf{T}$  is a linear function of  $\mathbf{n}$ . This tensor generally is referred to as the stress tensor  $\boldsymbol{\sigma}$  and is defined as:

$$\mathbf{T}(\mathbf{x}, t, \mathbf{n}) = \boldsymbol{\sigma} \cdot \mathbf{n} \quad (1.10)$$

Substituting the equation (1.10) into the (1.8) and applying the Stokes' theorem, we get the following local formulation of momentum equation:

$$\rho \dot{\mathbf{v}} = \mathbf{f} + \vec{\nabla} \cdot \boldsymbol{\sigma} \quad (1.11)$$

### 1.1.2 Hooke's law and general problem of elastodynamics

Generally the continuum problems are described by general equations, which represent the fundamental physical laws as the conservations of mass, energy and momentum, this latter being represented by equation (1.10). These equations have to be coupled with other laws, which are less general because they can be considered to hold only for the particular cases.

For seismic applications, waves are supposed to have an elastic behaviour during their propagation inside the Earth. By definition, a material is elastic if it instantaneously returns to its original condition after removing the applied loads, and if it is instantaneously deformed by the loads. Therefore for seismological applications an elastic constitutive law has to be used and, this relationship can be defined as linear, as far as the induced deformations are small with respect to the characteristic lengths of the problem. This linear relation between stress and strain involves a fourth-order tensor  $\mathbf{c}$ :

$$\sigma_{ij} = c_{ijkl} \epsilon_{kl} \quad (1.12)$$

Due to the symmetry of strain and stress tensors and of the potential energy form the tensor  $\mathbf{c}$  has only 21 independent components of its 81. For an isotropic medium the independent components are only 2 and:

$$c_{ijkl} = \lambda \delta_{ij} \delta_{kl} + G (\delta_{ik} \delta_{jl} + \delta_{il} \delta_{jk}) \quad (1.13)$$

where  $\lambda$  and  $G$  are generally referred to as Lamè constants and in particular  $G$  is generally referred to as the shear modulus in the classical theory of elasticity. Substituting the equation (1.13) into the (1.12) we obtain the well-known relationship for isotropic media:

$$\sigma_{ij} = \lambda \delta_{ij} Tr(\boldsymbol{\epsilon}) + 2G \epsilon_{ij} \quad (1.14)$$

Where  $Tr(\boldsymbol{\epsilon})$  is the trace of strain tensor. Putting now the (1.14) into the (1.11) we obtain:

$$\rho \ddot{u}_i = f_i + \frac{\partial}{\partial x_j} \left[ \lambda \delta_{ij} \frac{\partial u_k}{\partial x_k} + G \left( \frac{\partial u_i}{\partial x_j} + \frac{\partial u_j}{\partial x_i} \right) \right] \quad (1.15)$$

For a homogeneous medium, for which the Lamè constants are uniform in space, the equation (1.15) can be put in the vectorial form:

$$\rho \ddot{\mathbf{u}} = \mathbf{f} + (\lambda + 2G) \vec{\nabla} (\vec{\nabla} \cdot \mathbf{u}) - \mu \nabla \times \nabla \times \mathbf{u} \quad (1.16)$$

### 1.1.3 Initial and Boundary conditions

In order to obtain an unique solution for equation (1.16) initial and boundary conditions (hereinafter *i.c.* and *b.c.*) have to be defined depending on the characteristics of the specific problem. Since the (1.16) is a second order hyperbolic equation, the *i.c.* concern the knowledge of displacement  $\mathbf{u}$  and its time derivative  $\dot{\mathbf{u}}$  at a give time  $t_0$  everywhere in the investigation domain. *B.c.*, instead, regard the knowledge of displacement or its normal derivative on the boundary of the domain at each time. Depending on the problem, three different boundary conditions can be imposed: Dirichelet *b.c.* fix a displacement on the boundary, Neumann *b.c.* impose a

prescribed traction (the normal derivative of displacement), Robin *b.c.* express mixed statements acting both on displacement and on traction. If we decompose the whole boundary of the domain in three different domains  $\partial\Omega = \partial\Omega_D \cup \partial\Omega_N \cup \partial\Omega_R$ , such that their mutual intersections have always zero measure on each part of boundary the appropriate *i.c.* and *b.c.* can be summarized as follows:

$$\left\{ \begin{array}{l} \rho \ddot{u}_i = f_i + \frac{\partial}{\partial x_j} \left( \lambda \delta_{ij} \frac{\partial u_k}{\partial x_k} + G \left( \frac{\partial u_i}{\partial x_j} + \frac{\partial u_j}{\partial x_i} \right) \right) \\ \mathbf{u}(\mathbf{x}, t = t_0) = \mathbf{u}_0 \\ \dot{\mathbf{u}}(\mathbf{x}, t = t_0) = \dot{\mathbf{u}}_0 \\ \\ \mathbf{u}(\mathbf{x}, t) = \mathbf{g}(\mathbf{x}, t) \quad \text{on } \partial\Omega_D \\ \boldsymbol{\sigma}(\mathbf{x}, t) \cdot \mathbf{n}(\mathbf{x}) = \mathbf{T}(\mathbf{x}, t) \quad \text{on } \partial\Omega_N \\ \mathbf{h}(\mathbf{u}(\mathbf{x}, t), \boldsymbol{\sigma}(\mathbf{x}, t) \cdot \mathbf{n}(\mathbf{x})) = \mathbf{h}(\mathbf{x}, t) \quad \text{on } \partial\Omega_R \end{array} \right. \quad (1.17)$$

The typical boundary conditions for seismological problems are generally either rigid boundary or free surface conditions and they correspond respectively to Dirichelet and Neumann *b.c.* with zero prescribed displacement or traction on the respective boundary.

## 1.2 The extended source

Tectonic earthquakes are produced by relative sliding between two rock blocks. This motion occurs mainly along a surface, which is generally referred to as the fault plane while the thickness of the rock involved in the sliding is several orders of magnitude smaller and thus the wavelengths related to this thickness are generally difficult to be observed on seismic data and modelled by numerical methods.

For some applications the finite extension of seismic sources can be neglected and the approximation of point source can be used depending on the wavelength  $\lambda$  of observation with respect to the size of the fault ( $L$  and  $W$  refer to the length and the width respectively) and the distance source-receiver  $d$ . This approximation, also known as Fraunhofer approximation, can be summarized by the relationship  $L \ll \lambda \ll d$ . This is the case, for instance, of active seismology where artificial

sources are used, of teleseismic data, where the wavelength is generally comparable to the size of the source but the source-receiver distance is much larger, and of microseismicity for which the dimension of the source is neglectable.

Conversely, for realistic local modelling of moderate to large earthquakes, the dimensions of the source cannot be neglected. In order to implement in a reliable way the fault plane characteristics in numerical simulations some simple physical boundary conditions must be taken into account. In this section the so-called Signorini's contact condition and Coulomb's friction condition will be described in a continuum domain as well as the linear slip weakening constitutive law, postponing to next sections the description of their discrete implementation in SEM.

### 1.2.1 Fault boundary conditions

Let us consider an elastic body of volume  $\Omega$ , whose surface consists of an external surface  $\partial\bar{\Omega}$ , and an internal fault surface  $\Gamma(\mathbf{x})$ , with a normal  $\mathbf{n}(\mathbf{x})$  pointing outwards. We arbitrarily define also the two sides of the fault surface as  $\Gamma_+$  and  $\Gamma_-$  (see Figure 1.1).

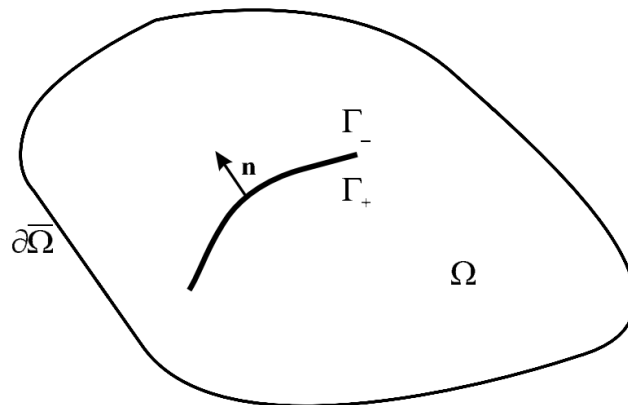


Figure 1.1 An elastic body  $\Omega$  with boundary surface  $\partial\bar{\Omega}$  and a fault surface  $\Gamma$

In this configuration the fault behaviour can be interpreted as a discontinuity of kinematic parameters across  $\Gamma$ . Let us define now a reference system  $\xi$  along  $\Gamma$  and let  $\mathbf{k}(\xi)$  be a vector field defined as:

$$\mathbf{k}_{\pm}(\xi) = \lim_{x \rightarrow \xi_{\pm}} \mathbf{k}(\mathbf{x}) \quad (1.18)$$

Where the subscripts  $\pm$  refer to the two sides of the fault and  $\mathbf{k}(\mathbf{x})$  is the same vector quantity defined in the whole elastic bulk. The discontinuity across the fault can be thus defined as:

$$\delta \mathbf{k}(\xi) = \mathbf{k}_{+}(\xi) - \mathbf{k}_{-}(\xi) \quad (1.19)$$

In the equation (1.19) the time-dependence is skipped. The kinematic quantities all along the fault are expected to be continuous and thus they can be obtained each other by time integration or derivation. If  $\Gamma$  is a regular surface a reference system  $(\mathbf{e}_{\xi_i}, \mathbf{n})$  local to the fault can be defined so that each quantity can be defined as follows:

$$\delta \mathbf{k} = \delta k^1 \mathbf{e}_{\xi_1} + \delta k^2 \mathbf{e}_{\xi_2} + \delta k^n \mathbf{n} \quad (1.20)$$

where the contributions  $\mathbf{e}_{\xi_i}$  represent any two orthogonal directions tangentially to the fault surface and can be grouped, whereas the normal direction  $\mathbf{n}$  is the direction orthogonal to the fault surface.

$$\delta \mathbf{k} = \delta \mathbf{k}' + \delta v^n \mathbf{n} \quad (1.21)$$

Generally the displacement and velocity discontinuity across the fault are referred to as slip and slip rate respectively and hereinafter we use  $\delta \mathbf{u}$  and  $\delta \mathbf{v}$  as symbols to represent them.

The total reactions  $\mathbf{R}_{T\pm}$  on the two sides of the fault satisfy the action-reaction principle:

$$\mathbf{R}_{T+} = -\mathbf{R}_{T-} = \mathbf{R}_T \quad (1.22)$$

It is the sum of a static term  $\mathbf{R}_0$ , given by initial stress state of the fault and a dynamic part  $\mathbf{R}$ , given by the elastodynamic contribution, which is:

$$\mathbf{R} = -\mathbf{T} = -\boldsymbol{\sigma} \cdot \mathbf{n} \quad (1.23)$$

It can be decomposed in the same reference system of (1.21) leading to:

$$\mathbf{R}_T = \mathbf{R}'_T + R''_T \mathbf{n} \quad (1.24)$$

Fault conditions can be defined as a relation between the kinematic quantities and the total reaction. The two following simple constraints represent a contact and a frictional condition, which were widely used in the current work.

### 1.2.2 Signorini's contact condition

Signorini's contact condition is the mathematical formalization of the impenetrability principle for the two sides of the fault. Moreover they allow to deal with the opening effects occurring when the two blocks start to move normally to the contact surface originating two free surfaces. These conditions can be expressed as:

$$\begin{cases} \delta u^n \geq 0; R_T^n \leq 0 \\ \delta u^n \cdot R_T^n = 0 \end{cases} \quad (1.25)$$

The Signorini's condition can be represented on a  $(\delta u^n, R_T^n)$  reference frame as in the Figure 1.2

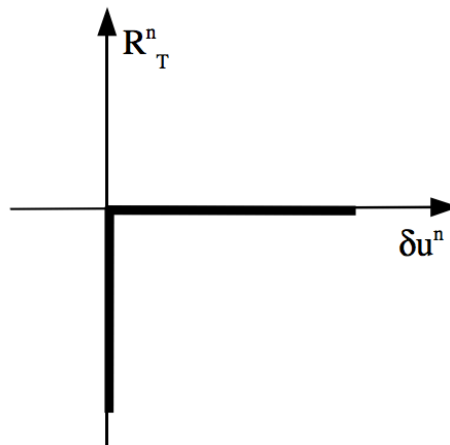


Figure 1.2: Signorini contact condition: either the two sides of the fault are stuck or, if opening occurs, both sides act like a free surface.

### 1.2.3 Coulomb's friction condition

According to the classical description of the friction, the system is at rest, until the tangential reaction reaches a failure threshold. Subsequently, the tangential reaction is constrained to a dynamic friction value and slip is activated allowing the slip rate to be different from zero. In the simplest Coulomb's friction law, the threshold value for the tangential reaction is proportional to the normal reaction  $R_T^n$  and here  $\mu$ , that is

the dimensionless proportionality factor, is generally referred to as the friction coefficient. If  $\delta v^t$  and  $R_T^t$  are respectively the tangential slip rate and the total tangential reaction the Coulomb condition can be summarized as:

$$\begin{cases} (|\mathbf{R}_T^t| + \mu R_T^n) |\delta v^t| = 0 \\ |\mathbf{R}_T^t| + \mu R_T^n \leq 0 \end{cases} \quad (1.26)$$

Since the tangential reaction is responsible for the sliding of the fault it is required to have the same direction and versus of slip rate. For a bidimensional problem the slip rate and the total reaction along the tangential component are scalar quantities and in that case a simple representation of Coulomb condition is shown in Figure 1.3

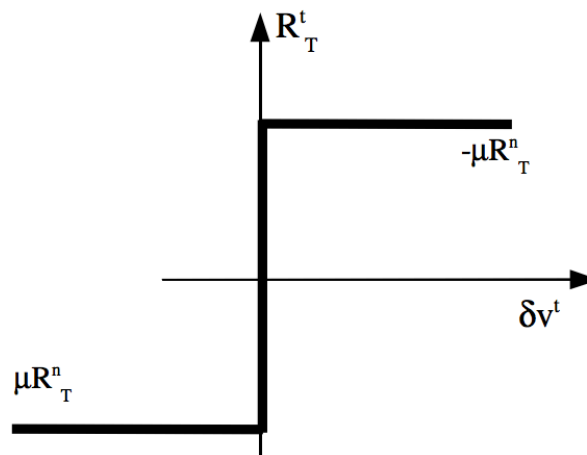


Figure 1.3 Coulomb frictional condition: the modulus of total tangential reaction is allowed to increase up to a prescribed threshold, until the system is at rest. While sliding it is constrained to the threshold value

#### 1.2.4 Frictional laws

For some general theoretical applications, the friction coefficient can be considered as a constant: this is the case of the analytical solutions proposed for a steady-state rupture propagating between different materials (Weertman, 1980; Ranjith and Rice, 2001). that will be analysed later. For realistic applications, instead, it may depend on several factors related to the kinematic parameters of the rupture and/or to state

variables depending on some properties of the contact surface (e.g. material, temperature, porosity etc.).

The simplest law used in mechanics is a two-value function according to which  $\mu = \mu_s$  until the system is at rest, whereas  $\mu = \mu_d$  while sliding, with  $\mu_s > \mu_d$ . For realistic applications the simplicity of this condition generates a singularity, which must be regularized, forcing to introduce some constraints leading to more complex problems.

The most used frictional laws are generally subdivided into two different categories: the Rate-and-State frictional laws (RSF) and the Slip Weakening Laws (SWL). In the former, the frictional coefficient generally depends both on the kinematics of the source and a state variable, that may macroscopically describe microscopic contact effects (Dietrich, 1979; Ruina, 1983; Dietrich & Kilgore, 1984, Scholz, 1998). A general representation of RSF can be given in terms of three constitutive parameters  $a, b$  and  $d_c$ , and a state variable  $K$ :

$$\mu(\delta v^t, K) = \mu^0 + a \log \frac{\delta v^t}{\delta v_0^t} + b \log \frac{K}{K_0} \quad (1.27)$$

With:

$$K = 1 - \frac{\delta v^t}{d_c} \quad (1.28)$$

Where  $d_c$  is a characteristic slip distance. This law also allows to take into account the different response to the increasing slip rate. Depending on  $a, b, \delta v_0^t$  and  $K_0$  the friction coefficient can either decrease originating unstable propagation (velocity weakening) or increase producing a stable sliding (velocity strengthening).

The SWF class assumes a frictional coefficient dropping from the static value to the dynamic one in a finite range of slip. The simplest SWF was proposed by Ida, 1972, according to which  $\mu$  drops over a prescribed slip length  $D_c$  generally referred to as critical slip value:

$$\mu(\delta u^t) = \begin{cases} \mu_s - \frac{\mu_s - \mu_d}{D_c} \delta u^t & \delta u^t < D_c \\ \mu_d & \delta u^t \geq D_c \end{cases} \quad (1.29)$$

Nor laboratory experiments neither seismological data allow to distinguish which kind of frictional law better fits the fault behaviour. Due to the simplicity in numerical implementation and its reliability deriving from laboratory and numerical experiments (Chambon et al., 2002; Bizzarri & Cocco, 2003) a linear SWL is used in this work for all numerical applications.

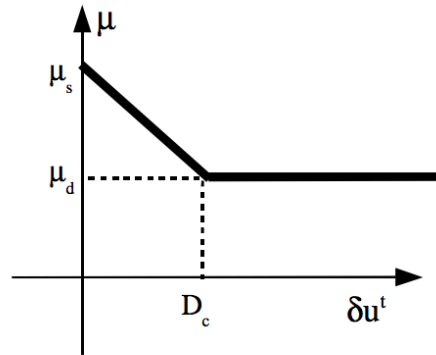


Figure 1.4 Linear slip weakening law

Finally the initial state of the fault can be inferred from the slip and rupture time maps obtained from waveform inversions or by using intermediary kinematic description of the rupture processes. It is worth to stress that due to the strong non-linearity of dynamic parameters the initial state of a fault before an earthquake is the most debated input for dynamic simulations and parametric studies are very often required to find the most reliable set up for complex and realistic applications.

### 1.3 Numerical models for seismological problems

As anticipated in the Introduction general problem presented in equation (1.17) can be analytically solved for very simple cases as for an isotropic and homogeneous domain of investigation. Moreover some analytical solutions can be found for a horizontally layered Earth imposing the appropriate boundary conditions between the layers.

Nevertheless when the equation (1.17) has to be used for realistic seismic waves propagation scenarios, which include complex geometries and velocity fields, the analytical solutions rapidly fail to exist and they need to be replaced by numerical techniques. As above mentioned for our purpose, a particular Finite Element Method,

known as Spectral Element Method (SEM), is suitable to handle this problem and in the next subsections the main features of the SEM will be introduced to model both the wave propagation and the fault rupture.

### 1.3.1 Variational formulation

A variational formulation of the general problem can be obtained multiplying each member of the equation (1.17) by test functions  $\mathbf{w}$ , which represent admissible perturbations for the displacement solutions. By analogy with the classical principle of the virtual work we have:

$$\int_{\Omega} \rho \ddot{\mathbf{u}} \mathbf{w} d\Omega = \int_{\Omega} \mathbf{f} \mathbf{w} d\Omega - \int_{\Omega} \bar{\nabla} \mathbf{w} : \mathbf{c} : \bar{\nabla} \mathbf{u} d\Omega + \int_{\partial\Omega_N} \mathbf{w} \mathbf{T} d\partial\Omega_N \quad (1.30)$$

The quantities  $\rho$ ,  $\mathbf{f}$ ,  $\mathbf{c}$  and  $\mathbf{T}$  have the same meaning as defined in the previous section and  $\mathbf{T}$  is defined on the Neumann boundary, which is a part of the whole boundary of domain. If  $\mathbf{u}$  is a solution of problem (1.17) it is easy to demonstrate, by integration by parts, that  $\mathbf{u}$  is also a solution of the problem (1.30). The viceversa is generally not true, in fact a solution of the differential formulation is supposed to have second derivatives everywhere, except possibly in a zero measure subset of the whole domain. Conversely the solutions of problem (1.30) have to belong to the following Sobolev space:

$$\tilde{H}_t^1(\Omega) = \left\{ \mathbf{v}'(\mathbf{x}, t) \in [H^1(\Omega) \times I]^{n_d}, \mathbf{v}'(\mathbf{x}, t) = \mathbf{g}(\mathbf{x}, t) \text{ on } \partial\Omega_D \right\} \quad (1.31)$$

where  $I$  is the interval of time variation, and the only requirement is thus that the first derivative is at least integrable on the domain and  $n_d$  represent the dimensionality of investigation domain (2 or 3 respectively for bi-dimensional and tri-dimensional seismological application).

From this point of view it is understandable why this problem is generally referred to as weak formulation. Moreover, in comparison with strong formulation of the problem, the weak formulation only requires that Dirichlet *b.c.* has to be verified by the solution, while the Neumann *b.c.* are included in the last integral of the second member of eq. (1.30). Neglecting that term the classical free-surface condition is naturally included in the solution. Also test functions  $\mathbf{w}$  have to belong to the Sobolev space:  $t = 0$

$$\tilde{H}_0^1(\Omega) = \left\{ \mathbf{w}(\mathbf{x}) \in [H^1(\Omega)]^{n_d}, \mathbf{w} = \mathbf{0} \text{ on } \partial\Omega_D \right\} \quad (1.32)$$

## 1.4 Spectral element method (SEM) for wave propagation

As already mentioned in Section 1.3 the Spectral Element Method is a particular Finite Element Method (FEM) presenting fast and more accurate convergence.

The FEM is mainly based on the idea of partitioning the domain of investigation with a set of simple geometrical entities (triangles or quadrangles for 2D and tetrahedra or hexahedra for 3D). Inside each element, the variational equation (e.g. (1.30)) is solved by constraining the solutions in a finite dimensional subspace, whose basis can be represented by polynomials. Once this approximation is performed the integrals can be solved either exactly or using a quadrature formula, which in any case allows to control the numerical dispersion. Since we integrate polynomials whose coefficients are unknown, the variational problem is reduced to an algebraic system, which is linear if the original problem is linear as the elasticity problem (1.30) is. The obtained matrices, which describe the algebraic system, are generally sparse due to the fact that each point is influenced only by its neighbourhoods.

As compared to the FEM, the SEM is based on a quadrangular discretization in bidimensional problem ( $n_d = 2$ ) and hexahedral in 3D ( $n_d = 3$ ), the integrals are computed on square elements  $[-1,1]^{n_d}$ , and both test functions  $\mathbf{w}$  and unknown fields are described by Lagrange polynomials associated to Gauss-Lobatto-Legendre integration formula points. Differently from the classical FEM, this scheme provides a mass matrix that is always diagonal. This reduces hugely the computational costs allowing to use high polynomial orders. In the following subsections the steps of the method will be presented.

### 1.4.1 Meshing and mapping over master element

Let us consider an investigation domain  $\Omega \subset \mathbb{R}^{n_d}$ , and  $n_{el}$  quadrangles or hexahedra  $\Omega_e$ , depending on whether a 2D or 3D problem is taken into account), such that  $\bigcup_{e=1}^{n_{el}} \Omega_e = \Omega$  and the measure  $\Omega_i \cap \Omega_j = \emptyset, \quad \forall i \neq j$ .  $\{\Omega_e\}$  is referred to as the set

of elements or the mesh covering the domain  $\Omega$ . Following from discretization of the domain and exploiting the additive property of the integration, the elastodynamic variational problem (1.30) can be expressed as follows:

$$\sum_{e=1}^{n_{el}} \int_{\Omega_e} \rho \ddot{\mathbf{u}} \mathbf{w} d\Omega = \sum_{e=1}^{n_{el}} \left( \int_{\Omega_e} \mathbf{f} \mathbf{w} d\Omega - \int_{\Omega_e} \bar{\nabla} \mathbf{w} : \mathbf{c} : \bar{\nabla} \mathbf{u} d\Omega + \int_{\partial\Omega_e \cap \partial\Omega_N} \mathbf{w} \mathbf{T} d\partial\Omega \right) \quad (1.33)$$

Where  $n_{el}$  is the number of elements and  $\Omega_e$  represents the domain related to each element. In order to use a quadrature formula, the integrals have to be evaluated on a master element  $\Lambda = [-1, 1]^{n_d}$ . Therefore we need a map (referred to as shape function), which is invertible with continuous first derivative. Generally linear or quadratic interpolations are preferred in order to reduce the quadrature errors. A linear 1D interpolation can be readily obtained between a line element  $[x_1; x_2]$  and the master on  $[-1; 1]$  simply imposing  $x(-1) = x_1$  and  $x(1) = x_2$ :

$$x(\zeta) = \frac{x_1}{2}(1 - \zeta) + \frac{x_2}{2}(1 + \zeta) \quad (1.34)$$

The terms containing the variable  $\zeta$  are the first order Lagrange polynomials associated to each point. To increase the degree of the shape function we contextually have to increase the number of control points and thus the number of Lagrange polynomials necessary to represent the mapping. Defining  $n$  interpolation points  $x_1, x_2, \dots, x_n$  the mapping (1.34) can be extended as follows:

$$x(\zeta) = \sum_i^n x_i L_i(\zeta) \quad (1.35)$$

where  $L_i(\zeta)$  are the  $n$  polynomials with degree  $n-1$  and they assume the following form:

$$L_i(\zeta) = \prod_{i \neq j} \frac{\zeta - \zeta_j}{\zeta_i - \zeta_j} \quad (1.36)$$

By construction, these polynomials satisfy the condition:  $L_i(\zeta_j) = \delta_{ij}$ .

The extension to a multidimensional mapping can be obtained by a tensor product as follows:

$$\mathbf{x}(\boldsymbol{\zeta}) = \sum_{i=1}^{N_p} \mathbf{x}_i L_i(\boldsymbol{\zeta}) \quad L_i(\boldsymbol{\zeta}) = \bigotimes_{j=1}^{n_d} L_i(\zeta^j) \quad (1.37)$$

The expression (1.37) is a product of polynomials and it represents a polynomial of degree  $K = k \cdot n_d$ . These polynomials do not contain a complete polynomial of degree  $K$ , but the maximum complete degree is  $k$ .

It is worth noting that if an edge of an element is the boundary between two elements the mapping of the common edge will be the same and thus independent of considered element (conforming mesh).

## 1.4.2 Galerkin approximation

As for the FEM, solutions and test functions are selected to belong to finite Sobolev subspaces. This approximation is the Galerkin approximation.

A particular Sobolev time-dependent subspace  $S_t^h(\Omega) \subset \tilde{H}_t^1(\Omega)$  with dimensionality  $h$  can be obtained by choosing appropriate basis functions  $\phi$ , defined from a set of collocation points. Thus in a  $n^d$  dimension domain with  $N$  defined collocation points  $N \times n_d$  basis function  $\phi_{K(j)}$  may be defined with  $K = 1, 2, \dots, N$  and  $j = 1, \dots, n_d$ . From this definition the approximate solution takes the form:

$$\mathbf{u}^h(\mathbf{x}, t) = \sum_{K=1}^N \sum_{j=1}^{n_d} \mathbf{U}^{K(j)}(t) \phi_{K(j)}(\mathbf{x}) \quad (1.38)$$

Where the coefficients  $\mathbf{U}^{K(j)}$  can be obtained substituting the equation (1.38) into the (1.33).

To get a set of basis function let us define a set of nodes  $\{\zeta_i\}_{i=1, \dots, N_e}$  on the master element  $\Lambda$ , and let us assume that the basis functions may be defined by the set of restrictions of such functions to the single elements. If we now consider a collocation node  $K$  of domain  $\Omega$  and if  $K$  does not belong to the element  $\Omega_e$ , then the restriction of the function to that element will be zero. Conversely in the element within which  $K$  is located, it will assume the value:

$$\phi_{K|\Omega_e} = \mathcal{F}_e \circ L_{K_e}(\zeta) \quad (1.39)$$

Where the subscript  $K_e$  represents an index for the node within the considered element, and  $\mathcal{F}_e$  is the local mapping related to the element  $e$  and expressed by equation (1.37). From the properties of Lagrange polynomials  $L$  the equation (1.39) is 1 on the node  $K_e$  and zero elsewhere.

### 1.4.3 Numerical integration: the Gauss-Lobatto-Legendre formula

The discrete problem expressed by equation (1.33) can be now solved in each element using the restriction given by equation (1.39). This leads to the following equation, which is valid within each element (Komatitsch & Vilotte, 1998):

$$\sum_{e=1}^{n_{el}} \int_{\Omega_e} \rho \ddot{\mathbf{u}}^h \mathbf{w}^h d\Omega = \sum_{e=1}^{n_{el}} \left( \int_{\Omega_e} \mathbf{f} \mathbf{w}^h d\Omega - \int_{\Omega_e} \bar{\nabla} \mathbf{w}^h : \mathbf{c} : \bar{\nabla} \mathbf{u}^h d\Omega + \int_{\partial\Omega_e \cap \partial\Omega_N} \mathbf{w}^h \mathbf{T} d\partial\Omega \right) \quad (1.40)$$

where the integrals are now defined in the finite  $h$ -dimensional Sobolev subspace  $S^h_t(\Omega) \subset \tilde{H}^1_t(\Omega)$  and in particular  $\mathbf{w}^h = \phi_{K(j)}$  are the basis functions of  $\mathcal{V}^h$  defined as:

$$\mathcal{V}^h(\Omega) = \left\{ \mathbf{w}^h(\mathbf{x}) \in [S^h(\Omega)]^{n_d}, \mathbf{w}^h = \mathbf{0} \text{ on } \partial\Omega_D \right\} \quad (1.41)$$

For sake of brevity only the inertial term is explicitly reported:

$$\sum_{e=1}^{n_{el}} \int_{\Omega_e} \rho \ddot{\mathbf{u}}^h \mathbf{w}^h d\Omega = \sum_{e=1}^{n_{el}} \sum_{M_e=1}^{N_e} \sum_{i=1}^{n_d} \ddot{U}^{M_e(i)} \int_{\Lambda} \rho \phi_{M_e(i)} \cdot \phi_{K_e(j)} J_e d\Lambda \quad (1.42)$$

Where  $J_e$  is the absolute value of the Jacobian of mapping  $\mathcal{F}_e$ ,  $M_e$  is an index, which runs along the points for each dimension.

The equation (1.42) is analytical integrable if  $\rho$  is a polynomial. The integrability of the first and third terms at second member depends on particular regularity conditions of the external forces and the traction. The second term at second member contains explicitly some derivative terms as  $\frac{\partial \xi^i}{\partial x^j}$ . These terms are ratios between polynomials and the integrals can be thus solved analytically as long as the zeroes of the denominators can be determined exactly.

Since the analytical integration is subjected to all presented constraints, numerical techniques are generally preferred to compute the integrals of equation (1.40). Moreover to get a numerical method, which is accurate and not expensive in terms of computation time, we prefer a quadrature formula rather than a numerical integration by intervals.

A numerical 1D quadrature formula approximates the integral with a sum:

$$\int_a^b f(x) dx \approx \sum_{i=0}^n \omega_i f(x_i) \quad (1.43)$$

Where  $x_i$  are  $n$  points in the interval of integration, whereas  $\omega_i$  are appropriate weights related to the points themselves. Within classical SEM a Gauss-Lobatto quadrature formula is selected. Considering that the integrals are always computed on the master element, the integration interval is  $[-1;1]$  and for a quadrature of order  $n$ , those zeroes are the roots of following polynomials:

$$P_n(\zeta) = (1 - \zeta^2) \mathcal{L}'_n(\zeta) \quad (1.44)$$

With  $\mathcal{L}'_n$  first derivative of Legendre polynomials of order  $n$ . It can be shown that for  $n \geq 2$  the (1.44) has  $n+1$  zeroes in the interval of master element with the first and the last which are properly  $-1$  and  $1$  (Schwab, 1998). Appropriate weights  $\omega_i$  can be obtained integrating the Lagrange polynomials related to the node  $\zeta_i$ . Moreover the Gauss-Lobatto-Legendre (GLL) is a really efficient quadrature formula because the polynomials of degree  $2n$  can be exactly integrated by using  $n+1$  GLL points (Maday & Patera, 1989). The GLL points are also selected as the collocation points where the solutions are computed.

The formulas for multi-dimensional problem can be obtained again by tensor product and the equation (1.42) can be developed as:

$$\begin{aligned} (\mathbf{w}^h, \rho \ddot{\mathbf{u}}) = & \sum_{e=1}^{N_e} \sum_{i_1, i_2, i_3} \sum_{n_1, n_2, n_3}^{n_d} U^{I_e(k)} \omega_{n_1} \omega_{n_2} \omega_{n_3} \rho J_{N_e} \\ & L_{i_1}(\zeta_{n_1}) L_{i_2}(\zeta_{n_2}) L_{i_3}(\zeta_{n_3}) L_{m_1}(\zeta_{n_1}) L_{m_2}(\zeta_{n_2}) L_{m_3}(\zeta_{n_3}) \end{aligned} \quad (1.45)$$

Where the point  $I_e$  is individuated by coordinates  $i_1, i_2, i_3$  and these indices are related also to the collocation points within the element (see Section 1.4.1). The other indices  $(n_1, n_2, n_3)$  are instead related to the GLL points.

The equation (1.45) (and the other terms of general problem) can be further simplified considering for the quadrature formula the collocation points deriving from Lagrange polynomials. This allows to exploit the numerical orthogonality of those polynomials leading to the following algebraic system:

$$\mathbf{M} \ddot{\mathbf{U}} = \mathbf{K} \mathbf{U} + \mathbf{F}^{ext} + \mathbf{B}^T \mathbf{T} \quad (1.46)$$

Where the terms  $\mathbf{M}$  and  $\mathbf{K}$  are respectively referred to as mass matrix and stiffness matrix, the vector  $\mathbf{F}^{ext}$  contains the contribution of external loads and the last term is related to the traction on the Neumann boundary. The term  $\mathbf{U}$  contains the value of displacement in the collocation points. For the numerical orthogonality of

Lagrange polynomials the mass matrix is diagonal and it can be inverted once at the beginning of the simulation to get an explicit time stepping. Moreover the mass matrix as well as the sparse stiffness matrix can be considered independent of time since the density and the elastic properties are pretty constant for all seismological applications.

#### 1.4.4 Time stepping evolution: the Newmark algorithm

The algebraic system expressed by (1.46) can be rewritten substituting the acceleration with velocity as follows:

$$\mathbf{M}\dot{\mathbf{V}} = \mathbf{F}^{\text{int}}(\mathbf{U}) + \mathbf{F}^{\text{ext}} \quad (1.47)$$

Where the term  $\mathbf{K}\mathbf{U}$  has been substituted by a general term representing the internal forces dependent on  $\mathbf{U}$  and the traction term vanishes assuming free surface boundary conditions.

The temporal evolution of the system can be achieved using a Newmark algorithm, which is based upon a Taylor expansion of displacement and velocity within each interval  $[t_n, t_{n+1}]$ . The Taylor series can be arrested to the second order, which is the minimum for second order problems (Zienkiwicz and Taylor, 2000).

In a velocity formulation we get the following expansion:

$$\mathbf{V}_{n+1} = \mathbf{V}_n + \Delta t \mathbf{M}^{-1} (\mathbf{F}^{\text{int}}(\mathbf{U}_{n+\alpha}) + \mathbf{F}_{n+\alpha}^{\text{ext}}) \quad (1.48)$$

Any quantity at time  $n + \alpha$  can be represented as:

$$\mathbf{U}_{n+\alpha} = (1 - \alpha)\mathbf{U}_n + \alpha\mathbf{U}_{n+1} \quad (1.49)$$

The displacement and acceleration can be in turn developed as:

$$\mathbf{U}_{n+1} = \mathbf{U}_n + \left(1 - \frac{\beta}{\gamma}\right) \Delta t \mathbf{V}_n + \frac{\beta}{\gamma} \Delta t \mathbf{V}_{n+1} + \Delta t^2 \left(\frac{1}{2} - \frac{\beta}{\gamma}\right) \mathbf{A}_n \quad (1.50)$$

$$\mathbf{A}_{n+1} = \frac{1}{\gamma \Delta t} (\mathbf{V}_{n+1} - \mathbf{V}_n) + \left(1 - \frac{1}{\gamma}\right) \mathbf{A}_n \quad (1.51)$$

In order to conserve the angular momentum  $\beta/\gamma = 0.5$  and  $\gamma = 1$  (Zienkiewicz and Taylor, 2000). In that case the displacement is independent of the acceleration and referring to the equation (1.49) we can develop an energy conservation scheme by using the condition  $\alpha = 1/2$ . For  $\alpha > 1/2$  we have a dissipative scheme, whereas the

condition  $\alpha < 1/2$  generates an infinite increasing of energy in the medium originating an unstable algorithm.

Starting from the Newmark scheme described by equations (1.48)-(1.49)-(1.50) a predictor corrector algorithm can be developed according to which during the prediction phase the velocity is assumed to be constant:

$$\tilde{\mathbf{V}}_{n+1} = \mathbf{V}_n \quad (1.52)$$

Which leads to the following predicted displacement value:

$$\tilde{\mathbf{U}}_{n+1} = \mathbf{U}_n + \frac{1}{2} \Delta t \mathbf{V}_n + \frac{1}{2} \Delta t \tilde{\mathbf{V}}_{n+1} \quad (1.53)$$

$$\mathbf{U}_{n+\alpha} = (1-\alpha)\mathbf{U}_n + \alpha\tilde{\mathbf{U}}_{n+1} \quad (1.54)$$

Where the terms with the tilde represent the predicted terms.

The correction phase instead use the equation (1.48) and (1.54) to update the term  $\mathbf{V}_{n+1}$  as follows:

$$\mathbf{V}_{n+1} = \mathbf{V}_n + \Delta t \left[ \mathbf{F}_{n+\alpha}^{\text{ext}} + \mathbf{F}^{\text{int}}(\tilde{\mathbf{U}}_{n+\alpha}) \right] \quad (1.55)$$

Finally, correcting the (1.53), the corrected displacement is:

$$\mathbf{U}_{n+1} = \tilde{\mathbf{U}}_{n+1} + \frac{1}{2} \Delta t (\mathbf{V}_{n+1} - \mathbf{V}_n) \quad (1.56)$$

Since the acceleration does not explicitly appear in the scheme it can be computed at the end of the temporal iteration simply using the equation (1.51).

This scheme leads to a rapid convergence after one iteration, thus we have chosen to use the value of displacement and velocity computed after only one correction such that the computational costs is drastically reduced. Nevertheless it is possible to achieve a most accurate solution imposing a tolerance threshold and performing a multi-corrector algorithm, starting from the just described scheme.

$$\mathbf{V}_{n+1,0} = \mathbf{V}_n$$

$$\mathbf{U}_{n+1,(k)} = \mathbf{U}_n + \frac{1}{2}\Delta t\mathbf{V}_n + \frac{1}{2}\Delta t\mathbf{V}_{n+1,(k)} \quad (1.57)$$

$$\mathbf{U}_{n+\alpha,(k)} = (1-\alpha)\mathbf{U}_n + \alpha\mathbf{U}_{n+1,(k)}$$

$$\mathbf{V}_{n+1,(K)} = \mathbf{V}_n + \Delta t \left[ \mathbf{F}_{n+\alpha}^{\text{ext}}(\mathbf{U}_{n+\alpha,(K-1)}) \right]$$

where the indices in the parenthesis are referred to the iterations in the multicorrection. This procedure is stopped when

$$\frac{\|\mathbf{V}_{n+1,(K)} - \mathbf{V}_{n+1,(K-1)}\|}{\|\mathbf{V}_{n+1,(K)}\|} < \varepsilon \quad (1.58)$$

with  $\varepsilon$  imposed tolerance.

## 1.5 The extended source with SEM

### 1.5.1 Domain decomposition and traction at split node method

To model the extended source with Spectral Element Method, let us consider the fault boundary conditions described in section 1.2.1 as shown in Figure 1.1. Since we expect to describe the discontinuity of kinematic fields along the fault, the problem may be tackled performing a domain decomposition in two parts. By analogy with Figure 1.1 with  $\Gamma$  as fault plane, the subdivision has to be performed over a surface  $\gamma \supseteq \Gamma$  (See Figure 1.5).

The decomposition of the domain is performed splitting the nodes on the fault onto the two regions and after the computation of traction the assembling is performed (traction at split node).

The equation (1.30) can be rewritten separately for each region:

$$\int_{\Omega_i} \rho_i \ddot{\mathbf{u}}_i \mathbf{w}_i d\Omega = \int_{\Omega_i} \mathbf{f}_i \mathbf{w}_i d\Omega - \int_{\Omega_i} \vec{\nabla} \mathbf{w}_i : \mathbf{c}_i : \vec{\nabla} \mathbf{u}_i d\Omega + \int_{\gamma} \mathbf{w}_i \mathbf{T}_i d\gamma \quad (1.59)$$

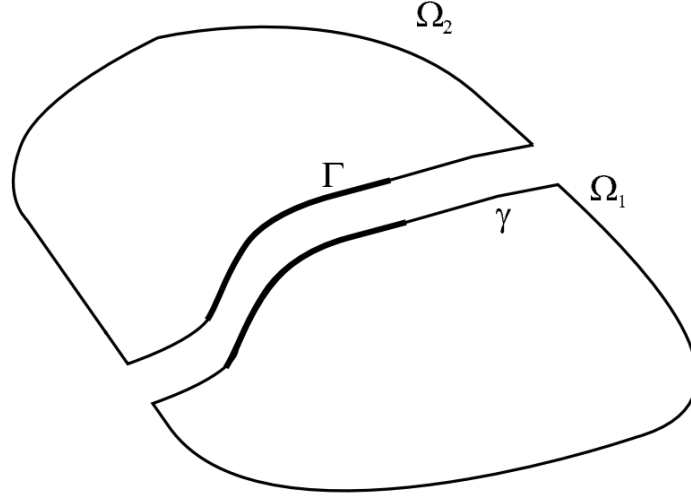


Figure 1.5 Domain decomposition for the numerical discretization of fault problem

Where the last term represents the traction term along  $\gamma$ . After discretization, the algebraic systems for each domain are:

$$\mathbf{M}_i \ddot{\mathbf{U}}_i = \mathbf{F}_i^{ext} + \mathbf{F}_i^{int} + \bar{\mathbf{B}}^T \mathbf{T}_i \quad (1.60)$$

The traction  $\mathbf{T}_i$  can be substituted with the reaction  $\mathbf{R}_i = -\mathbf{T}_i$  on the fault and considering the action-reaction principle on the interface between the two sides of the decomposition we can rewrite the equation (1.22) as:

$$\mathbf{R}_1 = -\mathbf{R}_2 = -\mathbf{R} \quad (1.61)$$

Since along  $\gamma - \Gamma$  the displacement and acceleration are continuous summing the equation (1.60) the standard assembling is recovered. On the other hand, both displacement and acceleration are expected to be discontinuous along  $\Gamma$  and they have to be evaluated from the intersection of conditions given by (1.60) with the contact and friction conditions (1.25)-(1.26). Thus we can consider the restriction of problem (1.60) to the fault surface. We get:

$$\mathbf{M}_i^f \ddot{\mathbf{U}}_i^f = \mathbf{F}_i^f - \mathbf{B}^T \mathbf{R}_i \quad (1.62)$$

where the terms with superscript  $\{ \}^f$  and the term  $\mathbf{B}^T$  are the restriction of corresponding matrices to the fault plane. The operator, which performs this

projection simply extracts some blocks from original matrices, thus  $\mathbf{M}_i^f$  holds the diagonality of  $\mathbf{M}$ . We can write an explicit scheme in acceleration:

$$\ddot{\mathbf{U}}_i^f = \tilde{\mathbf{M}}_i^{-1} \left( \tilde{\mathbf{F}}_i - \mathbf{B}^T \mathbf{R}_i \right) \quad (1.63)$$

On a conforming mesh (where the collocation points along discontinuity coincide) slip acceleration across the fault can be achieved from the difference between the equations (1.63):

$$\delta \ddot{\mathbf{U}}^f = \left( \tilde{M}_2^{-1} \tilde{\mathbf{F}}_2 - \tilde{M}_1^{-1} \tilde{\mathbf{F}}_1 \right) - \left( \tilde{M}_2^{-1} + \tilde{M}_1^{-1} \right) \mathbf{B}^T \mathbf{R} \quad (1.64)$$

where the action-reaction principle (1.61) is used. The (1.64) leads to a linear relation between the acceleration discontinuity  $\delta \ddot{\mathbf{U}}^f$  and the reaction  $\mathbf{R}$ .

The acceleration for zero reaction is:

$$\delta \ddot{\mathbf{U}}^{free} = \tilde{M}_2^{-1} \tilde{\mathbf{F}}_2 - \tilde{M}_1^{-1} \tilde{\mathbf{F}}_1 \quad (1.65)$$

and it would represent the slip acceleration obtained if free surface condition were imposed along both sides of the fault.

The equation (1.64), coupled with Signorini and Coulomb conditions allows to estimate the kinematic fields on the fault plane (Festa, 2004).

## 1.5.2 Time resolution algorithm

The equations (1.50) (considering the conservation of angular momentum) and (1.48), respectively for displacement and velocity lead to the following second order scheme for the elastodynamic equations condensed on the fault:

$$\delta \mathbf{U}_{p+1}^f = \delta \mathbf{U}_p^f + \frac{1}{2} \Delta t \delta \mathbf{V}_p^f + \frac{1}{2} \Delta t \delta \mathbf{V}_{p+1}^f \quad (1.66)$$

$$\delta \mathbf{V}_{p+1}^f = \delta \mathbf{V}_p^f + \Delta t \delta \dot{\mathbf{U}}_{p+\alpha}^{free} - \mathbf{C}_\Gamma \mathbf{R}_{p+\alpha} \quad (1.67)$$

where:

$$\mathbf{C}_\Gamma = \Delta t \left( \tilde{M}_2^{-1} + \tilde{M}_1^{-1} \right) \mathbf{B}^T \quad (1.68)$$

And the scheme (1.66)-(1.67) is obtained from equation (1.64). Since mass and interface matrices are diagonal with positive eigenvalues, the matrix  $\mathbf{C}_\Gamma$  is invertible and it has positive eigenvalues too.

Equation (1.67) provides a relation between the slip rate at time  $t_{p+1}$  and the reaction at time  $t_{p+\alpha}$ . Nevertheless it was show that if  $\alpha = 1$  was used (dissipative scheme cfr. Section 1.4.4) the numerical spurious oscillations due to the discontinuity are damped (Festa, 2004) and thus this scheme was used for all numerical problems with extended source in the current work. Therefore the (1.67) gives a direct relation between the slip rate and the reaction at time  $t_{p+1}$ , given the slip rate at the previous time step and the elastodynamic load ( $\delta\ddot{\mathbf{U}}^{free}$ ) predicted at time  $t_{p+1}$ . Now grouping all the quantities that can be computed we get:

$$\delta\mathcal{V}_p = \delta\mathbf{V}_p^f + \Delta t \delta\dot{\mathbf{U}}_{p+1}^{free} \quad (1.69)$$

and from (1.69) the following linear relation between slip rate and reaction can be obtained:

$$\delta\mathbf{V}_{p+1}^f = \delta\mathcal{V}_p - \mathbf{C}_\Gamma \mathbf{R}_{p+1} \quad (1.70)$$

Before using the (1.70) to determine the frictional sliding of the fault we should verify the Signorini's contact condition (1.25); thus using the (1.66) and the (1.70) we can obtain the following relation between the slip and the reaction at the instant  $t_{p+1}$ :

$$\delta\mathbf{U}_{p+1}^f = \delta\mathbf{U}_p^f + \Delta t \delta\mathbf{V}_p^f + \frac{1}{2} \Delta t^2 \delta\ddot{\mathbf{U}}_{p+1}^{free} - \frac{1}{2} \Delta t \mathbf{C}_\Gamma \mathbf{R}_{p+1} \quad (1.71)$$

By analogy with the (1.69) and (1.70) we can group the terms which can be computed before as:

$$\delta\mathcal{U}_p = \delta\mathbf{U}_p^f + \Delta t \delta\mathbf{V}_p^f + \frac{1}{2} \Delta t^2 \delta\ddot{\mathbf{U}}_{p+1}^{free} \quad (1.72)$$

To obtain a linear relation between slip and reaction:

$$\delta\mathbf{U}_{p+1}^f = \delta\mathcal{U}_p - \mathbf{Q}_\Gamma \mathbf{R}_{p+1} \quad (1.73)$$

with:

$$\mathbf{Q}_\Gamma = \frac{1}{2} \Delta t \mathbf{C}_\Gamma \quad (1.74)$$

According to the contact condition, the Signorini's law and the normal component of (1.73) have to be jointly verified. This result can be reached in two steps: first, normal slip is supposed to be zero at time  $t_{p+1}$  and the normal reaction from (1.73) is:

$$\mathbf{R}_{p+1}^n = \mathbf{Q}_\Gamma^{-1} \delta\mathcal{U}_p^n \quad (1.75)$$

Where the superscript  $\{ \}^n$  represents the normal component. To compute the total normal reaction the static part of normal reaction has to be added to the (1.75):  $(\mathbf{R}_{T,p+1}^n = \mathbf{R}_{p+1}^n + \mathbf{R}_{0,p+1}^n)$ , where the subscript  $\{ \}_T$  and  $\{ \}_0$  represent respectively the total and static contributions to normal reaction.

Equation (1.75) is a vector relation, involving all collocation points on the fault, whereas the Signorini's law is purely local. However the (1.75) can be referred to each collocation point due to the diagonality of matrix  $\mathbf{Q}_\Gamma$ . Considering the point  $K$  on the fault, the reaction at zero normal slip is:

$$R_{T,p+1}^{n,K} = \frac{1}{Q_\Gamma^{KK}} \delta U_p^{n,K} + R_{0,p+1}^{n,K} \quad (1.76)$$

If  $R_{T,p+1}^{n,K} \leq 0$ , the Signorini condition is automatically verified and the couple  $(0, R_{T,p+1}^{n,K})$  is the solution for the contact law. Otherwise, if  $R_{T,p+1}^{n,K} > 0$ , normal reaction is forced to be null and  $\delta U_{p+1}^{n,K}$  is achieved from the projection of linear law (1.73) onto the x-axis (See Figure 1.6):

$$\delta U_{p+1}^{n,K} = Q_\Gamma^{KK} R_{T,p+1}^{n,K} \quad (1.77)$$

Since  $Q_\Gamma^{KK} \geq 0$ , the intersection between Signorini and the equation (1.73) always has an unique solution.

From Signorini conditions, when opening occurs the two sides of the fault behave as free surfaces and Coulomb condition (1.26) is not required to be verified. Otherwise the Coulomb condition can be solved by analogy with the procedure adopted for Signorini. Let us consider the bidimensional case: the tangential slip velocity  $\delta \mathbf{V}_{p+1}^t$  is supposed to be null and the scalar tangential reaction can be computed from the (1.70):

$$\mathbf{R}_{p+1}^t = \mathbf{C}_\Gamma^{-1} \delta \mathcal{V}_p^t \quad (1.78)$$

Where the superscript  $\{ \}^t$  represents the tangential component. Now the total tangential reaction is:  $(\mathbf{R}_{T,p+1}^t = \mathbf{R}_{p+1}^t + \mathbf{R}_{0,p+1}^t)$  where the subscript  $\{ \}_T$  and  $\{ \}_0$  represent respectively the total and static contribution to tangential reaction.

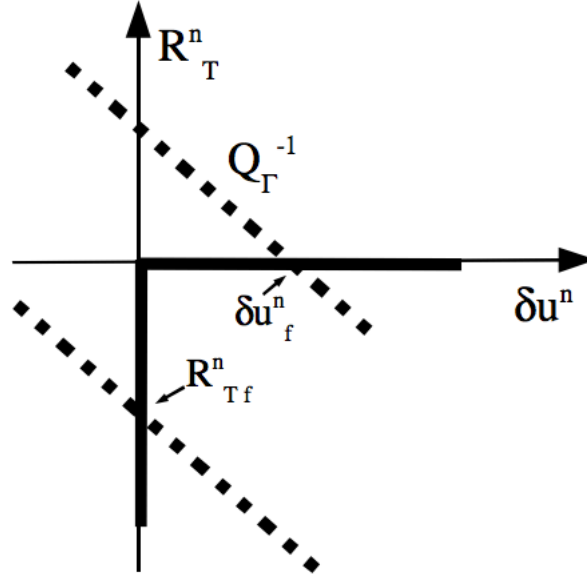


Figure 1.6 Intersection of Signorini law with eq. (1.73). Zero normal slip (no opening) gives a normal reaction estimate. If this estimate lies on the negative vertical axis,  $(0, R_y^n)$  is a solution. Otherwise the reaction value is projected on the positive horizontal axis, and the solution is  $(\delta u_f^n, 0)$

Again the relation (1.78), evaluated globally for the collocation points on the fault can be referred to the single point due to the diagonality of  $\mathbf{C}_\Gamma$ . If  $R_{T,p+1}^{t,K}$  represents the tangential reaction at the collocation point  $K$ , it should be compared with the threshold  $-\mu(\delta \tilde{u}_{p+1}^{t,K}) R_{T,p+1}^{n,K}$ , where  $\delta \tilde{u}_{p+1}^{t,K}$  is the slip estimated in the prediction phase and  $R_{T,p+1}^{n,K}$  is the normal reaction from Signorini condition. If total tangential reaction is smaller than the threshold:

$$R_{T,p+1}^{t,K} \leq -\mu(\delta \tilde{u}_{p+1}^{t,K}) R_{T,p+1}^{n,K} \quad (1.79)$$

the couple  $(0, R_{T,p+1}^{t,K})$  is the solution. Otherwise, the tangential reaction value should be projected onto the straight line  $R_{T,p+1}^{t,K} = -\mu(\delta \tilde{u}_{p+1}^{t,K}) R_{T,p+1}^{n,K}$  and the corresponding solution for slip rate is:

$$\delta V_{p+1}^{t,K} = \delta \mathcal{V}_p^{t,K} + C_\Gamma^{KK} \mu(\delta \tilde{u}_{p+1}^{t,K}) R_{T,p+1}^{n,K} \quad (1.80)$$

Thus when fault is frictionally sliding the solution is the couple  $(\delta V_{p+1}^{t,K}, -\mu(\delta \tilde{u}_{p+1}^{t,K})R_{T,p+1}^{n,K})$ . For 3D models, collinearity of tangential reaction and slip rate has to be added to the presented conditions:

$$\delta \mathbf{V}_{p+1}^{t,K} \times \mathbf{R}_{T,p+1}^{t,K} = \mathbf{0} \quad (1.81)$$

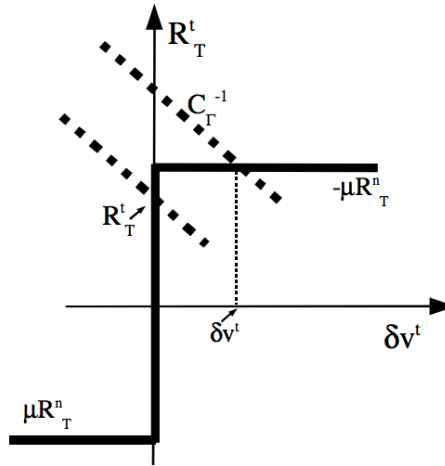


Figure 1.7 Intersection of Coulomb law and equation (1.78) for a given collocation point on the fault plane. A solution can be found comparing the reaction  $R_T^t$  (obtained from imposing zero slip rate), with the threshold  $-\mu R_T^n$ . If  $R_T^t \leq -\mu R_T^n$ , the couple  $(0, R_T^t)$  is the solution; otherwise equation (1.78) is projected onto the straight line  $R_T^t = -\mu R_T^n$  and the couple  $(\delta v^t, -\mu R_T^n)$  is the solution.

# 2 Bimaterial interfaces

## 2.1 Introduction

Seismic rupture often propagates at the interface between materials with different elastic properties. Several experimental observations, analytical results in the framework of fracture mechanics, laboratory and numerical experiments evidenced some particular features directly deriving from the propagation of fracture along these bimaterial interfaces. Geological observations highlighted the presence of a preferred direction of propagation during the bigger recent events recorded on the San Andreas Fault (Harris & Day, 2005). Other works demonstrated that this break of symmetry is also responsible for the asymmetric distribution of near-surface damage both for the Anatolian Fault (Dor *et al.*, 2005) and the San Andreas Fault (Dor *et al.*, 2006).

In the framework of fracture mechanics several efforts have been done to explain the near-crack tip oscillatory behaviour due to a crack propagating between different materials (Williams, 1959). This oscillatory feature has to be normalized by introducing complex Stress Intensity Factors (SIF) which in turn require the definition of an arbitrary length to be related to classical SIF definition, in order to achieve asymptotic solutions of classical types (Rice, 1988). Moreover the complex SIF couple unavoidably the normal and shear stress ahead the crack tip and thus the mode I and II of crack propagation. This mode mixity was widely investigated from an analytical point of view in the solutions provided by works of Cherepanov (1962), England (1965), Erdogan (1965) and Rice and Sih (1965)

The crack tip fields for bimaterial static cracks were analyzed by using classical Mushkelisvili (Mushkelisvili, 1953) formalism (Rice, 1988) and Stroh (Stroh, 1958, 1962) formalism (Suo, 1990). In both cases traction ahead the crack tip and displacement jump behind the crack tip were explicitly computed, showing clearly the effects of mode mixity, the presence of complex SIF and the need to establish a length to define asymptotic crack tip solutions. Later Yang *et al.* (1991) obtained similar

solutions for stationary cracks by using Stroh formalism and by postulating that in plane components are the leading singularities for the problem.

By adding the effects of other singular components Liu et al (1993) computed solutions for a not stationary growing crack. Later Nikolic and Djokovic (2009) have numerically confirmed these solutions, whereas Agraval and Karlsson (2006) provided a quantitative measurement of mode mixity by using the Virtual Crack Closure Technique (VCCT) both for stress field and energy release rate.

In the same framework Deng (1993a-b, 1994) has investigated the crack tip fields when a classical Coulomb friction law is imposed along the fault interface both in homogeneous and bimaterial background. In this case the oscillatory modes are not evidenced in the asymptotic solutions and when a bimaterial interface is taken into account the square root singularity ( $\tau(r) \propto r^{-1/2}$ ) becomes weaker or stronger ( $\tau(r) \propto r^{-1/2 \pm \delta}$ ) depending on the displacement conditions behind the crack tip. Moreover when the interface is a mirror plane for the two blocks the mode I and mode II of propagation are decoupled and the propagation of crack is only due to the shear loading.

Bimaterial problem was also analytically investigated in terms of slip response to small shear/normal perturbations around the yield stress and the most relevant result is that an unstable self-healing pulse can propagate only along a favoured direction also for constant friction coefficient and even if the shear stress is slightly lower than the yield stress (Weertman, 1980). This direction can be considered as a favoured direction for the system and it is always the direction of slip in more compliant medium. Moreover Weertman (1980) analytically showed that if small dissimilarity is considered between the layers on the two sides of interface a propagating generalized Rayleigh slip wave speed  $C_{gr}$  can be defined by analogy with the Rayleigh speed in homogeneous media. This speed is intermediate between the Rayleigh speeds in the two media and it represents properly the steady state propagation speed for the above mentioned slip pulse.

When a classical Coulomb friction law, the problem is analytical and physical ill-posed due to the lack of a length/time scale which express the normal/tangential stress coupling when the shear stress follow instantaneously the abrupt normal stress changes induced by the bimaterial propagation. Several works (Renardy, 1992;

Adams, 1995; Martins *et al.*, 1995 - Martins & Simões 1995 - Simões & Martins 1998, Ranjith & Rice, 2001) showed that this ill-posedness generates unstable diverging slip rate response to a single mode shear stress perturbation. As a consequence when numerical experiments are performed some unexpected features are developed as the split pulse evidenced by Andrews & Ben-Zion (1997) or unavoidable grid effects with non-convergent solutions for grid refinement (Cochard & Rice, 2000). These grid effects are evidenced also when a linear slip weakening law (Ide, 1972) is used to regularize the singularity at the crack tip (Harris & Day, 1997). Harris & Day (1997) also found that, even when the rupture can propagate bilaterally the direction of slip of more compliant medium is still a favoured direction in the sense of higher rupture acceleration, higher slip rate values in the vicinity of crack front and higher coseismic slip.

Experimental evidences showed the behaviour of frictional sliding as a consequence of variable normal pressure (Prakash & Clifton, 1993 - Prakash 1998). These experiments revealed a delayed frictional response to normal stress perturbations and this delay can be a function of increasing slip.

Cochard & Rice (2000) and Ranjith & Rice (2001) showed that an experimentally based regularization law, deriving from Prakash and Clifton observations provides regularization both from an analytical (the stability problem becomes well-posed for shear stress perturbations) and numerical (no grid dependence of solutions) point of view. This regularization provides for a delay between the abrupt normal stress variations induced by bimaterial propagation and the effects of these variations on the shear stress, giving to the shear stress itself a fading memory of the recent normal stress perturbations. This regularization is practically a relaxation mechanism that involves a time delay proportional to a characteristic slip distance, normalized by the local slip rate value at each point. Nevertheless this single mechanism does not allow to develop a spontaneous pulse growth from a pore pressure increasing with time, that is the nucleation proposed by numerical experiments by Andrews & Ben-Zion (1997). To aim this Cochard & Rice (2000) also proposed a new regularization involving contemporary two mechanisms of regularization, where the second one provides for a relaxation simply depending on time, modifying the expected frictional strength even if no frictional sliding is occurring. Ranjith & Rice (2001), summarizing all the previous analytical results, showed the intrinsic unstable modes growth, evidencing

that the higher is the frequency of single mode, the faster is the instability growth rate. They also showed what are the conditions for which a steady state mode propagating at  $C_{gr}$  can exist, when a Coulomb friction law and constant friction coefficient is used, and what are the expected stationary speeds for the unstable modes as a function of contrast of impedance and friction coefficient even if  $C_{gr}$  does not exist.

Rubin & Ampuero (2007) numerically investigated the bimaterial problem in the framework of linear slip weakening by using contemporary both regularization mechanisms depending on slip rate and time. They obtained bilateral ruptures with a favoured direction along the same direction found by Weertman (1980) and Harris and Day (1997). They also showed how this break of symmetry is due to the different features of normal stress perturbations along the opposite directions. In this way they were able to give an interpretation to the asymmetric distribution of aftershocks around the San Andreas Fault, in terms of bimaterial effects.

Laboratory experiments have confirmed the asymptotic speed  $C_{gr}$  for low shear wave speed ratios (Xia *et al.* 2004 - Xia *et al.* 2005). In these experiments, for particular conditions, supershear acceleration along not favoured direction were observed.

Langer *et al.*, 2012 showed the supershear transitions by performing numerical experiments involving bimaterial media. In particular these transitions along not favoured direction seems to be due to the extensional effect generated by waves ahead the crack front. These waves decrease the failure threshold along the not favoured direction allowing rupture to accelerate up to supershear velocities.

Starting from the relaxation mechanism deriving from Prakash and Clifton experiments, Kammer *et al.* (2014) have identified a critical length scale, below which the solutions become independent of the parameters of regularization performing numerical experiments for the arresting phase of a propagating rupture. To aim this they interpreted the Prakash-Clifton relaxation in terms of low-pass filter acting on dynamic normal stress perturbations. This filter should ideally damp the higher frequencies responsible for the fast growth of instability without attenuates the lower frequencies containing the physical information deriving from pressure changes. Nevertheless, they used contemporary both relaxation mechanisms (by time and slip) and the detected length is actually a slip and thus a local measure not directly related to a characteristic length of the rupture.

As far as we know, all numerical models proposed exploited the Prakash-Clifton experimentally-based regularization law only to avoid the numerical effects deriving from the ill-posedness of the bimaterial propagation coupled with a classical Coulomb friction law.

The numerical models proposed in this work aim to individuate the physical meaning of this regularization mechanism in terms of the missing length/time scale of shear/normal coupling and the effects of the regularization parameters on the numerical well-posed models. This is expected to lead to a physically reasonable way to relax the shear stress as response of normal stress perturbations and can allow to distinguish reliable physical solutions from simply numerical well-posed models. Moreover we aim to find a specific length related to the dynamics of crack, which can be considered as the characteristic length of coupling between shear traction and normal stress, in the framework of a linear slip weakening friction law.

To aim this a parametric study was performed involving separately the two relaxation mechanisms (based on slip rate and time) contained in the classical Prakash-Clifton-based regularization (Cochard & Rice, 2000) providing physical and numerical interpretation for the solutions obtained. Then a new regularization is also proposed where the time delay is proportional to a fraction of dissipation zone. This regularization ensures a non-local parameterization for relaxation, and connects the relaxation itself to a characteristic physical length of the problem. Since the dynamics of a growing crack is pretty different during the acceleration phase at the exit of nucleation phase and the stationary phase at the end of acceleration, the numerical solutions will be presented separately for the two regimes and both small and large dissimilarity between layers will be taken into account.

## **2.2 Stroh formalism for isotropic bimaterial interfaces**

In this section the results for the asymptotic crack tip fields, when a stationary rupture propagates between two different isotropic media, will be briefly described, in the framework of fracture mechanics in order to give a formal overview on the concepts of mode mixity, oscillatory fields and complex stress intensity factor. Then we show a strategy to neglect the effects of mode mixity in the vicinity of the crack tip mainly referring to the work of Rice (1988); we also show how the oscillatory

effects and the mode mixity disappear as a Coulomb friction law is considered along the interface (Deng, 1994).

### 2.2.1 Steady state crack propagation along bimaterial interface

Consider a planar crack propagating along an interface that separates two different materials as shown in Figure 2.1. The Navier equations governing for the displacement  $u_1, u_2, u_3$  can be written in the form:

$$\rho \ddot{u}_j = C_{ijkl} \frac{\partial^2 u_k}{\partial x_l \partial x_i} \quad (2.1)$$

Where the stiffness tensor  $C_{ijkl}$  and the density of the material  $\rho$  assumes different values for the two substrates. Without loss of generality the substrate (1) is assumed to have a lower Rayleigh wave speed, designated as  $C_R$ . Let us suppose the crack propagates at constant speed  $v = \dot{L}(t) < C_R$  (see Figure 2.1) and consider the following stretching of coordinates to follow the advancing of crack tip:

$$\begin{cases} \hat{x}_1 = x_1 - l(t) \\ \hat{x}_2 = x_2 \\ \hat{x}_3 = x_3 \end{cases} \quad (2.2)$$

For the singular fields close to the crack tip, among the four partial derivatives appearing in material derivative,  $\partial u_k / \partial \hat{x}_3$  and  $\partial u_k / \partial t$  are less singular than  $\partial u_k / \partial \hat{x}_1$  and  $\partial u_k / \partial \hat{x}_2$ , in the new system of coordinates given by the system (2.2) (Yang *et al.* 1991). Thus close to the tip, the acceleration can be approximated as:

$$\ddot{u}_j = v^2 u_{j,11} \quad (2.3)$$

Where the subscripts  $\{ \}_{,i}$  represents the derivative respect with the  $i$ -th component.

Let us consider now the  $C$  matrix for an isotropic medium:

$$\begin{aligned} C_{ijj} &= (\lambda + 2\mu) \delta_{ij} + \lambda (1 - \delta_{ij}) \\ C_{ijkl} &= \mu \delta_{ik} \delta_{jl} (1 - \delta_{ij}) \end{aligned} \quad (2.4)$$

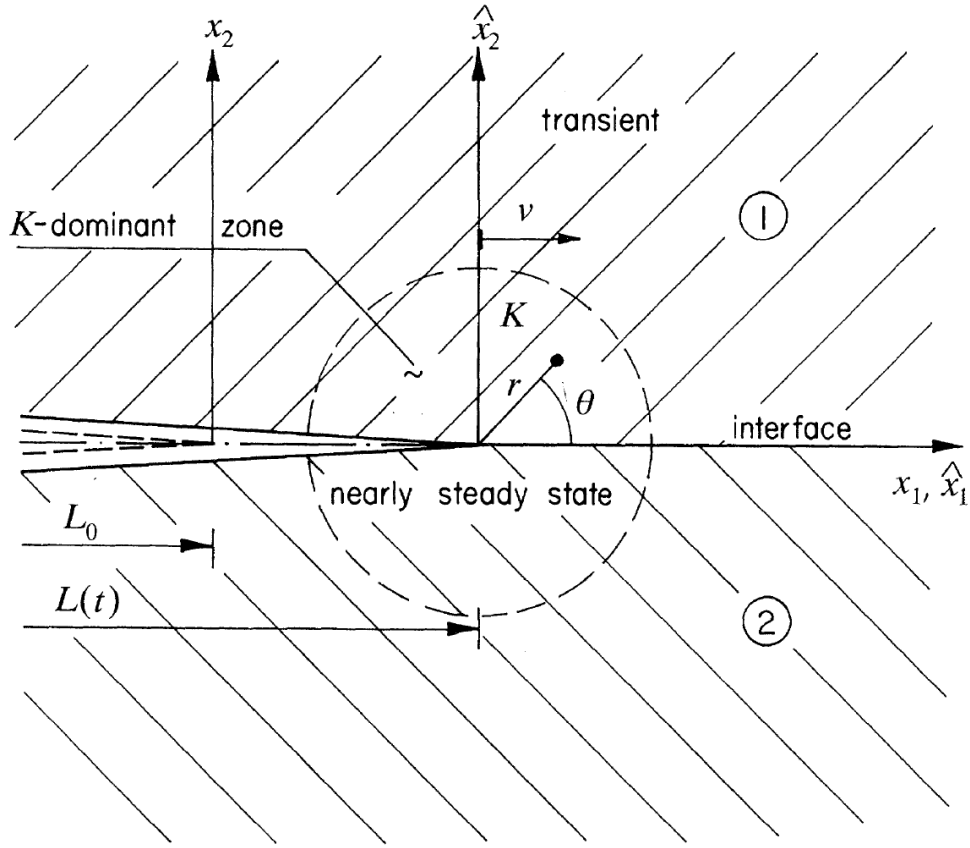


Figure 2.1 Scheme for a stationary crack propagating along a bimaterial interface (Yang *et al.*, 1991)

with  $\lambda$  and  $\mu$  Lamè constants. To avoid confusion in the notation it is worth to stress that  $\mu$  will represents the shear modulus (defined as  $G$  in Chapter 1) in all theoretical results presented in sections 2.2 and 2.3 (and their subsections); furthermore in theoretical results in section 2.2.7 and in section 2.3 (and its subsections) a constant friction coefficient will be used and it will be indicated as  $f$ .

Because of symmetry of stress and strain tensors the following relationships are also valid:

$$C_{ijkl} = C_{jikl} = C_{ijlk} = C_{klij} \quad (2.5)$$

Substituting the equation (2.4) into the general problem (2.1) and considering the approximation on the singularities given by the (2.3), we get:

$$\begin{aligned} \rho v^2 \frac{\partial^2 u_1}{\partial \hat{x}_1^2} &= (\lambda + 2\mu) \frac{\partial^2 u_1}{\partial \hat{x}_1^2} + \mu \frac{\partial^2 u_1}{\partial \hat{x}_2^2} + \\ &+ \mu \frac{\partial^2 u_1}{\partial \hat{x}_3^2} + (\lambda + \mu) \frac{\partial^2 u_2}{\partial \hat{x}_1 \partial \hat{x}_2} + (\lambda + \mu) \frac{\partial^2 u_3}{\partial \hat{x}_1 \partial \hat{x}_3} \end{aligned} \quad (2.6)$$

$$\begin{aligned} \rho v^2 \frac{\partial^2 u_2}{\partial \hat{x}_1^2} &= \mu \frac{\partial^2 u_2}{\partial \hat{x}_1^2} + (\lambda + 2\mu) \frac{\partial^2 u_2}{\partial \hat{x}_2^2} + \\ &+ \mu \frac{\partial^2 u_2}{\partial \hat{x}_3^2} + (\lambda + \mu) \frac{\partial^2 u_1}{\partial \hat{x}_1 \partial \hat{x}_2} + (\lambda + \mu) \frac{\partial^2 u_3}{\partial \hat{x}_2 \partial \hat{x}_3} \end{aligned} \quad (2.7)$$

$$\begin{aligned} \rho v^2 \frac{\partial^2 u_3}{\partial \hat{x}_1^2} &= \mu \frac{\partial^2 u_3}{\partial \hat{x}_1^2} + \mu \frac{\partial^2 u_3}{\partial \hat{x}_2^2} + \\ &+ (\lambda + 2\mu) \frac{\partial^2 u_3}{\partial \hat{x}_3^2} + (\lambda + \mu) \frac{\partial^2 u_1}{\partial \hat{x}_1 \partial \hat{x}_3} + (\lambda + \mu) \frac{\partial^2 u_2}{\partial \hat{x}_2 \partial \hat{x}_3} \end{aligned} \quad (2.8)$$

The first members of equations (2.6)-(2.8) can be moved to second members allowing to define a modified  $C$  tensor which takes into account the stationary propagation of the crack. In particular:

$$\hat{C}_{1111} = C_{1111} - \rho v^2; \hat{C}_{1221} = C_{1221} - \rho v^2; \hat{C}_{1331} = C_{1331} - \rho v^2 \quad (2.9)$$

Thus using the following:

$$\hat{C}_{\alpha j k \beta} = C_{\alpha j k \beta} - \rho v^2 \delta_{jk} \delta_{\alpha 1} \delta_{\beta 1} \quad (2.10)$$

The Navier problem presented in equation (2.1) can be expressed as:

$$\hat{C}_{\alpha j k \beta} u_{k, \alpha \beta} = 0 \quad (2.11)$$

### 2.2.2 Stroh formalism for isotropic homogeneous material

In this section we present the complex-variable representation due to Stroh (1962) in order to solve the planar differential equations (2.11) for stationary propagating speed in homogeneous media (material 1 and 2 in Figure 2.1 have the same elastic properties). From classical Airy stress formalism, the stress functions,  $\Phi_i$ , are defined such that (Yang *et al.*, 1991):

$$\sigma_{1i} = -\Phi_{i,2} + \rho v^2 u_{i,1} \quad \sigma_{2i} = \Phi_{i,1} \quad (2.12)$$

According to this formalism, the displacement and stress function,  $u_i$  and  $\Phi_i$ , are linear in the three analytic functions  $f_q$  (Eshelby *et al.*, 1953; Suo, 1958,1962):

$$u_i = 2 \operatorname{Re} \left\{ \sum_{q=1}^3 A_{iq} f_q(z_q) \right\} \quad \Phi_i = 2 \operatorname{Re} \left\{ \sum_{q=1}^3 L_{iq} f_q(z_q) \right\} \quad (2.13)$$

Where the complex argument takes the form:

$$z_q = \hat{x}_1 + p_q \hat{x}_2 \quad (2.14)$$

Substituting the equations (2.13) into the equations (2.6)-(2.8) and considering separately the equations involving the same  $p_q$ , we can define the matrix  $\mathbf{E}$  as:

$$\begin{vmatrix} (\lambda + 2\mu - \rho v^2 + \mu p_q^2) & (\lambda + \mu)p_q & 0 \\ (\lambda + \mu)p_q & [(\lambda + 2\mu)p_q^2 + (\mu - \rho v^2)] & 0 \\ 0 & 0 & [(\mu - \rho v^2) + \mu p_q^2] \end{vmatrix} \quad (2.15)$$

From matrix  $\mathbf{E}$  the following eigenvalue problem for  $p_q$  can be obtained:

$$|\mathbf{E}| \begin{vmatrix} \mathbf{A}_{1q} \\ \mathbf{A}_{2q} \\ \mathbf{A}_{3q} \end{vmatrix} = 0 \quad (2.16)$$

The eq. (2.16) admits not trivial solution only if the  $\det|\mathbf{E}| = 0$ . The eigenvalues  $p_q$  are the roots of a sixth-order equations and they are complex as long as  $v < C_s$ . The three roots with positive imaginary part are chosen and designated as  $p_1, p_2$  and  $p_3$ . The normalization of each column of  $\mathbf{A}$  is arbitrary. From Hooke's law we can get the row for matrix  $\mathbf{L}$ . We get:

$$\begin{cases} L_{1q} = -[p_q^{-1}(\lambda + 2\mu - \rho v^2)A_{1q} + \lambda A_{2q}] \\ L_{2q} = -[p_q^{-1}(\mu - \rho v^2)A_{2q} + \mu A_{1q}] \\ L_{3q} = -p_q^{-1}(\mu - \rho v^2)A_{3q} \end{cases} \quad (2.17)$$

The eigenvalue problem (2.16) is explicitly derived and solved in Appendix A1 at the end of the chapter.

The traction vector can be expressed as:

$$\sigma_{2i} = 2\text{Re} \left\{ \sum_{q=1}^3 L_{iq} f'_q(z_q) \right\} \quad (2.18)$$

The above presented basic equations for steady-state fields are identical to those for the static problem when  $\hat{x}_i$  and  $\hat{C}_{ijkl}$  are identified with  $x_i$  and  $C_{ijkl}$  (Suo, 1990; Yang et al., 1991). Accordingly, static results carry over the dynamic analysis.

Nevertheless, the presence of the term  $\rho v^2$  makes the eigenvalue from problem (2.16) no longer degenerating for isotropic case and thus the matrix  $\mathbf{A}$  and  $\mathbf{L}$  are not singular for dynamic isotropic problems.

Indeed non-singular matrix  $\mathbf{B}$  can be defined, for isotropic dynamic case as follows:

$$\mathbf{B} = i\mathbf{A}\mathbf{L}^{-1} \quad (2.19)$$

where  $i = \sqrt{-1}$  and standard matrix operations are implied. As we will see in the next subsections the matrix  $\mathbf{B}$  allows to express the asymptotic solutions for crack tip fields as a function of elastic parameters and crack speed. It is worth noting that when  $(\hat{x}_1, \hat{x}_2)$  is a mirror plane for the materials, the governing equation (2.11) decouples into antiplane shear and plane strain problems. They are treated separately as follows.

The antiplane shear problem is only governed by the equation for  $u_3$  (see equation (2.8)). The characteristic number is the root with positive imaginary part of the following equation:

$$\left[ (\mu - \rho v^2) + \mu p_3^2 \right] = 0 \Rightarrow p_3 = i \sqrt{1 - \frac{\rho v^2}{\mu}} = i\alpha_2 \quad (2.20)$$

Only the components  $| \cdot |_{33}$  of the matrices are not trivial. Thus we can arbitrary fix  $A_{33} = 1$  and:

$$L_{33} = \frac{1}{\alpha_2} (\mu - \rho v^2) A_{33} = i\mu\alpha_2 \quad (2.21)$$

where the (2.21) represents the only non-zero component of the third row of matrix  $\mathbf{L}$ . Thus for  $\mathbf{B}$

$$B_{33} = \frac{i}{L_{33}} = \frac{1}{\mu\alpha_2} \quad (2.22)$$

$L_{33} = 0$ , only if  $v = C_s$ . Therefore if  $p_3$  is complex the antiplane term  $B_{33}$  is always defined for subshear crack propagation.

Starting from the general definition of matrix  $\mathbf{E}$  (2.15), the in-plane problem can be described finding the eigenvalue  $p_q$  such that:

$$\det \begin{vmatrix} (\lambda + 2\mu - \rho v^2 + \mu p_q^2) & (\lambda + \mu) p_q \\ (\lambda + \mu) p_q & [(\lambda + 2\mu) p_q^2 + (\mu - \rho v^2)] \end{vmatrix} = 0 \quad (2.23)$$

and the two eigenvalues  $p_1$  and  $p_2$  have the form:

$$p_1 = i\alpha_1, \quad p_2 = i\alpha_2 \quad (2.24)$$

With:

$$\alpha_1 = \sqrt{1 - \frac{\rho v^2}{\lambda + 2\mu}} \quad (2.25)$$

Using the eigenvalues from (2.24) we can obtain the matrix  $\mathbf{A}$ , for in-plane ruptures:

$$\mathbf{A} = \begin{vmatrix} 1 & -i\alpha_2 \\ i\alpha_1 & 1 \end{vmatrix} \quad (2.26)$$

And then the matrices  $\mathbf{L}$  and  $\mathbf{B}$ :

$$\left\{ \begin{array}{l} \mathbf{L} = \mu \begin{vmatrix} 2i\alpha_1 & 1 + \alpha_2^2 \\ -(1 + \alpha_2^2) & 2i\alpha_2 \end{vmatrix} \\ \mathbf{B} = \frac{1}{\mu D} \begin{vmatrix} \alpha_2(1 - \alpha_2^2) & i(1 + \alpha_2^2 - 2\alpha_1\alpha_2) \\ -i(1 + \alpha_2^2 - 2\alpha_1\alpha_2) & \alpha_1(1 - \alpha_2^2) \end{vmatrix} \end{array} \right. \quad (2.27)$$

Where  $D = 4\alpha_1\alpha_2 - (1 + \alpha_2^2)^2$  is the classical Rayleigh function. Therefore the matrix  $\mathbf{L}$  is not singular for  $v < C_R$  and only in that case  $\mathbf{B}$  can be defined.

The explicit computations of eigenvalues and matrices are reported in Appendix A1.

### 2.2.3 Matrix $\mathbf{H}$ for bimaterial crack

Let us return to the general bimaterial problem presented in Figure 2.1. For what we will discuss in the current and next sections it is particularly useful to define a new matrix  $\mathbf{H}$ :

$$\mathbf{H} = \mathbf{B}_{(1)} + \bar{\mathbf{B}}_{(2)} \quad (2.28)$$

Where the subscripts  $\{ \}_{(1,2)}$  denote respectively the matrices  $\mathbf{B}$  related to blocks 1 and 2, and the over-bar indicates the complex conjugate of related matrix. The matrix  $\mathbf{H}$ , having the dimension of compliance, contains the characterization of the interface. For the anti-plane case:

$$H_{33} = \frac{1}{\mu_{(1)}\alpha_{2,(1)}} + \frac{1}{\mu_{(2)}\alpha_{2,(2)}} \quad (2.29)$$

Whereas the in-plane components give:

$$\mathbf{H}_{in-plane} = \begin{vmatrix} H_{11} & iH_{12} \\ -iH_{12} & H_{22} \end{vmatrix} \quad (2.30)$$

With:

$$\left\{ \begin{array}{l} H_{11} = \frac{\alpha_{2,(1)} (1 - \alpha_{2,(1)}^2)}{\mu_{(1)}D_{(1)}} + \frac{\alpha_{2,(2)} (1 - \alpha_{2,(2)}^2)}{\mu_{(2)}D_{(2)}} \\ H_{11} = \frac{\alpha_{1,(1)} (1 - \alpha_{2,(1)}^2)}{\mu_{(1)}D_{(1)}} + \frac{\alpha_{1,(2)} (1 - \alpha_{2,(2)}^2)}{\mu_{(2)}D_{(2)}} \\ H_{12} = \left[ \frac{(1 + \alpha_{2,(1)}^2 - 2\alpha_{1,(1)}\alpha_{2,(1)})}{\mu_{(1)}D_{(1)}} - \frac{(1 + \alpha_{2,(2)}^2 - 2\alpha_{1,(2)}\alpha_{2,(2)})}{\mu_{(2)}D_{(2)}} \right] \end{array} \right. \quad (2.31)$$

In conclusion the complete matrix  $\mathbf{H}$  can be written by using the 4 real quantities given by (2.29) and (2.31) as:

$$\mathbf{H} = \begin{vmatrix} H_{11} & -iH_{12} & 0 \\ iH_{12} & H_{22} & 0 \\ 0 & 0 & H_{33} \end{vmatrix} \quad (2.32)$$

Where the anti-plane and in-plane parts are still decoupled.

## 2.2.4 Crack tip fields

The matrices defined so far can lead to the definition of the asymptotic fields around the crack tip. Due to the total analogy of formalism with the static case we can use the same results as in Suo (1990), simply considering two isotropic media on the two sides of the fault and using  $\hat{x}_i$  and  $\hat{C}_{ijkl}$  as reference system and modified

Hooke's tensor. An important remark about the standard analytic continuation is needed. A function  $h(z)$  is an analytic function of  $z = \hat{x}_1 + p\hat{x}_2$  for  $\hat{x}_2 > 0$  (or  $\hat{x}_2 < 0$ ) for any  $p$  if it is analytic for  $\hat{x}_2 > 0$  (or  $\hat{x}_2 < 0$ ) for one  $p$ , where  $p$  is any complex number with positive imaginary part. Consequently, when talking about a function analytic in the upper (or lower) half-plane, one needs not refer to its argument, as long as the argument has the form  $z = \hat{x}_1 + p\hat{x}_2$  and  $\text{Im}(p) > 0$  (Smirnov, 1964). Therefore without loss of any information, we can and will present our solutions by using the function vector  $\mathbf{f}(z)$  defined as:

$$\mathbf{f}(z) = [f_1(z), f_2(z), f_3(z)]^T \quad (2.33)$$

Once the solution of  $\mathbf{f}(z)$  is obtained for a given boundary value problem, a replacement of  $z_1, z_2$  and  $z_3$  should be made for each component function to calculate field quantities from (2.13) and (2.18). To obtain the asymptotic fields (the traction ahead the crack tip and the displacement jump behind the crack tip) the following set of vectors defined along the  $\hat{x}_1$ -axis and expressed in terms of Airy potential has to be defined (Suo, 1990):

$$\begin{cases} \mathbf{u}(\hat{x}_1) = \{u_j(\hat{x}_1, 0)\} = \mathbf{A}\mathbf{f}(\hat{x}_1) + \overline{\mathbf{A}}\overline{\mathbf{f}}(\hat{x}_1) \\ \mathbf{T}(\hat{x}_1) = \{T_j(\hat{x}_1, 0)\} = -\mathbf{L}\mathbf{f}(\hat{x}_1) - \overline{\mathbf{L}}\overline{\mathbf{f}}(\hat{x}_1) \\ \mathbf{t}(\hat{x}_1) = \{\sigma_{2j}(\hat{x}_1, 0)\} = \mathbf{L}\mathbf{f}'(\hat{x}_1) + \overline{\mathbf{L}}\overline{\mathbf{f}}'(\hat{x}_1) \end{cases} \quad (2.34)$$

where standard matrix operations are implied.

Let the vector potentials defined in (2.33) be respectively  $\mathbf{f}_{(1)}(z)$  and  $\mathbf{f}_{(2)}(z)$  in the two blocks whereas  $\mathbf{L}_{(1)}$  and  $\mathbf{L}_{(2)}$  represent the matrices  $\mathbf{L}$  in each block. For sake of clarity, we recall that the bracketed subscripts  $\{ \}_{(i)}$  always indicate the quantities in each block and it must not be confused with the subscripts  $\{ \}_i$  that, as usual, indicate each component of vectorial/matricial quantities. Obviously the traction  $\mathbf{t}(\hat{x}_1)$  defined in (2.34) is continuous across the whole  $\hat{x}_1$ -axis, both on the bonded and cracked portion, so that:

$$\mathbf{L}_{(1)}\mathbf{f}'_{(1)}(\hat{x}_1) + \overline{\mathbf{L}}_{(1)}\overline{\mathbf{f}}'_{(1)}(\hat{x}_1) = \mathbf{L}_{(2)}\mathbf{f}'_{(2)}(\hat{x}_1) + \overline{\mathbf{L}}_{(2)}\overline{\mathbf{f}}'_{(2)}(\hat{x}_1) \quad (2.35)$$

To facilitate the analytic continuation we can rearrange the (2.35) as:

$$\mathbf{L}_{(1)} \mathbf{f}'_{(1)}(\hat{x}_1) - \bar{\mathbf{L}}_{(2)} \bar{\mathbf{f}}'_{(2)}(\hat{x}_1) = \mathbf{L}_{(2)} \mathbf{f}'_{(2)}(\hat{x}_1) - \bar{\mathbf{L}}_{(1)} \bar{\mathbf{f}}'_{(1)}(\hat{x}_1) \quad (2.36)$$

And by standard analytic continuation argument (Smirnov, 1964), it follows that:

$$\begin{cases} \mathbf{L}_{(1)} \mathbf{f}'_{(1)}(z) = \bar{\mathbf{L}}_{(2)} \bar{\mathbf{f}}'_{(2)}(z) & z \in (1) \\ \mathbf{L}_{(2)} \mathbf{f}'_{(2)}(z) = \bar{\mathbf{L}}_{(1)} \bar{\mathbf{f}}'_{(1)}(z) & z \in (2) \end{cases} \quad (2.37)$$

By using equation (2.37), a direct calculation gives:

$$\mathbf{t}(\hat{x}_1) = \mathbf{L}_{(1)} \mathbf{f}'_{(1)}(\hat{x}_1) + \mathbf{L}_{(2)} \mathbf{f}'_{(2)}(\hat{x}_1) \quad (2.38)$$

Now exploiting the definition of displacement jump across the interface as  $\mathbf{d}(\hat{x}_1) = \mathbf{u}(\hat{x}_1, 0^+) - \mathbf{u}(\hat{x}_1, 0^-)$ :

$$i\mathbf{d}'(\hat{x}_1) = i\mathbf{A}_{(1)} \mathbf{f}'_{(1)}(\hat{x}_1, 0^+) + i\bar{\mathbf{A}}_{(1)} \bar{\mathbf{f}}'_{(1)}(\hat{x}_1, 0^+) - i\mathbf{A}_{(2)} \mathbf{f}'_{(2)}(\hat{x}_1, 0^-) - i\bar{\mathbf{A}}_{(2)} \bar{\mathbf{f}}'_{(2)}(\hat{x}_1, 0^-) \quad (2.39)$$

Grouping the first and forth terms and the second and third terms on the right-hand side member, using the two relations from system (2.37) and exploiting the relations (2.19) and (2.28) we get:

$$\begin{aligned} i\mathbf{d}'(\hat{x}_1) &= (\mathbf{B}_{(1)} + \bar{\mathbf{B}}_{(2)}) \mathbf{L}_{(1)} \mathbf{f}'_{(1)}(\hat{x}_1, 0^+) - (\bar{\mathbf{B}}_{(1)} + \mathbf{B}_{(2)}) \mathbf{L}_{(2)} \mathbf{f}'_{(2)}(\hat{x}_1, 0^+) = \\ &= \mathbf{H} \mathbf{L}_{(1)} \mathbf{f}'_{(1)}(\hat{x}_1, 0^+) - \bar{\mathbf{H}} \mathbf{L}_{(2)} \mathbf{f}'_{(2)}(\hat{x}_1, 0^+) \end{aligned} \quad (2.40)$$

## 2.2.5 Real $\mathbf{H}$ -matrix

A very simple solution can be obtained if the hermitian matrix  $\mathbf{H}$  is real (e.g. crack in homogeneous solid). Continuity of the displacement across the bonded interface ahead the crack tip ( $\mathbf{d} = 0$ ) implies that:

$$\mathbf{L}_{(1)} \mathbf{f}'_{(1)}(z) = \mathbf{L}_{(2)} \mathbf{f}'_{(2)}(z) = \mathbf{h}(z), \quad z \notin C \quad (2.41)$$

The (2.41) directly derives from standard analytic continuation. The relation (2.41) is valid in whole complex plane except the crack line  $C$ . Using equation (2.38) and traction free condition on the crack, behind the crack tip, we get the following homogeneous Hilbert problem:

$$\mathbf{h}^+(\hat{x}_1) + \mathbf{h}^-(\hat{x}_1) = 0, \quad z \in C \quad (2.42)$$

Where  $\mathbf{h}^\pm = \mathbf{L}_{(1,2)} \mathbf{f}'_{(1,2)}$  and  $C$  represents the advancing crack line. An obvious admissible singular solution to problem (2.42) is:

$$\mathbf{h}(z) = \frac{1}{2} (2\pi z)^{-\frac{1}{2}} \mathbf{k} \quad (2.43)$$

Where the branch cut for  $\sqrt{z}$  is along the crack line. The undetermined constant vector  $\mathbf{k}$  generally consists of three complex constants. Nevertheless, since the traction is real,  $\mathbf{k}$  is a real vector, and each component has the dimension of a traction times a length to  $1/2$   $\left\{ [N] [m^{-2}] \left[ m^{\frac{1}{2}} \right] \right\}$ . The adopted normalization is consistent with the conventional definition of stress intensity factors (Scholz, 1990), with:

$$\mathbf{k} = [K_{II}, K_I, K_{III}]^T \quad (2.44)$$

The complete asymptotic solution (for  $z \rightarrow 0$  in the dynamic reference system given by the coordinates stretching (2.2)) is then given by:

$$\mathbf{L}_{(1)} \mathbf{f}'_{(1)}(z) = \mathbf{L}_{(2)} \mathbf{f}'_{(2)}(z) = \mathbf{h}(z) = \frac{1}{2} (2\pi z)^{-\frac{1}{2}} \mathbf{k} \quad (2.45)$$

Considering that  $\mathbf{L}_{(i)}$  are not singular for a sub-shear propagating crack, the elastic potentials can be computed for both half-spaces. The fields can be computed from (2.13) and (2.18) with  $z$  properly inferred from the eigenvalue problem (2.16). However we can immediately note that the crack-tip fields depend on the crack speed. The traction and the displacement on the  $x$ -axis in the points  $(\hat{x}_1, 0)$  at distance  $r$  from moving crack tip are:

$$\mathbf{t}(r) = (2\pi r)^{-\frac{1}{2}} \mathbf{k} \quad (2.46)$$

Obtained from equations (2.38) and (2.41), and:

$$\mathbf{d}(r) = \left( \frac{2r}{\pi} \right)^{\frac{1}{2}} \mathbf{H} \mathbf{k} \quad (2.47)$$

Deriving from the Hilbert problem (2.42) and multiplying for  $-i$  and integrating the equation (2.40). Each one of the above equations can be used for the definition of stress intensity factor and as already anticipated it assumes the classical form (2.44)

The energy release rate  $G$  for unit of area of interface to decohere can be written as (Irwin, 1957):

$$G \equiv \frac{1}{2\Delta} \int_0^\Delta \mathbf{t}^T (\Delta - r) \mathbf{d}(r) dr \quad (2.48)$$

Where  $\Delta$  is an arbitrary length scale. Incorporating the (2.46) and (2.47) in the (2.48) and considering that:

$$\int_0^1 \left( \frac{t}{1-t} \right)^q = \frac{q\pi}{\sin q\pi}, \quad [|\operatorname{Re}(q)| < 1] \quad (2.49)$$

We finally get:

$$G = \frac{\Delta}{2\pi\Delta} \mathbf{k}^T \mathbf{H} \mathbf{k} \int_0^1 \left( \frac{r}{1-r} \right)^{\frac{1}{2}} = \frac{1}{2\pi} \mathbf{k}^T \mathbf{H} \mathbf{k} \frac{1}{2} \pi = \frac{1}{4} \mathbf{k}^T \mathbf{H} \mathbf{k} \quad (2.50)$$

## 2.2.6 Complex $\mathbf{H}$ -matrix

In the general case, for bimaterial interface, the matrix  $\mathbf{H}$  is complex. The results until the equation (2.40) are still valid. The continuity of displacement across the bonded interface requires now the existence of a function  $\mathbf{h}(z)$ , analytic in the whole plane except on the crack lines, such that:

$$\mathbf{h}(z) = \mathbf{L}_{(1)} \mathbf{f}'_{(1)} = \mathbf{H}^{-1} \bar{\mathbf{H}} \mathbf{L}_{(2)} \mathbf{f}'_{(2)}, \quad z \notin C \quad (2.51)$$

Once  $\mathbf{h}(z)$  is obtained, the full-field solution is given by (2.51).

In the case of complex  $\mathbf{H}$  the equations (2.38) and (2.40) become:

$$\mathbf{t}(\hat{x}_1) = \mathbf{h}^+(\hat{x}_1) + \bar{\mathbf{H}}^{-1} \mathbf{H} \mathbf{h}^-(\hat{x}_1) \quad (2.52)$$

$$i\mathbf{d}'(\hat{x}_1) = \mathbf{H} [\mathbf{h}^+(\hat{x}_1) - \mathbf{h}^-(\hat{x}_1)] \quad (2.53)$$

Consider the asymptotic problem first. From equation (2.52) the traction-free condition for the cracked portion gives:

$$\mathbf{h}^+(\hat{x}_1) + \mathbf{H}^{-1} \mathbf{H} \mathbf{h}^-(\hat{x}_1) = 0, \quad z \in C \quad (2.54)$$

The (2.54) is a homogeneous Hilbert problem. Let a solution be in the form:

$$\mathbf{h}(z) = \mathbf{w} z^{\frac{1}{2} + i\epsilon} \quad (2.55)$$

Where  $\mathbf{w}$  is a constant vector and  $\epsilon$  a constant number both to be determined. The branch cut for the multi-valued function (2.55) is chosen to be along the crack line  $\hat{x}_1 < 0$ , and the phase angle of  $z$  is measured from the positive side of  $\hat{x}_1$ -axis.

Substituting the (2.55) into the general Hilbert problem given by the (2.54) we get the following eigenvalue problem:

$$\bar{\mathbf{H}}\mathbf{w} = e^{2\pi\epsilon}\mathbf{H}\mathbf{w} \quad (2.56)$$

For the case in study (crack interface advancing along the  $\hat{x}_1$ -axis) the complete matrix  $\mathbf{H}$  can be written as in equation (2.32) and to find not trivial solutions for the problem (2.56) we should solve the following characteristic equations:

$$\det \begin{vmatrix} H_{11}(1-e^{2\pi\epsilon}) & -iH_{12}(1+e^{2\pi\epsilon}) & 0 \\ iH_{12}(1-e^{2\pi\epsilon}) & H_{22}(1-e^{2\pi\epsilon}) & 0 \\ 0 & 0 & H_{33}(1-e^{2\pi\epsilon}) \end{vmatrix} = 0 \quad (2.57)$$

The three eigenvalues are:

$$\left\{ \begin{array}{l} \epsilon_1 = \left( \frac{1}{2\pi} \right) \ln \left( \frac{1-\beta}{1+\beta} \right) \\ \epsilon_2 = -\epsilon_1 \\ \epsilon_3 = 0 \end{array} \right. \quad (2.58)$$

with  $\beta = -H_{12}(H_{11}H_{22})^{-\frac{1}{2}}$ . It is worth noting that  $\beta$  is a generalized Dundurs' parameter, being an adimensionless parameter deriving from the impedance matrix  $\mathbf{H}$ .

From eigenvalues we can finally get the eigenvectors: for  $\epsilon_3 = 0$  (corresponding to the anti-plane deformation) we obtain:

$$\mathbf{w}_3 = \{0, 0, 1\} \quad (2.59)$$

Whereas for  $\epsilon_1$  and  $\epsilon_2$  we get:

$$\left\{ \begin{array}{l} \mathbf{w}_1 = \left\{ -\frac{i\eta}{2}, \frac{1}{2}, 0 \right\} \\ \mathbf{w}_2 = \left\{ \frac{i\eta}{2}, \frac{1}{2}, 0 \right\} = \bar{\mathbf{w}}_1 \end{array} \right. \quad (2.60)$$

With  $\eta = (H_{22}/H_{11})^{\frac{1}{2}}$ .

And finally the eigenpairs can be expressed as:

$$(\epsilon, \mathbf{w}) \quad (-\epsilon, \mathbf{w}) \quad (0, \mathbf{w}_3) \quad (2.61)$$

Where  $\epsilon = \epsilon_1$ ;  $\mathbf{w} = \frac{1}{2}\{-i\eta, 1, 0\}$ ; and  $\mathbf{w}_3$  is given by the (2.59). The solutions of eigenvalue problem (2.57) and the explicit computation for eigenvector (2.60) are reported in Appendix A2.

The three eigenvectors are orthogonal in the sense:

$$\mathbf{w}^T \mathbf{H} \mathbf{w} = \mathbf{w}^T \mathbf{H} \mathbf{w}_3 = \bar{\mathbf{w}}^T \mathbf{H} \mathbf{w}_3 = 0 \quad (2.62)$$

with the same relationships obtainable also for  $\bar{\mathbf{H}}$ . Therefore the system  $\{\mathbf{w}, \bar{\mathbf{w}}, \mathbf{w}_3\}$  is a base in this representation and every complex-valued vector  $\mathbf{g}$  can be represented as a linear combination of the three eigenvectors, that is:

$$\mathbf{g} = g_1 \mathbf{w} + g_2 \bar{\mathbf{w}} + g_3 \mathbf{w}_3 \quad (2.63)$$

and each components can be inferred from the so-defined scalar products:

$$g_1 = \frac{\bar{\mathbf{w}}^T \mathbf{H} \mathbf{g}}{\bar{\mathbf{w}}^T \mathbf{H} \mathbf{w}}, \quad g_2 = \frac{\mathbf{w}^T \mathbf{H} \mathbf{g}}{\mathbf{w}^T \mathbf{H} \bar{\mathbf{w}}}, \quad g_3 = \frac{\mathbf{w}_3^T \mathbf{H} \mathbf{g}}{\mathbf{w}_3^T \mathbf{H} \mathbf{w}_3} \quad (2.64)$$

With  $g_2 = \bar{g}_1$  and  $g_3$  is real. Now returning to the main problem expressed by (2.54) the admissible singular solution is a linear combination of three homogeneous solutions of form given by equation (2.55):

$$\mathbf{h}(z) = z^{-\frac{1}{2}} \left[ a \mathbf{w} z^{i\epsilon} + b \bar{\mathbf{w}} z^{i\epsilon} + c \mathbf{w}_3 \right] \quad (2.65)$$

Where  $a, b, c$  are three complex numbers. Substituting the (2.65) into the (2.52) and requiring that traction to be real along the interfaces,  $a$  and  $b$  cannot be independent and we get:

$$a = e^{2\pi\epsilon} \bar{b}, \quad \text{Im}(c) = 0 \quad (2.66)$$

Therefore only one complex constant  $K$  and one real constant are independent and:

$$\mathbf{h}(z) = \frac{e^{\pi\epsilon} K z^{i\epsilon} \mathbf{w} + e^{-\pi\epsilon} \bar{K} z^{-i\epsilon} \bar{\mathbf{w}}}{2(2\pi z)^{\frac{1}{2}} \cosh(\pi\epsilon)} + \frac{K_3 \mathbf{w}_3}{2(2\pi z)^{\frac{1}{2}}} \quad (2.67)$$

Substituting the (2.67) into the (2.52) we can get the traction on bonded interface on each point of coordinates  $(\hat{x}_1, 0)$  at distance  $r$  ahead the crack tip:

$$\mathbf{t}(r) = (2\pi r)^{-\frac{1}{2}} \left[ K r^{i\epsilon} \mathbf{w} + \bar{K} r^{-i\epsilon} \bar{\mathbf{w}} + K_3 \mathbf{w}_3 \right] \quad (2.68)$$

With the components in the sense of (2.64):

$$t_1(r) = \frac{Kr^{i\epsilon}}{(2\pi r)^{\frac{1}{2}}} = \bar{t}_2(r), \quad t_3(r) = \frac{K_3}{(2\pi r)^{\frac{1}{2}}} \quad (2.69)$$

It is worth noting that while  $K_3$  has the classical dimension of stress intensity factor  $\left\{ [N][m^{-2}][m^{\frac{1}{2}}] \right\}$ ,  $K$  has not, due to the presence of oscillatory term. In particular the dimensions of complex stress intensity factor are  $\left\{ [N][m^{-2}][m^{\frac{1}{2}}][m^{-i\epsilon}] \right\}$ . Moreover in equation (2.68) the mode I and the mode II the in-plane components are unavoidably coupled and the mode mixity postulated by Williams (1959) is thus retrieved (Suo, 1990).

The displacement jump in the points of coordinates  $(\hat{x}_1 < 0, 0)$  at distance  $r$  from the crack tip can be computed integrating and dividing for  $i$  the equation (2.53), obtaining finally:

$$\mathbf{d}(r) = (\mathbf{H} + \bar{\mathbf{H}}) \left( \frac{r}{2\pi} \right)^{\frac{1}{2}} \left[ \frac{Kr^{i\epsilon} \mathbf{w}}{(1+2i\epsilon)\cosh(\pi\epsilon)} + \frac{\bar{K}r^{-i\epsilon} \bar{\mathbf{w}}}{(1-2i\epsilon)\cosh(\pi\epsilon)} + K_3 \mathbf{w}_3 \right] \quad (2.70)$$

Once the traction ahead and the displacement jump behind the crack tip are explicitly found the energy release rate can be again computed by using the above mentioned Irwin formula:

$$G = \left( \frac{\mathcal{F}}{4\mu_1} \right) |K|^2 + \frac{1}{4} H_{33} K_3^2 \quad (2.71)$$

With  $\mathcal{F}$  given by:

$$\mathcal{F} = C_{1212}^{(1)} \left( H_{22} - \frac{H_{12}^2}{H_{11}} \right) = \mu_1 \left( H_{22} - \frac{H_{12}^2}{H_{11}} \right) \quad (2.72)$$

The computation of energy release rate given in the formula (2.71) is reported in Appendix A3. It is worth noting that, although the stress intensity factor is complex and thus not defined as in the classical homogeneous case, the energy release rate is well-posed due to the presence of term  $|K|^2$  in formula (2.71).

The complex stress intensity factor can be obtained from the traction (2.68) and for any interfacial crack problem it assumes the general form:

$$K = \Lambda T \sqrt{LL}^{-i\epsilon} \quad (2.73)$$

where  $L$  is a relevant length describing the geometry (say as example  $L(t)$  in Figure 2.1),  $T$  is an applied traction loading and  $\Lambda$  is a complex number, which may depend on the particular geometry and on the elastic parameters of the two layers.

The retrieved mode mixity, obviously implies rotational effects when the crack propagates in plane as effect of a shear stress load and in particular Rice (1988) showed that for the same loading  $T$  if the characteristic length of the rupture is changed from  $L$  to  $L'$  the new angle of loading  $\psi'$  with respect to the old angle  $\psi$  is given by:

$$\psi' = \psi + \epsilon \ln(L' / L) \quad (2.74)$$

For many material combinations of interest and small propagation velocity of the crack (at limit for static cracks),  $\epsilon$  is very small, and thus it produces very negligible rotational effects even when  $L(t_1)$  becomes some orders of magnitude larger than  $L(t_0)$  with  $t_1 > t_0$ .

As shown in equations (2.69) and (2.70) the crack tip fields, for in-plane deformations, always contain the term  $Kr^{i\epsilon}$ . This term is real and we can separate the real and complex part. Thus writing as example the in-plane components of traction given by the (2.68) as:

$$\mathbf{t}(r) = \sigma_{21} + i\sigma_{22} \quad (2.75)$$

and the term containing the stress intensity factor as:

$$Kr^{i\epsilon} = K_{II} + iK_I \quad (2.76)$$

the traction (2.68), for in plane deformations, can be defined similarly to the homogeneous case. The same is valid for the displacement (2.70) as long as the terms in  $\epsilon$  can be neglected. Thus to the extent that  $Kr^{i\epsilon}$  is sensibly independent of  $r$  over some range of interest for the application of fracture mechanics methodology, a value  $\hat{r}$  can be chosen and the crack tip fields can be characterized by a stress intensity factor of classical type defined as (Rice, 1988):

$$K_{II} + iK_I = K\hat{r}^{i\epsilon} = \Lambda T \sqrt{L} (\hat{r} / L)^{i\epsilon} \quad (2.77)$$

About the arbitrary choice of  $\hat{r}$ , according to the results of Rice (1988) for a static crack a good choice can be a fixed fraction of the crack length  $L$ . He shows, as example, how a choice of  $\hat{r} = L / 50$  is a good length to neglect the oscillatory term  $\epsilon$ ,

when it is in the range  $0.01-0.03$ . However, any choice for  $\hat{r}$  goes against the spirit of elastic fracture mechanics where the intention is to define parameters which fully characterize the effects of load and geometry on the crack tip fields and for clarity Rice proposed that one should refer to the (2.77) as the classical stress intensity factor based on the particular choice of  $\hat{r}$ . It is worth noting that for a stationary propagating crack at speed  $C$  as that described in this section the values of  $\epsilon$  can be considerably higher than those considered by Rice (see the form of  $\epsilon$  given by the (2.58) and the values of matrix  $\mathbf{H}$  elements as a function of  $\nu$  in equation (2.31)) since they depend also on the crack speed. Nevertheless for each  $\epsilon$  we can define an arbitrary  $\hat{r}(L(t))$  over which the mode mixity can be neglected.

### 2.2.7 Stroh formalism for Coulomb friction sliding rupture

The crack tip fields, the stress intensity factor and the energy release rate features presented in the above subsections are related to the free-surface crack conditions, which implies that the crack surfaces are not in contact. This condition is really simple from a mathematical point of view but it is really often violated in many realistic applications. Even when the cracks lie along bimaterial interfaces under mostly shear loadings, those lead to sizeable contact zone emerging around the crack tip (Willis, 1972; Comninou and Schmueser, 1979; Gutesen and Dundurs, 1988). When the crack faces are rough and rugged, as they often are, friction will be generated when contacting crack surfaces slide over each other (Deng, 1994)

Starting from these considerations, Deng (1994) obtained the explicit solutions for the asymptotic crack tip fields considering frictional contact along bimaterial interfaces, by using the Stroh formalism presented in the previous subsection.

The stress and displacement general conditions can be still represented by using the Airy stress potentials and the matrices obtained above and thus by using the equations (2.13) and (2.18). At the same time the vector  $\mathbf{h}(z)$  and the traction and displacement expressed in terms of  $\mathbf{h}(z)$  itself are still determined by equations (2.51) and (2.53). The boundary conditions are now different and they have to include the classical Coulomb friction conditions, which express the actual shear/normal coupling during the frictional sliding:

$$\begin{aligned}
\mathbf{t}_{(1)} &= \mathbf{t}_{(2)} \quad (\hat{x}_2 = 0, -\infty < \hat{x}_1 < \infty) \\
\mathbf{u}_{(1)} &= \mathbf{u}_{(2)} \quad (\hat{x}_2 = 0, 0 < \hat{x}_1 < \infty) \\
\sigma_{21} &= -f\sigma_{22}, \quad u_{2,(1)} = u_{2,(2)} \quad (\hat{x}_2 = 0, -\infty < \hat{x}_1 < 0)
\end{aligned} \tag{2.78}$$

with  $f$  that represents here the friction coefficient. The first condition of (2.78) is the same condition, which leads to the equation (2.35) (and (2.36) from analytical continuation). Nevertheless now the traction is not zero along the crack and thus the first of (2.78) has to be rearranged as:

$$\mathbf{h}_{(1)}(z) - \bar{\mathbf{h}}_{(2)}(z) = \mathbf{h}_{(2)}(z) - \bar{\mathbf{h}}_{(1)}(z) = \mathbf{g}(z) \tag{2.79}$$

where the subscripts refer to the two layers around the crack. The second condition for (2.78) leads to:

$$\mathbf{B}_{(1)}\mathbf{h}_{(1)}(z) + \bar{\mathbf{B}}_{(2)}\bar{\mathbf{h}}_{(2)}(z) = \mathbf{B}_{(2)}\mathbf{h}_{(2)}(z) + \bar{\mathbf{B}}_{(1)}\bar{\mathbf{h}}_{(1)}(z) \quad z \notin C \tag{2.80}$$

The equations (2.79) and (2.80) allow to express the functions  $\bar{\mathbf{h}}_{(1)}, \mathbf{h}_{(2)}$  and  $\bar{\mathbf{h}}_{(2)}$  in terms of  $\mathbf{h}_{(1)}(z)$  and  $\mathbf{g}(z)$ , and thus by using the same formalism as in the previous subsection we can use simply  $\mathbf{h}(z)$  to indicate  $\mathbf{h}_{(1)}(z)$  and once found it all the crack tip fields can be found as well as for traction-free case. It is convenient to introduce another hermitian matrix defined as:

$$\mathbf{G} = \bar{\mathbf{B}}_{(1)} - \bar{\mathbf{B}}_{(2)} \tag{2.81}$$

And by using the last condition in (2.78) we eventually get the following inhomogeneous Hilbert problem valid on the cracked portion of the rupture (Deng, 1994):

$$\mathbf{U}\mathbf{h}^+(\hat{x}_1) + \mathbf{V}\mathbf{h}^-(\hat{x}_1) = \mathbf{W}\mathbf{g}(\hat{x}_1) \tag{2.82}$$

With:

$$\begin{aligned}
U_{11} &= |\mathbf{H}|, & U_{12} &= f|\mathbf{H}|, & U_{21} &= iH_{12}, & U_{22} &= H_{22} \\
V_{11} &= H_{11}H_{22} + H_{12}^2 + 2ifH_{11}H_{12} \\
V_{12} &= -2iH_{22}H_{12} + f(H_{11}H_{22} + H_{12}^2) \\
V_{21} &= -iH_{12}, & V_{22} &= -H_{22} \\
W_{11} &= |\mathbf{H}| - G_{11}H_{22} + iG_{21}H_{12} + f(-iG_{11}H_{12} - G_{21}H_{11}) \\
W_{12} &= iG_{22}H_{12} - G_{12}H_{22} + f(|\mathbf{H}| - G_{22}H_{11} - iG_{12}H_{12}) \\
W_{21} &= W_{22} = 0
\end{aligned} \tag{2.83}$$

The conditions in (2.83) were directly given by the statement in Deng (1994, equation 13) using the matrix  $\mathbf{H}$  in the form (2.32). It is worth to stress that the matrix (2.32) is valid for isotropic media and when the crack interface separates the two layers as in Figure 2.1.

The problem (2.82) is the equivalent of Hilbert problem given by the (2.54). Now the problem is inhomogeneous due to the not-zero traction term and thus the general form of  $\mathbf{h}(z)$  consists of a particular and a homogenous part. The problem (2.82) has an infinite number of particular solutions, and it was shown that a simple one coincides with the solution of this equation (Deng, 1993b):

$$(\mathbf{H} + \bar{\mathbf{H}})\mathbf{h}(z) = (\mathbf{H} - \mathbf{G})\mathbf{g}(z) \tag{2.84}$$

And the particular solution obtained is identical in form to that for an interface crack without contact (Deng,1993a).

To arrive at the homogeneous part of the general solution for  $\mathbf{h}(z)$ , the general problem is reduced to the following eigenvalue problem proposed by Deng (1994):

$$\mathbf{U}\mathbf{q} = \lambda\mathbf{V}\mathbf{q} \tag{2.85}$$

This problem is totally equivalent to the (2.56) with  $\lambda = e^{2\pi\epsilon}$  and  $\mathbf{q} \equiv \mathbf{w}$ . Nevertheless introducing the friction condition the eigenvalues  $\epsilon$  for the in-plane deformation are now both complex and their values are:  $\epsilon_1 = i\delta$ ;  $\epsilon_2 = -i/2$ ; with  $\delta$  defined as:

$$\begin{cases} \tan \pi\delta = \mu\gamma \\ \gamma = H_{12} / H_{22} \end{cases} \tag{2.86}$$

for isotropic materials (Deng, 1994).

Therefore, for this case the general solution (2.55) has the following form, from the eigenvalue  $\epsilon_i$ , for the in-plane components:

$$\mathbf{h}_{\epsilon_1}(z) = \mathbf{w}_1 z^{-\frac{1}{2}+\delta}; \quad \mathbf{h}_{\epsilon_2}(z) = \mathbf{w}_2 \quad (2.87)$$

And the equivalent for the general form (2.67) can be expressed by analogy with the equation (19) in Deng (1994) as:

$$\mathbf{h}(z) = \frac{z^\delta \xi_1(z)}{2\sqrt{\pi z}} \mathbf{w}_1 + \xi_2(z) \mathbf{w}_2 \quad (2.88)$$

Where  $\xi_1(z)$  and  $\xi_2(z)$  are two arbitrary functions which are real-valued when the argument is a real number (as along the direction  $\hat{x}_1$ ).

We recall that the general solution is obtained combining the particular solution with the homogeneous one (2.88) and this involves other two component functions in  $\mathbf{g}(z)$  as arguable from (2.84). These functions can be expanded in Taylor series at the crack tip and the functions  $\xi_i$  are real-valued whereas the components of  $\mathbf{g}(z)$  are purely imaginary (Deng, 1994).  $\mathbf{g}(z)$  generates two sets of terms with integer powers of  $r$  (distance from the crack tip) as well as  $\xi_2(z)$ . Conversely  $\xi_1(z)$  generate terms with non-integer powers of  $r$  with the first producing the following only singular part of the crack tip fields:

$$\mathbf{h}(z) = \frac{z^\delta K}{2\sqrt{2\pi z}} \mathbf{w}_1 \quad (2.89)$$

Where  $K$  is the stress intensity factor. In conclusion the traction ahead the crack tip is found to be:

$$(\sigma_{21}, \sigma_{22}) = \frac{r^{-\frac{1}{2}+\delta} K}{\sqrt{2\pi}} (1, 0) \quad (2.90)$$

From equation (2.90) the stress intensity factor can be defined from the expression for  $\sigma_{21}$  through  $K = \lim_{r \rightarrow 0} \left[ (2\pi)^{1/2} \sigma_{21} r^{1/2-\delta} \right]$  along the bonded part of the crack. In this case, the traction along the interface has the same form as that for a crack in homogeneous material under mode II conditions, except that the singularity here is different. Practically the mode mixity is no longer found when a Coulomb friction law is imposed on the crack as well as the oscillatory behaviour for the crack tip fields and

thus the stress intensity factor is now well-posed (although its dimensions are no longer  $\left\{ [N][m^{-2}]\left[ m^{\frac{1}{2}} \right] \right\}$  but  $\left\{ [N][m^{-2}]\left[ m^{\frac{1}{2}-\delta} \right] \right\}$ ). To conclude it is worth noting that this conclusion is valid only when the matrix  $\mathbf{H}$  has real diagonal components and purely imaginary off-diagonal components (that is in the configuration of Figure 2.1). Otherwise the normal component is found to be:

$$\sigma_{22} = -\frac{r^{\frac{1}{2}+\delta} K \operatorname{Re}(H_{21})}{\sqrt{2\pi} H_{22}} \quad (2.91)$$

Therefore, although the oscillatory part is not present, mode I and II are still unavoidably coupled even for frictional sliding crack (Deng, 1994).

### 2.3 Bimaterial ill-posedness for Coulomb friction conditions

As anticipated in the introduction, several works (Renardy (1992), Adams (1995), Martins *et al.*, (1995), Martins & Simões (1995) and Simões & Martins (1998)) has shown the analytical ill-posedness of steady sliding of an elastic half-space against a dissimilar elastic-space when a Coulomb friction condition is used along the interface in terms of unstable slip response to stress perturbations. Later Ranjith & Rice (2001) have summarized these analytical results and they also showed that when a delay is introduced in the shear stress response to the normal stress perturbations the problem becomes well-posed. In this section the main analytical results about the frictional ill-posedness and the achieved well-posedness when a Prakash-Clifton regularization (Prakash & Clifton, 1993; Prakash, 1998) is taken into account will be presented.

Let us consider a steady-state slip pulse propagating along the direction  $x_1$ , which propagates along a bimaterial interface and let  $V$  denote its steady-state velocity as in Figure 2.2.

Let us consider the shear stress  $\tau$  at the interface and that it can be perturbed in a single spatial mode of wavenumber  $k$ :

$$\Delta\tau = Q(t)e^{ikx_1} \quad (2.92)$$

Where  $Q(t)$  is an arbitrary function of time  $t$ . The slip rate response to that perturbations can be written as:

$$\Delta V = A(k)e^{ik(x_1-ct)}e^{a|k|t} \quad (2.93)$$

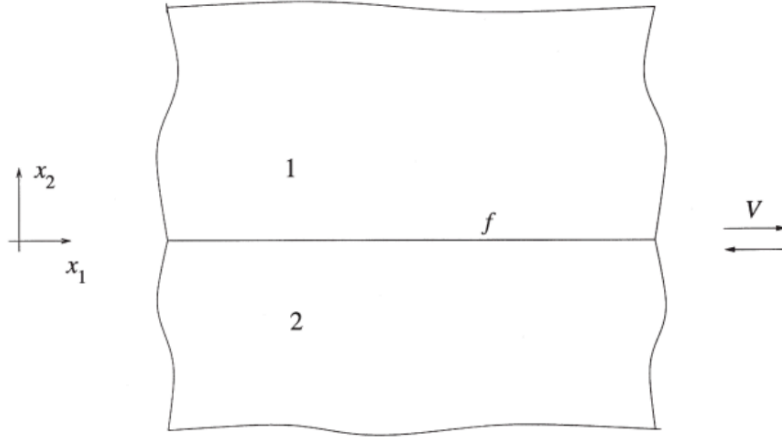


Figure 2.2 Frictional sliding along an interface between dissimilar materials (Ranjith & Rice, 2001)

$A(k)$  is the amplitude of the mode,  $a$  and  $c$  are independent of the wavelength, and for the case for which  $a$  is real and  $a > 0$ , all wavelengths in the slip response are unstable and the growth rate of instability is inversely proportional to the wavelength. In fact, when a realistic perturbation is taken into account an observer, which travels at the velocity  $c$  of instability sees a perturbation velocity field that is the sum of infinite number of modes, namely:

$$\Delta V(x + ct, t) = \int_{-\infty}^{\infty} A(k)e^{ikx}e^{a|k|t} dk \quad (2.94)$$

And the integral (2.94) fails to exist for real  $a > 0$ .

In order to find the conditions for which the instability arises we can consider the following perturbations to the slip  $\delta u$  induced by the shear stress perturbation (2.92):

$$\begin{cases} \delta u_t(x_1, t) = Vt + D_1(t)e^{ikx_1} \\ \delta u^n(x_1, t) = D_2(t)e^{ikx_1} \end{cases} \quad (2.95)$$

Where the subscript  $\{ \}_t$  and the superscript  $\{ \}^n$  represent respectively the tangential and normal components.

Now denoting the Laplace transform as:

$$\hat{g}(p) = \int_0^{\infty} e^{-pt} g(t) dt \quad (2.96)$$

following Geubelle & Rice (1995), it can be shown that, in  $p$ -domain, perturbations in slip are related to those in shear and normal stress by:

$$\begin{Bmatrix} \hat{D}_t \\ \hat{D}^n \end{Bmatrix} = \begin{vmatrix} \hat{K}_{11} & \hat{K}_{12} \\ \hat{K}_{21} & \hat{K}_{22} \end{vmatrix} \begin{Bmatrix} \hat{T} \\ \hat{N} \end{Bmatrix} \quad (2.97)$$

Where  $\hat{T}$  and  $\hat{N}$  represent respectively the Laplace transforms of shear and normal components of the stress;  $\hat{D}$  are the components of Laplace transform of the slip and the transfer coefficients in matrix  $\hat{K}$  depend on the elastic parameter of the two blocks, on the densities, on the wavenumber  $k$  and on the frequency  $p$ . The explicit forms of  $\hat{K}_{ij}$  are reported in Appendix A4.

The system (2.97) can be expressed also in the following inverse form:

$$\begin{Bmatrix} \hat{T} \\ \hat{N} \end{Bmatrix} = \begin{vmatrix} \hat{M}_{11} & \hat{M}_{12} \\ \hat{M}_{21} & \hat{M}_{22} \end{vmatrix} \begin{Bmatrix} \hat{D}_t \\ \hat{D}^n \end{Bmatrix} \quad (2.98)$$

Where  $\hat{M}_{11} = \hat{K}_{22} / D$ ;  $\hat{M}_{22} = \hat{K}_{11} / D$ ;  $\hat{M}_{12} = -\hat{K}_{12} / D = -\hat{M}_{21}$ ; and  $D = |\hat{K}|$ . It is worth noting that the single components  $K_{ij}$  as well as  $D$  have simple poles at  $s = \pm C_{r_1}; \pm C_{r_2}$ , with  $s = p/k$  and  $C_{r_i}$  are the Rayleigh speeds in the two layers.

Now adding to the (2.97) the contribution of shear perturbations given by the (2.92) we get:

$$\begin{Bmatrix} \hat{T} \\ \hat{N} \end{Bmatrix} = \begin{vmatrix} \hat{M}_{11} & \hat{M}_{12} \\ \hat{M}_{21} & \hat{M}_{22} \end{vmatrix} \begin{Bmatrix} \hat{D}_t \\ \hat{D}^n \end{Bmatrix} - \begin{Bmatrix} \hat{Q} \\ 0 \end{Bmatrix} \quad (2.99)$$

Where  $\hat{Q}(p)$  is the Laplace transform of  $Q(t)$  and in the next subsections we will show the sliding response  $\hat{D}_t$  due to the applied  $\hat{Q}$  when either no friction contact is considered or a Coulomb condition is taken into account.

### 2.3.1 Frictionless sliding

If no friction conditions are considered along the interfaces we can set  $\hat{T} = 0$ , whereas, the no opening statement implies that  $\hat{D}^n = 0$ . Therefore we have:

$$\hat{D}_t = -\frac{\hat{K}_{11}\hat{K}_{22} - \hat{K}_{12}\hat{K}_{21}}{\hat{K}_{22}}\hat{Q} \quad (2.100)$$

As noted earlier the Rayleigh poles in the denominator and numerator of the transfer function cancel each other and thus the only poles are the roots of equation  $\hat{K}_{22}(s) = 0$  with  $s = p/k$  and considering the explicit forms of  $\hat{K}_{22}$  (see Appendix A4) it is properly the generalized Rayleigh wave equation found by Weertman (1963, 1980) and Achenbach & Epstein (1967). They showed that when two materials are slightly dissimilar that equation has two imaginary roots  $s = \pm iC_{gr}$  corresponding to a steady state interfacial propagating wave. When the Rayleigh in the stiffer material is lower than the shear wave speed in more compliant medium this solution always exist and it is intermediate between the two Rayleigh speeds.

### 2.3.2 Friction sliding: the Coulomb conditions

Without loss of generality we consider  $V > 0$  such that  $\hat{T} = -f\hat{N}$  where  $f$  is the friction condition and the expression for  $\hat{T}$  represents the Coulomb condition. The transfer function (2.100) change as:

$$\hat{D}_1 = -\frac{\hat{K}_{11}\hat{K}_{22} - \hat{K}_{12}\hat{K}_{21}}{\hat{K}_{22} - f\hat{K}_{21}}\hat{Q} \quad (2.101)$$

Therefore to have an unstable slip response we need that a root of the equation:

$$\hat{K}_{22}(s) - f\hat{K}_{21}(s) = 0 \quad (2.102)$$

has a real part  $> 0$ .

From the explicit form of  $\hat{K}_{22}$  and  $\hat{K}_{21}$  (see Appendix A4) we derive that the former is inversely proportional to  $|k|$ , whereas the latter depends on  $k$ , therefore the roots of (2.102) depend only on the sign of  $k$ . Moreover it can be demonstrated that if  $s^*$  is a root,  $-s^*$  is also a root, and if  $s^*$  and  $-s^*$  are roots for  $k$ ,  $\bar{s}^*$  and  $-\bar{s}^*$  are roots for  $-k$ . Now considering:

$$\text{Re}(s^*) = a; \quad -\text{sign}(k)\text{Im}(s^*) = c \quad (2.103)$$

The slip response to the perturbations with wavenumber  $k$  (or  $-k$ ) has the following form:

$$\delta u_t(x_1, t) \propto \left( e^{ik(x_1-ct)} e^{a|k|t}, e^{ik(x_1+ct)} e^{-a|k|t}, e^{-ik(x_1-ct)} e^{a|k|t}, e^{-ik(x_1+ct)} e^{-a|k|t} \right) \quad (2.104)$$

Practically the modes propagate bilaterally. When a mode has a real  $a > 0$  it grows with a rate of  $a|k|$  whereas the other decays with the same rate. All the growing modes propagate at the same velocity given by imaginary part of the roots from equation (2.102): if  $c > 0$  it will proceed along the positive  $x_1$  directions and viceversa.

As shown in the section 2.3.1 the frictionless problem admits two purely imaginary roots  $s_0 = \pm iC_{gr}$ . For small values of friction we may expect roots  $s$  close to  $s_0$ , Thus using a perturbation expansion in the form:

$$s = s_0 + fs_1 + \dots \quad (2.105)$$

Neglecting the  $O(f)$  and considering the root of equation (2.102) we get:

$$s_1 = \hat{K}_{21}'(s_0) / \hat{K}_{22}'(s_0) \quad (2.106)$$

Since  $\hat{K}_{21}(s_0)$  and  $\hat{K}_{22}(s_0)$  are purely imaginary,  $s_1$  is a real number (Ranjith & Rice, 2001). Therefore, the term  $fs_1$  in the perturbation expansion is real for both roots  $s_0 = \pm iC_{gr}$  of frictionless problem. Therefore the problem is unstable for arbitrary small friction values for the cases where the generalized Rayleigh wave exists in the frictionless contact.

Conversely when the two solids are more dissimilar such that the generalized Rayleigh roots do not exist the frictionless problem  $\hat{K}_{22}(s) = 0$  do not have root in the whole complex plane (Ranjith & Rice, 2001). This obviously implies that there is an interval  $-f_c < f < f_c$  for which the friction problem (2.102) has no root too. This in turn implies that there exists an interval around  $f = 0$  for which the response to a single modal shear stress perturbation is stable.

Starting from the results presented in this section Ranjith & Rice (2001) performed a parametric study to characterize the slip response to shear stress perturbations for different contrasts of elastic parameters. The results are summarized in the Figure 2.3. In Figure 2.3a-b the locations of the roots for the problem (2.102) are shown respectively for small (existing  $C_{gr}$ ) and higher contrasts between layers. In the first

case an unstable mode can be detected already for  $f$  slightly higher than 0 and it propagates at generalized Rayleigh speed (Figure 2.3a). Conversely when  $C_{gr}$  does not exist for small friction coefficients ( $f < 0.03$  in Figure 2.3b) no unstable roots are found and the problem can be considered well-posed. Finally in Figure 2.3c the stability diagram is shown: for each shear wave speed ratio (and for two different density ratios) the response is shown to be either well or ill-posed accordingly to the friction coefficient. When  $C_{gr}$  exists the problem is always ill-posed and the unstable modes can propagate properly at expected Generalized Rayleigh speed. Conversely when it does not exist the slip response is expected to be well-posed for small coefficients of friction, whereas for higher  $f$  the modes are unstable and they can propagate at speed slightly higher than shear wave speed in more compliant medium. As we will see, these results (concerning a propagating slip pulse at constant friction of coefficient) about the expected speed for the propagating modes will be retrieved in regularized numerical models both for existing and not existing  $C_{gr}$  when a growing crack is considered in the framework of linear slip weakening.

### 2.3.3 Stability problem for regularized solutions

To conclude this analysis it is worth to show how the friction problem expressed by (2.102) is modified when a regularization is introduced. The laboratory experiments performed by Prakash & Clifton (1993) and Prakash (1998) suggested that when an abrupt normal stress perturbations is considered along an interface there is no instantaneous change in shear strength but rather gradual change which occurs over a finite time scale or a finite amount of sliding. Thus a fading memory of normal stress variations can be taken into account as follow:

$$\dot{\tau} = \left(\frac{V}{L}\right)(\tau + f\sigma^n) \quad (2.107)$$

Where  $V$  is the unperturbed slip rate,  $L$  is the characteristic slip scale over which the change occurs and  $\sigma^n$  is the normal stress. Taking the Laplace transform and considering a single mode as previously done, we get now, for the tangential traction in  $p$ -domain:

$$p\hat{T} = -\left(\frac{V}{L}\right)(\hat{T} + f\hat{N}) \quad (2.108)$$

and solving for  $\hat{D}_1$  with no opening conditions we transform the problem (2.101) into:

$$\hat{D}_1 = \frac{(pL/V + 1)\hat{K}_{11}\hat{K}_{22} - \hat{K}_{12}\hat{K}_{21}}{(pL/V + 1)\hat{K}_{22} - f\hat{K}_{21}}\hat{Q} \quad (2.109)$$

Thus the equation, which governs the stability is:

$$(sq + 1)\hat{K}_{22}(s) - f\hat{K}_{21}(s) = 0 \quad (2.110)$$

With  $q = L|k|/V$  and as usual  $s = p/|k|$ .

In the long wavelength limit ( $|k| \rightarrow 0$ ) the (2.110) simply reduces to the (2.101). Nevertheless, since the ill-posedness is related to the response for high  $|k|$  it is interesting to understand if there is stability at short wavelengths. For high  $|k| > k_{cr}$  (where  $k_{cr}$  is an arbitrary critical wavenumber) the problem can be approximated to  $K_{22}(s) = 0$  which is the same equation for frictionless problem. Thus when  $C_{gr}$  does not exist the problem is stable as well as the not regularized problem with low friction coefficient. For cases for which  $C_{gr}$  exists a perturbations expansion in powers of  $1/|k|$ , for the roots, gives the root location at large  $|k|$  as:

$$s = p/|k| = s_0 + is_1/|k| + (s_2 + is_3)/k^2 + \dots \quad (2.111)$$

With  $s_0 = \pm iC_{gr}$ ,  $s_1, s_2$  and  $s_3$  are real numbers with  $s_2 > 0$  for one of the two values of  $s_0$ . Therefore, a perturbation with large wavenumber  $k$  grows as  $e^{s_2 t/|k|}$  and this ensures a finite integral over all excited modes at all times and thus regularizes the problem. In conclusion, although all wavelengths are still unstable with the friction law (2.108) as it was with the Coulomb friction law, the stability problem expressed by the infinite sum of all modes is now well-posed. As shown by numerical models (Cochard & Rice, 2000; Rubin & Ampuero, 2007; Ampuero & Ben-Zion, 2008) this type of regularization friction law can provide numerical stable solutions in terms of models independent on the discretization. In the next sections new numerical models will be shown aimed to distinguish among the numerical well-posed solutions the most reliable physical models.

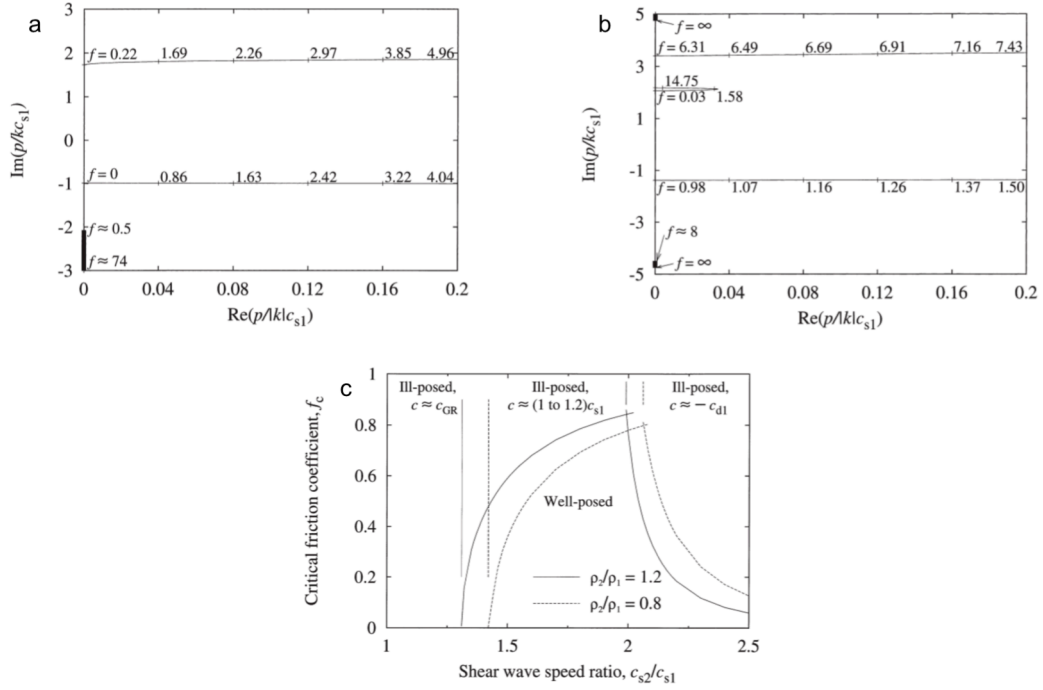


Figure 2.3 (a) Root locations of problem (2.102) in the complex right-half  $s$ -plane as a function of friction coefficient when  $C_{gr}$  exists. For arbitrary small friction coefficient an instability propagating at  $C_{gr}$  can be detected. (b) Root locations of problem (2.102) in the complex right-half  $s$ -plane as a function of friction coefficient when  $C_{gr}$  does not exist. For the particular choice of contrast we need a friction  $f > 0.03$  to have an unstable modes propagating at P-wave speed of more compliant medium.

(c) Stability diagram for two different density ratios. When  $C_{gr}$  exists, the modes are always unstable and the expected speed is properly  $C_{gr}$ . When  $C_{gr}$  does not exist the response can be ill-posed, whereas for higher friction coefficient it is ill-posed again and unstable modes, slightly faster than shear speed in more compliant medium, are roots for the problem (2.102). Ranjith & Rice (2001)

## 2.4 Numerical modelling for bimaterial interfaces

### 2.4.1 Prakash-Clifton regularization

As seen in the previous section, in the framework of classical Coulomb friction, the problem of a rupture propagating along a bimaterial interface is ill-posed, due to the instantaneous response of the tangential traction to abrupt changes in normal stress. Based on the numerical experiments of Prakash & Clifton (1993), the problem was shown to become well-posed when introducing a delay between normal stress perturbation and the frictional response (Cochard & Rice, 2000, Ranjith & Rice, 2001). This delay can be accounted for, introducing the new variable  $T_{eff}^n$ , the

effective normal traction, which is related to the normal traction by an exponential relaxation law, while it replaces the normal traction in equation (1.26) for the definition of the Coulomb's conditions:

$$\frac{\partial T_{eff}^n}{\partial t} = \frac{1}{t^*} (T^n - T_{eff}^n) \quad |\mathbf{T}^t| = \mu T_{eff}^n \quad (2.112)$$

In the above equation  $t^*$  is the characteristic time of the relaxation and, in this section,  $\mu$  always indicates the friction coefficient. In the following sub-sections, several bi-dimensional numerical models will be presented. For those cases the quantity  $T_{eff}^n$  and  $T^n$  will be referred to respectively as  $\sigma_{eff}$  and  $\sigma^n$ , while the  $|\mathbf{T}^t|$  will be simply referred to as  $\tau$ .

In general, the relaxation time can vary on the fault and may depend on the rupture dynamics. e.g Cocharad & Rice (2000) suggested  $t^* = t^*(\delta v)$  and:

$$\frac{1}{t^*} = \frac{|\delta v|}{\delta l} + \frac{1}{t_c} \quad (2.113)$$

where  $\delta l$  is a characteristic slip length, competing with  $D_c$ , and  $t_c$  is a constant time uniform for all the fault plane. We also refer to  $\delta l$  as the relaxation slip parameter. The relaxation time given in (2.113) can be interpreted as the sum of two contributions, one depending on a constant time scale and the other one depending on slip (Rubin & Ampuero, 2007). This form was introduced to follow slow nucleations, as considered by Andrews & Ben-Zion (1997), where the rupture is originated by an external normal stress load. Nevertheless in many numerical simulations (e.g. Ampuero & Ben-Zion, 2007; Langer *et al.*, 2012; Rubin & Ampuero, 2007) only the constant time scale was used to study bimaterial ruptures.

In this work, we started to separately study the two limit cases in which only one of the two contributions is taken into account. We define  $t_d = \delta l / |\delta v|$  as the dynamic time scale and  $t_c$  as the constant time scale. We performed a parametric study, which allows to find numerically well-posed models, as the solutions showing convergence for grid refinement (Cocharad & Rice, 2000) and to discriminate physically reliable solutions, as independent of the specific selection of regularization parameters. It is worth noting that the normal stress perturbations are due to both dynamic sliding and elastodynamic flux due to wave propagation. Nevertheless the latter variations are not expected to make the problem ill-posed ahead of the rupture front. Since the spectral

element method allows to properly model the wave propagation above a minimum wavelength without any relaxation, we switched on the regularization mechanism at a given point on the fault, only when it starts to slide, independently of the specific selected relaxation scheme.

## 2.4.2 Numerical discretization

In this section the numerical implementation of the above-presented regularization will be presented.

Starting from equation (1.75) we have seen that the actual value of normal stress is computed contextually with the verification of Signorini's contact conditions.

In particular if no opening occurs the rupture can frictionally sliding and for homogeneous case the Coulomb condition as presented in section 1.5 has to be verified. Conversely, for bimaterial interface the quantity  $\sigma_{eff}$  has to be computed.

By using the equation (2.112) the computation of  $\sigma_{eff}$  can be performed by using a forward time scheme as follow:

$$\sigma_{eff\ p+1} = \left(1 + \frac{\Delta t}{t_{p+1}^*}\right)^{-1} \left[ \sigma_{eff,p} + \frac{\Delta t}{t^*} \sigma_{p+1}^n \right] \quad (2.114)$$

Where  $\sigma^n$  is the normal stress computed from Signorini's condition and the subscripts  $\{ \}_p$  indicates the time step.

Since the static parts for  $\sigma^n$  and  $\sigma_{eff}$  coincide, it is easy to show that the equation (2.112) and its discrete version (2.114) are exactly the same both for total tractions and their dynamic parts. Thus without loss of generality the (2.114) can be simply used to compute the dynamic part of  $\sigma_{eff}$ . Moreover  $t^*$  may explicitly depend on the slip rate value  $\delta v$ : in that case a prediction-correction scheme was used; in the prediction phase  $\delta \tilde{v}_{p+1} = \delta v_p$ , then the Coulomb condition was verified giving a corrected  $\delta v_{p+1}$  which in turn is used to recompute the Coulomb statement.

The Coulomb friction conditions can be verified as follows:

1. the effective normal stress for the frictional strength at time  $p+1$  is given by

$$\sigma_{T,p+1} = \sigma_{eff,p+1} + \sigma_0^n .$$

2. The elastodynamic flux, at the same time, gives the dynamic tangential traction  $\tau_{p+1}$  and the total tangential traction is:  $\tau_{T,p+1} = \tau_{p+1} + \tau_0$  with  $\tau_0$  that represents the remote shear stress.
3.  $\tau_{T,p+1}$  has to be compared with  $\mu\sigma_{T,p+1}$  (with  $\sigma_{T,p+1}$  obtained at step 1. and  $\mu$  given by the linear slip weakening law, see section 1.2.4) and from the intersection described in Figure 1.7 the solutions for slip rate and tangential stress are indeed obtained. It is worth noting that the projection described in Figure 1.7 has to be performed onto the straight line  $\tau = -\mu\sigma_{T,p+1}$  where the dynamic part  $\sigma_{T,p+1}$  is now the effective normal stress  $\sigma_{eff,p+1}$ .

### 2.4.3 Simulation setup

Rubin & Ampuero (2007) first analysed the problem of a bimaterial growing crack in the framework of linear slip weakening constitutive law. In order to compare the results deriving from our parametric study with Rubin & Ampuero numerical models a similar modelling set up was chosen and its characteristics will be described in the current subsection.

The geometrical model is described in Figure 2.4a and it consists of a bidimensional domain, within which the fault can be considered as a line, which separates the two blocks. The densities  $\rho_i$  and the body seismic wave velocities  $C_{s_i}$  and  $C_{p_i}$  are assigned to each block. In our configuration the expected favoured direction is towards the right being the direction of the slip in the more compliant medium. The dynamics of the rupture is driven by the four dimensionless parameters  $C_{s_1}/C_{s_2}$ ,  $\rho_1/\rho_2$ ,  $\nu_1$  and  $\nu_2$  with  $\nu_i$  are the Poisson's coefficient. In our simulations we always assume Poissonian media ( $\nu_1 = \nu_2 = 0.25$ ). From the analytical results of Weertman (1980), Rubin & Ampuero argued that the dynamic features (asymmetry of slip rate, normal stress evolution, etc.) are mainly sensitive to the ratio  $\gamma = C_{s_1}/C_{s_2}$ , while they are poorly influenced by the density ratio.

Weertman showed that a steady state slip pulse can propagate along the favoured direction along a bimaterial interface inducing the following shear and normal stress perturbations:

$$\left\{ \begin{array}{l} \Delta\tau(x) = \frac{\bar{G}}{2\pi} \int_{-\infty}^{\infty} \frac{d\delta u / dx}{x-s} ds \\ \Delta\sigma^n(x) = G^* \frac{d\delta u}{dx} \end{array} \right. \quad (2.115)$$

Where  $\delta u$  is the slip and the moduli  $\bar{G}$  and  $G^*$  depend on both elastic properties and rupture velocity. In particular  $\bar{G}$  decreases with the increasing rupture speed and for small contrasts of impedance there exists a real rupture velocity for which  $\Delta\tau(x)=0$ . By analogy with the homogeneous case, this speed is defined as Generalized Rayleigh speed ( $C_{gr}$ ) and it is the expected asymptotic speed for a growing crack. The explicit expression for  $\bar{G}$  can be found in the Appendix A of Rubin & Ampuero (2007) (equation A2) and for sake of completeness it is reported here:

$$\left[ G_1\gamma_2(1-\alpha_2^2)(\gamma_1\beta_1-\alpha_1^4) + G_2\gamma_1(1-\alpha_1^2)(\gamma_2\beta_2-\alpha_2^4) \right] = 0 \quad (2.116)$$

with:

$$\begin{aligned} \alpha_i &\equiv \sqrt{1 - C^2 / 2C_{s_i}^2} \\ \beta_i &\equiv \sqrt{1 - C^2 / C_{s_i}^2} \\ \gamma_i &\equiv \sqrt{1 - C^2 / C_{p_i}^2} \end{aligned} \quad (2.117)$$

$G_i$  are the shear moduli for the two layers and the roots  $C$  have to be found.

When  $C_{gr}$  exists it is an intermediate speed between the two expected Rayleigh speeds within each block. Keeping uniform the density across the two layers and using  $v_1 = v_2 = 0.25 C_{gr}$  it was shown to be real when  $\gamma < 1.359$  (Harris & Day, 1997). In any case the equations (2.116) and (2.117) allows to compute the Generalized Rayleigh speed for each contrast of density.

When the fault is a bimaterial interface the linear slip weakening constitutive law introduces new complexities due to the perturbations of normal stress. In fact, when a homogeneous medium is taken into account the static and dynamic level of traction are fixed by the static value  $\sigma_0^n$  and friction coefficients  $\mu_s$  and  $\mu_d$ , and the weakening is actually linear for all points on the fault interface. As consequence the fracture energy  $E_{Gc}$  (defined as the area below the weakening curve in a slip-traction

reference) is simply given by  $E_{Gc} = 0.5D_c(\mu_s - \mu_d)\sigma_0^n$ ; on the other hand, in the case of bimaterial,  $\sigma_{eff}$  changes dynamically as response to normal stress perturbations as well as the total effective normal stress. In particular at the receivers placed along the favoured direction the expected slip weakening for a homogeneous medium was compared to the actual weakening obtained in bimaterial models. During the acceleration phase, the increasing compressive variations ahead the crack tip increase more and more the yield stress, whereas the strong extensive perturbations induced by crack front arrival make the weakening sharper. Finally the dynamic level is lower than the homogeneous case. Therefore the fracture energy  $E_{Gc}$  also dynamically changes as well as the normal stress (see Figure 2.4b).

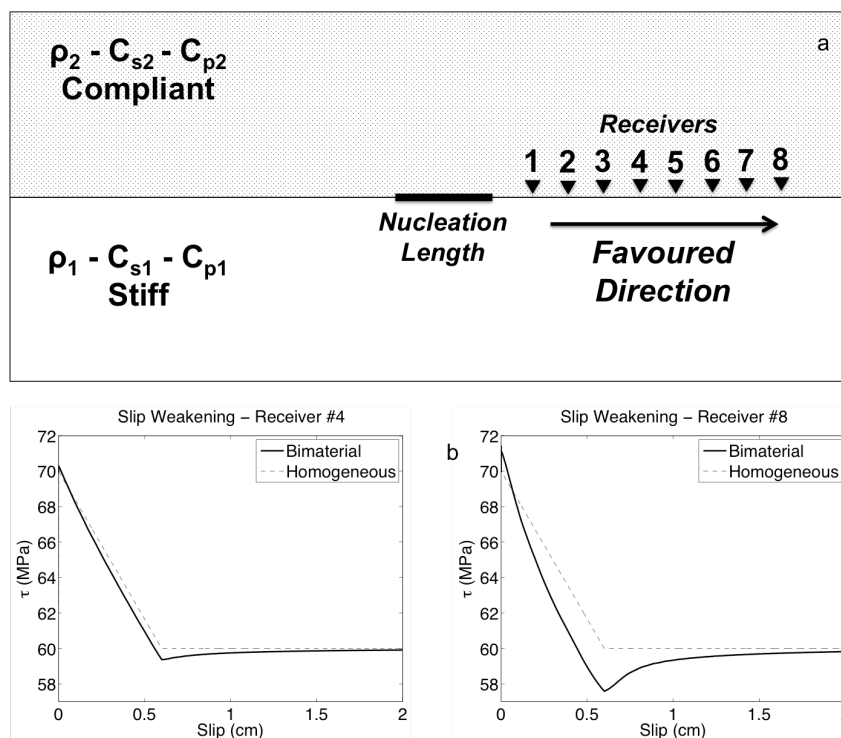


Figure 2.4 (a) The simulation setup for the numerical models: below half-space is always the stiffer one; some receiver are located along favoured direction (to the right of nucleation) to store the variation of kinematic and dynamic quantities as a function of time. (b) The expected linear slip weakening for homogeneous case (dashed lines) is compared to the actual weakening recorded at two receivers.

In most of the simulations and unless otherwise stated, we fixed a uniform density at a reliable crustal value ( $\rho_1 = \rho_2 = 2700 \text{ kg / m}^3$ ), while we tested several values of gamma, corresponding to existence or not  $C_{gr}$ .

On the fault, the initial normal stress is set to the uniform value  $\sigma_0^n = -100 \text{ MPa}$ , whereas the initial shear stress is  $\tau^0 = 62.5 \text{ MPa}$ . The linear slip weakening parameters are  $\mu_s = 0.7$ ,  $\mu_d = 0.6$  and  $D_c = 6 \text{ mm}$ . With these setup the strength parameter  $s = \frac{\mu_s \sigma_0^n - \tau}{\tau - \mu_d \sigma_0^n} = 3$ . The rupture is initiated bringing the initial tangential traction slightly above the yield stress (0.5%) over a fixed length. the size of this patch has to be larger than the nucleation length  $L_c$  for slip-weakening rupture (Uenishi & Rice, 2003; Rubin & Ampuero 2007) for a homogeneous medium:

$$L_c = 1.118 \frac{G'}{W} \quad (2.118)$$

Where the effective elastic modulus for quasi-static plane strain deformation  $G'$  depends on the shear moduli  $G_i$  and Poisson coefficients  $\nu_i$  in the two layers (Rubin & Ampuero, 2007).  $W$  is the initial slope of slip weakening law at the nucleation:

$$W = \frac{\sigma_0^n (\mu_s - \mu_d)}{D_c} \quad (2.119)$$

where the perturbation on the normal and tangential traction can be neglected. Using the equations (2.118) and (2.119) the rupture can proceed in unstable way, mimicking the propagation of a seismic rupture without considering the quasi-static phase related to the nucleation.

For numerical simulations with spectral element method we use a regular mesh, with square elements of  $9 \times 9$  Gauss Lobatto Legendre collocation points. The maximum element size  $h$  for all the simulations that guarantees to have at least 5 point per wavelength during the rupture propagation in an equivalent homogeneous medium is  $h = 12 \text{ m}$ . The Courant number for the simulation is always smaller than 0.3, thus warranting stability for explicit time stepping (Komatitsch & Vilotte, 1998). To avoid the influence of boundary conditions other than the fault slip, we assume that the fault is embedded in an infinite medium, mimicked by Perfectly Matching Layers (Festa & Nielsen, 2003; Festa & Vilotte, 2006) as absorbing layers along the

edges of the numerical domain. All the presented initial conditions are reported in Table 2-1.

#### 2.4.4 Regularization parametric study: dynamic time scale

When a dynamic time scale is used ( $t^* = t_d = \delta l / |\delta v|$ ), the relaxation slip parameter  $\delta l$  is the only parameter that affects the regularization. It is chosen in the range ( $2\%D_c - 100\%D_c$ ) to ensure that the regularization of normal stress perturbations induced by the propagating rupture occurs in the vicinity of crack front.

Table 2-1: Initial simulation setup

PARAMETER	SYMBOL	VALUES
Initial normal stress	$\sigma_0^n$	$-100 \text{ MPa}$
Static friction coefficient	$\mu_s$	0.7
Dynamic friction coefficient	$\mu_d$	0.6
Initial shear stress	$\tau_u$	62.5
Strength parameter	$s$	3
Density for both layers	$\rho = \rho_1 = \rho_2$	$2700 \text{ kg/m}^3$
Shear speed ratio	$C_{s2}/C_{s1}$	1.18 – 1.80
Effective shear modulus	$G'$	$28.1 \text{ GPa}$
Initial crack length	$L_c$	24 m
slip weakening distance	$Dc$	6 mm
Relaxation slip value	$\delta l$	1% – 100% $Dc$
Constant time scale	$t_c$	$6 \cdot 10^{-5} - 6 \cdot 10^{-3} \text{ s}$
Element Size	$h$	2/3/4/6/12 m

Since the regularization depends on the slip rate  $\delta v$ , the relaxation time of the regularization is local to the point on the fault and its variation is relevant around the crack tip within the dissipation zone, where the slip rate sharply increases to its maximum and then decreases to an almost constant value outside the cohesive zone. Thus, within this latter region the dynamic regularization behaves as the constant time regularization with a larger relaxation time.

As a first study we want to investigate the convergence of the solutions. For this regularization, we have two kinds of convergence as a function of the grid size  $h$  and  $\delta l$  respectively. Convergence for grid refinement provides numerically well-posed solutions in the sense of Cochard & Rice (2000). In this case, we investigated the maximum value of grid size  $h$  for fixed  $\delta l$ , below which the solutions do not depend on the grid size within the dispersion error. We then explored the numerically stable solutions as a function of  $\delta l$ . We expected an upper limit for the relaxation slip parameter  $\delta l_{\max}$ , below which the solution does not depend on  $\delta l$ , within the dispersion error (Kammer *et al.* 2014). This convergence is here referred to as physical convergence of the solutions.

The comparison between solutions will be described both in space and time domains.

In the space domain the comparison is based on the slip rate that allows to identify the position of crack tip, to characterize the rupture speed, and in turn to define the degree of asymmetry between the two directions of the crack. In time domain we represent the effective normal stress  $\sigma_{eff}$  recorded at receivers located on the fault at increasing distance from the nucleation zone, as indicated in Figure 2.4a. The selected quantities are representative of the rupture dynamics during its acceleration from the end of the nucleation to the stationary phase.

We started in investigating a model for which the Generalized Rayleigh speed exists ( $\gamma = 1.18$   $C_{s_2} = 2.620 \text{ km/s}$  and  $C_{s_1} = 3.092 \text{ km/s}$ ).

Figure 2.5a shows the slip rate profile at time step  $t_0 = 0.12 \text{ s}$  obtained for  $\delta l = 2\% D_c$ , which is the smallest value used in this study. Figure 2.5b is a zoom of Figure 2.5a around the crack front. We analysed the convergence for mesh sizes of  $h = 2, 3, 4, 6, 12 \text{ m}$ .

For coarser grids ( $h > 4m$ ) the rupture is faster in both directions as compared to finer grids (Figure 2.5a-d). Additionally for  $\delta l = 2\%D_c$  strong oscillations occur, also producing pathological effects in the not favoured direction, such as multiple pulses due to continuous arresting and restarting of the rupture (Figure 2.5a). These results hold for all the acceleration phase of the rupture.

Figure 2.5c-d are the same representation of Figure 2.5a-b at the same time step, for  $\delta l = 10\%D_c$ . In this case, the oscillations of the slip rate in the coarser meshes are considerably damped (Figure 2.5c). Nevertheless when zooming around the crack front (Figure 2.5d), the rupture for coarser meshes are still in advance as compared to the slip rate evolution observed in finer grids. For both showed  $\delta l$  grid convergence is achieved when  $h \leq 4m$ .

We obtained the same convergence condition from the analysis of  $\sigma_{eff}$  as a function of time at receiver 5. For  $\delta l = 2\%D_c$  (Figure 2.6a), the coarser meshes ( $h = 6m$  and  $h = 12m$ ) clearly show strong oscillations, whose characteristics are similar to the ones retrieved by Kammer *et al.* (2014) for slip rate, while the maximum value of the effective stress occurs earlier in time (Figure 2.6b). For finer meshes ( $h \leq 4m$ ) the curves are overlapped (Figure 2.6a-b).

This feature is preserved also for larger  $\delta l$ , for which the oscillations of  $\sigma_{eff}$  are more and more damped (Figure 2.6c-d).

This convergence analysis, in space domain, is summarized in Figure 2.7. Figure 2.7a-b show the normalized difference of the maximum amplitude of slip rate  $\delta v_{max}$ , along favoured direction between the results obtained for  $h = 3, 4, 6, 12m$  and  $h = 2m$  as a function of time. This difference  $\Delta\delta v_{max}$  can be defined as:

$$\Delta\delta v_{max}(t) = \frac{\delta v_{max}(h, t) - \delta v_{max}(h = 2m, t)}{\delta v_{max}(h = 2m, t)} \quad (2.120)$$

As shown by Figure 2.7a-b respectively for  $\delta l = 2\%D_c$  and  $\delta l = 10\%D_c$  for  $h \leq 4m$  we have an error  $\Delta\delta v_{max} < 0.02$  for all the duration of the simulations. Similar results are shown in Figure 2.7c-d where the normalized differences  $\Delta X$  between the positions of crack tip X defined as:

$$\Delta X(t) = \frac{|X(h,t) - X(h=2m,t)|}{|X(h=2m,t)|} \quad (2.121)$$

are shown with  $\Delta X(t) < 0.01$  for  $h \leq 4m$

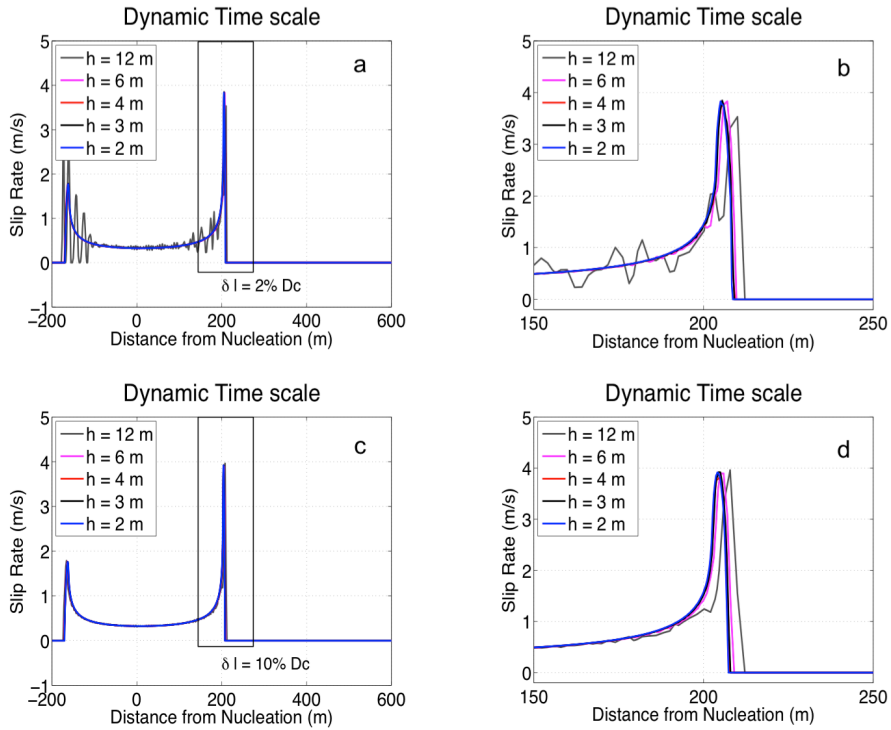


Figure 2.5 Grid refinement in space domain, slip rate at the same time step ( $t_e = 0.12s$ ) for  $\delta l = 2-10\%Dc$  : (a) When solutions are not convergent strong oscillations of slip rate can emerge up to pathological effects (e.g. stop and go of rupture). Those effects can boost the rupture producing unreliable acceleration of the rupture front. The black square indicates the zoom around the crack front (b). Even for highest  $\delta l$  (c) for which the oscillatory effects are damped solutions for coarsest meshes do not converge with those obtained from finest ones. When solutions converge position of crack front and amplitude of the maximum coincide. The black square indicates the zoom around the crack front (d)

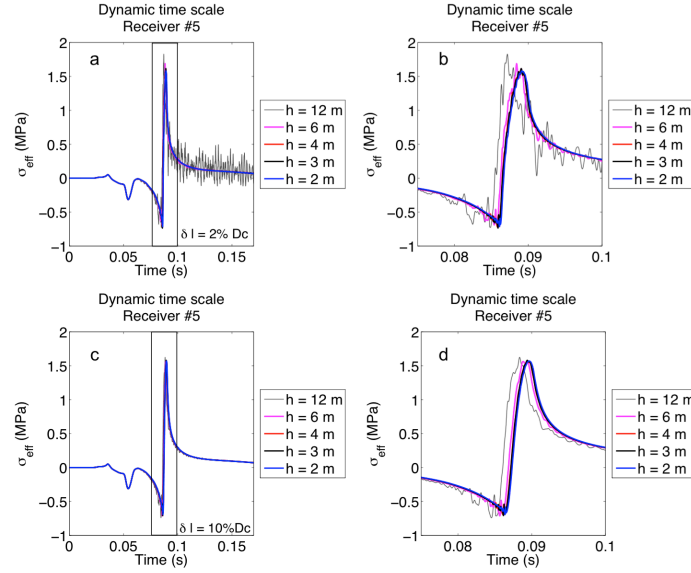


Figure 2.6  $\sigma_{eff}$  as a function of time for all used grid sizes and for two different relaxation slip at receiver 5: (a)  $\delta l$  is equal to  $2\%D_c$ : the coarsest meshes show strong oscillations and they are not convergent with the results coming from the finest meshes. The black square indicates the zoom around the crack front (b). (c)  $\delta l$  is equal to  $10\%D_c$ : the coarsest meshes show less evident oscillations but they are still not convergent with the results coming from the finest meshes. The black square indicates the zoom around the crack front (d)

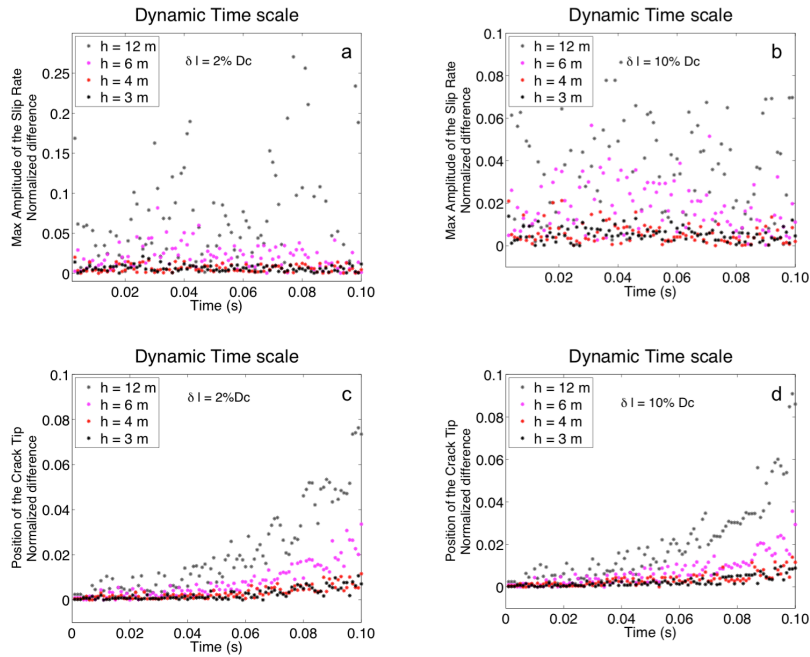


Figure 2.7: Numerical convergence analysis for dynamic time scale: (a)-(b) the maximum amplitude of slip rate for  $\delta l = 2\% - 10\%D_c$  and for  $h = 3, 4, 6, 12m$  are compared with the same quantity obtained with  $h = 2m$  and the normalized difference  $\Delta\delta v_{max}(t)$  is shown. (c)-(d) show the results based on the difference between the crack tip positions  $\Delta X(t)$ .

We finally found that the maximum value of the grid size, below which we observe stable solutions, is almost independent of the specific value of  $\delta l$ . In our analysis we get numerically well posed solutions for  $h \leq 4m$ . This finding is slightly different from the results of Kammer *et al.* (2014), obtained for an arresting slip pulse, for which smaller  $\delta l$  values require finer meshes.

After finding the grid size, which provides stable solutions for the investigated  $\delta l$  we studied the physical convergence as a function of  $\delta l$ .

Figure 2.8a shows the slip rate profiles at time step  $t_0=0.12s$  for different  $\delta l$ , while Figure 2.8b shows the zoom of the same profile around the crack front of the favoured direction. The pictures show the expected asymmetry for bimaterial propagation with larger variations around the crack front in the favoured direction. Here, convergence of maximum amplitude of slip rate is achieved for  $\delta l \leq 20\%D_c$ , whereas the maximum amplitude is lowered as  $\delta l$  increases beyond this value. Furthermore the position of the crack tip is more sensitive to the regularization and only for  $\delta l \leq 10\%D_c$  it is independent of the parameterization while the rupture goes slower for larger  $\delta l$  (Figure 2.8b and c). The normal stress perturbation in the favoured direction changes its sign moving from a compressive regime ahead of the crack tip to an extensive regime behind the tip. The increase of  $\delta l$  corresponds to larger and larger relaxation times, which are not able to properly capture the sharp variation of the normal stress at the crack tip. The regularization subtracts high frequency energy to the propagating rupture within the dissipation zone, decreasing the maximum amplitude of the slip rate and preventing fast acceleration of the rupture. In the not favoured direction we experienced the opposite behaviour as a function of  $\delta l$ , although this effect is less pronounced as compared to the favoured direction. In the not favoured direction, indeed, the normal stress perturbations are extensional ahead of the crack and compressive behind the tip. In Figure 2.8c we represent the rupture speed normalized to  $C_{gr}$  as a function of the distance from the rupture initiation, along the favoured direction. We observe that convergence is achieved again for  $\delta l \leq 10\%D_c$ , all along the rupture. The figure also indicates that the rupture is accelerating towards the expected limit speed  $C_{gr}$ . Collecting the results for the whole rupture propagation, we get physically convergent solutions for  $\delta l \leq 10\%D_c$ .

The convergence of solutions can be also shown in time domain referring to the variations of  $\sigma_{eff}$ . Figure 2.9a,b,c show the evolution of  $\sigma_{eff}$  respectively at receivers 2, 5 and 8. The curves superimpose, before the arrival of the crack, as expected because ahead of the crack tip the solutions are not regularized. Then, behind the tip, the curves are different depending on  $\delta l$ . These differences are enhanced in the zoom around the maximum of the effective stress (for receiver 5), which is shown in Figure 2.9d, where the convergence of the solutions can be argued from the superposition of the curves. Even in this case, the convergence is achieved for  $\delta l \leq 10\% Dc$ . The curves for  $\delta l > 10\% Dc$ , still represent numerically well-posed solutions, but they depend on the specific selection of the regularization parameters. The same results hold for all the acceleration phase.

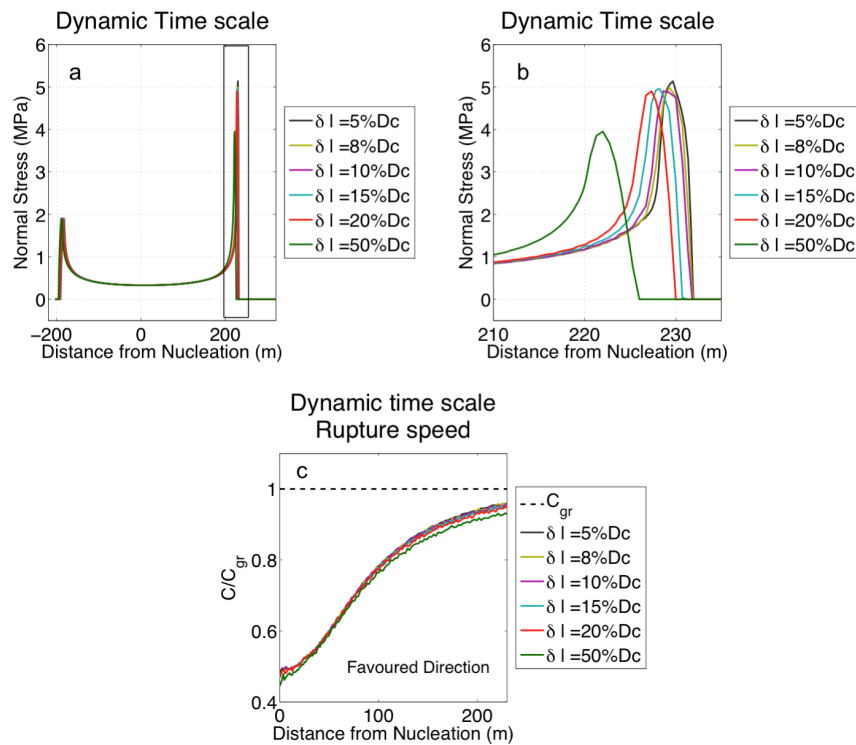


Figure 2.8 Physical convergence for decreasing relaxation slip in space domain: (a) shows the slip rate profiles at a fixed time step and it shows the expected typical bimaterial asymmetry. The zoom (b) show the convergence for small  $\delta l$  in terms of maximum amplitude and position of the crack front. (c)

Rupture speed along the favoured direction normalized to  $C_{gr}$  as a function of distance from nucleation, the overlapping of convergent curves is evident as well as the capability of the rupture to accelerate almost up to  $C_{gr}$ . The non convergent solutions are slower than the convergent ones

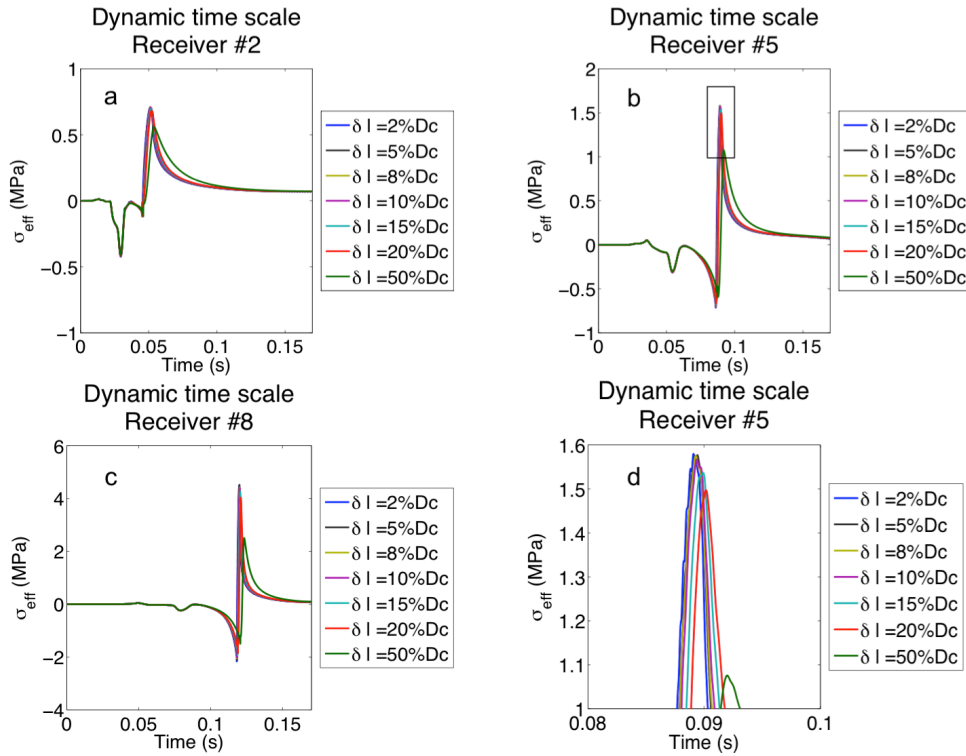


Figure 2.9 Physical convergence for decreasing relaxation slip in time domain.  $\sigma_{eff}$  is shown at three different receiver points (a-b-c). The induced perturbations are huger and sharper moving away from the nucleation and they are smoothed for increasing  $\delta l$ . The black square in (b) indicates the zoom around the crack front (d) for receiver 5; the convergence of maximum amplitude for  $\sigma_{eff}$  is evident for  $\delta l \leq 10\%D_c$

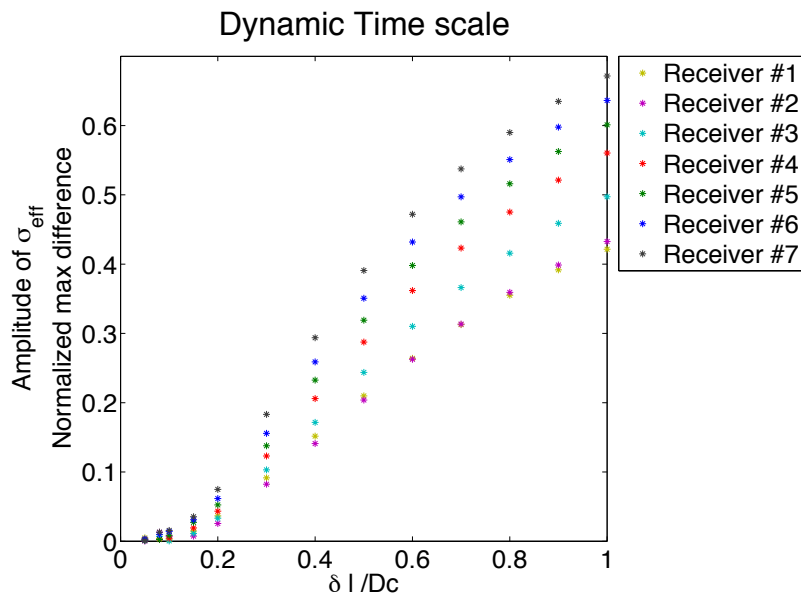


Figure 2.10 Physical convergence shown by plotting the quantity  $\Delta\sigma_{eff,max}$  as function of  $\delta l / D_c$  for the receivers along the acceleration phase. For  $\delta l \leq 10\%D_c$  the convergence is achieved.

Similarly to the grid refinement convergence analysis, this physical convergence can be summarized defining a normalized difference  $\Delta\sigma_{eff,max}$  between the maximum values of  $\sigma_{eff,max}$  recorded at each receiver along the acceleration phase:

$$\Delta\sigma_{eff,max}(\delta l, x_R) = \frac{\sigma_{eff,max}(\delta l, x_R) - \sigma_{eff,max}(\delta l = 2\%D_c, x_R)}{\sigma_{eff,max}(\delta l = 2\%D_c, x_R)} \quad (2.122)$$

Where  $x_R$  is the position of the receiver and all maximum effective stress differences are normalized to that obtained for the smallest considered  $\delta l$ . In figure Figure 2.10  $\Delta\sigma_{eff,max}$  tends to zero for  $\delta l \leq 10\%D_c$  independently of the receiver, and thus independently of rupture speed and maximum of slip rate around the crack front.

The capability of the regularization based on the dynamic time scale to preserve the physical convergence below a fixed parameter  $\delta l$  during the whole acceleration phase, owes to the fact that the relaxation mechanism is an adaptive low-pass filter of the normal stress, whose cut-off threshold changes locally as a function of the slip rate by analogy with the results of Kammer *et al.* (2014). The dynamic time scale provides inhomogeneous cut-off frequencies along the rupture. As the rupture accelerates toward the asymptotic speed, the slip rate at the crack front sharply increases, also increasing the cut-off frequency of the filter. To clarify this interpretation we represent in Figure 2.11 the amplitude spectrum of  $\sigma_{eff}$  at the same receivers analysed in Figure 5. Along the spectra different physical and numerical characteristic frequencies can be detected. These frequencies are marked with dashed lines in Figure 2.11b (for receiver 5): the lowest frequency is related to the largest time scale in the normal stress perturbation and it usually corresponds to a first change of slope in the spectrum (black line). As the rupture accelerates, this scale is associated with the duration of the weakening process at a given point of the fault. At a shorter time scale, within the dissipation zone, the frequency related to the coupling between normal stress and tangential traction can be individuated (red line); this coupling time scale is estimated as the delay between the maximum of slip rate and the rupture tip. Since the instability of the bimaterial rupture comes from the high-frequency coupling between normal and shear stress, the regularization cut-off frequency has to be located between the characteristic frequency of the normal stress variation and the coupling frequency, in order to preserve the characteristic time scales of the propagating rupture, while damping the unstable frequencies. Finally, the numerical resolution

frequency can be individuated as the maximum well resolved frequency for the defined mesh, which for spectral element method depends on the smallest velocity and on the minimum number of points ( $\sim 5$ ) required per wavelength (Komatitsch et Vilotte, 1998). During acceleration phase both the physical and the coupling frequencies increase, as observed in Figure 2.12, which shows the slip rate and the normal stress at three receivers at increasing distance from the rupture initiation. As the rupture progresses, the dissipation zone shrinks, and consequently the slip rate increases, while the normal stress perturbations follow the same evolution of the slip velocity. Indeed we argue that a relaxation filter, which adapts the cut-off frequency to slip rate variations, is able to properly filter the normal stress close to the crack front all along the acceleration phase.

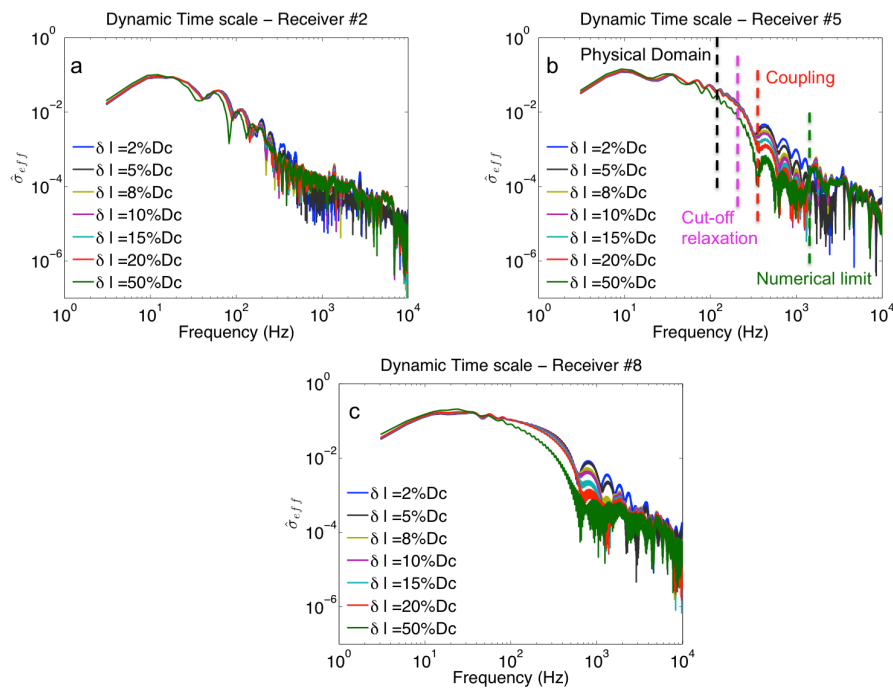


Figure 2.11 Physical convergence for decreasing relaxation slip in frequency domain: amplitude spectra for the perturbations described in Figure 2.10. In figure (b) the characteristic frequencies of the physical and numerical problem are explicitly reported as example (dashed lines). The magenta dashed line is the characteristic cut-off frequency deriving from the relaxation mechanism (for  $\delta l = 10\% Dc$ ).

The numerical limit (green dashed line) is related to the mesh with  $h = 4 m$

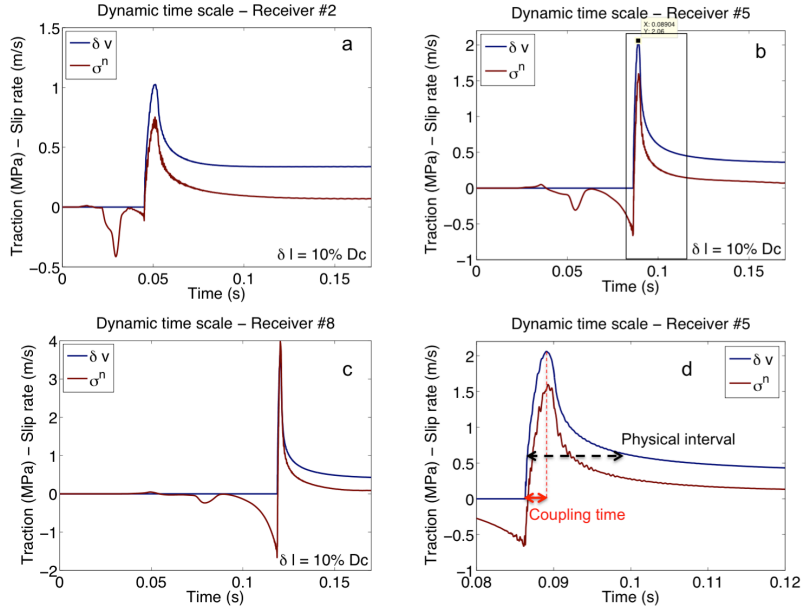


Figure 2.12 Normal stress perturbations accordingly to slip rate variations at the same points of Figure 2.9 and Figure 2.11. The physical content of the two variations is the same for the two quantities and it increases moving away from the nucleation. Without loss of generality the pictures refer to the simulation performed with a mesh size  $h = 4m$  and  $\delta l = 10\% D_c$ . The black square in (b) indicates the zoom around the crack front (d) where the coupling time and the physical time interval from which the respective frequency are inferred are explicitly shown (cfr. Figure 2.11d).

The time scale from which the physical frequency domain and the coupling frequency are inferred from the zoom of Figure 2.12b (Figure 2.12d).

In Figure 2.13 we investigated the difference  $\sigma^n - \sigma_{eff}$  as a function of slip, for the all receivers represented in Figure 2.4. For fixed slip relaxation parameter, the slip value  $\delta u^*$  at which  $\sigma_{eff}$  joins  $\sigma^n$  behind the crack tip does not depend on the position of receivers and thus is independent of slip rate and rupture speed, although the maximum of the difference between  $\sigma^n$  and  $\sigma_{eff}$  increases as the crack grows up. Furthermore if  $\delta l \leq 10\% D_c$ , then  $\delta u^* < D_c$  ( $\delta u^* \sim 95\% D_c$  warm colours in Figure 2.13). When  $\delta l = 15\% D_c$   $\delta u^* \sim D_c$ , whereas for higher values of the relaxation slip parameter  $\delta u^* > D_c$  (cold colours in Figure 2.13). Indeed we can argue that the regularization is effective when the slip scale, over which it works, is smaller than the slip scale over which the dissipation takes place. For  $\delta l > 10\% D_c$ , the filter operates over a scale larger than the dissipation and indeed also filters the physical scale we

would like to preserve during the propagation. Since the problem in the framework of linear slip weakening is scalable with  $D_c$ , this result can be generalized to arbitrary slip weakening distance.

The same convergence analyses were performed also for a higher impedance contrast ( $\gamma = 1.80$ ) for which the Generalized Rayleigh speed does not exist. To analyse this case, we did not change the density in the two blocks while the ratio between the shear wave speeds is varied keeping constant the effective shear modulus  $G'$ . This allows to start the rupture using the same initiation length as in the previous case (see section 2.4.3).

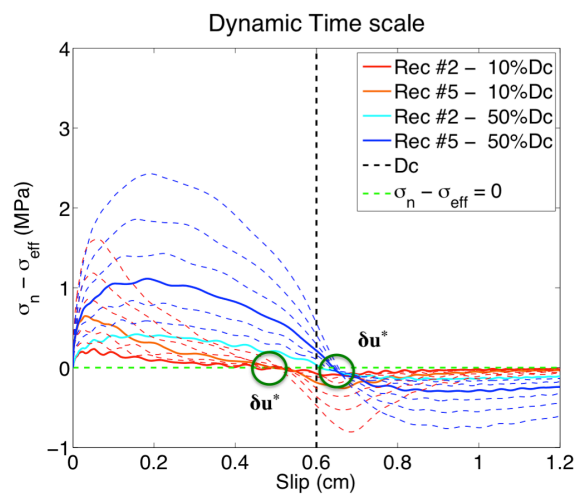


Figure 2.13  $\sigma_{eff} - \sigma^n$  after the initiation of slip and the contemporary triggering of relaxation. Warm colours full lines represent simulations with  $\delta l = 10\%Dc$  (convergent solutions) for two receiver points, whereas cold colours full lines are relative to  $\delta l = 50\%Dc$  (non convergent solutions) for the same receivers. The zero crossing recorded at other receivers is plotted with dashed lines respectively with warm and cold colours. Green circles marks the slip  $\delta u^*$  for the two cases.

When  $\gamma$  is higher the rupture is faster along the favoured direction and slower along the opposite side exhibiting a more pronounced rupture asymmetry (Figure 2.14). Nevertheless, the convergence analysis for grid refinement and decreasing  $\delta l$  show analogous results. Specifically Figure 2.15 shows the evolution of  $\sigma_{eff}$  with time (Figure 2.15a-b) and with frequency (Figure 2.15c). Again physical convergence is achieved when  $\delta l \leq 10\%Dc$ . Since the stationary phase is approached faster when  $\gamma = 1.80$ , for sake of clarity in those figures the receiver 3 is considered to ensure to be still in the acceleration phase. Moreover the slip  $\delta u^*$  is still independent of the

receivers during the acceleration phase and it is  $\sim 95\%D_c$  when  $\delta l = 10\%D_c$  (Figure 2.15d).

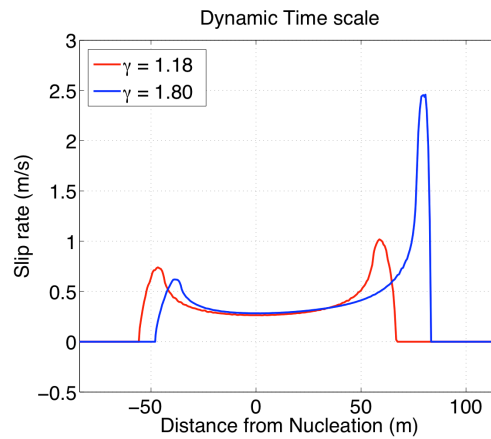


Figure 2.14 A slip rate profile at the same time for the two analysed contrast of impedance: when  $\gamma$  is higher the rupture accelerates faster towards the asymptotic speed. The slip rate is sharper along the favoured direction and the asymmetry is more pronounced.

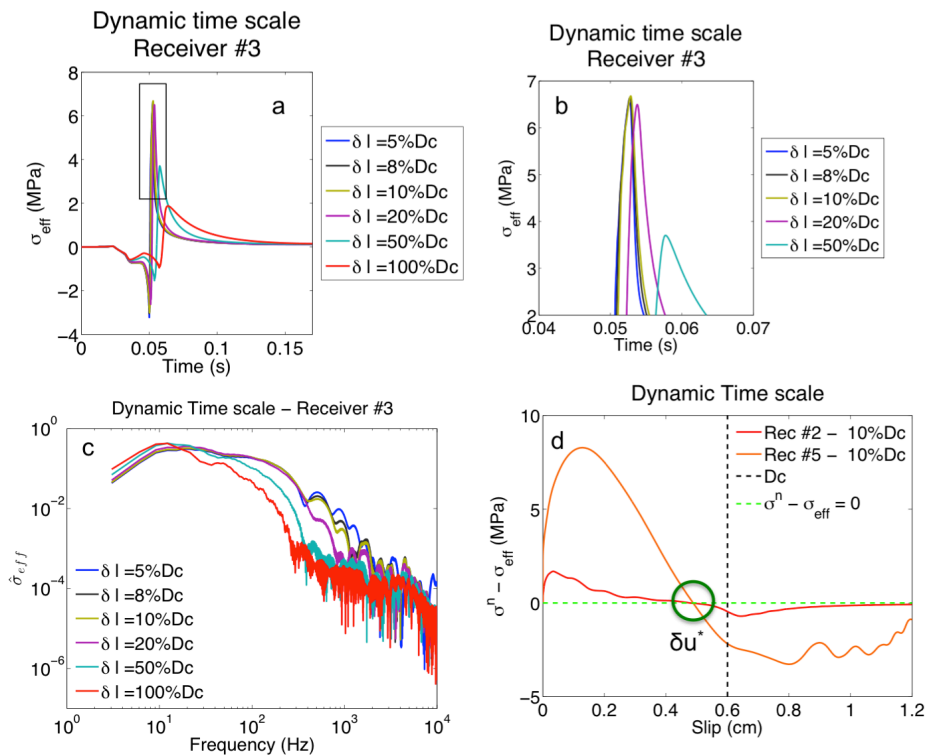


Figure 2.15 (a) Physical convergence for decreasing relaxation slip in time domain: the zoom beside shows that convergence is still achieved when  $\delta l \leq 10\%D_c$ . The black square indicates the zoom around the crack front (b). The convergence is still driven by the introduce filtering and the figure (c) shows the amplitude spectra for different  $\delta l$ . (d) Even for higher  $\gamma$ ,  $\delta u^*$  is fixed by dynamic time scale and it is lower than  $D_c$  when  $\delta l \leq 10\%D_c$ .

### 2.4.5 Regularization parametric study: constant time scale

When a constant time scale  $t_c$  is used the coupling between the normal stress perturbations and the shear traction is driven by a unique relaxation time, which is independent of the kinematic and dynamic features of the rupture.

The parametric study was performed selecting  $t_c$  in the range  $1.2 \cdot 10^{-4} s \leq t_c \leq 6.0 \cdot 10^{-3} s$ . Relating  $t_c$  to the classical formula for the regularization (Cochard & Rice, 2000) for which  $t_c = \delta l / \delta v^*$ , this range corresponds to a variation of  $\delta l$  between 2%Dc and 100%Dc for  $\delta v^* = 1 m/s$ , hence allowing to directly compare the constant time scale regularization to the dynamic one described in the previous subsection.

As for dynamic time scale, two parametric analyses were performed to study the numerical and the physical convergences. All the results presented here refer to the case  $\gamma = 1.18$  with the same elastic properties as used in the section 2.4.4.

The numerical convergence analysis provided very similar results with respect to the dynamic time scale. The analysis can be summarized looking at the slip rate profiles at time step  $t_0 = 0.12 s$  in space domain for the smallest value of  $t_c$  ( $t_c = 1.2 \cdot 10^{-4} s$ , Figure 2.16a-b) and for  $t_c = 6.0 \cdot 10^{-4} s$  (Figure 2.16c-d). As well as for the dynamic time scale, the coarser meshes ( $h = 6 m$  and  $h = 12 m$ ) provide non-convergent solutions. In the first case, pathological oscillatory effects are observed (zoom from Figure 2.16b) while in the second case the oscillations within the crack are damped (Figure 2.16d). Thus, even in this case the numerically well-posed solutions are obtained for  $h \leq 4 m$ , and the convergence is guaranteed for all acceleration phase.

The achieved numerical convergence can be also shown plotting the quantities  $\Delta \delta v_{\max}(t)$  and  $\Delta X(t)$  of equations (2.120) and (2.121) as well as for dynamic time scale (Figure 2.17).

We then investigated the influence of time scale, varying  $t_c$ . Differently from the dynamic time scale, decreasing the time parameter no convergence is achieved. This can be observed both for the kinematic and dynamic fields, in space and time domains.

To show this result, the curves of  $\sigma_{eff}$  can be plotted in time domain at two receivers. Although at the beginning of acceleration phase the solutions are overlapped below a given  $t_c$ , (Figure 2.18a) the differences become detectable at receiver 8, which is located close to the end of the acceleration phase (Figure 2.18c).

The interpretation for this missing convergence when a constant time scale is used can be provided in the same framework described for the retrieved convergence in the dynamic case. Figure 2.19 shows the evolution of slip rate with respect to the time at receivers 2, 5, 8 (the same receiver analysed for dynamic time scale) and we can estimate an equivalent  $\delta l_{eq}^{max}$  for the constant time scale at each receiver all along the rupture as:  $\delta l_{eq}^{max} = \delta v_{max} \cdot t_c$  where  $\delta v_{max}$  is the maximum for slip rate at each receiver and for the receivers of Figure 2.19 it assumes the following values:  $\delta v_{max\#2} \sim 1.0 m/s$ ;  $\delta v_{max\#5} \sim 2.0 m/s$ ;  $\delta v_{max\#8} \sim 3.4 m/s$ ;

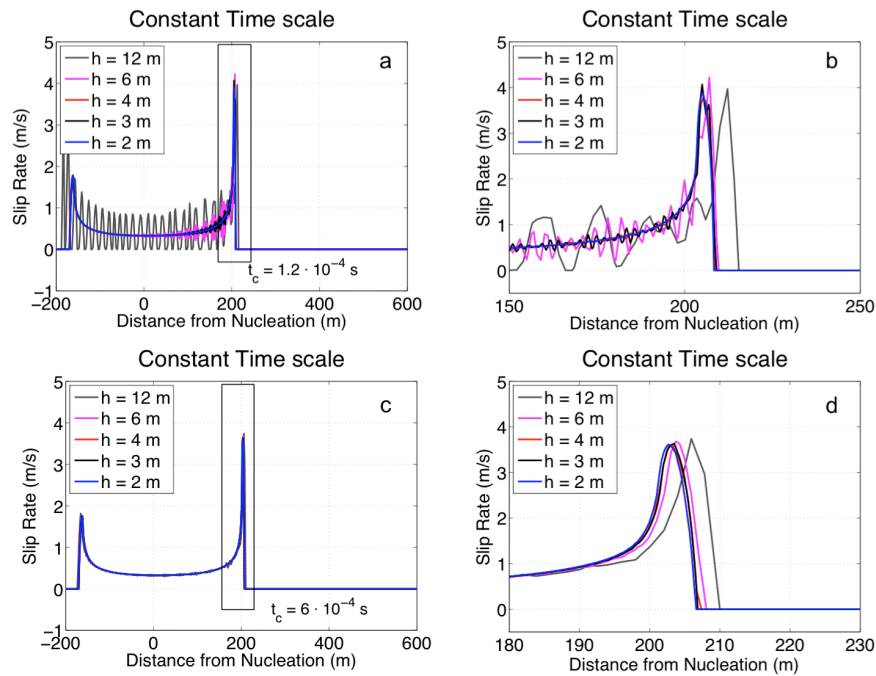


Figure 2.16 Grid refinement in space domain, slip rate at the same time step for  $t_c = 1.2 \cdot 10^{-4} s$  : (a) when solutions are not convergent strong oscillations of slip rate can emerge up to pathological effects (e.g. stop and go of rupture). Those effects can boost the rupture producing unreliable acceleration of the rupture front. The black square indicates the zoom around the crack front (b). (c) Even for highest  $t_c$  for which the oscillatory effects are dumped solutions for coarsest meshes do not converge with those obtained from finest ones. When solutions converge position of crack front and amplitude of the maximum coincide. The range of mesh convergence is the same found for dynamic time scale. The black square indicates the zoom around the crack front (d)

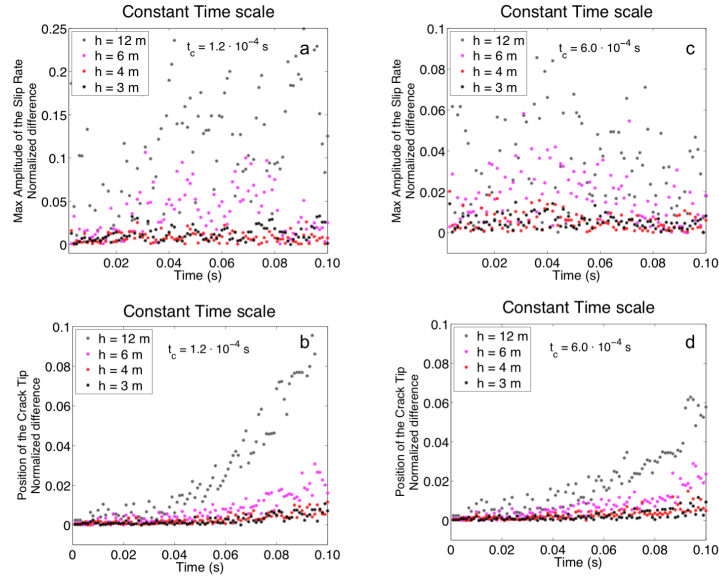


Figure 2.17 Numerical convergence analysis for constant time scale: (a)-(b) the maximum amplitude of slip rate for  $t_c = 1.2 \cdot 10^{-4} \text{ s} - 6.0 \cdot 10^{-4} \text{ s}$  for  $h = 3, 4, 6, 12 \text{ m}$  are compared with the same quantity obtained with  $h = 2 \text{ m}$  and the normalized differences  $\Delta \delta v_{\max}(t)$  are shown. (c)-(d) show the convergence analysis based on the difference between the crack tip positions  $\Delta X(t)$ .

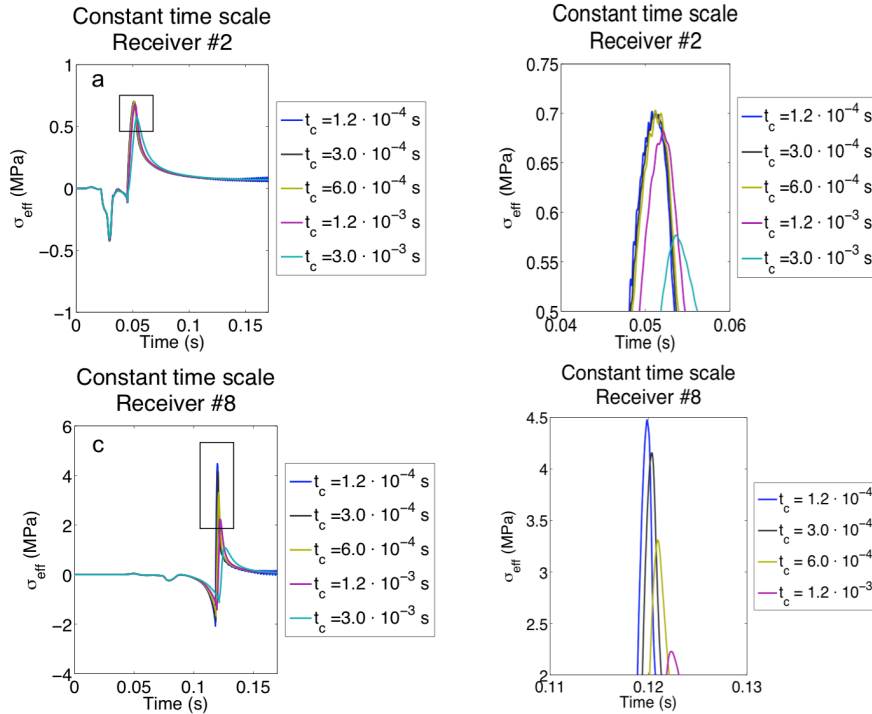


Figure 2.18 Physical convergence for decreasing relaxation slip in time domain.  $\sigma_{\text{eff}}$  is shown at the receiver 2 (a) and 8 (c). No convergence can be evidenced for constant time scale even for really small  $t_c$ . Even when solutions are similar at the beginning of acceleration phase the differences increase more and more with the crack growth. The black squares indicate the zooms around the crack front (b-d) for the two receivers.

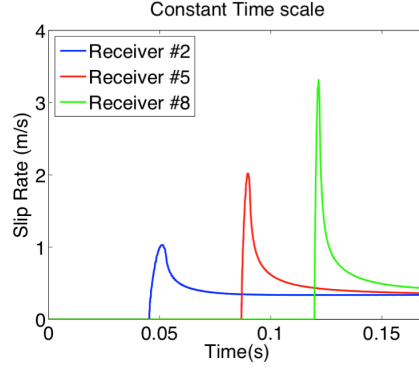


Figure 2.19 Slip rate, as a function of time, recorded at the receivers 2, 5, 8

As expected  $\delta l_{eq}^{\max}$  increases with crack growth accordingly with  $\delta v_{\max}$  and considering  $t_c = 6 \cdot 10^{-4}$  s it assumes the following values for the considered receiver points:

$$\begin{aligned}
 \delta l_{eq\#2}^{\max} &\sim 6.0 \cdot 10^{-4} \text{ m} = 10\% Dc \\
 \delta l_{eq\#5}^{\max} &\sim 1.2 \cdot 10^{-3} \text{ m} = 20\% Dc \\
 \delta l_{eq\#8}^{\max} &\sim 2.4 \cdot 10^{-3} \text{ m} = 30\% Dc
 \end{aligned} \tag{2.123}$$

Indeed the equivalent  $\delta l$  increases as the rupture tip distance from the initiation zone increases, owing to a sharpening of the slip rate. For the specific selection of  $t_c$ , at the receiver 8, the  $\delta l_{eq}^{\max}$  is well outside the physical convergence range found when the dynamic time scale is used. The non-convergence of solutions can be also inferred from the quantity  $\Delta \sigma_{eff, \max}$  of equation (2.122) simply replacing the parameter  $\delta l$  with  $t_c$ . Figure 2.20 shows as  $\Delta \sigma_{eff, \max}$  increases as the crack grows up even for smaller  $t_c$ .

Analysing the solutions in frequency domain (Figure 2.21), a fixed time scale implies a fixed cut-off frequency from regularization for all the acceleration phase (magenta dashed lines in Figure 2.21a-b-c). Conversely the physical and the coupling frequencies increase with the crack growth (respectively black and red dashed lines in Figure 2.21a-b-c). Since the size of the dissipation zone goes to zero as the rupture approaches the asymptotic speed, there will be always a position on the fault after which the physical frequency will go beyond the cut-off filter frequency of the regularization for any  $t_c$ . In this case, the regularization will overfilter the physical process providing no longer convergent solutions.

An effect deriving from the lack of physically convergence is the slower acceleration of the rupture towards the asymptotic speed as compared to the dynamically regularized solutions. In Figure 2.22 we show the instantaneous rupture speed (normalized to  $C_{gr}$ ) as the rupture propagates along the fault for the constant (blue line) and dynamic time scales (red line). For an assigned  $t_c$ , the solutions are initially superimposed. During crack growth, when convergence is no longer kept, the speed for the two cases differ more and more, due to the excess of filtering of the constant time scale regularization

In light of this parametric study, a new interpretation for the classical Prakash-Clifton regularization emerges. This regularization (equations (2.112) with  $t^*$  given by the (2.113)) can be rewritten as:

$$\frac{\partial \sigma_{eff}}{\partial t} = (f_d + f_c)(\sigma_n - \sigma_{eff}) \quad (2.124)$$

Where  $f_d = |\delta v| / \delta l$  is the dynamic frequency and  $f_c$  is a constant cut-off frequency. The former provide a self-adaptive scheme which leads to convergent solutions independent from chosen slip regularization parameter within a finite range; the latter still provides numerical well-posed solutions but it does not allow to define a physical convergence range. When either a small  $f_c$  is used or the absolute value of the slip rate is large enough to give  $f_d \gg f_c$  the solutions can be considered as almost equivalent to those provided by the dynamic time scale. Nevertheless, when  $f_c \geq f_d$  the solutions, although convergent for grid refinement, strictly depend on the parameterization.

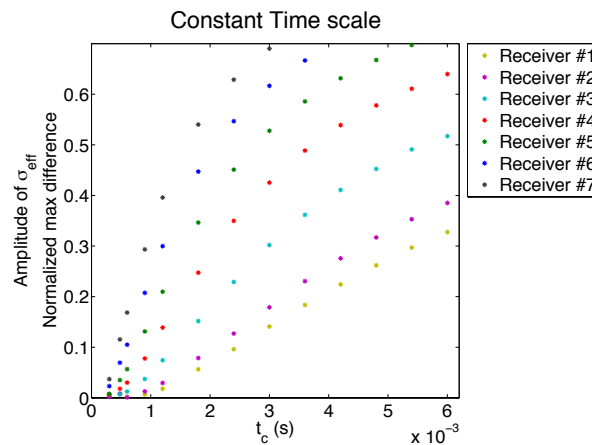


Figure 2.20 Physical non-convergence shown by plotting the quantity  $\Delta \sigma_{eff,max}$  as function of  $t_c$  for the receivers along the acceleration phase.

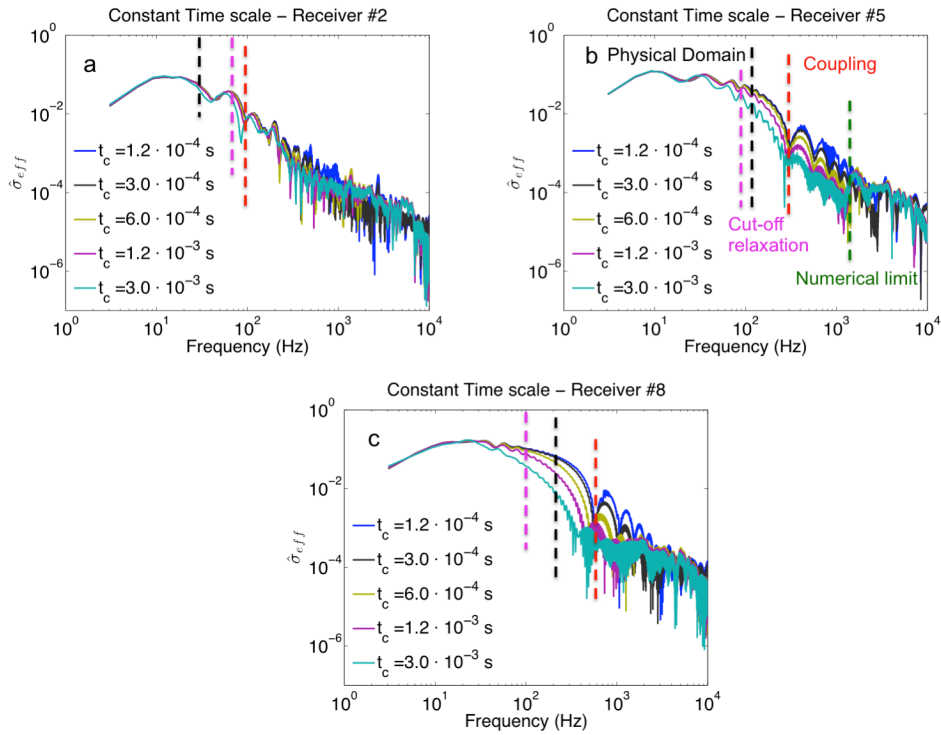


Figure 2.21 Physical convergence for decreasing constant time scale in frequency domain at three different receivers (2 (a) - 5 (b) - 8 (c)). The non-convergence of solutions can be argued by the increasing difference among the low-frequency parts of amplitude spectra. The cut-off frequency (related to  $t_c = 1.2 \cdot 10^{-3} s$ ) is fixed (magenta dashed lines). The physical domain (black dashed lines) and the coupling frequencies (red dashed lines) increase as expected with the crack growth

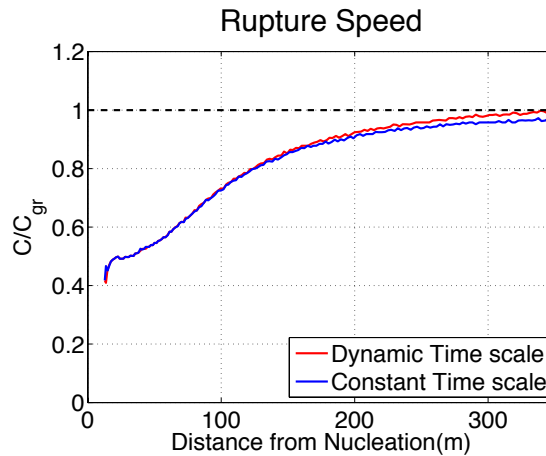


Figure 2.22 Acceleration of the rupture towards the asymptotic speed ( $C_{gr}$ ) for dynamic and constant time scales: while a convergence among different time scales is still detectable the acceleration is equivalent to that deriving from dynamic time scale models. Conversely when the time scale is too large to properly regularize the problem the rupture speeds differ more and more and the acceleration is less strong for the constant time scale.

### 2.4.6 Alternative regularization

The dynamic time scale was shown to provide physical convergent solutions as long as the relaxation of tangential traction occurs over a slip length smaller than the slip weakening distance  $D_c$ .

This aspect seems to suggest that, the instability of the solutions for bimaterial interfaces comes from the normal –tangential coupling at the scale of cohesive zone, where most of the dissipation and wave emission takes place. In the context of slip weakening, the cohesive zone contains all the points, which are actually sliding at a friction level  $\mu > \mu_d$  and it can also be referred to as dissipation zone.

For this reason an alternative regularization is proposed in order to link the relaxation time scale to the size of dissipation length. We can express it as:

$$\frac{\partial \sigma_{eff}}{\partial t} = \frac{1}{t_{L_d}} (\sigma^n - \sigma_{eff}); \quad t_{L_d} = \frac{\beta L_d}{V^a} \quad (2.125)$$

Where  $L_d$  is the length of dissipation zone,  $V^a$  is a reference rupture speed (e.g. the expected asymptotic speed) and  $\beta$  is a parameter used to perform parametric analyses by analogy with the previously described dynamic time scale.

The (2.125) still provides a dynamic time scale; in fact the acceleration of rupture generates a shrinking of dissipation zone, which in turn provides smaller and smaller relaxation time. Differently from the dynamic time scale depending on the slip rate this scale is not a local quantity but it is related to a characteristic length of the rupture.

Also the dissipative length scale provides numerically well-posed solutions for the finest meshes ( $h \leq 4m$ ), whereas the coarser grids show the usual spurious features, that is the pathological strong oscillations for slip rate profile at time step  $t_0 = 0.12s$  for the lowest values of  $\beta$  (Figure 2.23a-b) and not convergent position for the crack front even if the spurious oscillations are damped increasing the  $\beta$  parameter (Figure 2.23c-d).

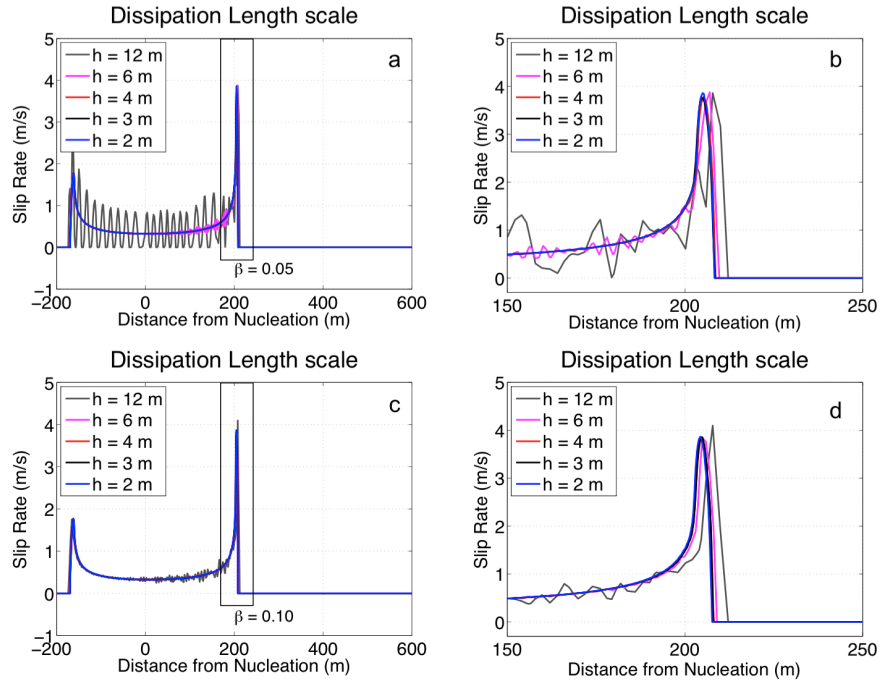


Figure 2.23 Grid refinement in space domain: slip rate for two different parameters  $\beta$  when a dissipation length scale is used: the features for all simulations are pretty the same obtained for dynamic and constant time scales (a-c). The black square indicates the zoom around the crack front (b-d).

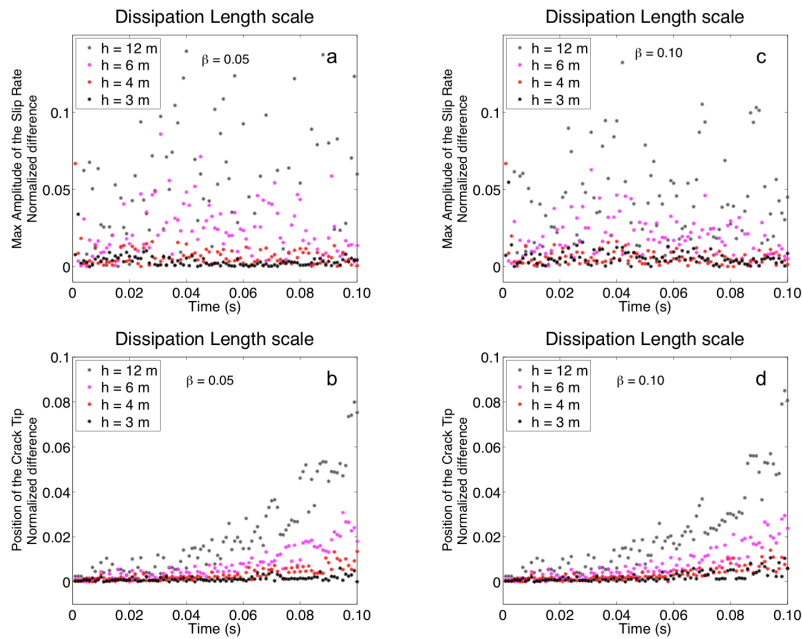


Figure 2.24 Numerical convergence analysis for constant time scale: (a)-(b) the maximum amplitude of slip rate for  $\beta = 0.05 - 0.10$  for  $h = 3, 4, 6, 12m$  are compared with the same quantity obtained with  $h = 2m$  and the normalized differences  $\Delta\delta v_{\max}(t)$  are shown. (c)-(d) show the same analysis based on the difference between the crack tip positions  $\Delta X(t)$ .

As well as for the constant and dynamic time scales these conclusions about numerical convergence can be shown in terms of maximum amplitude of slip rate and position of crack front (Figure 2.24).

Then among the mesh convergent models a parametric study was performed, decreasing  $\beta$  in order to achieve physical convergence and, as usual, the solutions were compared in space as well as in time/frequency domain to investigate the influence of parameterization on the crack dynamics during acceleration phase. Similarly to the dynamic time scale solutions the convergence is achieved for small  $\beta$  for which  $\sigma_{eff}$  becomes independent of the parameterization at each receiver. To show this result in the Figure 2.25a-c the time evolution of effective stress is plotted for different  $\beta$  at receivers 2 and 5 and the zooms of Figure 2.25b-d show that the convergence is achieved for  $\beta < 0.10$ . We again argued that this convergence is due to the fact that the cut-off frequency dynamically follows the variations of physical and coupling frequencies due to the crack growth and it still locates between them. The Figure 2.26a-b show the amplitude spectra for  $\sigma_{eff}$  at receivers 2 and 5 and for  $\beta < 0.10$  the spectra superimpose at lower frequency. The achieved convergence can be also shown by considering the normalized difference between the maximum amplitude of effective stress  $\Delta\sigma_{eff,max}(\beta, x_R)$  by analogy with the case for which a dynamic time scale is used. This normalized difference for the receivers along the acceleration phase is plotted in Figure 2.27 and as for the dynamic time scale within the convergence range this difference is shown to be independent of the chosen parameterization.

Figure 2.28 shows that this regularization mechanism also fixes a slip  $\delta u^*$  depending only on  $\beta$  and again for convergent solutions we have:  $\beta \leq 0.10 \Rightarrow \delta u^* < D_c$  whereas for  $\beta > 0.10 \Rightarrow \delta u^* > D_c$ .

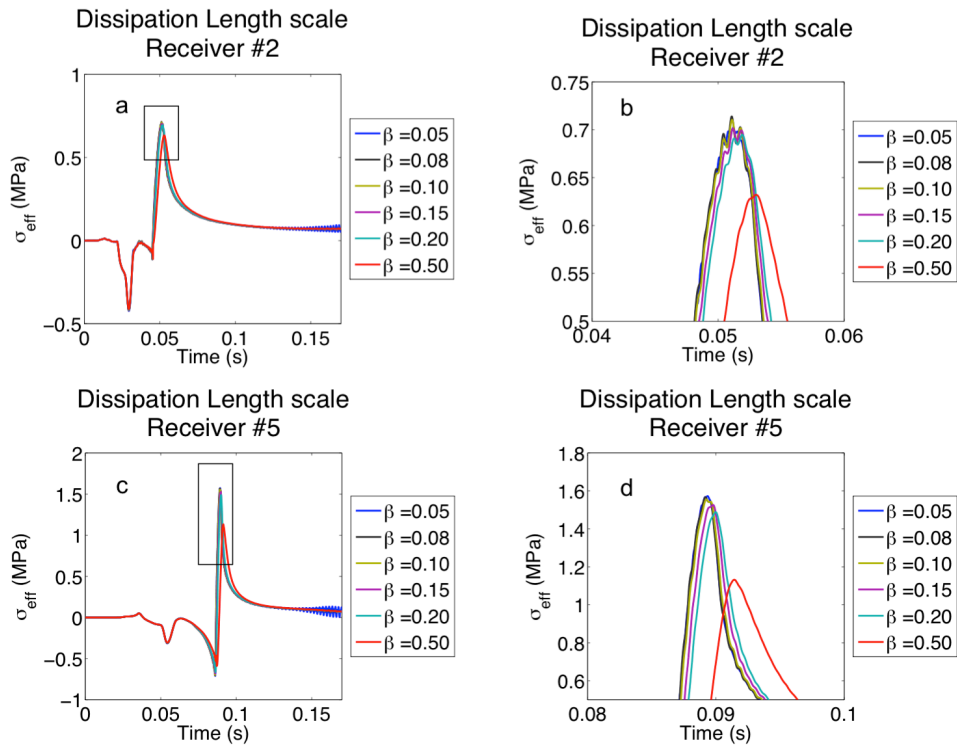


Figure 2.25 Convergence analysis for decreasing  $\beta$  in time domain (a-c): Variations with respect to the time of  $\sigma_{eff}$  are plotted for receivers 2 (a) and 5 (b). The black square indicates the zoom around the crack front (b-d). The plots show the physical convergence of solutions for  $\beta \leq 0.1$ .

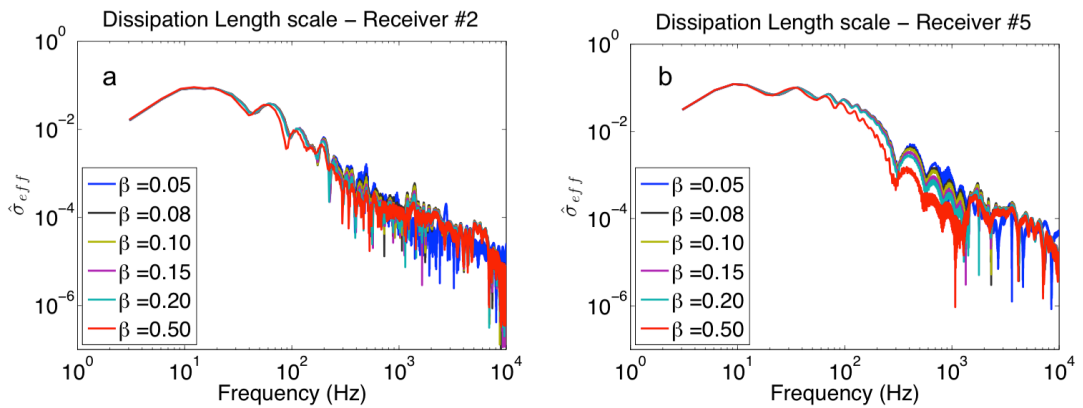


Figure 2.26 Convergence analysis for decreasing  $\beta$  in frequency domain for the same receivers in Figure 2.25. The physical convergence of solutions for  $\beta \leq 0.1$  is still due to the overlapping of amplitude spectra in low frequency band as well as for dynamic time scale.

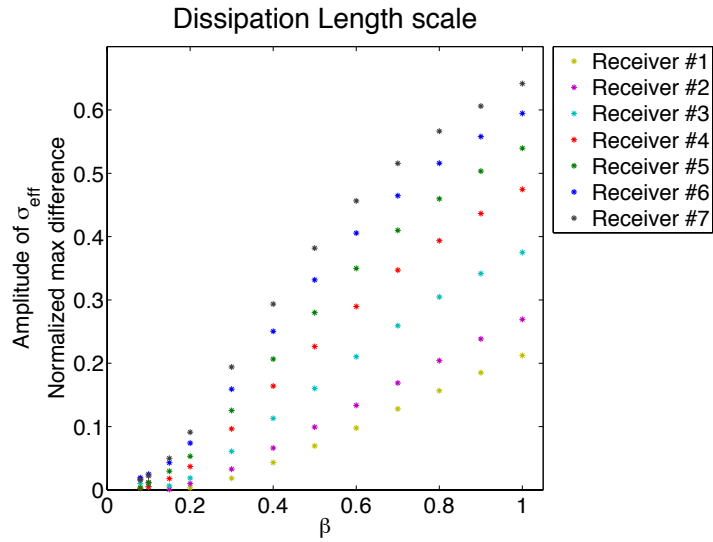


Figure 2.27 Physical convergence shown by plotting the quantity  $\Delta\sigma_{eff,max}$  as function of  $\beta$  for the receivers along the acceleration phase. For  $\beta \leq 0.1$  the convergence is achieved.

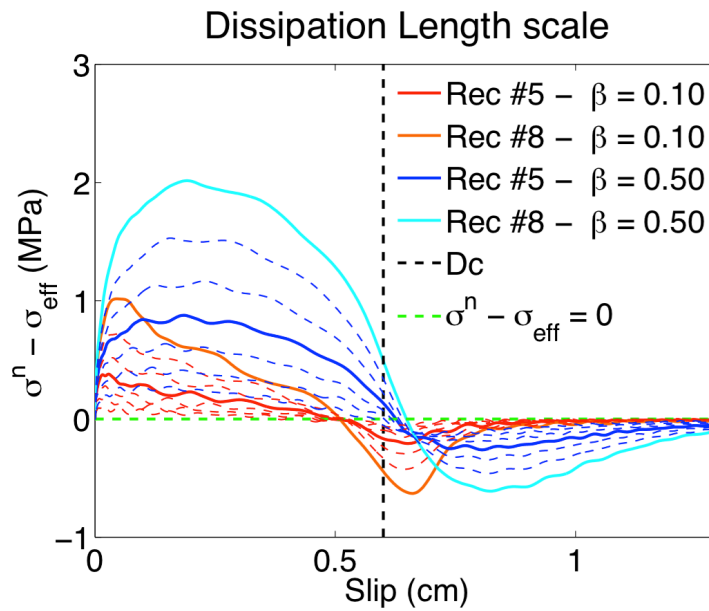


Figure 2.28  $\sigma_{eff} - \sigma^n$  after the initiation of slip and the contemporary triggering of relaxation. Warm colours full lines represent simulations with  $\beta = 0.10$  (convergent solutions) for two receiver points, whereas cold colours full lines are relative to  $\beta = 0.50$  (non convergent solutions) for the same receivers. The zero crossing recorded at other receivers is plotted with dashed lines and respectively with warm and cold colours

Due to the similarity of results obtained from regularizations driven by dissipation length and slip rate, a direct comparison between the models can be performed. Thus a non-local slip rate-based regularization was implemented choosing as velocity scale the maximum of the slip rate  $\delta v_{\max}$ , which is recorded in the vicinity of the crack front:

$$\frac{\partial \sigma_{eff}}{\partial t} = \frac{1}{t_d} (\sigma_n - \sigma_{eff}); \quad t_d = \frac{\delta l}{\delta v_{\max}} \quad (2.126)$$

The obtained models from the two regularizations in the respective ranges of convergence are in turn converging to each other in the sense of maximum amplitude of kinematic fields and position of crack front and thus the two mechanisms can be considered as totally equivalent as arguable from slip rate profile at time step  $t_0 = 0.13s$  plotted in Figure 2.29a-b. Moreover since the used relaxation slip can be also expressed as  $\delta l = \beta Dc$  the equivalence between the time scales also implies the following general result:

$$\frac{Dc}{\delta v_{\max}} = \frac{L_d}{V^a} \Rightarrow L_d \propto \frac{1}{\delta v_{\max}} \quad (2.127)$$

That is the dissipation zone length is conversely proportional to the maximum slip rate value around the crack front during the acceleration phase for a crack propagating along a bimaterial interface.

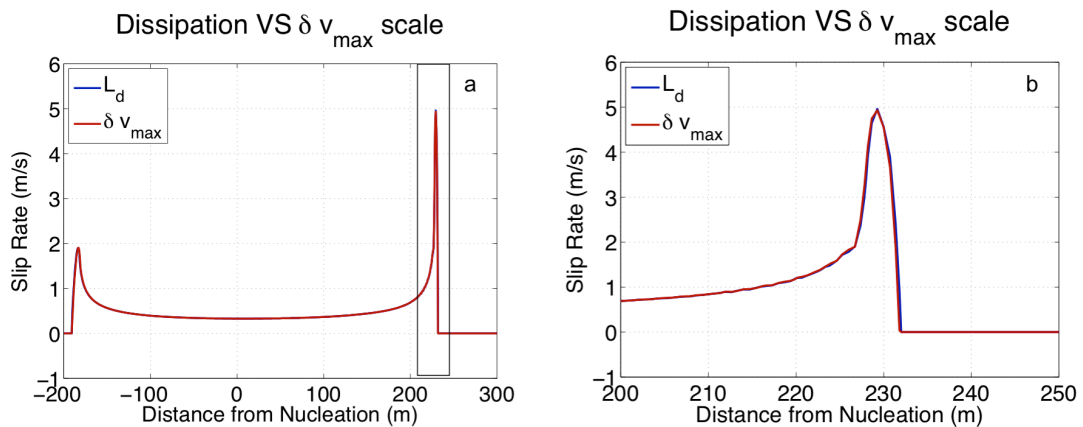


Figure 2.29 Slip rate profiles at a fixed time step (a) for dissipation length scale ( $L_d$  in the legend) and maximum slip rate scale ( $\delta v_{\max}$  in the legend). The black square indicates the zoom around the crack front (b). The two regularizations are convergent in the sense of crack front position and maximum of slip rate amplitude

### 2.4.7 Stationary phase

The results presented so far provide several answers about the features of a growing crack and the shear/normal stress coupling during the acceleration phase, when a slip weakening constitutive law is used.

When the acceleration phase is going to end, the rupture is expected to enter in a stationary phase.

Theoretically, for sub-shear rupture, during this phase the rupture should proceed at a constant speed and the slip rate and stress drop should shrink until to become singular. For a homogeneous medium the asymptotic sub-shear speed is the Rayleigh speed of the medium as confirmed by study about rupture velocities of realistic earthquakes (Gutenberg, 1995) and by fracture mechanics for brittle cracks (Freund, 1990; Broberg, 1999). Weertman (1963) and Achenbach & Epstein (1967) showed that along not opening frictionless interfaces between two different materials, if the contrast of impedance is not very high an interfacial wave solution will exist: its value is intermediate between the two Rayleigh speeds and when the materials are identical it is reduced to Rayleigh wave of medium. Therefore it is generally referred to as generalized Rayleigh speed ( $C_{gr}$ ). Weertman (1980) argued from analytical results that when this speed exists a self-healing pulse can propagate properly at  $C_{gr}$  and as shown in previous sections Ranjith & Rice (2001) analytically showed that even if an experimentally-based regularization law (Prakash & Clifton, 1993; Prakash, 1998) is used to resolve the intrinsic ill-posedness deriving from Coulomb friction law applied to bimaterial interface,  $C_{gr}$  is still an admissible solution for a steady-state propagating slip pulse. This result was confirmed by numerical simulations of growing crack (Rubin & Ampuero, 2007), which clearly show that the rupture can monotonically accelerate along the favoured direction, towards the expected  $C_{gr}$ . As already seen previously, when the contrast between the two materials is too high this speed does not exist. According to Harris & Day (1997) numerical models, for the elastic parameters considered so far (Poisson's solids with the same density)  $C_{gr}$  exists for  $C_{s_1} / C_{s_2} < 1.359$ .

As seen in section 2.3, for a not-regularized friction problem, Ranjith & Rice (2001) found that an unstable steady-state mode can propagate at a speed included between  $C_{s_1}$  and  $1.2C_{s_2}$  when  $C_{gr}$  does not exist. This observation was never

confirmed by numerical experiments and according to Rubin & Ampuero (2007) models,  $C_{s_2}$  acts as a limit for growing bimaterial cracks

In the next subsections the numerical models for stationary phase both for not existing and existing  $C_{gr}$  will be presented.

#### 2.4.8 Stationary phase: not existing $C_{gr}$

As shown by Rubin & Ampuero (2007), the dissimilarity between the two blocks is mainly driven by the ratio  $\gamma$  and poorly influenced by  $\rho_1 / \rho_2$ . In this subsection the models obtained for large  $\gamma$  will be presented both for the case  $\rho_1 = \rho_2 = 2700 \text{ kg} / \text{m}^3$  and for  $\rho_1 / \rho_2 \neq 1$ . In any case for all initial conditions, considered here, the equation (2.116) does not provide real roots and therefore  $C_{gr}$  does not exist. For the analysis conducted on the acceleration phase the shear wave ratio  $\gamma$  is modified such that the effective elastic modulus  $G'$  is kept constant ( $G' = 28.1 \text{ GPa}$ ); in this way the rupture initiation size is independent from the particular dissimilarity between the two layers as described in section 2.4.3. Since the features of stationary phase, e.g. the asymptotic rupture speed, can be reasonably considered independent from the nucleation phase,  $\gamma$  is varied without taking into account the influence of modulus  $\mu'$ . To analyse the features of stationary phase for such contrasts of impedance the set of numerical models were obtained using a dynamic time scale within the range of convergence found in section 2.4.4.

First, seven different contrasts of impedance  $\gamma$  were used, with  $\rho_1 = \rho_2 = 2700 \text{ kg} / \text{m}^3$  and  $C_{s_1} = 4.06 \text{ km} / \text{s}$ ; whereas the shear wave in more compliant medium (and accordingly  $C_{p_1}$  to keep  $v_1 = v_2 = 0.25$ ) is varied to obtain a  $\gamma$  ranging from 1.5 and 2.1.

The most relevant result concerns the achieved asymptotic speed (along favoured direction) normalized to the respective  $C_{s_2}$ : it increases with  $\gamma$  and it is in any case higher than  $C_{s_2}$  (Figure 2.30a). Thus  $C_{s_2}$  does not act as a limit speed, as found by numerical solutions of Rubin & Ampuero (2007), but at the stationary phase the rupture can proceed similarly to the unstable steady-state slip pulse analytically found by Ranjith & Rice (2001); the increasing of average stationary speed (normalized to

the respective  $C_{s_2}$ ) as a function of  $\gamma$  is shown in Figure 2.30b, where the error bars represent the standard deviation for the computed average rupture velocity.

The capability of rupture to accelerate, at a speed, which is higher than the shear wave speed in the more compliant medium, generates some peculiar effects. Until the rupture proceeds at sub-shear regime the radiation emitted, although asymmetric (both along the two propagation directions and between the two sides of the fault) shows the classical pattern with the P and S waves clearly recognizable ahead the rupture (Figure 2.31a showing the kinetic energy field). On the other hand during stationary phase the rupture continues to emit ahead in the medium below the fault, but in the above half-space the fault emits at considerably higher energy behind the crack tip generating a half Mach cone, typical of super-shear propagation regime (Figure 2.31b). This acceleration also generates a change in the normal stress perturbations pattern along favoured direction. Beyond the compressive effect ahead the crack tip and the strong extensional effect at the crack front, already recognizable during acceleration, the S waves emitted behind generate a new small extensional variations just behind the dissipation zone and evidenced by the black circle in the Figure 2.31c.

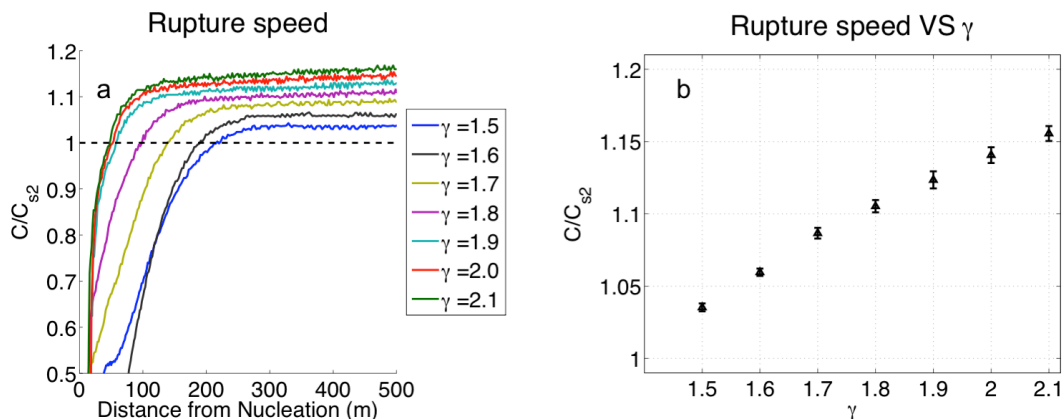


Figure 2.30 Acceleration of rupture, along favoured direction, for high contrast of impedance obtained varying  $C_{s_2}$ . (a). Under these conditions the rupture can accelerate towards speeds higher than  $C_{s_2}$ . (b) Average speed during stationary phase as a function of increasing contrast of impedance  $\gamma$

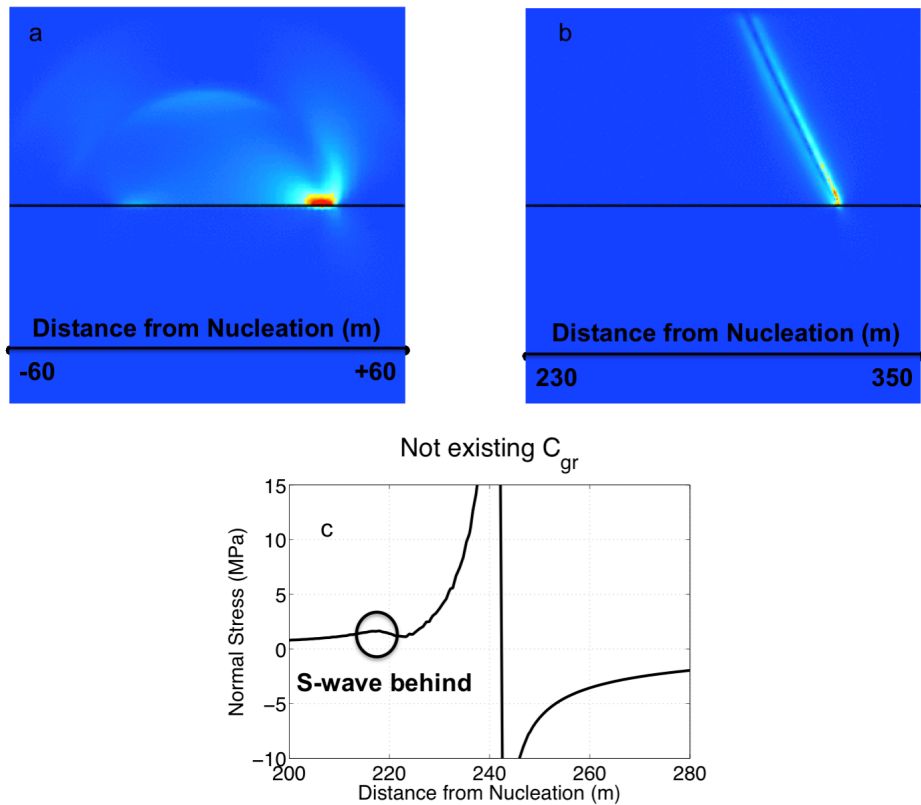


Figure 2.31 Kinetic energy field before (a) and after (b) the acceleration of the rupture beyond  $C_{s_2}$  the emission of S-wave behind in more compliant medium (Mach-cone) is evident in figure (b). Perturbation of normal stress snapshot (c) at the same time step of figure (b): the extensive effect due to the S wave emitted behind is evidenced (black circle).

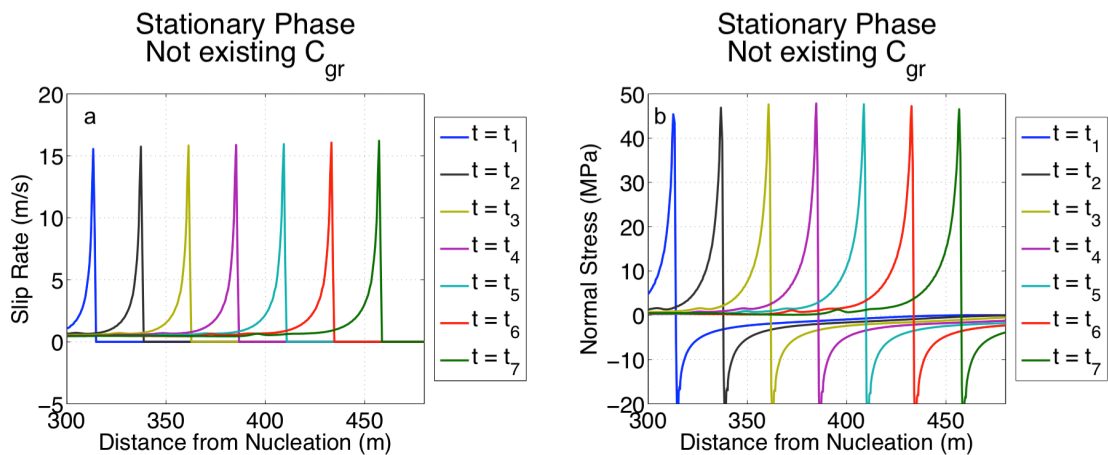


Figure 2.32 Slip rate (a) and Normal stress perturbations (b) during stationary phase at seven different time steps when  $C_{gr}$  does not exist (variable  $C_{s_2}$  with uniform  $\rho$ ). The rupture proceeds with stable maximums both for slip rate and normal stress. The dissipation zone size is stable too and it contains enough points to be numerically modelled. As example these plots are related to the case  $\gamma = 1.90$

As expected, during stationary phase the slip rate at crack front is also pretty constant (Figure 2.32a), as well as the traction perturbations (Figure 2.32b) and the size of dissipation zone; The stationary phase can be thus modelled with enough grid points all along the stationary phase until the end of fault line.

By using each ratio  $C_{s_1} / C_{s_2}$  as in the previous analysis and varying the contrast of density we are still in the range for which  $C_{gr}$  does not exist. Two different cases were analysed; in the former three different ratios  $\gamma = C_{s_1} / C_{s_2}$  were used ( $\gamma = 1.7, 1.9, 2.1$ ), whereas the density ratio is fixed to be larger than 1 ( $\rho_1 / \rho_2 = 1.2$ ;  $\rho_1 = 3240 \text{ kg/m}^3$ ;  $\rho_2 = 2700 \text{ kg/m}^3$ ). The ruptures are again able to accelerate beyond the respective shear wave speed in more compliant medium and, as expected, even in this case, the higher is  $\gamma$  the higher is the stationary speed normalized to  $C_{s_2}$ ; in Figure 2.32a the accelerations of the rupture for these cases are shown. For the other set of simulations the ratio  $\gamma$  is fixed and four different contrasts of density are tested: even in those cases the rupture can accelerate in super-shear regime for the half-space above the fault and the higher is the contrast of density, the faster is the rupture during stationary phase, in particular Figure 2.32b shows the rupture accelerations for the case  $\gamma = 1.9$  and with the density ratios  $\rho_1 / \rho_2 = 1.0, 1.2, 1.4, 1.6$ . To obtain these density ratios  $\rho_2$  is always fixed at  $2700 \text{ kg/m}^3$ .

Thus for the last two presented set of models the results shown in Figure 2.31 and Figure 2.32 are still valid with emission backward of S-wave in the more compliant medium which in turn generates a further small extensive normal stress variation behind the crack front.

In conclusion, in all studied cases, when  $C_{gr}$  does not exist the acceleration phase is properly modelled by using a dynamic time scale to regularize the normal stress perturbations and physically convergent models are found. The acceleration, along the favoured direction, brings the rupture up to a stationary phase during which the rupture itself can propagate at speed  $C > C_{s_2}$  and numerical models are shown to be able to follow this propagation until the end of fault. This aspect is not trivial and conversely, as we will see in the next subsection, when  $C_{gr}$  exists the total shrinking

of dissipation zone will not allow to numerically model the stationary phase independently from the chosen regularization and elastic parameters.

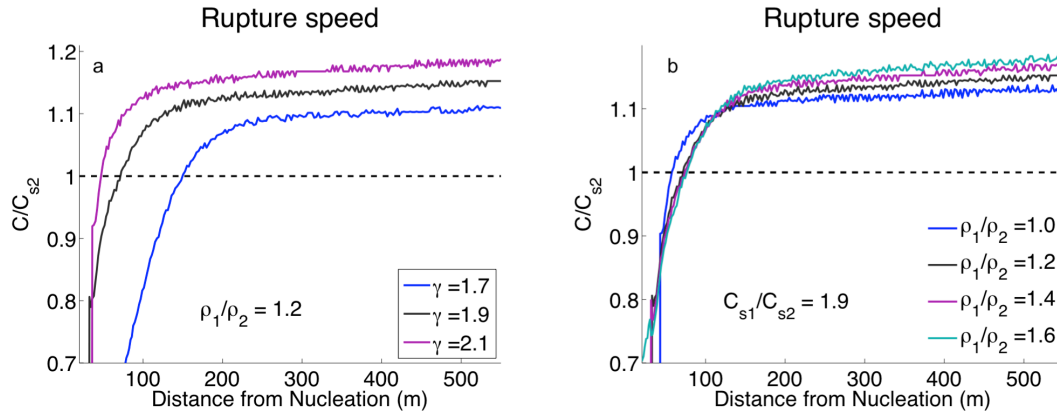


Figure 2.33 Acceleration of rupture when  $C_{gr}$  does not exist. In figure (a) three different ratios  $\gamma$  are used, whereas the ratio  $\rho_1 / \rho_2$  is fixed at 1.2 . In figure (b) four different ratios  $\rho_2 / \rho_1$  are used, whereas the ratio  $\gamma$  is fixed at 1.9

#### 2.4.9 Stationary phase: existing $C_{gr}$

When the density is uniform across the two media and the values of  $\gamma$  are lower than 1.359 (for uniform density in both media) the Generalized Rayleigh equation (2.116) has a real root  $C$  and that root represents the generalized Rayleigh speed  $C_{gr}$  (Harris & Day, 1997, Rubin & Ampuero, 2007). This is also the case of the first analysis performed in the section 2.4.4 and described from Figure 2.5 to Figure 2.15. This velocity is intermediate between the two Rayleigh speed in the two half-spaces and it is the expected asymptotic speed, which the bimaterial rupture tends to, at the end of acceleration phase, at least along the favoured direction. As seen in sections 2.4.4 and 2.4.6, when a dynamic time scale is used to describe the shear/normal coupling during acceleration phase, a range can be found within which the solutions become independent from the used regularization parameters; the slip scale and the length scale which determines this convergence are respectively of the same orders of slip weakening distance and dissipation zone size. In those analysis  $\gamma = 1.18$  was used and considering the given velocity field  $C_{gr} = 2.570 \text{ km/s}$ . This speed is correctly reached at the end of acceleration phase as already shown in the Figure 2.22.

Before showing the numerical description of stationary phase, in the case of existing  $C_{gr}$ , it is important to show that, when  $C_{gr}$  exists, it is the asymptotic speed, along favoured direction, independently of the contrast  $\gamma$ . A value  $\gamma = 1.10$  can be obtained keeping again the density uniform across the two media at  $\rho_1 = \rho_2 = 2700 \text{ kg/m}^3$  and increasing the value  $C_{s_2}$  (and accordingly  $C_{p_2}$  to preserve  $v_1 = v_2 = 0.25$ ) with respect to the case  $\gamma = 1.18$ . In this case  $C_{gr}$  is slightly higher and its value is  $C_{gr} = 2.694 \text{ km/s}$ ; in Figure 2.34a, the acceleration of the rupture to that asymptotic speed is shown. Now decreasing  $C_{s_2}$  at uniform  $\rho$  in order to achieve a  $\gamma = 1.25$ , the expected  $C_{gr}$  is smaller ( $2.456 \text{ km/s}$ ) and this asymptotic speed is correctly reached at the end of acceleration phase, as shown in Figure 2.34b.

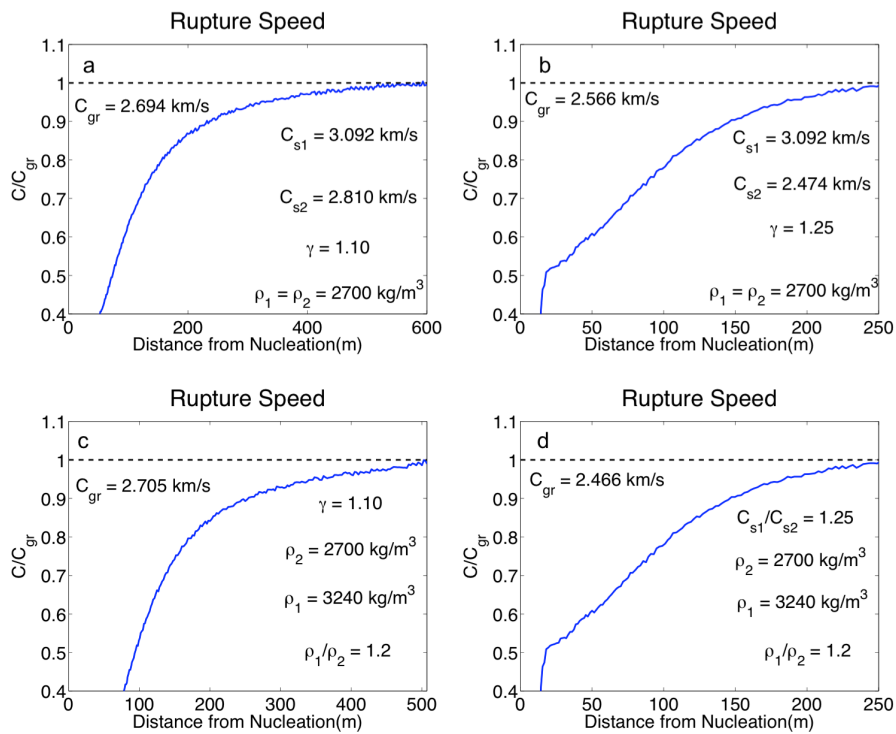


Figure 2.34 Acceleration of the rupture towards  $C_{gr}$  for 4 different contrast of impedance: (a) uniform density across the media and shear wave speed ratio is 1.10. (b) Uniform density and shear wave speed ratio 1.25. (c) The shear wave speed ratio is the same as in figure (a), and the densities ratio is 1.2. (d) The shear wave speed ratio is the same as in figure (b), and the density ratio is 1.2. All ruptures accelerate towards the respective  $C_{gr}$ .

With the same body waves velocities the acceleration of the rupture was investigated also for  $\rho_1 / \rho_2 = 1.2$ . In both cases the asymptotic speeds are slightly larger than the case with  $\rho_1 / \rho_2 = 1$  and they are again correctly reached at the end of acceleration phase (Figure 2.34c-d).

As seen in Figure 2.22, when a dynamic time scale is used the rupture accelerates faster towards the asymptotic speed due to the self-adaptive feature of the regularization depending on the actual value of slip rate. Nevertheless for all studied cases, when  $C_{gr}$  is achieved the simulations become more and more noisy and they rapidly blow up not allowing to follow the stationary propagation of the crack front. The slip rate profiles at different time steps (see Figure 2.35a) show the initial phase of instability of numerical models and finally, at last shown time step, the slip rate solution becomes totally unreliable due to the spurious oscillations emerged. The normal stress perturbations at the same time steps also show the same noisy phases appearing behind the crack front; from that moment the part of the fault involved in the normal stress variations shrinks more and more, and it first becomes pretty singular then it blows up as well as the slip rate (Figure 2.35b). Figure 2.35c-d show the slip rate profiles contextually with the number of points within the dissipation zone as a function of position of crack front (respectively just before and after the beginning of unstable propagation) and those plots demonstrate that the noisy phases appear when the dissipation zone shrinks at less of three points.

In other words as the rupture approaches  $C_{gr}$  the absolute amplitude of the compressive normal stress perturbation just ahead of the crack tip increases, increasing more and more the yield strength of the fault. Just behind the tip, the stress perturbation changes its sign, becoming more and more extensional and increasing the energy release rate as the rupture advances at a speed close to  $C_{gr}$ . The behaviour of the normal stress perturbation does not limit the further increase of the slip rate toward a singularity. As a consequence, the dissipation zone continues to shrink. When it is represented by less than three discretization points, the numerical grid is no longer able to properly propagate the high frequencies generated at the rupture front. Hence, spurious oscillations rapidly pollute the signal and grow until blowing up the simulation. During the initial phase of the instability, a slip pulse emerges (Figure 2.35c), almost generated by the spurious noise, locally pushing the rupture to go

below the frictional level, then after few iterations the simulation blows up (Figure 2.35d).

As discussed before, physically convergent solutions are obtained when an adaptive time scale is selected, because the regularization properly filters the normal-shear stress coupling without perturbing the time scale associated to energy balance that allows the rupture to progress. This latter scale is associated with the size of the dissipation zone. To analyse the behaviour of  $\sigma_{eff}$  during stationary phase in time/frequency domain other receivers were added to those indicated in Figure 2.4a. When the coupling scale approaches the limiting frequency that a numerical grid can propagate (Figure 2.36a-b), the coupling frequency and thus the filter of the regularization competes with the filter of the numerical grid and aliasing effects can occur, with generation of numerical oscillations (Festa & Vilotte 2006). At following receivers (e.g. receiver 14 in Figure 2.36c-d) the coupling frequency is practically overlapped to the numerical limit and the simulations blow up due to these numerical oscillations. It is worth noting that at receiver 14 (Figure 2.36c-d) the smaller values for  $\delta l$  ( $2\%, 5\% D_c$ ) have already led to unstable solutions and for sake of clarity they are not included in the figures. In fact, as expected, when a larger  $\delta l$  is used, the rupture can propagate for a longer distance. This is due both to a larger smoothing effect of the normal-shear stress coupling all along the acceleration phase and a larger attenuation of the spurious oscillations. Nevertheless we found that, when the rupture get close to  $C_{gr}$ , the emergence of the oscillations cannot be avoided in all cases, leading to unstable solutions for all  $\delta l$ . It is worth to note that also for a homogeneous medium and for a bimaterial interface when  $C_{gr}$  does not exist the cohesive zone shrinks and tends to become zero as the rupture approaches the asymptotic speed. Nevertheless, in those cases numerically stationary solutions are achieved, with rupture speed slightly slower than the expected one from analytical results (e.g. Rayleigh speed for homogeneous case). This speed approaches more and more the asymptotic rupture velocity as the grid size decreases. However, for those models, we still have at least three points to describe the cohesive zone. Hence, we can argue that the different behaviour of bimaterial interface running close to  $C_{gr}$  derives from the singular behaviour of the normal stress perturbation with a change of sign at the rupture tip. This is indeed not observed in the case of a rupture in

homogeneous medium and uniform initial conditions, where the normal stress perturbations are zero by symmetry. In the case of non-existing  $C_{gr}$ , since the rupture speed overcomes the S wave velocity of the more compliant medium, further variations of the normal stress perturbation mainly affect the region behind the crack front, as discussed in the previous section, but they do not contribute to further increase the normal stress perturbation at the crack tip.

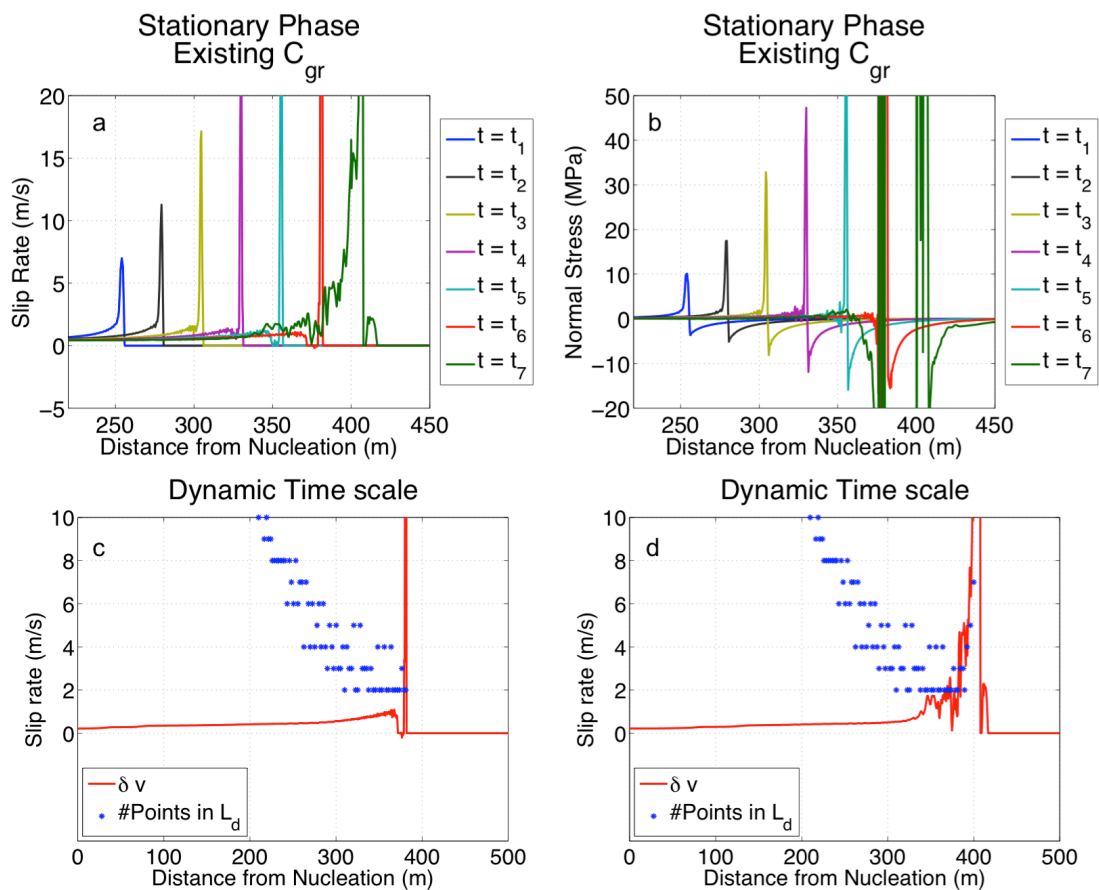


Figure 2.35 Approach to the stationary phase when  $C_{gr}$  exists: (a) The slip rate profiles are shown at different time steps: when the dissipation zone shrinks noisy phases appear behind the crack front, when the asymptotic speed is reached this noise totally pollute the simulations making the solutions no longer reliable. (b) The portion of the rupture involved in the perturbation of normal stress continues to shrink until it becomes a singularity, which does not allow to control the numerical models. When the dissipation zone shrinks at less of 3 points a slip pulse is generated (c) and after few iterations the models blow up (d)

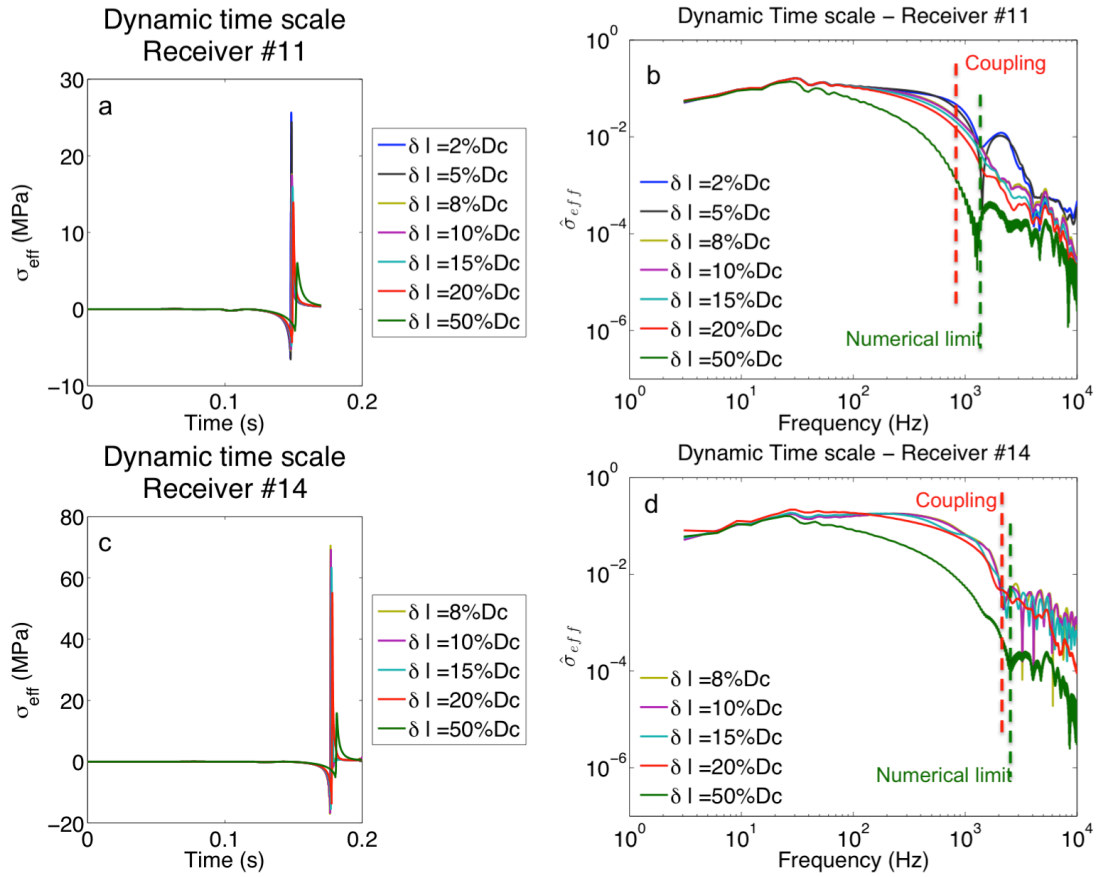


Figure 2.36  $\sigma_{eff}$  in time and frequency domain: (a) when the receiver is placed just after the acceleration phase the solutions no longer converge in the sense of maximum amplitude of  $\sigma_{eff}$ . (b) Amplitude spectra of  $\sigma_{eff}$  just after the acceleration phase when the coupling frequency is moving towards the numerical limit; just ahead this receiver smallest  $\delta l$  rapidly lead to ill-posed solutions (and thus their  $\sigma_{eff}$  are not included in next figure). (c)– (d) When the speed is really close to  $C_{gr}$  the normal stress perturbations continue to shrink and the coupling frequency moves on. When this frequency goes really close to the numerical limit the increasing amplitude of spurious frequencies makes the filter inefficient, not allowing to numerical model the propagation at  $C_{gr}$

To try to mitigate the continuous shrinking of the process zone, we then investigated the possibility to introduce a switch in the regularization, moving to a constant time scale when the stationary phase is approached. This change can be controlled by the number of points in the cohesive zone and the switch is activated when we have less than 5 points in the dissipation zone (i.e. half an element in our

simulations). This switch can be naturally implemented in the non local regularization based on the size of the dissipation length, by imposing a lower limit on  $L_d$ . Additionally, we also tested this switch in the dynamic regularization, by fixing an upper limit for the slip rate or by jumping from the dynamic to a constant time scale regularization, with a variety of  $t_c$  values, ranging over two orders of magnitude. However, in all cases, we eventually delayed the occurrence of the instability but we were not able to remove it. Moreover, the smaller  $t_c$  the longer the rupture can propagate. In addition, a metastable slip pulse is generated that propagates at almost  $C_{gr}$  for a while before the simulation blows up.

The described slip pulse is a very debated point in the context of a dynamic bimaterial rupture. Weertman (1980) obtained the perturbation of normal stress and the stress drop for a self-healing pulse propagating at the interface between dissimilar materials as reported in equation (2.115). The analytical results, summarized in section 2.3 have shown that, when  $C_{gr}$  exists, a shear stress perturbation along a bimaterial interface generates an unstable response in slip rate for a steady state slip pulse sliding at velocity  $V$ , when a Coulomb friction condition is imposed (with constant coefficient of friction). In that case all wavelengths are unstable and the growth rate of the instability is inversely proportional to the frequency of the considered mode; moreover unstable modes are generated for all friction coefficients and they can propagate properly at Generalized Rayleigh speed. Due to this instability the family of steady-state pulses found analytically by Rice (1997) and Adams (1998) cannot be considered as physically reliable. Furthermore Adda-Bedia & Ben Amar (2003) have also found a continuous set of slip-pulse, which are still unphysical because they show a singular behaviour in slip velocity. They also showed that even if a Prakash-Clifton regularization is used the degeneracy of slip-pulse solutions is not suppressed and no slip pulse is selected.

The Weertman solutions (equation (2.115)) are valid for steady state propagation; nevertheless Rubin & Ampuero (2007) showed that the equation for  $\sigma''$  can be considered a reliable approximation of normal stress variations even in the case of smoothly growing cracks in the framework of linear slip weakening.

The onset of slip pulse, already found by Rubin & Ampuero (2007) only when a constant time scale is used as limit case of classical Prakash-Clifton regularization (see equations (2.112) and (2.113)) is thus related to a local minimum of function

$\delta u(x)$  (red curve in Figure 2.37). The extensive variation of normal stress at crack front (blue curve in Figure 2.37) generates a dynamic overshoot for the stress drop behind the crack tip (green curve in Figure 2.37), but the further compression within the crack brings the dynamic level ( $\mu_d \sigma_T^n$ ) above the total tangential traction causing the locking of the fault between the slip pulse propagating and the open crack behind.

In our models the propagation of emerging pulse can be numerically followed only if the constant time scale is used to regularize the normal stress variations as for Rubin & Ampuero (2007). However in that case we have found no physical convergence of solutions during acceleration phase and this unavoidably lead to different pulse onsets depending on used relaxation time  $t_c$ . In particular when a smaller  $t_c$  is considered the pulse can emerge after a shorter propagation distance (blue curve in Figure 2.38) and the higher is the relaxation time, the longer is the distance needed for the emerging of the pulse itself (red and green curve in Figure 2.38).

Conversely the slip pulse onset is not sensitive to the different grids: in fact even halving the dimension of the elements the emerging of the pulse occurs after the same propagation distance and this is true for all considered  $t_c$  (Figure 2.39). Eventually this means that even if the emerging of the pulse can be considered numerically well-posed in the sense of Cochard and Rice (2000) convergence, according to our analysis it cannot be considered as physically reliable.

In any case, even for the largest  $t_c$ , after a certain distance the pulse emerges and furthermore after a while the slip pulse starts to show spurious oscillations leading to totally unreliable solutions as for the dynamic time scale. This means that, although more slowly, even for this case, the acceleration towards  $C_{gr}$  makes the dynamic fields pretty singular bringing the coupling frequency closer and closer to the numerical limit for all considered grids and for all parameterization adopted.

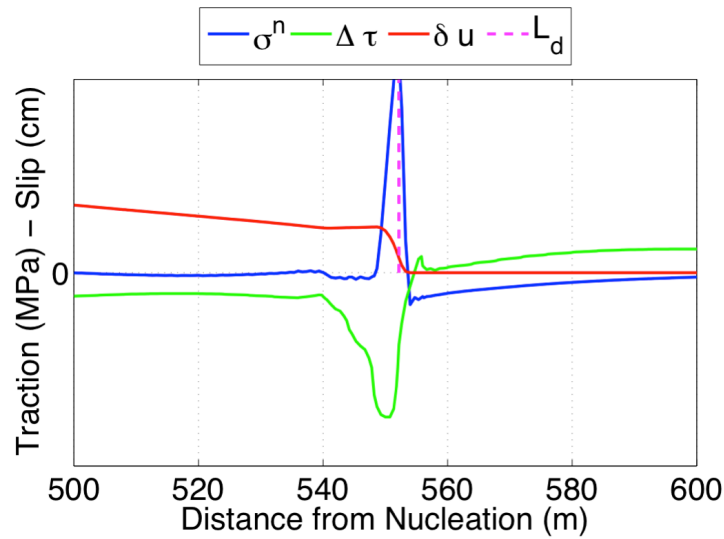


Figure 2.37 Slip pulse emerging at the end of acceleration phase, when a constant time scale is used to regularize. The blue curve represents the normal stress perturbations and when the slip pulse emerges it clearly show a slightly compressive variation just behind the pulse. As expected from Weertman analytical results (equation (2.115)) this change in the sign of  $\sigma^n$  is due a local minimum in the slip profile (red curve). The green curve represent the stress drop: as expected it has a maximum due to the extensive normal stress variation and a change of slope where  $\sigma^n$  is compressive, where the slip rate is zero (between the pulse and the open crack behind) the further compression bring the total tangential traction below the dynamic level. Finally the magenta dashed line tracks the last point within the dissipation zone.

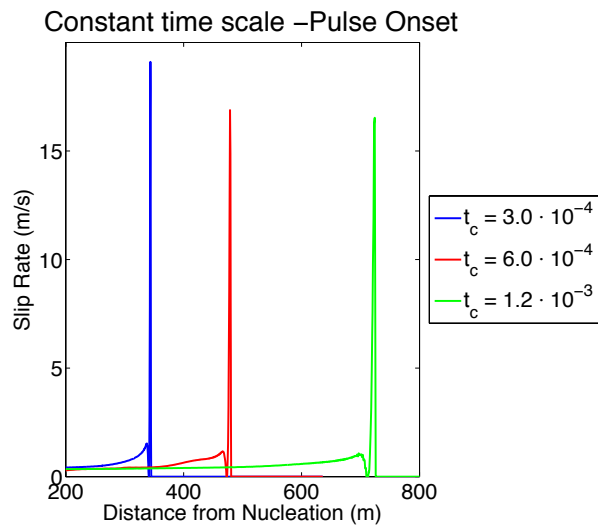


Figure 2.38 Pulse onset for different constant time scale: the smallest  $t_c$  leads to a faster generation of the pulse (blu curve). higher time scales (red and green curves) lead to the onset of a pulse too, over longer propagation distances

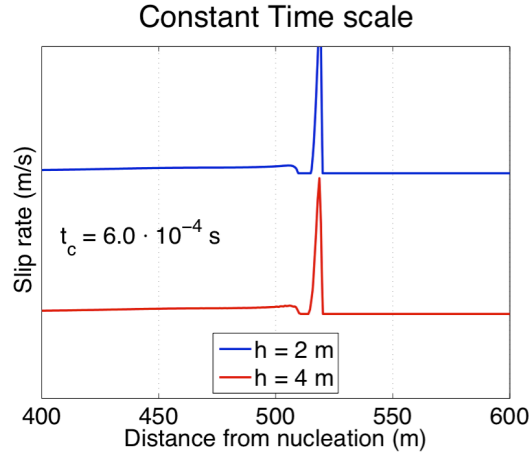


Figure 2.39 Pulse onset for a fixed constant time scale: comparison between two different grid sizes: the pulses are generated after the same propagation distance

Once the pulse is generated its size can be considered as constant within the errors due to the non-regular discretization adopted for Spectral Element Method; nevertheless this size proves to be strictly dependent on the regularization adopted. When a small relaxation time is considered ( $t_c = 3.0 \cdot 10^{-4} s$ ) the pulse has an average size  $\tilde{L}_p \approx 3 m$ . Doubling the relaxation time ( $t_c = 6.0 \cdot 10^{-4} s$ ) the average size also double ( $\tilde{L}_p \approx 6 m$ ) and a further doubling for  $t_c$  leads to  $\tilde{L}_p \approx 10 m$  (Figure 2.40a). The pulse size is shown to be also related to the grid size adopted (Figure 2.40b); however, in this case, halving the element size from  $4 m$  to  $2 m$  the reduction of  $\tilde{L}_p$  is shown to be less important ( $\tilde{L}_p(h = 4 m) \approx 6 m$ , whereas  $\tilde{L}_p(h = 2 m) \approx 5 m$ ).

In conclusion the slip pulse, generated by an inversion of slip gradient (as expected from Weertman formulation) during the acceleration of rupture towards the asymptotic speed  $C_{gr}$ , can be clearly detected and followed only when a constant time scale is used. In that case the solutions for the acceleration phase are not reliable from a physical point of view due to the unavoidably dependence from the chosen regularization parameter  $t_c$ . Therefore, although the pulse propagation can be considered numerically well-posed its onset results to be closely connected to the adopted filtering, as well as its size, which is preserved for all its propagation. Moreover after a certain distance the generated pulse unavoidably becomes more and

more noisy and after that the numerical solutions blow up. Therefore it cannot be considered as physical reliable solutions for the stationary bimaterial propagation.

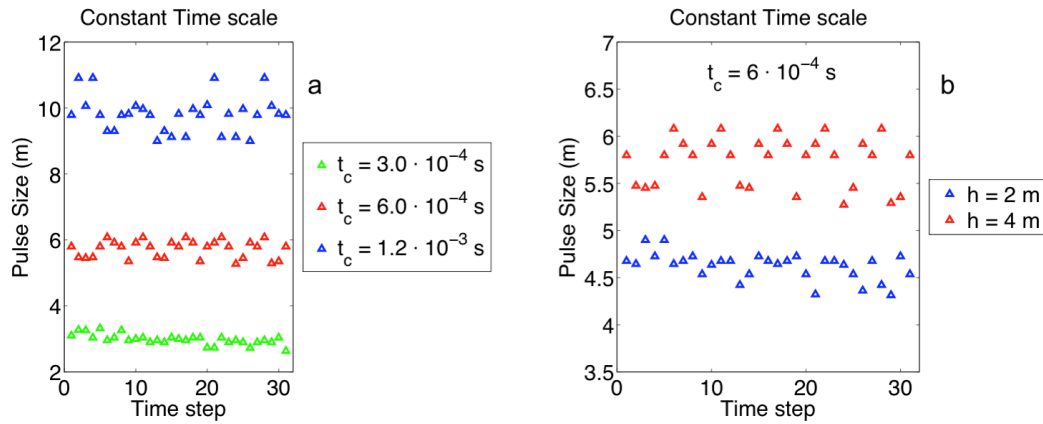


Figure 2.40 Pulse size for different models obtained for constant time scale regularizations: (a) The sizes, at different time steps, are compared for different  $t_c$ . In all cases the pulse size is pretty constant for all propagation and when a larger  $t_c$  is used the average size of the pulse is quite larger. (b) The pulse size seems to be less sensitive to the variation

## 2.5 Conclusions

In this chapter the problem of a bimaterial rupture was investigated firstly in the framework of fracture mechanics for a stationary propagating crack, in order to find the explicit analytical form of asymptotic crack tip fields, that is the displacement jump behind the crack front and the traction ahead the crack front and thus the related stress intensity factors. When no friction law is considered along the interface the singularity at the crack tip, for in-plane deformation, presents an oscillatory behaviour as found in the pioneering work of Williams (1959). For a stationary crack propagating between two different isotropic media the crack tip fields can be normalized by using a complex stress intensity factor (SIF) for the in-plane deformation and a real stress intensity factor for the anti-plane shear. For the in-plane deformations the mode I and mode II of propagation are coupled, in the sense that the angular distribution of the traction over the crack depends on the particular geometry of the problem both for static and propagating stationary crack. For particular conditions an arbitrary length can be defined and over this length the mode mixity and the oscillatory behaviour of crack tip fields can be neglected leading to define a classical real stress intensity factor  $(K_{II}, K_I)$ .

In the same framework, the crack tip fields were computed when a Coulomb friction law is imposed on the interface. In that case the oscillatory term disappears and the crack tip singularities are weaker or stronger than the homogeneous singularities ( $\tau(r) \propto r^{-1/2 \pm \delta}$ ) depending on the displacement conditions behind the crack tip (Deng, 1994).

From an analytical point of view the bimaterial propagation of a slip pulse was shown to be ill-posed in the sense of unstable diverging slip response to a single mode shear stress perturbations. Starting from the results of Ranjith & Rice (2001) this instability was addressed in terms of contrasts of impedance and friction coefficient showing what is the expected propagation speed for a steady state slip pulse in a broad range of parameters. In particular it was shown that when the generalized Rayleigh wave speed  $C_{gr}$  exists the problem is ill-posed for all friction coefficients and the expected speed for the unstable mode is properly  $C_{gr}$ . Conversely, when  $C_{gr}$  does not exist there is a critical friction coefficient  $f_c$  below which the problem is well-posed; Above  $f_c$  the unstable modes can propagate at a speed which is slightly higher than the shear wave speed in the more compliant medium. The ill-posedness is due to the instantaneous response of shear stress to the normal stress perturbations and when a delayed shear/normal coupling is introduced by analogy with the experimental results of Prakash & Clifton (1993, 1998) the stability problem, that is the integral over all the perturbation modes, becomes well-posed both when  $C_{gr}$  exists and does not.

In the section 2.4 (and subsections) the results from several numerical simulations, for a plane growing crack, propagating along a bimaterial interface were presented.

In the framework of a linear slip weakening friction law, the role of the parameters involved in the Prakash-Clifton regularization was investigated in order to understand what are the conditions for which the delayed shear/normal coupling provides numerical well-posed solutions, that is results that are independent of the grid size, and physical well-posed solutions, that is results that are independent of the chosen parametrization.

When a dynamic time scale is used with the relaxation time inversely proportional to the actual value of slip rate and proportional to a slip parameter (chosen of the order of critical slip distance  $D_c$ ) the solutions are numerically well-posed for smaller

grid size respect to the rougher discretization capable to properly model the homogeneous propagation and it means that the shear/normal coupling introduce new time/length scales which needs to be modelled more finely. Moreover for a slip parameter  $\delta l \leq 10\%D_c$  the solutions are also physically well-posed and this result can be interpreted considering the regularization as a low-pass filter. When the cut-off frequency is able to properly damp the frequency deriving from the time scale of physical coupling between normal stress perturbations and the shear stress response and as long as this frequency is lower than the maximum frequency solvable by the chosen grid the problem is physically well-posed. Within the physical convergence range this cut-off frequency is higher than the frequency given by the time scale over which the normal stress is perturbed around the crack front. A dynamic time scale, which adapts the cut-off frequency with the increasing slip rate, is shown to be able to preserve the cut-off frequency between the physical and coupling frequencies all along the acceleration phase. The range of convergence found is independent of the contrast of impedance between the two layers and it was shown that as long as the time scale introduced is smaller than the weakening time the cut-off frequency is included between physical and coupling frequencies and therefore the solutions are physically well-posed.

Although the conditions for the numerical convergence are pretty the same, when a constant time scale is used to model the shear stress response no physical convergence is achieved. This is substantially due to the fact that physical and coupling frequencies increase as effect of shrinking of dissipation zone during crack growth, whereas the cut-off frequency is fixed for all simulations. Therefore even if the solutions are convergent at the beginning of acceleration phase there will be always a position on the fault after which the physical frequency will go beyond the cut-off filter frequency of the regularization for any  $t_c$ .

In other words there exists a time  $t_0$  after which the weakening time  $t_w < t_0$  and the relaxation will occur over a slip scale larger than  $D_c$ . For what discussed for the dynamic time scale for  $t > t_0$  the results will be outside of physical convergence range.

From these results about the time scales of relaxation and weakening, it emerges that the ill-posedness mainly derives from shear/normal coupling at the scale of dimension of the dissipation zone, which is the area within which the energy is

dissipated as emitted seismic waves. Therefore an alternative regularization was proposed according to which the relaxation time is proportional to the size of dissipation zone normalized to a reference rupture speed (e.g. the expected asymptotic speed). This regularization time is dynamic due to the shrinking of process zone, but it is not local being based on a characteristic length of the rupture and it showed both numerical and physical convergence as well as the relaxation driven by the classical dynamic time scale as far as the relaxation occurs over crack length comparable with the size of the cohesive.

Moreover the dissipation length regularization was shown to be totally equivalent to the dynamic time scale when the local value of slip rate  $\delta v$  is replaced by the maximum  $\delta v_{\max}$  recorded in the vicinity of crack front. Thus, from the equivalence of the two time scales, we inferred that for a bimaterial crack, along the favoured direction, the size of dissipation zone is inversely proportional to the maximum amplitude of slip velocity all along the acceleration phase.

In conclusion the dissipation zone size can be considered as the missing physical length scale, which makes the bimaterial problem coupled with the classical Coulomb friction law ill-posed

For what concern the stationary phase several numerical simulations was performed. When the generalized Rayleigh speed  $C_{gr}$  does not exist it was shown that the rupture can accelerate towards to a speed which is higher than the shear wave speed in the more compliant medium and this causes some peculiar effects; in fact the rupture starts to emit behind in the more compliant medium generating a half Mach cone well visible in the kinetic energy field. This back-emission also causes a variation in the pattern of normal stress perturbations along the favoured direction with a new small extensive effect behind the strong normal stress perturbation due to the propagating crack tip. Therefore, when the rupture accelerates to this supershear regime the emissions, occurring behind, no longer perturbs the normal stress variations ahead the rupture front and the propagation continues in a stationary way. This feature is general and it was observed that when the density ratio is increased, for a fixed shear wave speed ratio, the ruptures are able to accelerate towards to a higher asymptotic speed. Nevertheless, as also argued by Rubin & Ampuero (2007) from the analytical results of Weertman (1980) the solutions are less sensitive to the variation of density ratio respect to the variation of  $\gamma = C_{s_1} / C_{s_2}$ .

As expected, when  $C_{gr}$  exists the acceleration leads the rupture properly to that speed.  $C_{gr}$  can be easily computed when the elastic parameters of the two layers are known. Nevertheless, in this case, the simulations become more and more noisy and finally they blow up independently of regularization parameterization. This effect is due to the total shrinking of the area involved in the normal stress perturbations, which leads the above described physical frequency closer and closer to the numerical limit whatever is the size of the grid.

When a constant time scale is used before the emerging of the instability during the stationary phase a slip pulse can be detected. The onset of this slip pulse can be considered as numerically well posed because it is independent on the grid size, but it strictly depends on the chosen  $t_c$ . Its size is independent of time but it is also dependent on the used parameterization and thus it cannot be considered as a physically reliable solution for the bimaterial propagation. In conclusion the expected stationary speed for the unstable slip pulse computed by Ranjith & Rice (2001) was shown to be the effective stationary speed reached along the favoured direction at the end of the acceleration phase even for growing cracks, both when  $C_{gr}$  exists and it does not.

# Appendix A

## A.1 Eigenvalue problem for general homogeneous case

Substituting the equations (2.13) into the equations (2.6)-(2.8) we get:

$$\begin{aligned}
 & (\lambda + 2\mu - \rho v^2)A_{11}f_1'' + (\lambda + 2\mu - \rho v^2)A_{12}f_2'' + (\lambda + 2\mu - \rho v^2)A_{13}f_3'' + \\
 & \quad + \mu A_{11}p_1^2 f_1'' + \mu A_{12}p_2^2 f_2'' + \mu A_{13}p_3^2 f_3'' + \\
 & \quad + (\lambda + \mu)A_{21}p_1 f_1'' + (\lambda + \mu)A_{22}p_2 f_2'' + (\lambda + \mu)A_{23}p_3 f_3'' = 0
 \end{aligned} \tag{A.1}$$

$$\begin{aligned}
 & (\lambda + \mu)A_{11}p_1 f_1'' + (\lambda + \mu)A_{12}p_2 f_2'' + (\lambda + \mu)A_{13}p_3 f_3'' + \\
 & \quad + (\mu - \rho v^2)A_{21}f_1'' + (\mu - \rho v^2)A_{22}f_2'' + (\mu - \rho v^2)A_{23}f_3'' + \\
 & \quad + (\lambda + 2\mu)A_{21}p_1^2 f_1'' + (\lambda + 2\mu)A_{22}p_2^2 f_2'' + (\lambda + 2\mu)A_{23}p_3^2 f_3'' = 0
 \end{aligned} \tag{A.2}$$

$$\mu A_{31}p_1^2 f_1'' + \mu A_{32}p_2^2 f_2'' + \mu A_{33}p_3^2 f_3'' = 0 \tag{A.3}$$

Where the following relations are implied deriving directly from the equation (2.14):

$$p_i \frac{\partial^2 f_i}{\partial x_1^2} = \frac{\partial^2 f_i}{\partial x_1 \partial x_2} = p_i f_i'' \quad p_i^2 \frac{\partial^2 f_i}{\partial x_1^2} = \frac{\partial^2 f_i}{\partial x_2^2} = p_i^2 f_i'' \tag{A.4}$$

Grouping correctly the derivative of  $f_q$  from equations (A.1)-(A.3) we get the following 9 equations:

$$\begin{cases}
 (\lambda + 2\mu - \rho v^2 + \mu p_1^2)A_{11} + (\lambda + \mu)p_1 A_{21} = 0 \\
 (\lambda + 2\mu - \rho v^2 + \mu p_2^2)A_{12} + (\lambda + \mu)p_2 A_{22} = 0 \\
 (\lambda + 2\mu - \rho v^2 + \mu p_3^2)A_{13} + (\lambda + \mu)p_3 A_{23} = 0
 \end{cases} \tag{A.5}$$

$$\begin{cases}
 (\lambda + \mu)p_1 A_{11} + [(\lambda + 2\mu)p_1^2 + (\mu - \rho v^2)A_{21}] = 0 \\
 (\lambda + \mu)p_2 A_{12} + [(\lambda + 2\mu)p_2^2 + (\mu - \rho v^2)A_{22}] = 0 \\
 (\lambda + \mu)p_3 A_{13} + [(\lambda + 2\mu)p_3^2 + (\mu - \rho v^2)A_{23}] = 0
 \end{cases} \tag{A.6}$$

$$\begin{cases} [(\mu - \rho v^2) + \mu p_1^2] A_{31} = 0 \\ [(\mu - \rho v^2) + \mu p_2^2] A_{32} = 0 \\ [(\mu - \rho v^2) + \mu p_3^2] A_{33} = 0 \end{cases} \quad (\text{A.7})$$

Considering the equations involving the same  $p_q$  in equations (A.5)-(A.7) we get the eigenvalue problem in equation (2.16). The explicit computation of the eigenvalues  $p_3$  for the anti plane shear has been reported above (equation (2.20)). To compute the eigenvalue  $p_1$  and  $p_2$  we can start from the restriction of general eigenvalue problem expressed by the equation (2.23). From that we obtain the following characteristic equation:

$$\begin{aligned} (\lambda + 2\mu)\mu p_q^4 + [(\lambda + 2\mu)(\lambda + 2\mu - \rho v^2) + \mu(\mu - \rho v^2) - (\lambda + \mu)^2] p_q^2 + \\ + (\lambda + 2\mu - \rho v^2)(\mu - \rho v^2) = 0 \end{aligned} \quad (\text{A.8})$$

solving the bi-quadratic equation (A.8) for  $t = p_q^2$  we get:

$$\begin{aligned} t = \frac{\frac{\rho v^2}{2} [(\lambda + 3\mu) \pm (\lambda + \mu)] - \mu(\lambda + 2\mu)}{\mu(\lambda + 2\mu)} \Rightarrow \\ \Rightarrow t_1 = \frac{\rho v^2}{\lambda + 2\mu} - 1 \vee t_2 = \frac{\rho v^2}{\mu} - 1 \end{aligned} \quad (\text{A.9})$$

if  $v < C_s \Rightarrow t_i < 0 \quad \forall i$ , and the solutions for  $p_q$  are purely imaginary as already claimed in the section 2.2.2 and the two roots with positive imaginary part can be written as reported in (2.24)-(2.25) with  $\alpha_2$  arguable from (2.20).

As seen the normalization of each column of  $\mathbf{A}$  is arbitrary, and from that the row of matrix  $\mathbf{L}$  can be explicitly computed as follow starting from the Hooke's law. In fact:

$$\begin{aligned} \sigma_{11} &= (\lambda + 2\mu)\varepsilon_{11} + \lambda(\varepsilon_{22} + \varepsilon_{33}) = (\lambda + 2\mu) \frac{\partial u_1}{\partial x_1} + \lambda \left( \frac{\partial u_2}{\partial x_2} + \frac{\partial u_3}{\partial x_3} \right) \\ \sigma_{12} &= 2C_{1221}\varepsilon_{21} = \mu \left( \frac{\partial u_1}{\partial x_2} + \frac{\partial u_2}{\partial x_1} \right) \\ \sigma_{13} &= 2C_{1331}\varepsilon_{31} = \mu \left( \frac{\partial u_1}{\partial x_3} + \frac{\partial u_3}{\partial x_1} \right) \end{aligned} \quad (\text{A.10})$$

Now combining the (2.12) and (2.13) with the (A.10) we get:

$$\begin{aligned} & -p_1 L_{11} f'_1 - p_2 L_{12} f'_2 - p_3 L_{13} f'_3 + \rho v^2 (A_{11} f'_1 + A_{12} f'_2 + A_{13} f'_3) = \\ & = (\lambda + 2\mu) (A_{11} f'_1 + A_{12} f'_2 + A_{13} f'_3) + \lambda (p_1 A_{21} f'_1 + p_2 A_{22} f'_2 + p_3 A_{23} f'_3) \end{aligned} \quad (\text{A.11})$$

$$\begin{aligned} & -p_1 L_{21} f'_1 - p_2 L_{22} f'_2 - p_3 L_{23} f'_3 + \rho v^2 (A_{21} f'_1 + A_{22} f'_2 + A_{23} f'_3) = \\ & = \mu (A_{21} f'_1 + A_{22} f'_2 + A_{23} f'_3) + \mu (p_1 A_{11} f'_1 + p_2 A_{12} f'_2 + p_3 A_{13} f'_3) \end{aligned} \quad (\text{A.12})$$

$$\begin{aligned} & -p_1 L_{31} f'_1 - p_2 L_{32} f'_2 - p_3 L_{33} f'_3 + \rho v^2 (A_{31} f'_1 + A_{32} f'_2 + A_{33} f'_3) = \\ & \mu (A_{31} f'_1 + A_{32} f'_2 + A_{33} f'_3) \end{aligned} \quad (\text{A.13})$$

Where the following relationships are considered:

$$p_i \frac{\partial f_i}{\partial x_1} = \frac{\partial f_i}{\partial x_2} = p_i f'_i \quad (\text{A.14})$$

From equations (A.11)-(A.12)-(A.14) we obtain respectively the row of matrix  $\mathbf{L}$  :

$$\left\{ \begin{array}{l} L_{1q} = -[p_q^{-1}(\lambda + 2\mu - \rho v^2)A_{1q} + \lambda A_{2q}] \\ L_{2q} = -[p_q^{-1}(\mu - \rho v^2)A_{2q} + \mu A_{1q}] \\ L_{3q} = -p_q^{-1}(\mu - \rho v^2)A_{3q} \end{array} \right. \quad (\text{A.15})$$

And the second row of stress tensor can be expressed as above indicated in equation (2.18).

Once explicitly obtained the eigenvalue, the matrix  $\mathbf{A}$  and  $\mathbf{L}$  can be in turn explicitly expressed in terms of elastic parameters of the layer. For sake of simplicity the values  $A_{33}$  and  $L_{33}$  has been already reported in section 2.2.2, in the part related to anti-plane shear. Below the values for the plane propagation are obtained. Using the eigenvalues  $p_1$  and  $p_2$  from the (2.24) (with the conditions (2.25) and (2.20)) and in first two equations of (A.5) (or equivalently of (A.6)) we have two degrees of freedom. Thus we can fix arbitrary  $A_{11} = A_{22} = 1$  and solve the following system:

$$\left\{ \begin{array}{l} (\lambda + 2\mu - \rho v^2 - \mu \alpha_1^2) + (\lambda + \mu) i \alpha_1 A_{21} = 0 \\ (\lambda + 2\mu - \rho v^2 - \mu \alpha_2^2) A_{12} + (\lambda + \mu) i \alpha_2 = 0 \end{array} \right. \quad (\text{A.16})$$

From which directly descend:  $A_{12} = -i\alpha_2$  and  $A_{21} = i\alpha_1$ , and therefore the matrix (2.26). The matrices  $\mathbf{L}$  and  $\mathbf{B}$  in the equation (2.27) are directly computed from the (A.15) and (2.19), and it is worth noting that the Rayleigh function  $D$  in equation (2.27) is defined such that  $\det|\mathbf{L}| = \mu^2 D$

## A.2 Eigenvalue problem for bimaterial case (general complex matrix $\mathbf{H}$ )

To solve the eigenvalue problem the equation (2.57) can be rearranged as:

$$H_{33}(1 - e^{2\pi\epsilon}) \left[ H_{11}H_{22}(1 - e^{2\pi\epsilon})^2 - H_{12}^2(1 + e^{2\pi\epsilon})^2 \right] = 0 \quad (\text{A.17})$$

The third eigenvalue (for the anti-plane) is readily computed and it is  $\epsilon_3 = 0$ . To compute the other two eigenvalues, the term in the square bracket of (A.17) has to be equal to zero. It leads to:

$$H_{12}(1 + \phi) = \pm \sqrt{H_{11}H_{22}}(1 - \phi) \quad (\text{A.18})$$

With  $\phi = e^{2\pi\epsilon}$  and the solutions for  $\phi$  are:

$$\phi = \frac{\sqrt{H_{11}H_{22}} \pm H_{12}}{\sqrt{H_{11}H_{22}} \mp H_{12}} \quad (\text{A.19})$$

This implies that:

$$\epsilon_1 = -\epsilon_2 = \left( \frac{1}{2\pi} \right) \ln \left( \frac{1 - \beta}{1 + \beta} \right) \quad (\text{A.20})$$

As reported in equation (2.58). The eigenvector related to the eigenvalue  $\epsilon_3$  is expressed by the (2.59). For  $\epsilon_1$  we can arbitrary fix  $\mathbf{w}_1^{(2)} = 1/2$  (here the superscript refers to the component of vector) and thus:

$$H_{11} \frac{2\beta}{1 + \beta} \mathbf{w}_1^{(1)} = iH_{12} \frac{1}{1 + \beta} \Rightarrow \mathbf{w}_1^{(1)} = -i \frac{H_{12}}{2H_{11}} \left( \frac{\sqrt{H_{11}H_{22}}}{H_{12}} \right) = -\frac{i\eta}{2} \quad (\text{A.21})$$

With  $\eta = (H_{22} / H_{11})^{\frac{1}{2}}$ . Similarly for  $\epsilon_2 = -\epsilon_1$ :

$$H_{11} \left( -\frac{2\beta}{1-\beta} \right) \mathbf{w}_2^{(1)} = iH_{12} \frac{1}{1-\beta} \Rightarrow \mathbf{w}_2^{(1)} = i \frac{H_{12}}{2H_{11}} \left( \frac{\sqrt{H_{11}H_{22}}}{H_{12}} \right) = \frac{i\eta}{2} = \bar{\mathbf{w}}_1^{(1)} \quad (\text{A.22})$$

Thus the eigenpairs are those expressed by the equation (2.61)

### A.3 Energy release rate for bimaterial case (general complex matrix $\mathbf{H}$ )

From equations (2.68) and (2.70) we can compute the energy release rate  $G$  as a function of the complex stress intensity factor  $K$  and the real one  $K_3$  using the Irwin formula. For sake of clarity we write here the equations (2.68) and (2.70) that represent the traction ahead the crack tip and the displacement behind:

$$\mathbf{t}(r) = (2\pi r)^{-\frac{1}{2}} \left[ Kr^{i\epsilon} \mathbf{w} + \bar{K}r^{-i\epsilon} \bar{\mathbf{w}} + K_3 \mathbf{w}_3 \right] \quad (\text{A.23})$$

$$\mathbf{d}(r) = (\mathbf{H} + \bar{\mathbf{H}}) \left( \frac{r}{2\pi} \right)^{\frac{1}{2}} \left[ \frac{Kr^{i\epsilon} \mathbf{w}}{(1+2i\epsilon) \cosh(\pi\epsilon)} + \frac{\bar{K}r^{-i\epsilon} \bar{\mathbf{w}}}{(1-2i\epsilon) \cosh(\pi\epsilon)} + K_3 \mathbf{w}_3 \right] \quad (\text{A.24})$$

Considering the forms of  $\mathbf{w}, \mathbf{w}_3, K$  and  $K_3$  the equations (A.23) and (A.24) lead to the following form for the energy release rate  $G$ :

$$\begin{aligned} G = & \frac{1}{2\Delta} \frac{1}{2\pi} \mathbf{w}^T (\mathbf{H} + \bar{\mathbf{H}}) \mathbf{w} K^2 \int_0^\Delta \left( \frac{r}{\Delta-r} \right)^{\frac{1}{2}} \frac{(\Delta-r)^{i\epsilon} r^{i\epsilon}}{(1+2i\epsilon) \cosh \pi\epsilon} dr + \\ & + \frac{1}{2\Delta} \frac{1}{2\pi} \mathbf{w}^T (\mathbf{H} + \bar{\mathbf{H}}) \bar{\mathbf{w}} |K|^2 \int_0^\Delta \left( \frac{r}{\Delta-r} \right)^{\frac{1}{2}} \frac{(\Delta-r)^{i\epsilon}}{r^{i\epsilon} (1-2i\epsilon) \cosh \pi\epsilon} dr + \\ & + \frac{1}{2\Delta} \frac{1}{2\pi} \bar{\mathbf{w}}^T (\mathbf{H} + \bar{\mathbf{H}}) \mathbf{w} |K|^2 \int_0^\Delta \left( \frac{r}{\Delta-r} \right)^{\frac{1}{2}} \frac{r^{i\epsilon}}{(\Delta-r)^{i\epsilon} (1+2i\epsilon) \cosh \pi\epsilon} dr + \quad (\text{A.25}) \\ & + \frac{1}{2\Delta} \frac{1}{2\pi} \bar{\mathbf{w}}^T (\mathbf{H} + \bar{\mathbf{H}}) \bar{\mathbf{w}} \bar{K}^2 \int_0^\Delta \left( \frac{r}{\Delta-r} \right)^{\frac{1}{2}} \frac{1}{(\Delta-r)^{i\epsilon} r^{i\epsilon} (1-2i\epsilon) \cosh \pi\epsilon} dr + \\ & + \frac{1}{2\Delta} \frac{1}{2\pi} \mathbf{w}_3^T (\mathbf{H} + \bar{\mathbf{H}}) \mathbf{w}_3 K_3^2 \int_0^\Delta \left( \frac{r}{\Delta-r} \right)^{\frac{1}{2}} dr \end{aligned}$$

The first and fourth terms on the right-hand side member of equation (A.25) vanish because of the orthogonality of  $\mathbf{w}$  expressed by the (2.62). Moreover it can be readily shown that:

$$\mathbf{w}^T (\mathbf{H} + \bar{\mathbf{H}}) \bar{\mathbf{w}} = \bar{\mathbf{w}}^T (\mathbf{H} + \bar{\mathbf{H}}) \mathbf{w} = H_{22} \quad (\text{A.26})$$

Thus the equation (A.25) can be rearranged as:

$$\begin{aligned} G = \frac{1}{2\Delta} \frac{1}{2\pi} \bar{\mathbf{w}}^T (\mathbf{H} + \bar{\mathbf{H}}) \mathbf{w} |K|^2 & \left\{ \int_0^\Delta \left( \frac{r}{\Delta-r} \right)^{\frac{1-i\epsilon}{2}} \frac{1}{(1-2i\epsilon)\cosh \pi\epsilon} dr + \right. \\ & \left. \int_0^\Delta \left( \frac{r}{\Delta-r} \right)^{\frac{1+i\epsilon}{2}} \frac{1}{(1+2i\epsilon)\cosh \pi\epsilon} \right\} + \\ & + \frac{1}{2\Delta} \frac{1}{2\pi} \mathbf{w}_3^T (\mathbf{H} + \bar{\mathbf{H}}) \mathbf{w}_3 K_3^2 \int_0^\Delta \left( \frac{r}{\Delta-r} \right)^{\frac{1}{2}} dr \end{aligned} \quad (\text{A.27})$$

The three integrals in (A.27) can be resolved using the general formula (2.49) with  $q = \frac{1}{2} \mp i\epsilon, \frac{1}{2}$  respectively, leading to:

$$G = \frac{1}{4\pi} \bar{\mathbf{w}}^T (\mathbf{H} + \bar{\mathbf{H}}) \mathbf{w} |K|^2 \left\{ 2 \left[ \frac{\pi}{2 \cosh^2 \pi\epsilon} \right] \right\} + \frac{1}{4\pi} \mathbf{w}_3^T (\mathbf{H} + \bar{\mathbf{H}}) \mathbf{w}_3 K_3^2 \frac{\pi}{2} \quad (\text{A.28})$$

Where the identity  $\sin(\pi/2 \pm i\pi\epsilon) = \cosh(\pi\epsilon)$  has been used. Finally we get:

$$G = \frac{1}{4} \frac{\bar{\mathbf{w}}^T (\mathbf{H} + \bar{\mathbf{H}}) \mathbf{w} |K|^2}{\cosh^2 \pi\epsilon} + \frac{1}{8} \mathbf{w}_3^T (\mathbf{H} + \bar{\mathbf{H}}) \mathbf{w}_3 K_3^2 \quad (\text{A.29})$$

Using the expression for  $\beta$  given in the equation (A.20):

$$4 \cosh^2(\pi\epsilon) = e^{2\pi\epsilon} + e^{-2\pi\epsilon} + 2 = \left( \frac{1-\beta}{1+\beta} \right) + \left( \frac{1+\beta}{1-\beta} \right) + 2 = \frac{4}{1-\beta^2} \quad (\text{A.30})$$

The matrix  $(\mathbf{H} + \bar{\mathbf{H}})$  is the diagonal matrix with elements  $2H_{ii}$  and considering the equation (A.26) and the following position:

$$\mathbf{w}_3^T (\mathbf{H} + \bar{\mathbf{H}}) \mathbf{w}_3 = 2H_{33} \quad (\text{A.31})$$

We can write:

$$G = \frac{1}{4} \left( H_{22} - \frac{H_{12}^2}{H_{11}} \right) |K|^2 + \frac{1}{4} H_{33} K_3^2 \quad (\text{A.32})$$

Thus defining the energy factor  $\mathcal{F}$  as in equation (2.72) the general form (2.71) for  $G$  is achieved.

#### A.4 Shear-displacement relationship in $p$ -domain: matrix $\hat{K}$

Following Geubelle & Rice (1995) it can be shown that, in  $p$ -domain, the relation between the tangential and normal displacement  $\hat{U}_t$  and  $\hat{U}^n$  and the traction  $T$  and  $N$  at  $x_2 = 0^+$  in the reference system of Figure 2.2:

$$\begin{Bmatrix} \hat{U}_t^+ \\ \hat{U}^{n,+} \end{Bmatrix} = \begin{bmatrix} \hat{C}_{11}^+ & \hat{C}_{12}^+ \\ \hat{C}_{21}^+ & \hat{C}_{22}^+ \end{bmatrix} \begin{Bmatrix} \hat{T} \\ \hat{N} \end{Bmatrix} \quad (\text{A.33})$$

with:

$$\begin{aligned} \hat{C}_{11}^+(p,k) &= -\frac{1}{\mu_1|k|} \frac{\alpha_{s1}(1-\alpha_{s1}^2)}{R_1(s)} \\ \hat{C}_{22}^+(p,k) &= -\frac{1}{\mu_1|k|} \frac{\alpha_{d1}(1-\alpha_{s1}^2)}{R_1(s)} \\ \hat{C}_{12}^+(p,k) &= -\frac{1}{i\mu_1 k} \frac{2\alpha_{s1}\alpha_{d1} - (1+\alpha_{s1}^2)}{R_1(s)} = -\hat{C}_{21}^+(p,k) \end{aligned} \quad (\text{A.34})$$

and:

$$\begin{aligned} \alpha_{s1} &= \sqrt{1+s^2/c_{s1}^2}; \quad \alpha_{d1} = \sqrt{1+s^2/c_{d1}^2}; \quad s = p/|k| \\ R_1(s) &= 4\alpha_{s1}\alpha_{d1} - (1+\alpha_{s1}^2)^2 \end{aligned} \quad (\text{A.35})$$

with  $c_{s1}$  shear wave speed in the medium,  $c_{d1}$  P-wave speed in the medium and  $R_1(s)$  having two roots at  $\pm ic_{r1}$  with  $c_{r1}$  Rayleigh speed in the medium.  $\mu_1$  is the shear modulus.

Similar relationships can be achieved at  $x_2 = 0^-$  in the reference system of Figure 2.2:

$$\begin{Bmatrix} \hat{U}_t^- \\ \hat{U}^{n,-} \end{Bmatrix} = \begin{bmatrix} -\hat{C}_{11}^- & \hat{C}_{12}^- \\ \hat{C}_{21}^- & -\hat{C}_{22}^- \end{bmatrix} \begin{Bmatrix} \hat{T} \\ \hat{N} \end{Bmatrix} \quad (\text{A.36})$$

with:

$$\begin{aligned}
\hat{C}_{11}^{-}(p,k) &= -\frac{1}{\mu_2|k|} \frac{\alpha_{s_2}(1-\alpha_{s_2}^2)}{R_2(s)} \\
\hat{C}_{22}^{-}(p,k) &= -\frac{1}{\mu_2|k|} \frac{\alpha_{d_2}(1-\alpha_{s_2}^2)}{R_2(s)} \\
\hat{C}_{12}^{-}(p,k) &= -\frac{1}{i\mu_2 k} \frac{2\alpha_{s_2}\alpha_{d_2} - (1+\alpha_{s_2}^2)}{R_2(s)} = -\hat{C}_{21}^{-}(p,k)
\end{aligned} \tag{A.37}$$

and:

$$\begin{aligned}
\alpha_{s_2} &= \sqrt{1+s^2/c_{s_2}^2}; \quad \alpha_{d_2} = \sqrt{1+s^2/c_{d_2}^2}; \quad s = p/|k| \\
R_2(s) &= 4\alpha_{s_2}\alpha_{d_2} - (1+\alpha_{s_2}^2)^2
\end{aligned} \tag{A.38}$$

with  $c_{s_2}$  shear wave speed in the medium,  $c_{d_2}$  P-wave speed in the medium and  $R_2(s)$  having two roots at  $\pm ic_{r_2}$  with  $c_{r_2}$  Rayleigh speed in the medium.  $\mu_2$  is the shear modulus.

Subtracting the (A.36) from equation (A.33) at low slip rates,  $V \ll c_{s_1}$ , we get the equation (2.97) and thus the explicit form form the components  $\hat{K}_{ij}$ :

$$\hat{K}_{11} = \hat{C}_{11}^{+} + \hat{C}_{11}^{-}; \quad \hat{K}_{22} = \hat{C}_{22}^{+} + \hat{C}_{22}^{-}; \quad \hat{K}_{12} = \hat{C}_{12}^{+} - \hat{C}_{12}^{-} = -\hat{K}_{21} \tag{A.39}$$

# 3 Free surface interactions

## 3.1 Introduction

Historically, seismological research has focused on vertical strike-slip faults such as the San Andreas Fault (Burridge & Halliday, 1971; Archuleta & Frazier, 1978). Nevertheless for compressive tectonic regimes (thrust faulting) such as the Los Angeles area, Japan, and Central and South America, and in extensional regimes (normal faulting) such as the Mediterranean and the Great Basin of Nevada, Utah, and Idaho the seismogenic areas appears rather as nonvertical (dipping) faults (Oglesby *et al.*, 1998). The most evident difference between non-vertical and vertical dipping fault is the break of geometrical symmetry that may generate heterogeneous stress fields to fit the Neumann boundary conditions at the free surface. In particular this interaction may cause perturbations in the normal stress along the fault during the rupture propagation as it happens for bimaterial interfaces. The analysis of ground motion caused by recent both thrust and normal events have reinforced this view, systematically showing larger ground motion on the hanging wall with respect to the footwall with larger asymmetry for reverse faulting. Moreover tsunamigenic events as the Tohoku earthquake have shown very large slip values around the trench as evidenced in several works (e.g. Satriano *et al.*, 2014).

Nielsen (1998) addressed the differences between a plane fault embedded in a homogeneous infinite medium and a dipping fault reaching the free surface in the framework of the dynamic rupture propagation.

In the case of an in-plane crack in an infinite medium the shear stress ahead the crack tip develops a double peak during dynamic propagation at a sub-Rayleigh wave velocity (Burridge, 1973; Andrews, 1985) At an observation point ahead of the crack tip, the transient stress increases at the S wave arrival time, then momentarily drops, until the stress concentration in the immediate vicinity of the crack tip becomes dominant. At this point, the stress increase induces the fracture and the friction drops down to the dynamic value. Under favorable initial stress conditions, the first stress peak associated with the S wave can reach a sufficient large value to induce the

rupture before the arrival of the main rupture front. In this case the rupture front suddenly jumps ahead of the mother front, eventually pushing the rupture at supershear velocity (Burridge, 1973).

Consider now the following free surface boundary conditions, for a plane 2D interface oriented along the x axis:

$$\sigma_{xx}^{fs} = \sigma_{xx}; \quad \sigma_{yy}^{fs} = \sigma_{xy}^{fs} = 0 \quad (3.1)$$

with the superscript  $\{ \}^{fs}$  indicating the condition at the free surface. Nielsen (1998) and Oglesby *et al.*, (1998) demonstrated that for a normal dipping fault the failure threshold ahead the crack tip is lowered, favouring an acceleration of the rupture, whereas for a thrust dipping fault the compressive variation of normal stress ahead the rupture harden the fault plane increasing the failure threshold. In spite of this hardening, over most of the dip angle range, the fault is still brought towards the failure; it is merely not brought as close to failure as it would have been without considering the free surface interaction. Oglesby *et al.* (1998) showed that when the rupture front reaches a particular distance close to the surface, the normal stress variation changes its sign (by analogy with the observed normal stress perturbations for bimaterial propagation) and this produces a weaker drop in shear stress for normal faults and a stronger stress drop for a reverse fault when a Coulomb friction law is considered. As a consequence, in both cases we experience a strong asymmetry between the particle motion in the hanging wall with respect to the footwall and this asymmetry is more pronounced for thrust faults and for decreasing dip angles. Of course it is enhanced close to the free surface as compared to deep zones of the fault. Furthermore, while the fault is slipping trapping radiated waves in the hanging wall further amplify ground motion on the hanging wall and thus the slip over the fault.

As addressed by Nielsen (1998) the rupture can show a stronger acceleration towards the surface for normal faults, whereas no particular effects on rupture speed can be detected for reverse faulting. Thus the strong dishomogeneity of the slip as a function of depth evidenced during the biggest subduction seismic events, and in particular for the Tohoku earthquake, can be considered also driven by the break of symmetry introduced when the fault interacts with the free surface in the vicinity of the trench.

Other peculiar effects were numerically investigated in the framework of a dipping fault reaching the free surface. Rudnicki & Wu (1995) showed that only for extensional regimes and when the shear-normal coupling is taken into account the fault can be separated in zones where either shear sliding or opening can occur. They used a Coulomb friction law with a constant friction coefficient but their results are misleading due to the absence of a characteristic length that scales with the size of the opening zone. As we will show in our numerical simulations, when a slip weakening is used, the opening can occur over a finite length for compressive regime as effect of further normal stress decrease behind the crack tip.

Performing 3D dynamic simulations for a strike-slip fault, Kaneko & Lapusta (2010) have showed that when a supershear transition is generated for a dipping fault reaching the free surface, it is mainly driven by the phase conversion of SV to Pwaves at the free surface. Additionally weaker supershear slip is due to the generalized Burridge–Andrews mechanism driven by P and SV-waves ahead the rupture and caused by the low strength in the shallow portions of the fault with respect to the deep regions.

Finally, Xu *et al.*, (2015) showed that a deeply nucleated main rupture finally reaching the surface, can cause a slip reversal from thrust to normal along the reactivated backthrust.

## 3.2 Geometrical models and simulations setup

To numerically study how the coupling between normal and shear stress can drive the rupture dynamics of a dipping fault three different bi-dimensional fault geometries were considered, with different angles between the fault and the top edge of the domain. On this edge a free surface boundary condition (3.1) is imposed, whereas on the other three edges of the domain absorbing boundary conditions are implemented by using Perfectly Matching Layers (Festa & Nielsen, 2003; Festa & Vilotte, 2006).

The first model (Figure 3.1a) consists of a vertical fault reaching the free surface, with the tangential traction  $\tau$  as projected on the fault oriented upward. The model shown in Figure 3.1b represents a dipping fault with  $\alpha = 45^\circ$ , where  $\alpha$  is the angle between the fault and the free surface, whereas in Figure 3.1c a similar model with  $\alpha = 10^\circ$  is taken into account. In the last two models the tangential traction is oriented to mimic the typical mechanism of a reverse fault. The three faults are embedded in a

homogeneous isotropic medium such that normal stress perturbations are generated from the interaction between the waves radiated by the rupture and the free surface. In all models the deep end of the fault is modelled as a fixed point. Conversely the other edge of the fault impacting the free surface is free to slip both normally and along tangential direction respect to the fault, while satisfying the free surface conditions.

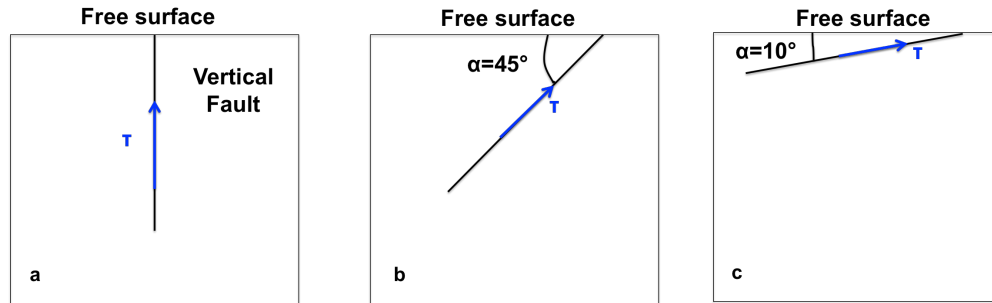


Figure 3.1 Geometrical initial conditions for the numerical simulations: (a) vertical fault ( $\alpha = 90^\circ$ ) with the traction  $\tau$  oriented upward. (b-c) dipping faults respectively with  $\alpha = 45^\circ$  and  $\alpha = 10^\circ$ . The tangential traction  $\tau$  is oriented in order to model a thrust fault.

The simulations presented here were performed using a dimensionless set of parameters here briefly described.

We briefly recall the standard elastodynamic equations and the linear slip weakening law imposed on the fault :

$$\rho \frac{\partial^2 \mathbf{u}}{\partial t^2} = \nabla \cdot \boldsymbol{\sigma}; \quad \boldsymbol{\sigma} = \mathbf{c} : \nabla \mathbf{u} \quad (3.2)$$

$$\mu = \begin{cases} \mu_s - \frac{\mu_s - \mu_d}{D_c} \delta u & \delta u < D_c \\ \mu_d & \delta u \geq D_c \end{cases} \quad (3.3)$$

All the displacements can be renormalized by the slip weakening distance obtaining:

$$\tilde{\mathbf{u}} = \frac{\mathbf{u}}{D_c} \quad (3.4)$$

with the tilde representing the dimensionless variables. The (3.4) renormalizes the linear slip weakening as:

$$\mu = \begin{cases} \mu_s - (\mu_s - \mu_d) \delta \tilde{u} & \delta \tilde{u} < 1 \\ \mu_d & \delta \tilde{u} \geq 1 \end{cases} \quad (3.5)$$

For what concern the stress, each component of the stress tensor  $\boldsymbol{\sigma}$  can be renormalized for  $\Delta\sigma$ , the stress drop computed as the difference between the initial and the dynamic level of tangential stress, whereas the Hooke's tensor  $\mathbf{c}$  is normalized by using the shear modulus  $G$ :

$$\tilde{\boldsymbol{\sigma}} = \frac{\boldsymbol{\sigma}}{\Delta\sigma}; \quad \tilde{\mathbf{c}} = \frac{\mathbf{c}}{G} \quad (3.6)$$

The (3.6) lead to:

$$\tilde{\boldsymbol{\sigma}} = \left( \frac{GD_c}{\Delta\sigma} \right) \tilde{\mathbf{c}} : \nabla \tilde{\mathbf{u}} \quad (3.7)$$

In order to have the Hooke's linear law, for dimensionless parameter in the same form of the second equation in the (3.2), we can normalize the distances  $x_i$  in the domain as:

$$\tilde{x}_i = \frac{\Delta\sigma}{GD_c} x_i \Rightarrow \tilde{\nabla} = \frac{GD_c}{\Delta\sigma} \nabla \Rightarrow \tilde{\boldsymbol{\sigma}} = \tilde{\mathbf{c}} : \nabla \tilde{\mathbf{u}} \quad (3.8)$$

Finally exploiting the normalization (3.4)-(3.8) the dimensionless time stepping can be obtained from the first equation in the (3.2):

$$\rho D_c \frac{\partial^2 \tilde{\mathbf{u}}}{\partial t^2} = \left( \frac{\Delta\sigma^2}{GD_c} \right) \tilde{\nabla} \cdot \tilde{\boldsymbol{\sigma}} \quad (3.9)$$

Now substituting  $\rho = G/v_s^2$ , with  $v_s$  velocity of s-wave in the bulk, into the (3.9) we have:

$$\frac{\partial^2 \tilde{\mathbf{u}}}{\partial t^2} = \left( \frac{v_s \Delta\sigma}{GD_c} \right)^2 \tilde{\nabla} \cdot \tilde{\boldsymbol{\sigma}} \quad (3.10)$$

finally yielding to:

$$\tilde{t} = \frac{v_s \Delta\sigma}{GD_c} t \quad (3.11)$$

and:

$$\frac{\partial^2 \tilde{\mathbf{u}}}{\partial \tilde{t}^2} = \tilde{\nabla} \cdot \tilde{\boldsymbol{\sigma}} \quad (3.12)$$

For what concern the initial stress conditions, we assume that they linearly increase from zero at the free surface as a function of depth, in order to preserve a constant strength excess  $s$ , defined as:

$$s = \frac{\mu_s \sigma_0^n - \tau_0}{\tau_0 - \mu_d \sigma_0^n} \quad (3.13)$$

for all presented models  $s$  is fixed at 1.2. It is worth noting that this condition implies that the stress drop  $\Delta\sigma$  also increases with depth, being the denominator of the second member of the (3.13).

Figure 3.2a-b-c show the initial stress conditions respectively when a vertical fault and a dipping fault with  $\alpha = 45^\circ$  and  $10^\circ$  are considered. The failure threshold is given (blue lines) by  $\mu_s \sigma_0^n$  with  $\mu_s = 0.7$ , whereas the dynamic level (red lines) is  $\mu_d \sigma_0$  with  $\mu_d = 0.25$ . The asperity in initial shear stress (green lines) represents the initiation of the rupture over a length  $L > L_c$ , where  $L_c$  is fixed from the Uenishi & Rice (2003) formula (equations (2.118)-(2.119)).

As shown in the Figure 3.2c the dimension of the fault for  $\alpha = 10^\circ$  is about three times with respect to the other two cases and the initiation of rupture is located close to the deepest part of fault to avoid that the interaction between the propagating rupture and the free surface begins before that the nucleation phase is terminated. The size of an element for the case of vertical fault is  $\sim 0.3$ ; whereas it is  $\sim 0.4$  and  $\sim 1.2$  respectively for  $\alpha = 45^\circ$  and  $10^\circ$ . These dimensions have to be interpreted in the sense of dimensionless quantities in the first equation of (3.8).

Without loss of generality, for all simulations, we fixed the dimensionless S-wave velocity  $C_s$  to 1 as well as the density  $\rho = 1$ . We also consider the fault as embedded in a homogeneous Poisson's solid with the P-wave velocity  $C_p = \sqrt{3}C_s$ . The slip weakening distance  $D_c$  is fixed at 1.5.

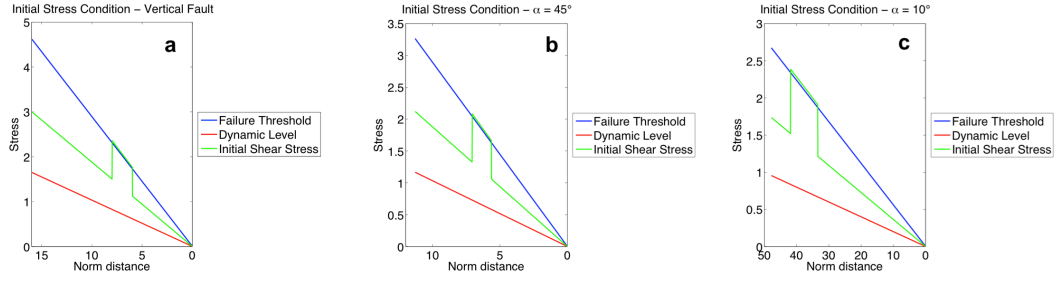


Figure 3.2 Initial stress conditions for vertical fault (a) and when  $\alpha = 45^\circ$  (b) and  $\alpha = 10^\circ$  (c) as a function of normalized distance from the intersection between the fault and the free surface.

### 3.3 Results

#### 3.3.1 Vertical fault

When a vertical fault is considered (Figure 3.1a-Figure 3.2a) the dynamic rupture propagation is expected to be symmetric.

Figure 3.3 and Figure 3.4 show the snapshots of the kinetic energy and the rotational wavefield respectively for a rupture propagating along a vertical fault. In particular the latter highlights the strong variation of the direct S-wave, the P converted to S at the surface and the S component of surface waves. (in the 5<sup>th</sup> snapshot of Figure 3.4 these phases are explicitly marked). In the first snapshot, for both representations at the dimensionless time step  $\tilde{t} = 0.9$ , the direct S front reaching the free surface is shown. Before that moment most of the energy is concentrated around the crack front along the downward propagation as the effect of the increasing stress drop with depth. After the beginning of the interaction more and more energy is reflected from the surface as effect of the free surface boundary condition, and the reflected waves both propagate symmetrically along the free surface and come back along the fault.

Figure 3.5 shows the effects of the propagation on the slip (normalized to  $D_c$ ) as a function of time and distance from the free surface along the fault. In particular from the zoom of Figure 3.5b we can infer the rupture propagation speed from the slope of the edges of the slip map (dashed white line) and we can note that the rupture rapidly accelerates to the Rayleigh wave speed for the bulk. After the beginning of interaction with the free surface, an acceleration of the slip is also noted properly as effect of this interaction.

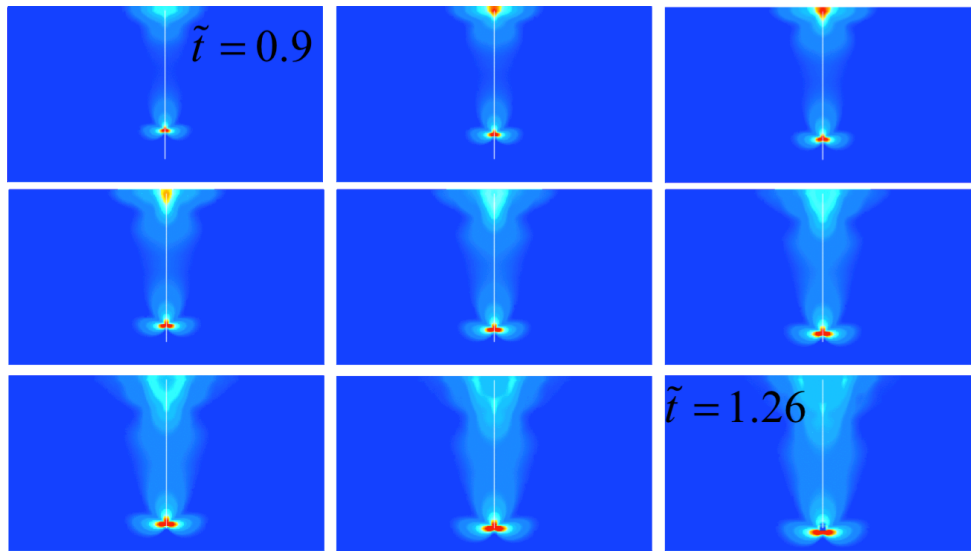


Figure 3.3: Snapshots of kinetic energy field for a propagating rupture along a vertical fault reaching the free surface at different increasing dimensionless time steps (from left to right, from top to bottom). In the first snapshot ( $\tilde{t} = 0.9$ ) the interaction between the fault and free surface begins. In subsequent snapshots the energy from the surface both interacts with the fault and propagates symmetrically along the surface.

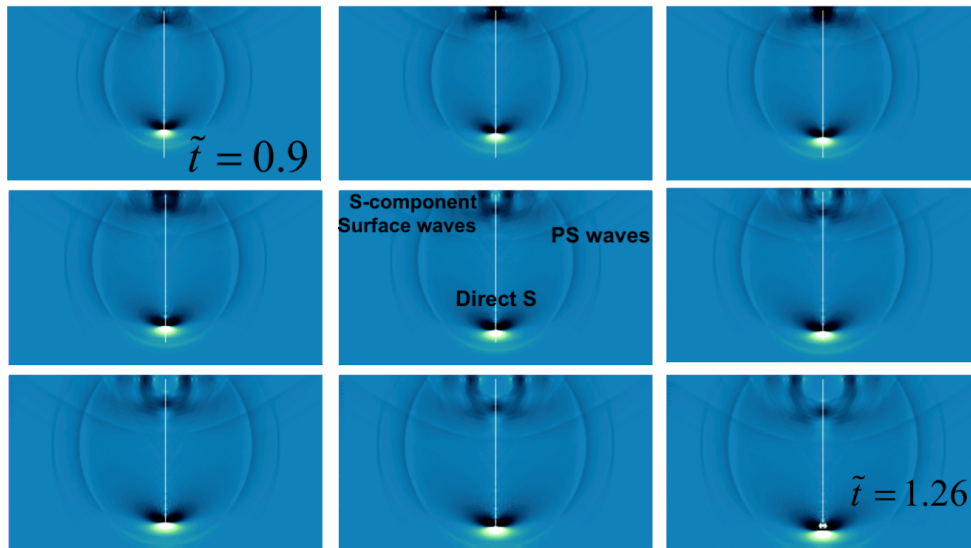


Figure 3.4 Snapshots of rotational wavefield for a propagating rupture along a vertical fault, reaching the free surface, at the same time steps as in Figure 3.3.

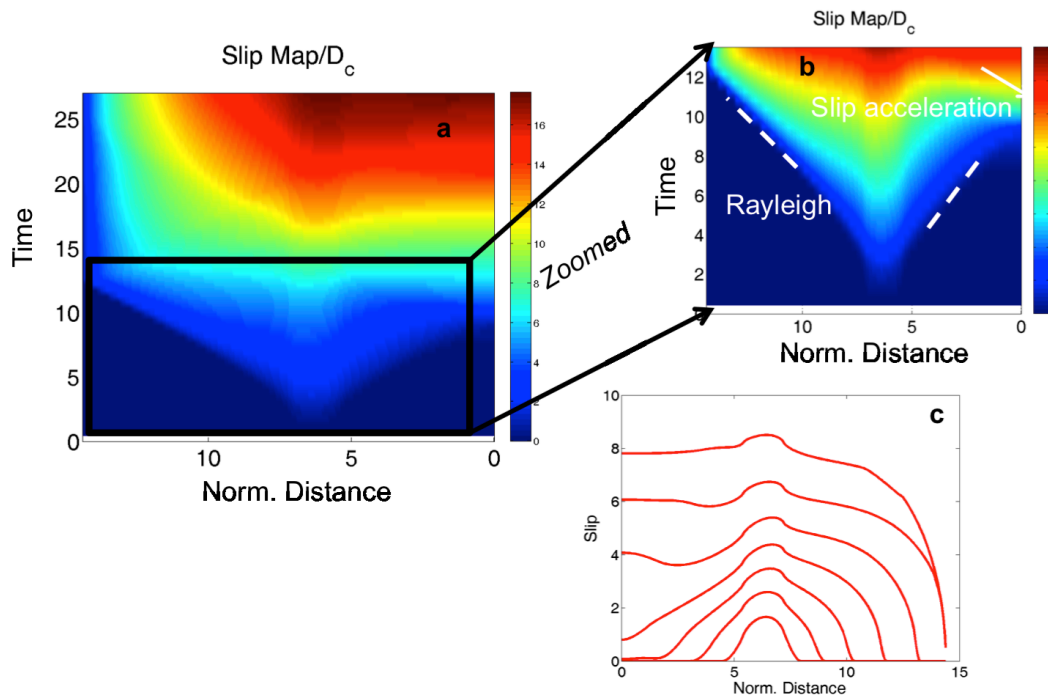


Figure 3.5: (a) slip map at different time steps as a function of distance from the free surface. In the zoom of (b) the rapid acceleration to Rayleigh speed of bilateral rupture is shown as well as the final slip acceleration due to the interaction with the waves coming from the free surface. (c) Profiles of slip as a function of distance for different time steps. The interaction with free surface increases the slip in the vicinity of the surface.

Figure 3.5c shows the slip profiles at different time steps as a function of distance from the surface. The above described interaction coupled with the fact that the last point, located on the surface, is free to slide, contributes to increase the final slip values in the vicinity of the free surface. This brings the coseismic slip close to the value computed around the nucleation and these values are pretty higher than those computed in the deep part where the last point is locked.

Slip rate profiles and dynamic shear stress are plotted together in Figure 3.6 as a function of distance from the surface and for different time steps. The strong overshoot in the middle of the fault is due to the higher level of initial stress imposed for the initiation of the rupture and the asymmetry between the two sides of the bilateral rupture is driven by the increasing remote shear and normal stresses with depth as shown in Figure 3.2a. This increases contemporary the frictional strength and the stress drop in order to preserve a constant strength parameter (3.13).

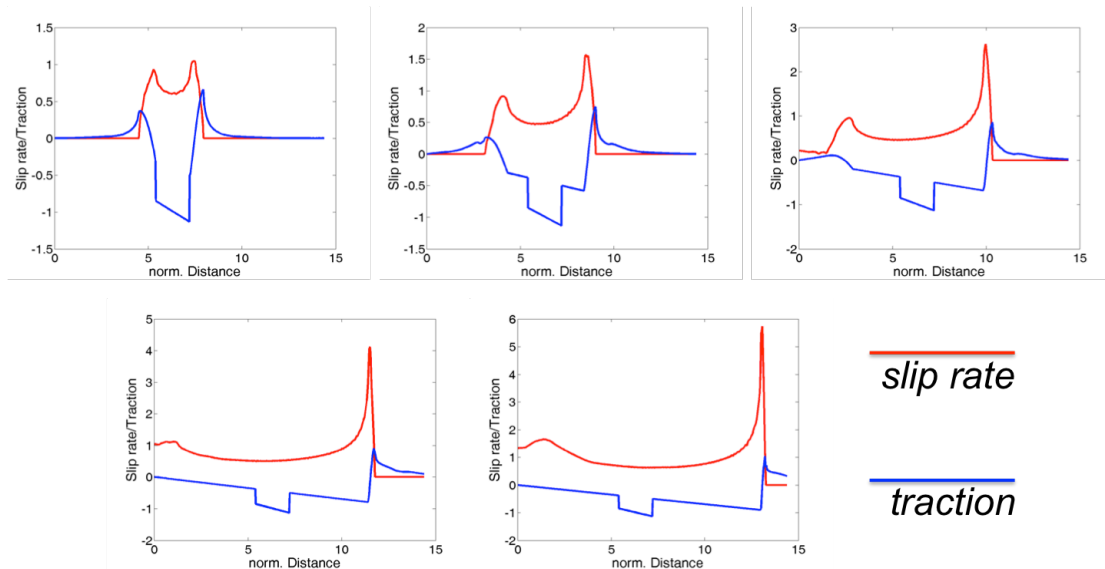


Figure 3.6 Snapshots showing the slip rate profiles (red curve) and the dynamic shear traction (blue curve) at different time steps as a function of the normalized distance from the surface.

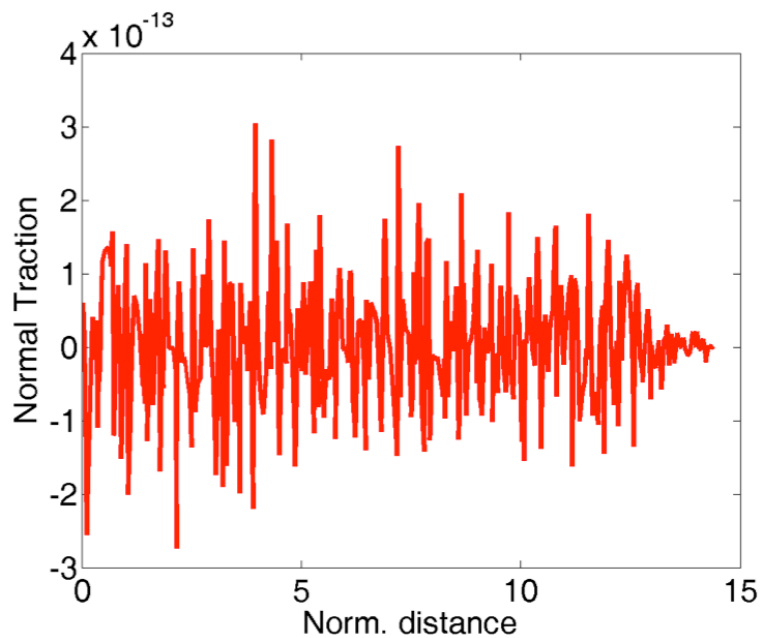


Figure 3.7: Negligible normal stress oscillations during the propagation along a vertical fault.

To conclude this brief overview on the dynamic results for a rupture propagating along a vertical fault is interesting to note that, as expected, the normal stress perturbations are totally negligible (oscillation level is well below the dispersion error). This leads to symmetric solutions and the only effect is the acceleration of slip in the vicinity of the surface already described in Figure 3.5.

### 3.3.2 Dipping fault with $\alpha = 45^\circ$

The vertical fault described in previous subsection can be considered as a dipping fault with  $\alpha = 90^\circ$  (see Figure 3.1a and Figure 3.2a). When dipping faults with  $\alpha < 90^\circ$  are taken into account we should expect a break of symmetry due to the normal stress perturbations, which are coupled with the shear stress through the classical Coulomb friction condition.

In this section the results of dynamic simulations obtained from the initial conditions described in the Figure 3.1b and Figure 3.2b are shown. These refer to a dipping fault with  $\alpha = 45^\circ$ .

Figure 3.8 shows several snapshots of the kinetic energy field at different time steps. During the initial phase of the propagation (first two rows in Figure 3.8) no interaction is detected and the symmetry between the ground motion on the hanging wall and the footwall is preserved, with a more energetic emission downward due to the higher stress drop. Later on, in the vicinity of the surface the waves generated at the surface and close to the fault start to interact ( $\tilde{t} = 1.00$ ). When interaction begins, it rapidly generates large ground motion on the hanging wall over a finite length in the vicinity of the surface ( $\tilde{t} = 1.20$ ). Then, this length slowly increases as effect of multiple reflection of the trapped waves ( $\tilde{t} = 1.49$ ).

A first order estimate of the interaction length can be computed from the following simple considerations. The dynamics of a propagating rupture is summarized in Figure 3.9: the red and black thick lines are respectively the fault and the free surface, whereas the blue and brown arcs represent respectively the S-wave front ahead of the crack tip (proceeding at  $v_s$ ) and the rupture tip (proceeding at Rayleigh speed  $v_R$ );  $L$  is the distance between the middle of the nucleation patch and the free surface along the fault. We can reasonably infer that the interaction starts when the rupture tip is on the same vertical line as the intersection of the S-wave front with the free surface and therefore the interaction length  $l$  can be estimated as the distance between the crack tip at this time and the surface along the fault; from simple geometrical considerations  $l$  can be approximated as:

$$l \left( L, \theta, \frac{v_R}{v_s} \right) \approx L \frac{v_s - v_R}{v_s - v_R + v_R \sin^2 \theta} \quad (3.14)$$

As shown in equation (3.14) the initial interaction length is a function of distance  $L$ , of the angle  $\theta$  between the fault and the free surface and of the ratio between Rayleigh and S-wave speed, while it can be considered independent of the initial stress conditions. When a small stress drop is considered in the vicinity of the surface, as in this case (and as expected for realistic applications in subduction zone), the wavelength associated with this interaction dominates the emitted radiation. In fact in the deepest part the acceleration of the rupture leads to a shrinking of dissipation zone, which in turn implies an increasing of high-frequency emitted radiation. Conversely the interaction with free surface and the low stress drop prevent the shrinking of cohesive zone and the emission of high-frequency phases. In Figure 3.10 The slip rate and stress profiles show the shrinking of dissipation zone in the deepward propagation and its enlarging trenchward as effect of fault/surface interaction.

When this interaction starts it can allow the rupture to rapidly jump on the surface. Figure 3.11 shows the time of activation of the slip as a function of the distance from the surface (black dots) and the end of dissipation zone at the same time steps (red dots). Whereas in the deepest part the shrinking of dissipation zone produces higher and higher frequency radiation, towards the surface the dissipation zone does not shrink due to the jump induced by the interaction with the free surface. The dashed green lines in Figure 3.11 provide an estimate of the interaction length  $\tilde{l}$  which is in agreement with the length  $l$  computed in equation (3.14).

The slip map (normalized to  $D_c$ ) is plotted in Figure 3.12a (and its zoom in Figure 3.12b). The dislocation is shown to be pretty symmetric until the beginning of the interaction with a rapid acceleration of the rupture towards the Rayleigh speed along both directions. The interaction with the free surface and the consequent jump generates a slip acceleration (white arrow in Figure 3.12b) and contemporary a small increase of the slip measured in the shallow part of the fault. This is due to the larger ground motion on the hanging wall, as shown in Figure 3.12c, where the slip profiles are plotted, at different time steps, as a function of the distance from the surface.

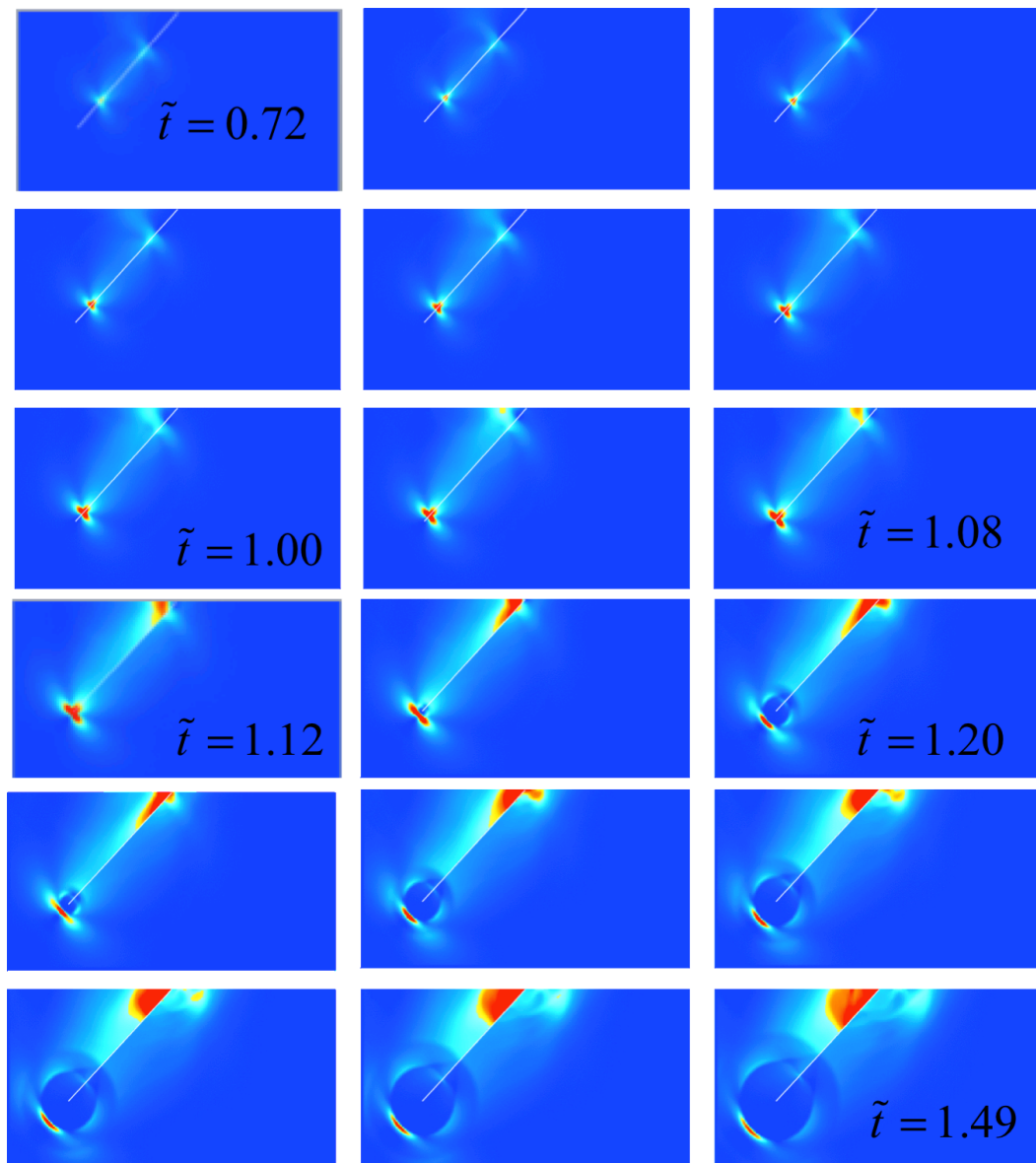


Figure 3.8 Kinetic energy field snapshots for  $\alpha = 45^\circ$ . When the shallow part of the fault starts to interact with the free surface the symmetry is broken and larger ground motion is recorded in the hanging wall respect to the footwall.

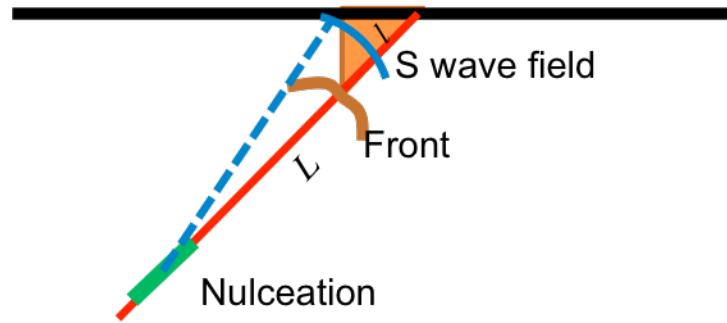


Figure 3.9 Scheme of rupture dynamics for a dipping fault with  $\alpha < 90^\circ$ . The blue arc represents the S-wave front ahead the rupture tip, whereas the brown arc is the rupture front advancing at Rayleigh speed. The red line is the fault and  $L$  is the distance between the middle of nucleation area and the free surface. The estimate  $l$  of the interaction length is substantially the hypotenuse of the orange triangle.

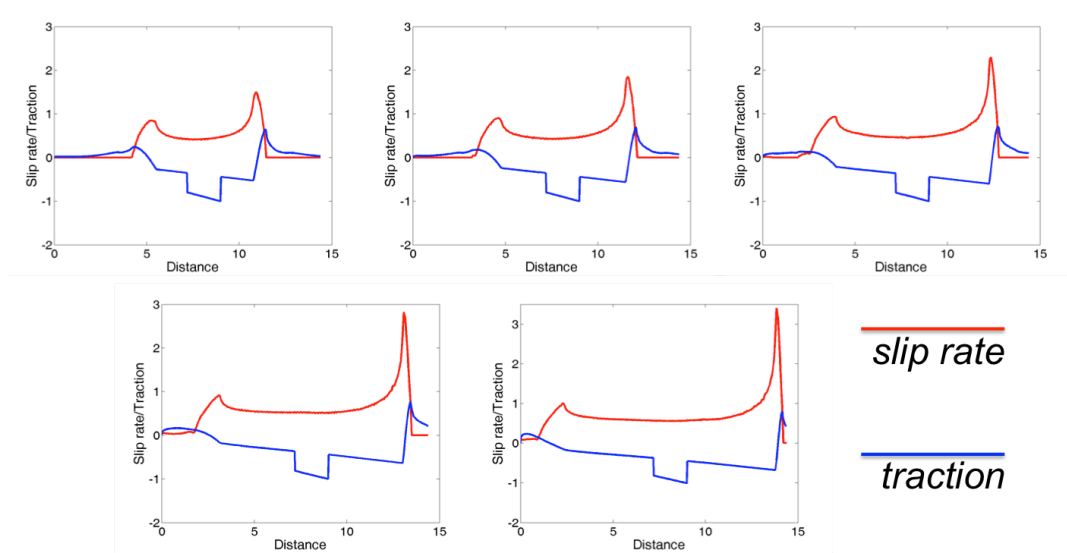


Figure 3.10 Snapshots showing the slip rate profiles (red curve) and the dynamic shear traction (blue curve) at different time steps as a function of normalized distance from the surface when  $\alpha = 45^\circ$ .

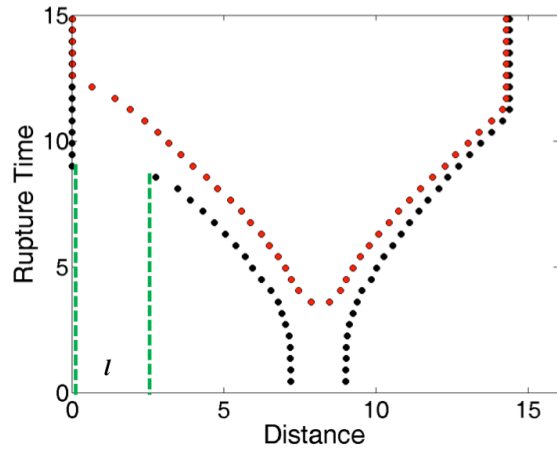


Figure 3.11 Time of activation of slip as a function of distance from free surface for  $\alpha = 45^\circ$ . Black dots are the position of crack tip whereas the red dots are the end of dissipation zone. When waves starts to interact with the rupture, the tip suddenly jumps at the surface.

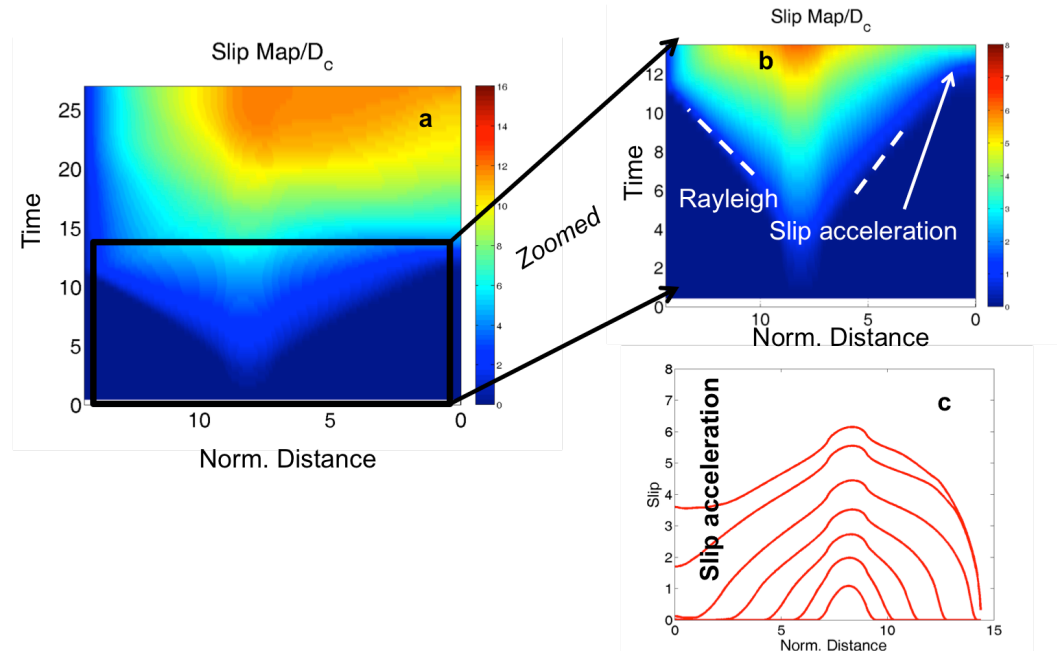


Figure 3.12 (a) slip map at different time steps as a function of distance from the free surface. In the zoom of (b) rapid acceleration to Rayleigh speed of bilateral rupture is shown as well as the final slip acceleration due to the interaction with the waves coming from the free surface. (c) Profiles of coseismic slip as a function of distance for different time steps. The interaction with free surface slightly increases the slip in the vicinity of the surface.

Differently from the case of a vertical fault, the induced normal stress perturbations has to be taken into account to fully characterize the dynamics of rupture. As shown in Figure 3.13a, the normal stress perturbation ahead the crack tip, induced by the

waves from the free surface is compressive just before the crack front reaches the surface, whereas it is extensive behind the crack tip. Figure 3.13b shows the rotational wavefield at the same time step of the blue dotted curve (Figure 3.13a) and it evidences both the interaction ahead of the crack tip and the crack front that rapidly reaches the surface. When the crack front impacts against the surface the normal stress perturbation rapidly changes its sign becoming extensive. At that point the normal stress variations coupled with the low normal traction on the shallow part produces a rapid opening over a finite length of the fault. The thick green curve in Figure 3.13a shows the evolution of the opening with time (from the surface to the discontinuity, where  $\sigma^n = -\sigma_0^n$ ) Figure 3.13c is the rotational wavefield at the same timestep of the thick green normal stress profile and it shows the break of symmetry and the larger ground motion on the hanging wall.

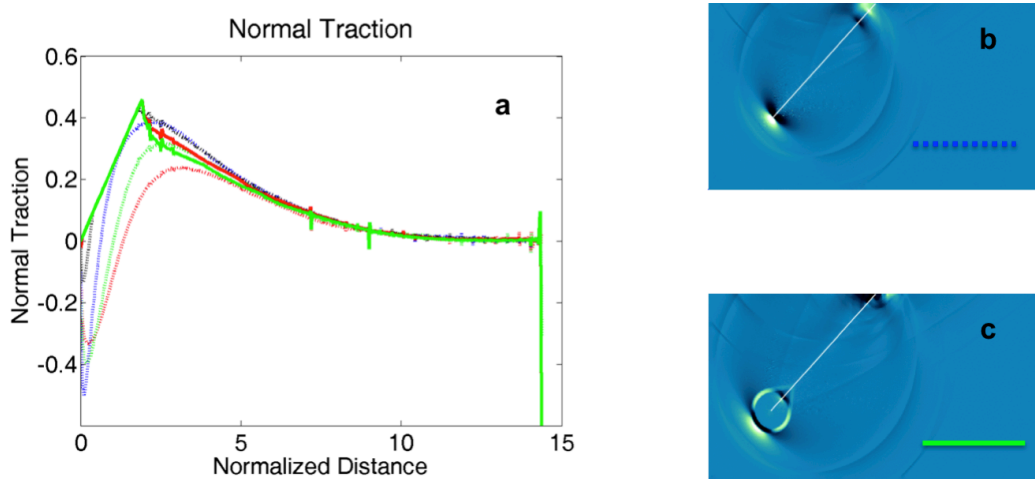


Figure 3.13 (a) Normal stress perturbations at different times steps as a function of distance from surface. The dotted colored lines show the increasing of the extensive perturbation. The thick green line shows the dynamic normal stress when the opening occurs. (b) Rotational wavefield at the same time step of the dotted blue curve in (a). (c) rotational wavefield at the same time step of the thick green curve (a).

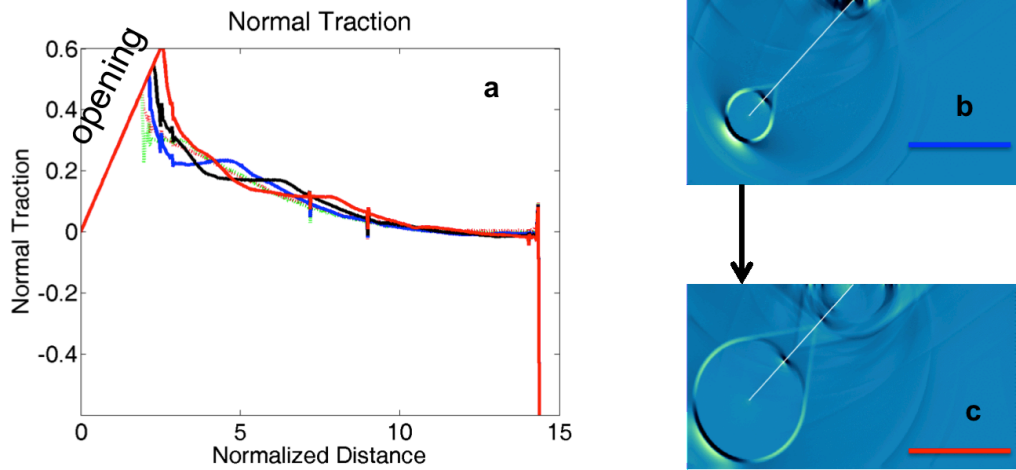


Figure 3.14 (a) Normal stress perturbations at different times steps as a function of distance from the surface after the occurrence of the opening in the shallow part.(b) Rotational wavefield at the same time step of the thick blue curve in (a). (c) Rotational wavefield at the same time step of the thick red curve curve in (a).

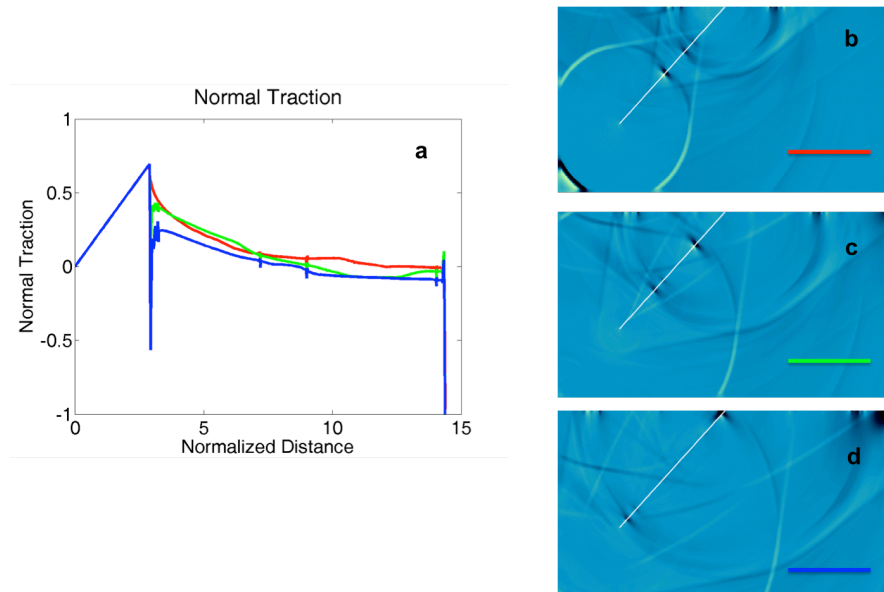


Figure 3.15 Normal stress perturbations at different times steps as a function of distance from surface. After the occurrence of the opening in the shallow part a singularity develops between the sliding and the open part of the fault (b)-(c)-(d) Rotational wavefield snapshots at the same time steps of respectively the red, green and blue curves in (a).

After the opening has occurred its size along the shallow part of the fault slowly increases with time as an effect of the interactions with the waves coming back on the hanging wall as shown in Figure 3.14a. The rotational wavefield in Figure 3.14b-c is related to the timesteps of blue and red curves in Figure 3.14a respectively and it shows how the domain of interaction increases with time as the waves interact with the crack in the shallow part of the fault.

Finally, during final phase of the rupture a singularity in normal stress emerges between the shallow part of the fault (where hanging wall and footwall behave as free surfaces) and the deep part where the rupture is still frictionally sliding (Figure 3.15a). The rotational wavefields in Figure 3.15b-c-d show the final phase of the crack they are respectively related to the blue, green and red curves in Figure 3.15a.

The singularity can be considered as a physical reliable feature for the dipping faults due to the fact that the opening point no longer changes with time and it cannot accommodate more slip.

### 3.3.3 Dipping fault with $\alpha = 10^\circ$

In this subsection a dipping fault with an angle between the fault and the free surface of  $\alpha = 10^\circ$  is taken into account (Figure 3.1c) with the initial conditions of Figure 3.2c. The dynamics of rupture can be still described through the help of the kinetic energy field at different time steps. The interaction still starts when the rupture tip lies vertically below the intersection of S-wave front and the free surface ( $\tilde{t} = 2.4$  in Figure 3.16). At that point a strong break of symmetry emerges and the ground motion on the hanging wall rapidly increases generating again a patch of large slip in the vicinity of the surface. After the beginning of interaction the reflected waves coupled with the very low threshold generate a supershear acceleration after which the rupture can rapidly reach the surface ( $\tilde{t} = 3.9$  in Figure 3.16). Then the reflected waves propagating backward interact with the fault line reaching the deepest part ( $\tilde{t} = 6.6$  in Figure 3.16). The supershear acceleration is readily evidenced in Figure 3.17 where the activation times of the slip (black dots) are shown as a function of distance from the surface (contemporary with the end of dissipation zone at the same time steps marked with the red dots). The evident discontinuity of slope marks the begins of the interaction and the acceleration of the rupture towards the surface. The inset of Figure 3.17 shows the strong fault/free surface interaction in terms of induced normal stress perturbations. Even in this case the low remote normal traction imposed in the shallow part leads to a rapid opening effect over a length included in the interaction length scale  $l$ . The green dots in Figure 3.17 show how the size of the opening area slowly increases with time.

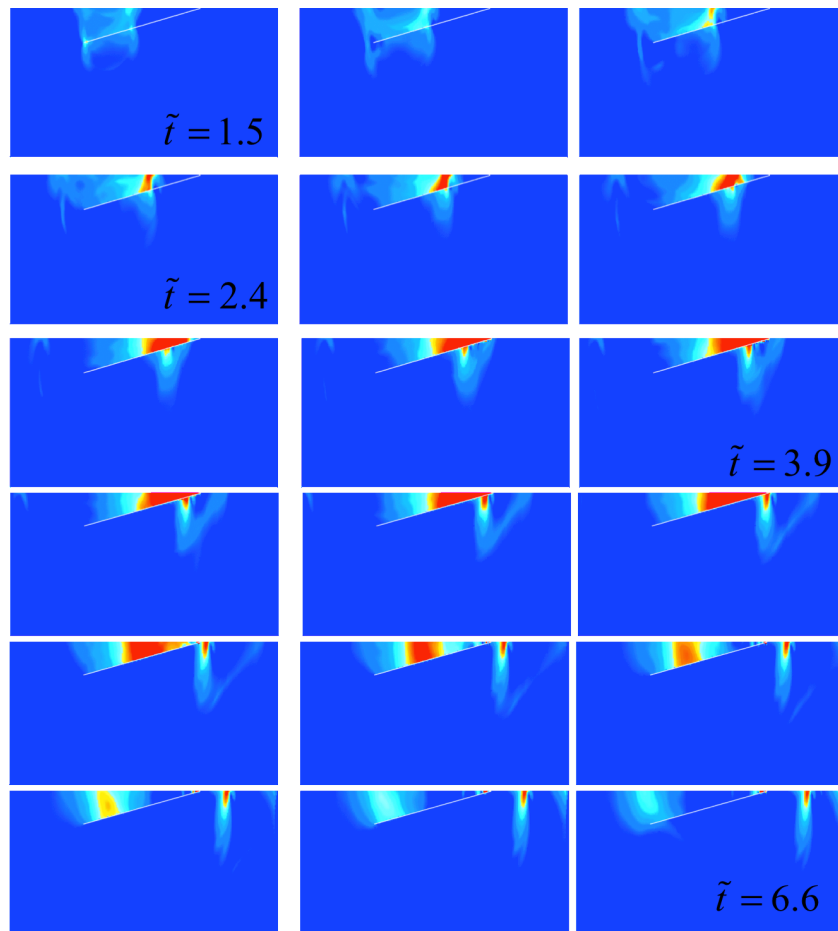


Figure 3.16 Kinetic energy field snapshots for  $\alpha = 10^\circ$ . When the shallow part of the fault starts to interact with the free surface the symmetry is broken and larger ground motion is recorded in the hanging wall respect to the footwall

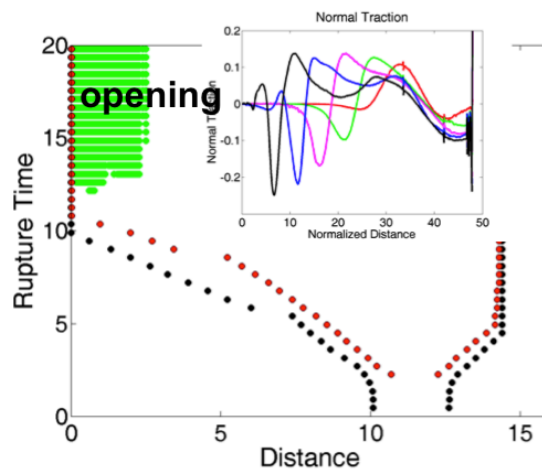


Figure 3.17 Time of activation of slip as a function of distance from free surface for  $\alpha = 10^\circ$ . Black dots are the position of crack tip whereas the red dots are the end of dissipation zone. The change of slope represents the acceleration to supershear speed. The inset shows the strong fault/surface interaction in terms of normal stress perturbations whereas the green dots mark the opening area at increasing time.

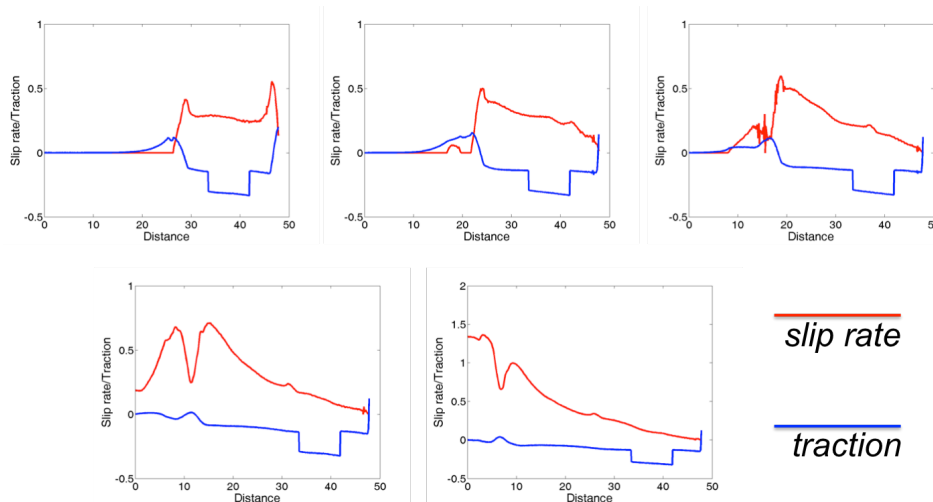


Figure 3.18 Snapshots showing the slip rate profiles (red curve) and the dynamic shear traction (blue curve) at different time steps as a function of normalized distance from the surface when  $\alpha = 10^\circ$ .

An important result can be argued from the slip rate and the traction profiles in Figure 3.18. Even in this case, when the strong interaction can allow the rupture acceleration towards supershear speeds (from third snapshot in Figure 3.18) the very low value of stress drop imposed close to the surface does not allow the dissipation zone to shrink as it does in the deepest part of the fault. Therefore the wavelength associated with the characteristic interaction length still dominates and the emitted radiation is still depleted in high-frequency. Nevertheless the coseismic slip driven by the large shallow ground motion in the hanging wall significantly increases in the shallow part Figure 3.19a and it eventually dominates the slip profiles as the fault/surface interaction occurs (Figure 3.19b).

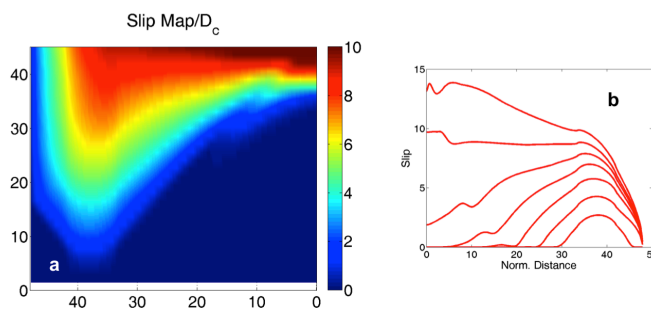


Figure 3.19 (a) slip map at different time steps as a function of distance from the free surface (b) (c) Profiles of coseismic slip as a function of distance from surface for different time steps. The slip in the shallow part dominates as the fault/surface interaction occurs.

### 3.3.4 Regularization of normal stress perturbations

In this subsection some interesting aspects emerged during this analysis and concerning the normal stress variation will be described. These features have to be further investigated to achieve a more complete understanding of the shear/normal stress coupling deriving from the free surface interaction.

In the cases described in sections 3.3.2 and 3.3.3 no regularization was used to manage the shear stress response to normal stress perturbation. The shear stress instantaneously follows the variation of normal stress; differently from the bimaterial case no oscillatory effects were evidenced and the obtained results can be considered both numerically and physically stable. This is due to the large time scales of normal stress variations induced by the free surface interactions when a flat free surface is considered.

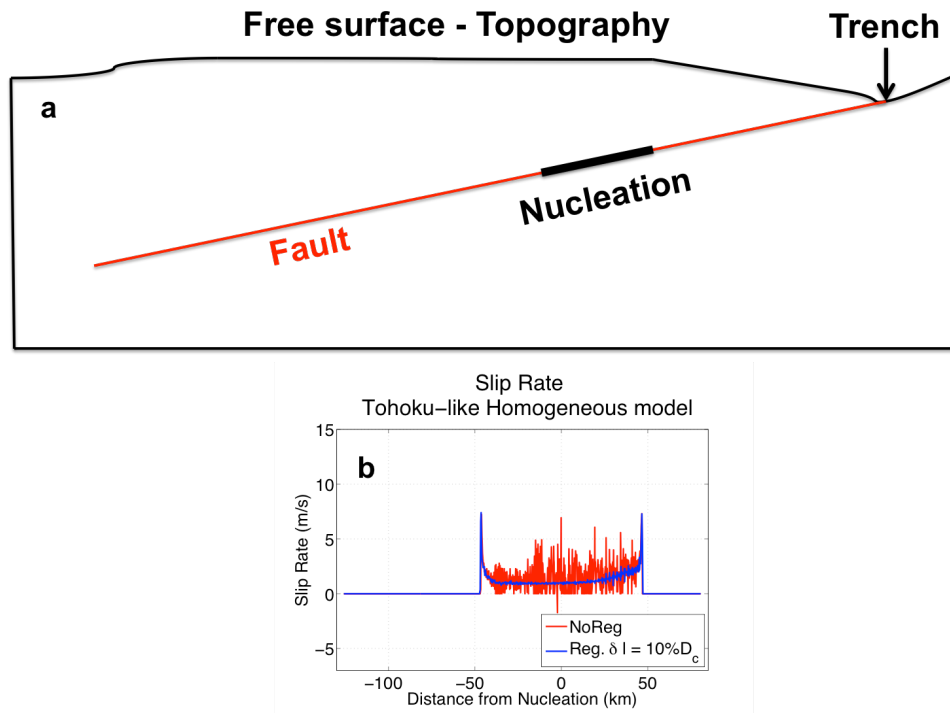


Figure 3.20 (a) Tohoku-like along dip model, with a planar fault reaching the free surface in the vicinity of the trench. A realistic topography is considered as free surface. (b) a slip rate profile comparing the results obtained for no regularized and regularized solutions ( $\delta l = 10\%D_c$ ).

Instead, when a complex topography is considered some high-frequency normal stress oscillations emerge and this can rapidly lead to unstable results if the shear stress follows instantaneously these variations. Figure 3.20a shows a simplified along-dip Tohoku-like model including a realistic topography as free surface. The fault is a

planar segment (red line in Figure 3.20a) reaching the free surface in the vicinity of the trench with an angle  $\alpha \sim 11^\circ$ . The nucleation area is marked with a thick black line over the fault and homogeneous conditions are considered with realistic elastic parameters ( $v_s = 3.0 \text{ km/s}$ ;  $v_p = 6.3 \text{ km/s}$ ;  $\rho = 2700 \text{ kg/m}^3$ ), in order to account only for the normal stress perturbations deriving from free surface interactions. Figure 3.20b shows the slip rate profiles at the same time step both when the normal stress perturbations are not regularized (red curve) and when they are regularized with a dynamic time scale ( $\delta l = 10\% D_c$ ), as described in the chapter 2. The figure clearly shows that a regularization similar to that imposed for bimaterial rupture is needed to obtain reliable solutions. In other words, the discontinuities in the topography can generate high-frequency phases interacting with the dipping fault in the vicinity of the trench and these phases can in turn produce abrupt normal stress variations. If the shear stress immediately follows these sharp variations the problem is ill-posed as well as for the bimaterial propagation.

Similar pathological effects emerged also when a flat free surface is considered but an extensive regime is imposed on the fault (Figure 3.21a). In particular the slip rate profiles show the emerging of pathological oscillatory effects around the crack tip propagating towards the surface (red curve in Figure 3.21b). If normal stress variations are regularized by analogy with the bimaterial regularization, with  $\delta l = 10\% D_c$ , the solutions no longer exhibit oscillations and they can be considered stable (blue curve in Figure 3.21b). The emerging of this instability always occurs in correspondence of a sharp local maximum in compressive perturbation around the crack tip (red arrow in Figure 3.21c). This sharp change of sign of normal stress, when a normal fault is considered, has to be investigated in more detail. It can provide an important benchmark concerning the shear/normal coupling for dipping faults and interesting clues about the necessity to consider a proper time/length scale of coupling for normal stress perturbations induced by the interaction with the free surface.

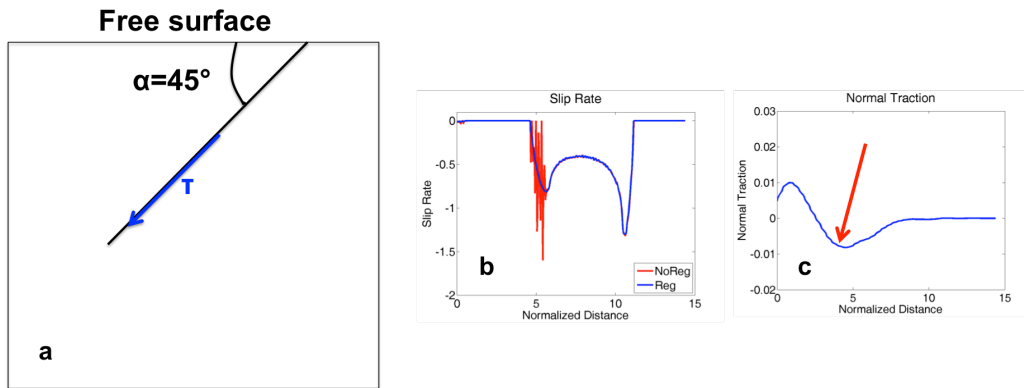


Figure 3.21 (a) Geometrical model for a normal fault (extensive regime) with  $\alpha = 45^\circ$ . (b) slip rate profile VS the normalized distance from the surface when the normal stress perturbation are not regularized (red curve) and when a dynamic time scale ( $\delta l = 10\% D_c$ ) is used (blue curve). The pathological oscillations in (b) always emerges in correspondence of the local maximum compressive normal stress close to the crack tip (red arrow in (c)).

### 3.4 Conclusions

In this chapter the coupling between normal and shear stress was investigated in the framework of a dipping fault, reaching the free surface, within a homogeneous medium.

Bidimensional numerical simulations were performed and the most interesting results can be summarized as a function of the angle between the fault and the free surface.

In particular, when a vertical fault is considered (angle  $\alpha = 90^\circ$  between the fault and the free surface) the symmetry is preserved due to the total absence of normal stress oscillations all along the fault. Once the S-wave front reaches the surface it is reflected on the fault and the wave-fault interaction only produces slip acceleration and the rapid increases of slip values in the vicinity of the free surface.

When  $\alpha < 90^\circ$  and a reverse fault is considered the symmetry is broken as an effect of normal stress perturbations and a larger ground motion is evidenced on the hanging wall; the ground motion over the upper part of the fault is then further increased by multiple reflections of the waves trapped between the fault and the surface. This break of symmetry occurs when the crack lies on the vertical below the intersection between the S-wave front and the surface, that is when the waves on the surface start to interact with the propagating crack. Therefore, this interaction is

associated with a finite length, which increases as the angle  $\alpha$  decreases. This interaction length was shown to drive the slip rate variations around the crack front in the vicinity of the surface and when low values of stress drop are considered in that area the long wavelengths associated are expected to dominate the emitted radiation. Moreover, if initial stress increasing with depth is imposed on the fault (as expected in subduction zones) the waves-fault coupling can generate rapid opening effects over a portion of the interaction length; furthermore the size of the opening area can slowly increase as the effect of the multiple reflections and a singularity develops at the boundary between the crack and the area involved in the opening. This singularity can be considered as physically reliable due to the fact that the last opening point cannot accommodate more slip, acting as an edge of frictional sliding rupture.

When small angles are considered (as expected in the vicinity of the trench in subduction zones) a further acceleration of the slip can occur leading the rupture to supershear regime. In that case very large coseismic slip are produced in the shallow part as effect of the significant break of symmetry between hanging wall and footwall. Even in this case high-frequency radiations are not produced close to the surface, because the large interaction length still dominates the slip rate profiles when low normal stress are considered.

For all models concerning a reverse fault with a flat free surface no regularization is needed for the normal stress perturbations. However when a realistic topography is introduced, e.g. referring to a homogeneous Tohoku-like model, some high-frequency normal stress variations emerge; in that case a regularization similar to that used for bimaterial normal perturbations is needed in order to achieve stable solutions.

Even if a normal fault is considered abrupt normal stress variations (generally related to sharp local maximum of compressive perturbations) generate unstable solutions and also in this case the only way to stabilize the models is to introduce a dynamic delay between the normal stress perturbations and their effect on the shear stress. Further investigation about this topic can lead to a full understanding of the shear/normal coupling during the along-dip propagation of subduction rupture where both bimaterial and surface interactions has to be taken into account.

In conclusion our numerical tools was shown to properly tackle with the main asymmetries generated by the complex shear/normal coupling expected for a subduction zones. In light of this, in the next chapter, some bidimensional along-dip

numerical models for the Tohoku earthquake will be presented, including realistic velocity fields and geometrical discontinuities.

# 4 Tohoku 2D dynamic models

## 4.1 Introduction

In the light of the results described in the previous chapters concerning the bimaterial rupture propagation and the rupture-free surface interaction, simplified bi-dimensional dynamic simulations were performed for the case study of Tohoku earthquake using the spectral element method. The event occurred on , March 11,2011, off the east coast of Japanese peninsula causing several damages and casualties in particular in the Sendai prefecture, the closest region to the hypocentre.

The moment magnitude  $M_w$  measured from teleseismic and geodetic data is  $M=9.0$  and the event generated a huge tsunami wave that swept the coast causing further damages.

Although the area was often involved by big seismic events, even in recent past (Miyagi,1978  $M_w = 7.7$ ) such event was unexpected both in terms of depth of hypocentre (shallower than the previous big events) and for the extension of fractured area which have produced the large magnitude . The event was nucleated in a crustal area of the slab where the oceanic crust sinks below the continental crust until to the continental mantle. The rupture propagated bilaterally in a small stripe of the fault plane for about  $260km$  along the dip direction, reaching the shallower part of the subduction zone close to the trench, where the huge tsunami was originated- and the event also ruptured the deep part of the plate at the boundary between the slab and the continental mantle wedge, where the above-mentioned recent events mostly nucleated. Later, the rupture extended over a large portion of subduction area (about  $500km$ ) along the strike direction.

The state of the art seismic, geodetic and mareographic measurements allowed for a rapid convergence in the description and extension of the rupture (Simons *et al.*, 2011; Ide *et al.*, 2011; Sato *et al.*, 2011; Ozawa *et al.*, 2011), which is characterized by an extremely compact region of large slip (whose value ranges between  $30$  and  $60 m$ ) extending for  $\sim 100km$  along-dip. Tracking the travel-times on local strong

motion records, several authors (Lee *et al.*, 2011; Suzuki *et al.*, 2011) inferred a rupture made of 3/4 sub events, associated with asperities in the deeper part of the seismic zone (Asano & Iwata, 2012; Kurahashi & Irikura, 2013). This aspect was also investigated in the framework of dynamic bidimensional simulations showing how the presence of deep radiators in the continental mantle part of the slab can contribute to the high-frequency feature of the emitted radiation (Huang *et al.*, 2011). Many studies (Honda *et al.*, 2011; Ishii, 2011; Meng *et al.*, 2011; Wang & Mori, 2011; Maercklin *et al.*, 2012) using back-projection or similar techniques evidenced the deep origin of high-frequency radiation, reinforcing the idea of the partitioning between deep regions of high-frequency radiation and shallow regions of large slip associated with low frequency radiation. Satriano *et al.*, (2014) studied the 2011 Tohoku megathrust rupture combining back-projection imaging of coherent high-frequency radiation source with low-frequency kinematic inversion of coseismic slip. They interpreted the broadband characteristics of this rupture as the signature of along-dip segmentation and segment interactions resulting also from plate geometry and mechanical variations along the plate boundary interface. In particular, they claimed that downdip the rupture propagated along the stiff slab-mantle interface, with moderate coseismic slip and coherent high-frequency radiation. Conversely, the rupture propagates updip along the slab-crust interface with very large coseismic slip toward the trench and no detectable high-frequency sources. In the next subsections we investigated how dynamic models can reproduce these features and how the geometry and the structure of the fault plane along the dip can drive the retrieved asymmetry. In particular we present how the introduced coupling delay for bimaterial rupture can drive the asymmetry in radiation and how the free surface interaction may contribute to produce large coseismic slip around the trench. Finally the dynamically driven features of Tohoku rupture has been used to produce modified stochastic slip distributions in order to include the site specific informations in the probabilistic slip distributions widely used as input for the generation of tsunami scenarios and the estimates of tsunami hazard.

## **4.2 Initial conditions and simulation setup**

The geometry of the fault plane and the velocity model for the North-East pacific subduction area was inferred from tomographic studies and from the location of

seismicity characterizing the area in the recent past. These informations were obtained from the works of Takahashi *et al.*, (2004), Ludwig *et al.*, (1971) and Yamada & Iwata (2005) together with some tomographic maps provided by the Earthquakes Research Promotion of Japanese government (as the “Velocity structure model of the Headquarters for Earthquakes Research Promotion” and “The Long-Period Ground Motion Hazard Maps 2009”). To produce bi-dimensional dynamic simulations of Tohoku earthquake a stripe of the fault plane was extracted with fixed latitude given by the location of the main event ( $38.1035^{\circ}N, 142.8610^{\circ}W$ ; JMA hypocenter). The initial model extended for  $\sim 260km$  along dip ( $\sim 150km$  westward toward the coast and  $\sim 110km$  eastward toward the trench) and for a depth of  $\sim 70km$ . Since the geometry and structure are well-constrained they were used to produce the input mesh for all simulations; the Figure 4.1 shows an example of the geometry and structure of the considered area from Takahashi *et al.* (2004), while the Figure 4.2 shows the discretization of the domain for our dynamic simulations. The colours represent the different elastic properties of the layers, whereas the red line is the fault. The black layers along three of the four edges represent the absorbing layers (PML), whereas the top edge is considered as a free surface. The blue line represents the coastline whereas the black portion of the fault line is the nucleation patch, where the nucleation is addressed as explained for numerical simulations in Chapters 2 and 3.

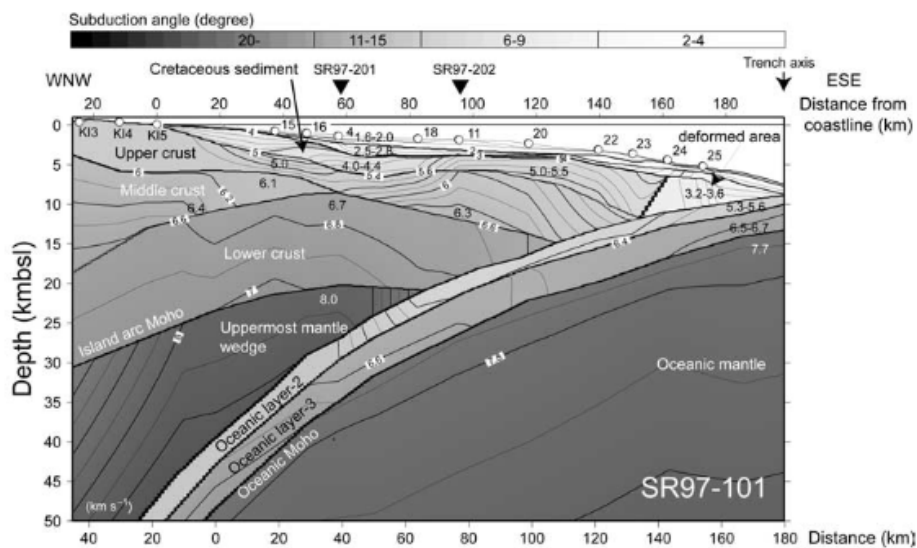


Figure 4.1 Geometry and structure of an along-dip stripe of the fault plane in the area of Tohoku earthquake (Takahashi *et al.*, 2004)

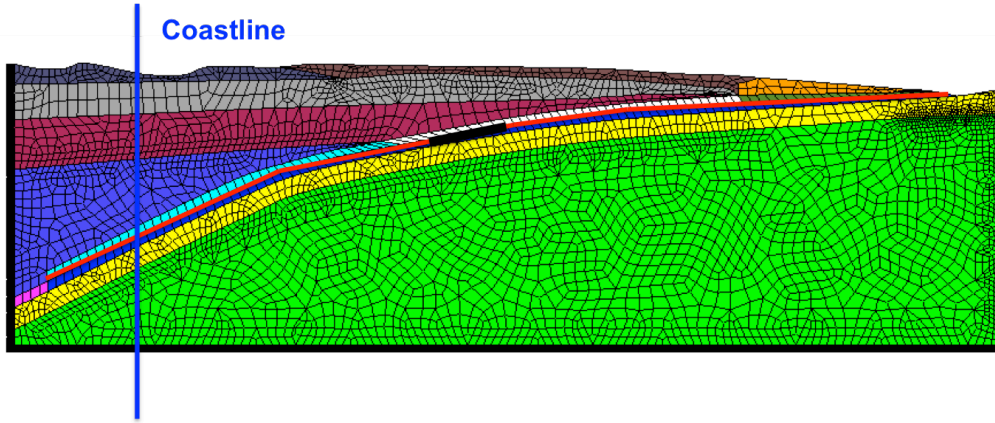


Figure 4.2 Mesh for spectral element method used for the case study of Tohoku earthquake. Red line is the fault; blue line is the coast line and the black line is the part of the fault where the rupture is initiated

Below the fault a thin oceanic layer is considered and it extends all along the fault length; according to the tomographic studies the following average values are considered to characterize that layer  $C_s = 2.9 \text{ km/s}$  ;  $C_p = 5.0 \text{ km/s}$  and  $\rho = 2400 \text{ kg/m}^3$  (blue and magenta elements just below the fault in Figure 4.2). Below that, a stiffer oceanic layer is located (yellow elements in Figure 4.2) with  $C_s = 4.0 \text{ km/s}$  ,  $C_p = 6.8 \text{ km/s}$  and  $\rho = 2900 \text{ kg/m}^3$  . Finally below it we have the Oceanic mantle (light green elements) characterized by  $C_s = 4.7 \text{ km/s}$  ,  $C_p = 8.0 \text{ km/s}$  ,  $\rho = 3200 \text{ kg/m}^3$  .

Above the fault, on the west side, the continental mantle wedge is located (blue and light blue elements) and it is characterized by the following elastic parameters:  $C_s = 4.5 \text{ km/s}$  ,  $C_p = 7.5 \text{ km/s}$  ,  $\rho = 3200 \text{ kg/m}^3$  . Above the middle part of the slab, where the nucleation is located the lower crust layer (white and red element) is characterized by  $C_s = 3.8 \text{ km/s}$  ,  $C_p = 6.4 \text{ km/s}$  ,  $\rho = 2800 \text{ kg/m}^3$  , whereas the shallow part of the fault as well as the upper part of the crust (dark green, orange and brown elements) had  $C_s = 2.9 \text{ km/s}$  ,  $C_p = 5.0 \text{ km/s}$  ,  $\rho = 2600 \text{ kg/m}^3$  . In some simulations the orange and dark green elements are used to mimic the presence of an accretionary prism in order to study the influence of a low velocity layer in the free surface interaction in the vicinity of the trench. Finally the purple and grey elements represent

two landward portions of the continental crust and they were respectively characterized by the following elastic parameters:

$$C_s = 3.4 \text{ km/s}, C_p = 5.8 \text{ km/s}, \rho = 2700 \text{ kg/m}^3 ; C_s = 3.2 \text{ km/s}, C_p = 5.5 \text{ km/s}, \rho = 2650 \text{ kg/m}^3 .$$

From Figure 4.1 and 4.2 the fault slope is well-constrained by tomography and historical seismicity and it varies from an almost horizontal trench ( $\sim 2^\circ$ ) to about  $25^\circ$  in the deepest part below the mantle wedge.

No water layer is considered above the top surface of the investigation domain. It was shown that this layer has a negligible effect on the rupture propagation and final kinematic fields (Kozdon & Dunham, 2013).

All the simulations were performed using a linear slip weakening law with a critical slip distance  $D_c = 1 \text{ m}$ .

Unless otherwise noted a dynamic time scale is used to regularize the shear stress response to the normal traction perturbation induced by the fact that the Tohoku fault behaves as a bimaterial interface. Nevertheless a comparison between the results obtained for different regularizations will be later explicitly reported.

The other initial parameters (the initial conditions of shear and normal stress and the friction conditions) are arbitrary and their variability is used to generate different models. We hence studied such models that approach as much as possible to the general observations derived by source studies.

### 4.3 Uniform regional stress condition

The first “Tohoku” model was obtained considering a uniform regional stress condition for all the fault. In particular, studying the stress field obtained in the Tohoku area, before March 2011, from inversion of focal mechanisms it was shown that the maximum compressive stress  $\sigma_1$  is oriented pretty horizontally. In this configuration the stress  $\sigma_3$  represents the lithostatic load. These initial conditions are schematically represented in Figure 4.3 with the most important discontinuities: the black line is the fault; the red one is the boundary of the continental wedge, while the yellow line represents the topography. Considering an average stress drop  $\Delta\tau$  of  $\sim 10 \text{ MPa}$  and arbitrarily fixing the static and dynamic coefficients of friction as  $\mu_s = 0.6$  and  $\mu_d = 0.2$  we get  $\sigma_1 = 244 \text{ MPa}$  and  $\sigma_3 = 91 \text{ MPa}$ . However this choice

on the direction of principle stresses implies a tangential stress vanishing along the horizontal direction. Defining the local stress drop as:

$$\Delta\tau(r, t_0) = \tau_0(r) - \mu_d(r) |\sigma_0^n(r)| \quad (4.1)$$

with  $r$  distance from the hypocentre and  $t_0$  initial time, this leads to a negative stress drop in the vicinity of the trench, while the stress drop in the deepest part is larger than zero and it increases until to  $\sim 35MPa$  (see Figure 4.4).

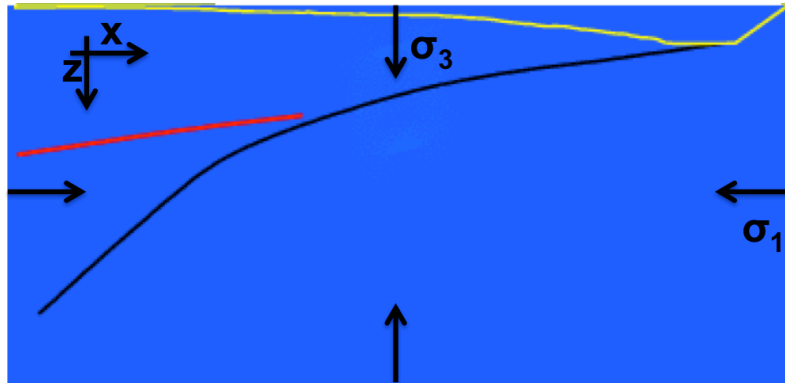


Figure 4.3 Direction of principle stresses over the investigation domain ( $\sigma_1 > \sigma_3$ ). The main discontinuities are considered: the black line is the fault, the red line is the boundary of the continental mantle and the yellow line represents the topography.

The Figure 4.5 shows the slip map as a function of the distance from nucleation and time; the negative distances represent the downdip propagation, whereas the positive distances indicate the trenchward advancing of the rupture. The maximum slip is located in the vicinity of the hypocentre with a very large value ( $\sim 120m$ ) due to the very low value of the dynamic level with respect to the failure threshold. Propagating updip the rupture stops after a while as the effect of the entrance in the area where the stress drop is negative (red ellipse is Figure 4.5). Nevertheless the rupture can restart as the effect of interaction with the free surface that contributes to decrease the actual local value of the normal stress.

Figure 4.6 shows the kinetic energy field associated with propagating rupture at three different time steps. In particular in Figure 4.6a, for timestep  $t = 15s$ , the rupture is propagating, but after a while, at  $t = 35s$  the rupture stops as the effect of entrance in the area where the stress drop is negative (Figure 4.6b).

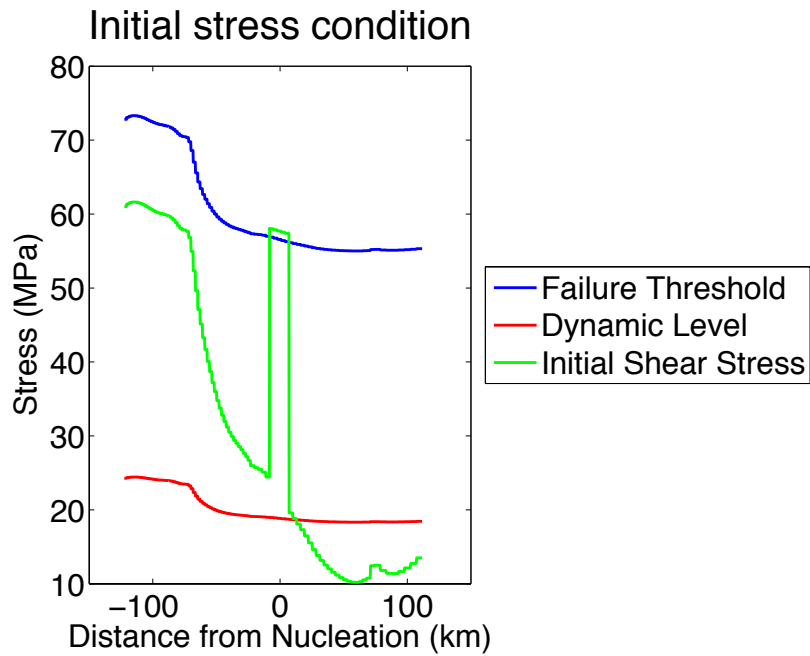


Figure 4.4 Initial stress condition when a regional uniform remote stress is defined when the maximum compressive stress is directed horizontally

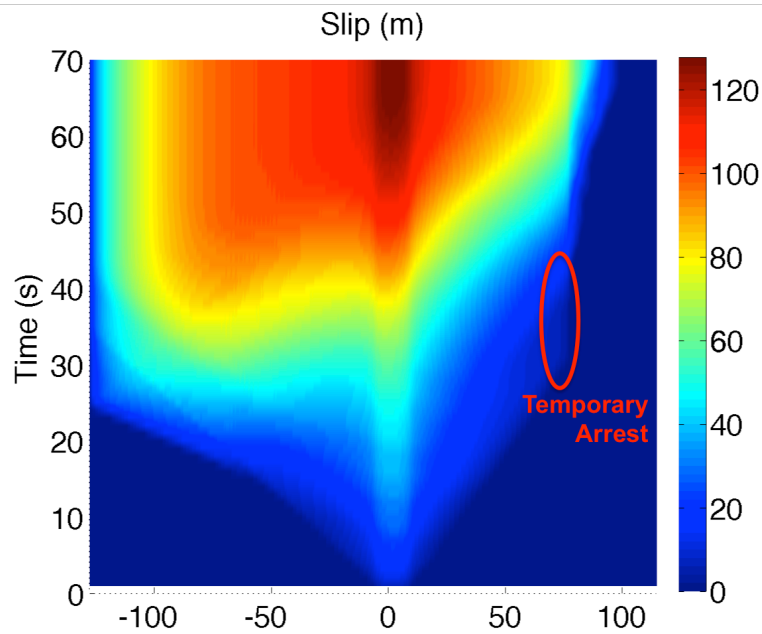


Figure 4.5 Slip map as a function of distance from nucleation and time, obtained for a regional uniform remote stress with the maximum principal stress oriented horizontally

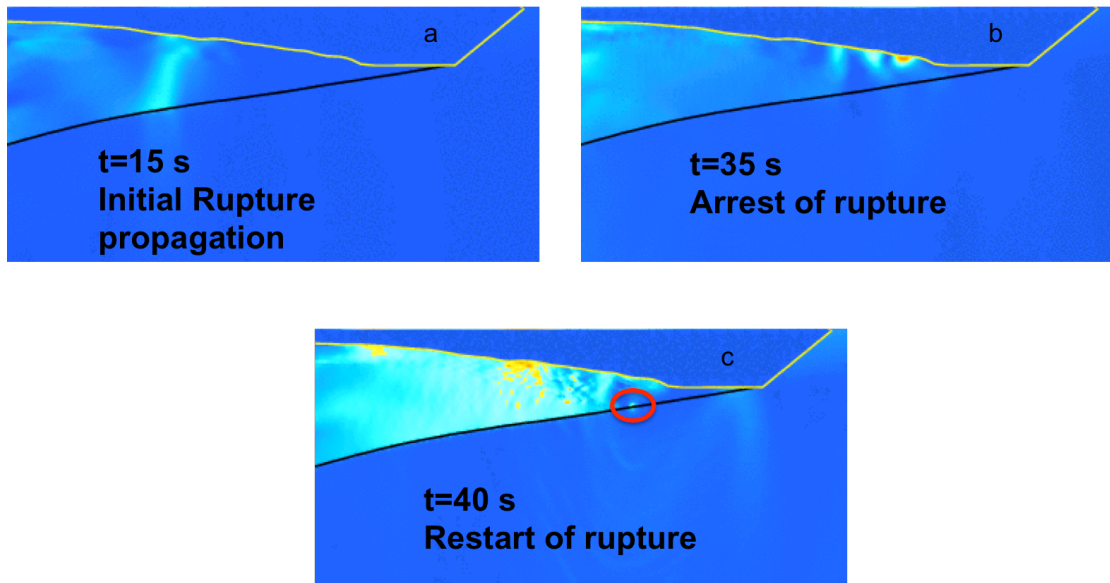


Figure 4.6 Kinetic energy field in the vicinity of the trench at different timesteps: (a) initial propagation of the rupture; (b) arrest of the rupture as the effect of the entrance in the area where the stress drop is negative; (c) The rupture restarts (red circle) boosted by the interaction with waves reflected by the free surface.

Finally in Figure 4.6c the restarting of rupture at  $t = 45$  s is evidenced with a red circle as well as the interaction of the waves propagating close to the surface in the vicinity of the trench.

To conclude the analysis of this Tohoku model Figure 4.7 shows the time of slip activation as a function of distance from the nucleation. The red dashed line is the boundary between the crustal area of the slab and the continental mantle wedge, whereas the blue dashed line is the boundary between the lower crust and the upper crust close the trench. From this figure the average rupture speed can be inferred for each region along the fault. From this point of view, already in the first part of propagation, where the rupture propagates bilaterally in the lower part of crustal slab, an asymmetry in rupture speed can be evidenced with the rupture faster downward along the favoured direction in the sense of a bimaterial propagation (the more compliant medium is the oceanic layer below the fault). Moreover the rupture can accelerate also due to the entrance in the mantle, where the contrast of impedance significantly increases. This strongest acceleration further boosted by the change of slope and the increasing of stress drop occurring at the geometrical discontinuity within the continental mantle wedge leads the rupture velocity towards the P-wave

speed in the stiffer material producing the Mach-cone typical of the supershear regime as evidenced by the kinetic energy field at  $t = 20s$  in Figure 4.8. Upward, before the stopping phase, the rupture speed is pretty constant ( $2.6km/s$ ), and slower than the Rayleigh wave speed in the two blocks below the trench.

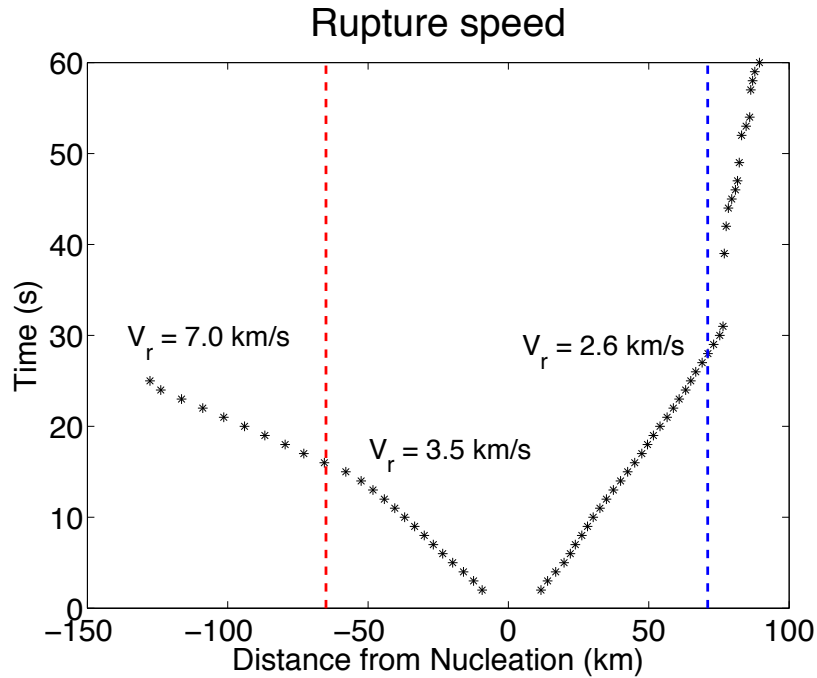


Figure 4.7 The time of activation of slip as a function of distance from nucleation. From this picture the average rupture speeds can be inferred for each region. Blue and red dashed lines represent the boundary between regions with different elastic properties

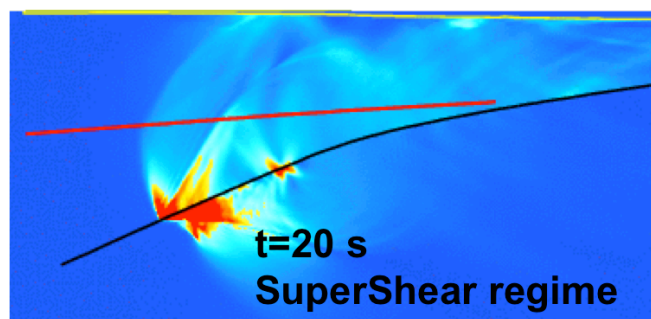


Figure 4.8 Kinetic energy field for downward propagation. The geometrical discontinuity within the mantle wedge generates a strong acceleration of the rupture until a supershear regime.

#### 4.4 Normal stress increasing with depth

Since source inversions for Tohoku earthquake never evidenced the emerging of supershear propagation, the dynamic level of friction was increased to  $\mu_d = 0.4$  or  $\mu_d = 0.5$  in order to decrease the stress drop in the deepest part of the mantle part of the slab. Moreover in order to model the trenchward propagation, preventing the arrest and the restarting of the rupture, the stress initial conditions have to be derived from a coupling between the regional stress and some considerations about lithostatic loading and pore pressure.

A reasonable hypothesis is to consider a normal stress increasing with depth as effect of increasing lithostatic load with depth and increasing pore pressure in the shallow part. The total normal stress acting on the fault can be considered as deriving from both contributions, that is:

$$\Delta\sigma_{tot}^n = \Delta\sigma^n - p \quad (4.2)$$

with  $\Delta\sigma^n$  lithostatic load and  $p$  pore pressure contribution. For the shallower part  $p$  can be reasonably considered as the hydrostatic pressure, giving a total  $\Delta\sigma_{tot}^n \sim 10MPa$  while at higher depth the variation of pore pressure follows the increase of lithostatic rather than the hydrostatic load giving a pretty constant total normal stress  $\sim 100MPa$ . (Huang *et al.*, 2012). Therefore, in our models, the normal stress changes accordingly to the shear stress expected from the regional remote stress in order to have everywhere a positive stress drop. In this way when  $\mu_d = 0.4$  we have an average stress drop  $\Delta\tau \approx 5MPa$ , whereas for  $\mu_d = 0.5$   $\Delta\tau \approx 1MPa$ . The described initial conditions are shown in Figure 4.9a-b respectively for the two values of the dynamic friction coefficient. It is worth noting that in both cases the stress drops trenchward are similar whereas for  $\mu_d = 0.4$  the stress drop in deepest part is significantly higher.

This still leads to the emerging of a supershear propagation at the geometrical discontinuity within the mantle and therefore the results presented here are only related to the case  $\mu_d = 0.5$ .

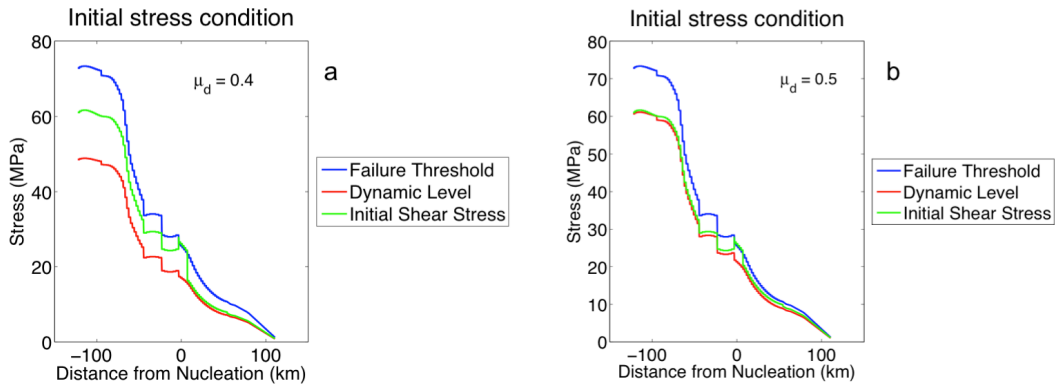


Figure 4.9 Initial stress conditions for  $\mu_d = 0.4$  (a) and  $\mu_d = 0.5$  (b) when a normal stress increasing with depth is taken into account.

Figure 4.10 shows the slip map as a function of the distance from nucleation area and time. In spite of the low values of stress drop the rupture proceeds very fast trenchward due to the interaction of the fault plane with the waves reflected from the free surface and two patches of slip are evidenced in the vicinity of the trench: the former closer to the nucleation is larger and the slip values ranges from 15 to 30m . The latter is a very thin region nearby the trench with slip  $\delta u \sim 30m$  . Elsewhere, downward from the nucleation, the coseismic slip  $\delta u \leq 10m$  .

Figure 4.11 shows the time of slip activation as a function of distance from nucleation, the blue and red dashed lines represent the boundary between materials with different elastic properties, whereas the green dashed line marks the geometrical discontinuity within the mantle wedge. Upward, after a short slow propagation, the rupture rapidly accelerates until to the generalized Rayleigh wave speed for the bimaterial interface, which separates the two sides of the fault. This rapid acceleration is boosted by the interaction with the waves reflected by the free surface. The downward propagation is slower, but two acceleration phases are visible during the dynamic propagation: the former is due to the entrance in the mantle, where the bimaterial contrast, between the two sides, significantly increases and the average rupture speed goes from  $\sim 0.9km/s$  to  $\sim 1.9km/s$  . Later, the geometrical discontinuity further accelerates the rupture, bringing it to an average velocity is  $\sim 2.2km/s$  .

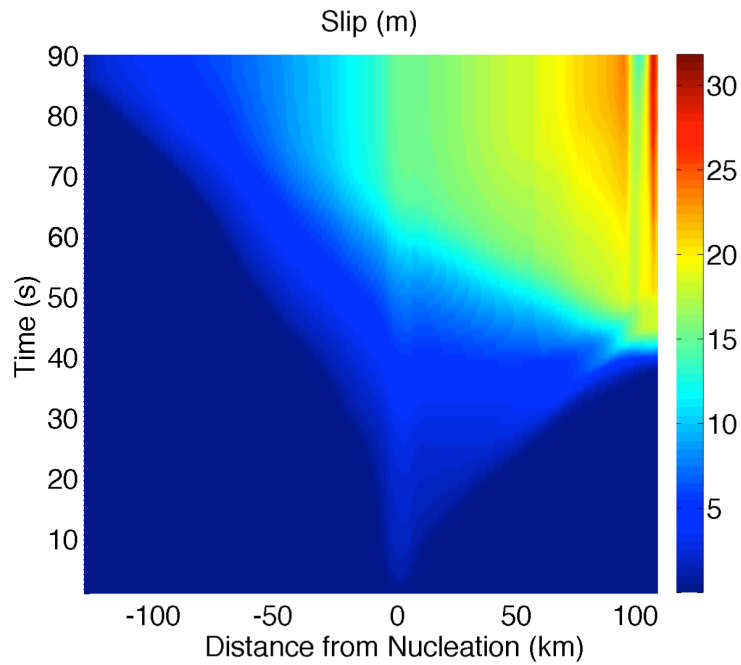


Figure 4.10 Slip map as a function of distance from nucleation and time for the case  $\mu_d = 0.5$  when the initial conditions in Figure 4.9b are taken into account

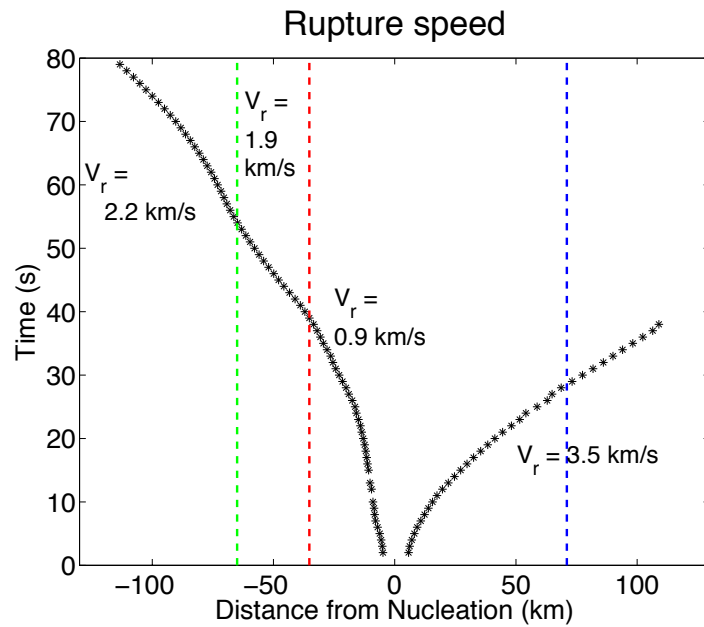


Figure 4.11 The time of activation of slip as a function of distance from nucleation. From this picture the average rupture speeds can be inferred for each region of the propagation area. Blue and red dashed lines represent the boundary between regions with different elastic properties, whereas the green dashed line marks the geometrical discontinuity within the mantle

#### 4.4.1 Accretionary prism

At the model described in the previous section a low velocity layer is added above the fault in the vicinity of the trench to mimic the presence of the accretionary prism. To the orange and dark green elements in Figure 4.2 I assigned the following elastic parameters:  $C_s = 1.4 \text{ km/s}$ ,  $C_p = 2.6 \text{ km/s}$ ,  $\rho = 1600 \text{ kg/m}^3$  making the shallower part of the fault significantly more compliant than in the previous cases.

The presence of a more compliant layer just above the fault in the vicinity of the trench changes the influence of reflected waves over the shallower part of the fault and we aim to characterize the influence of this layer on the characteristics of the rupture.

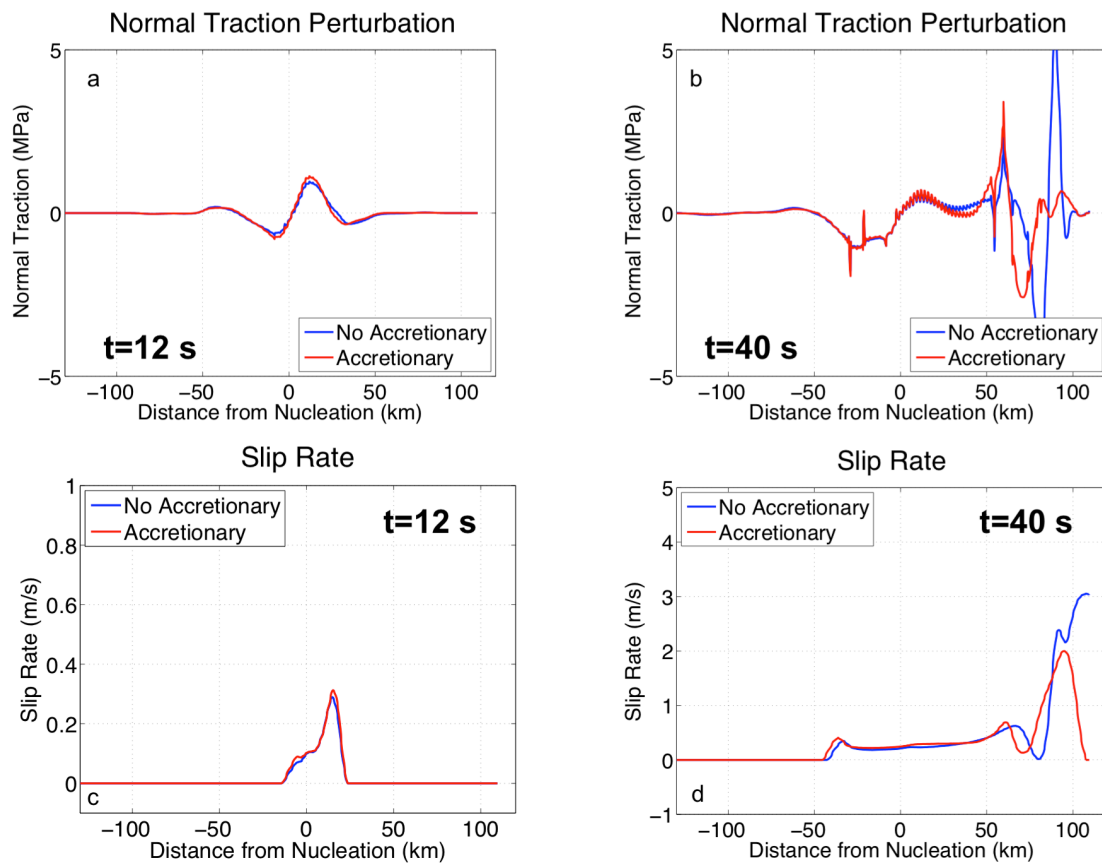


Figure 4.12 Normal stress perturbations as a function of distance from nucleation when the accretionary prism either is or is not taken into account at two different instants ( $t = 12 \text{ s}$  (a) and  $t = 40 \text{ s}$  (b)). At the same time the slip rate profiles are plotted in figure (c) and (d)

Figure 4.12 shows the perturbation of normal traction and the slip rate profiles as a function of distance from nucleation at  $t = 12 \text{ s}$  and  $t = 40 \text{ s}$  both when the accretionary prism is considered and when it is not included in the model. As shown in Figure 4.12a, before the beginning of fault/surface interaction the normal stress

perturbations, only derived by the bimaterial effect and the geometrical effects, are pretty similar (Figure 4.12a) as well as the slip rate profiles (Figure 4.12c). Later, when the interaction with free surface becomes dominant for the rupture dynamics, the presence of a low-velocity layer produces less sharp normal stress perturbations (Figure 4.12b) which in turn implies a slower propagation of the rupture and maximum decrease in the amplitude of the slip rate (Figure 4.12d).

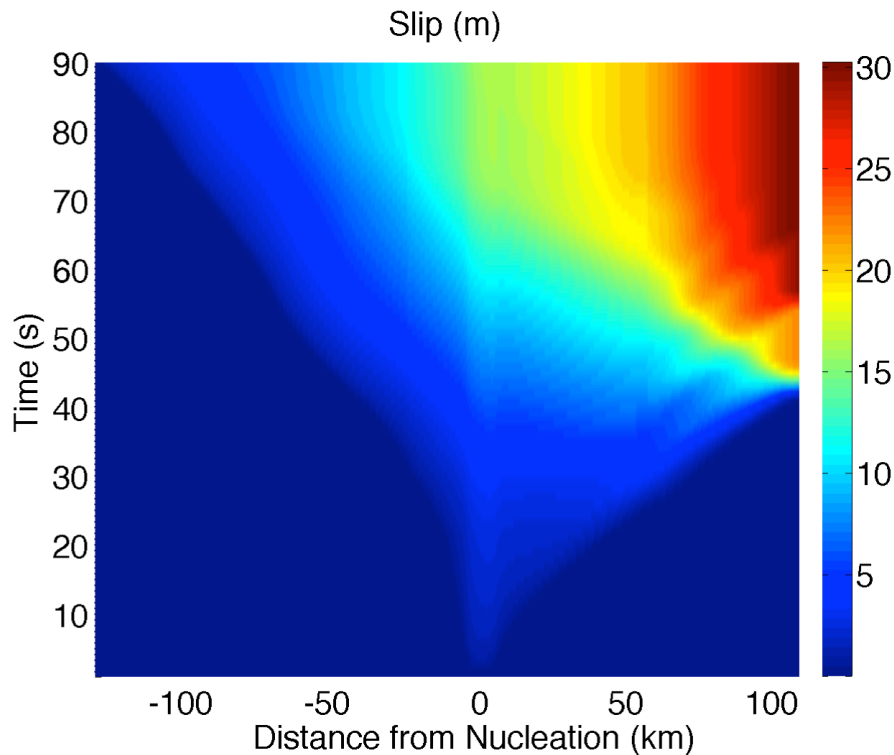


Figure 4.13 Slip map as a function of distance from nucleation and time when the accretionary slip is considered above the shallower part of the fault

The most important difference introduced by the accretionary prism is in the slip map, shown in Figure 4.13 as a function of the distance from nucleation and time . In this case a very large compact patch of slip is obtained in the vicinity of the trench with the maximum slip  $\delta u \sim 30m$  at the trench.

In conclusion the whole dynamics of the rupture can be summarized analysing the snapshots, which show the kinetic energy field at different times during propagation (Figure 4.14).

Figure 4.14a shows the nucleation phase occurring in a crustal area of the slab at a depth of  $\sim 30km$  as known from JMA location. The rupture propagates upward with larger energy emission due to the interaction with the waves reflected from the free

surface, which also significantly accelerate the rupture as the normal stress is reduced on the fault (Figure 4.14b). The initially slow propagation downwards is accelerated first at the entrance in the mantle wedge as the effect of the increase of the bimaterial contrast between the two sides of the interface (Figure 4.14c). Then, the rupture further accelerates as the effect of a geometrical variation at the kink within the mantle wedge.

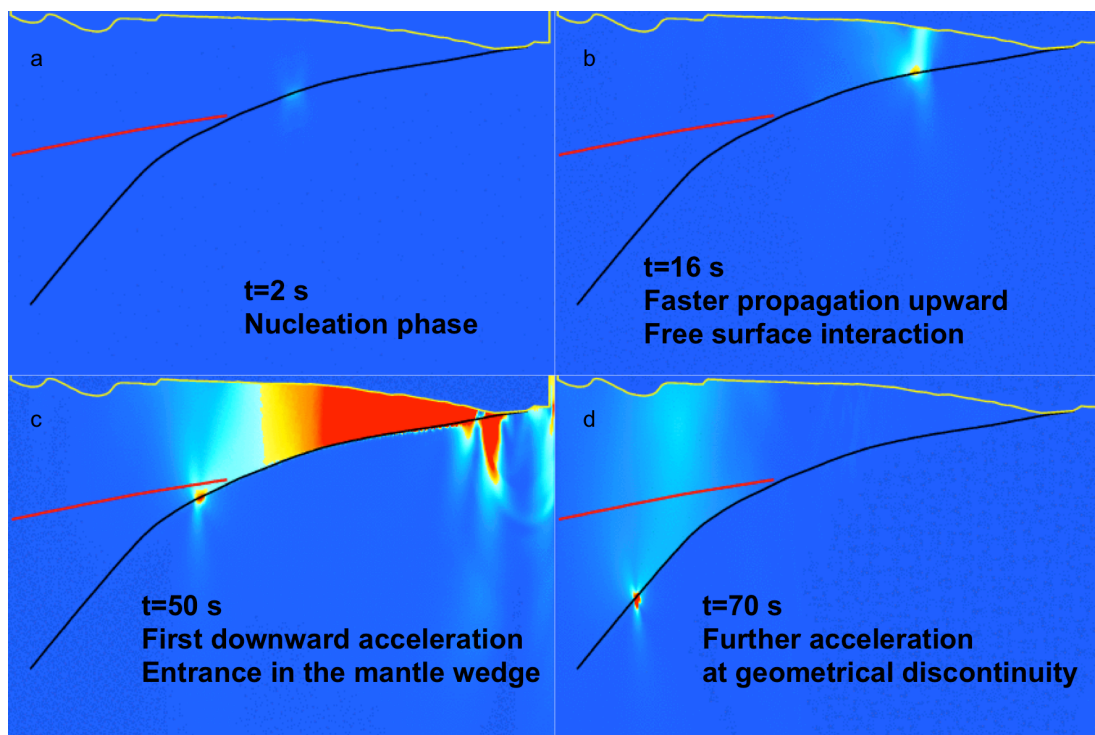


Figure 4.14 Snapshots of kinetic energy field: (a) nucleation phase ( $t = 2s$ ), (b) faster acceleration upward and interaction with free surface ( $t = 16s$ ), (c) first downward acceleration phase at the entrance in the mantle wedge ( $t = 50s$ ), (d) further downward acceleration at the geometrical discontinuity.

## 4.5 Bimaterial regularization for Tohoku models

In all simulations presented so far the fault is a bimaterial interface. Moreover along the various segments of the fault the bimaterial features vary up to a very large contrast at the interface between the oceanic layer and the continental mantle wedge. All the results are obtained using a dynamic time scale to delay the shear stress response with respect to the abrupt normal stress perturbations induced by the

propagation along the Tohoku fault. By analogy with the analysis presented in Chapter 2 I imposed a  $\delta l = 10\%D_c$  ; this ensures that the solutions are physically convergent at least up to the acceleration of the rupture at the expected asymptotic speed.

Now the results presented in the previous sections will be compared with the solutions deriving from simulations performed with different time scales and mechanisms to regularize the bimaterial problem.

First a comparison with a different dynamic time scale is presented, choosing a  $\delta l = 5\%D_c$  . Figure 4.15 shows the slip rate profiles in the area of continental mantle wedge at time  $t = 60s$  where the strongest deep accelerations are expected due to geometrical and structural discontinuities. Although the solutions within the crack appear noisier for  $\delta l = 5\%D_c$  , the two results are convergent around the crack front both in terms of maximum amplitude of slip rate and position of crack front. The presence of the oscillations is mainly related to the grid size, which is not able to catch the space scale of the coupling.

Now the results obtained for  $\delta l = 10\%D_c$  are compared with a constant time scale regularization and two value of  $t_c$ :  $t_c = 1s$  and  $t_c = 0.1s$  . We can note that the two chosen constant time scales can be obtained from the classical Prakash & Clifton regularization, considering  $\delta l = 10\%D_c = 0.1m$  and imposing as reference slip rate values  $\delta v^* = 0.1m/s$  and  $1m/s$  respectively.

Figure 4.16 shows that for  $t_c = 1s$  , after a while, during the acceleration within mantle, the constant time scale solutions are delayed with respect to those obtained from the dynamic time scale in terms of crack tip position. Furthermore the maximum amplitude of the slip rate for dynamic time scale is larger.

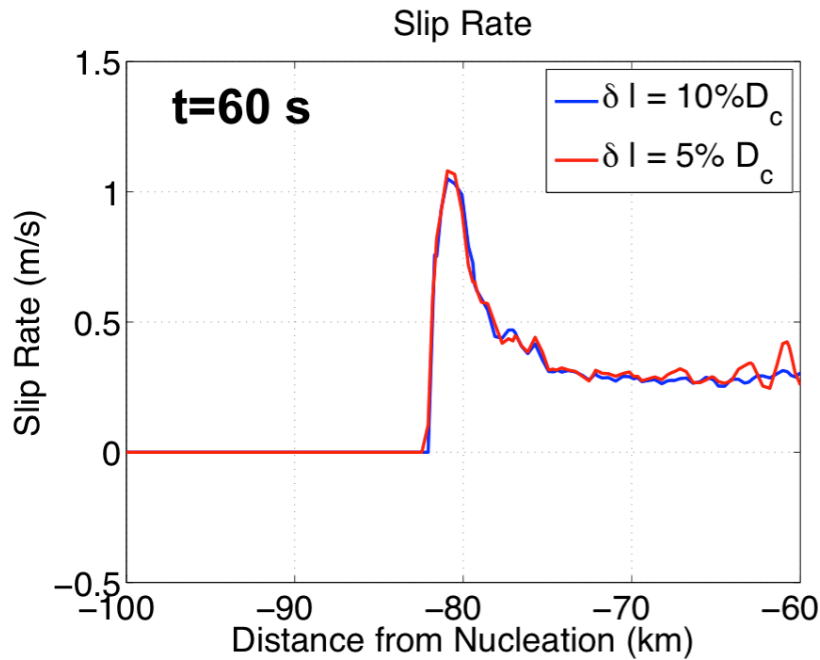


Figure 4.15 Slip rate profile for downward propagation at time  $t = 60s$ . Comparison between two dynamic time scales obtained with different relaxation slip parameter  $\delta l$

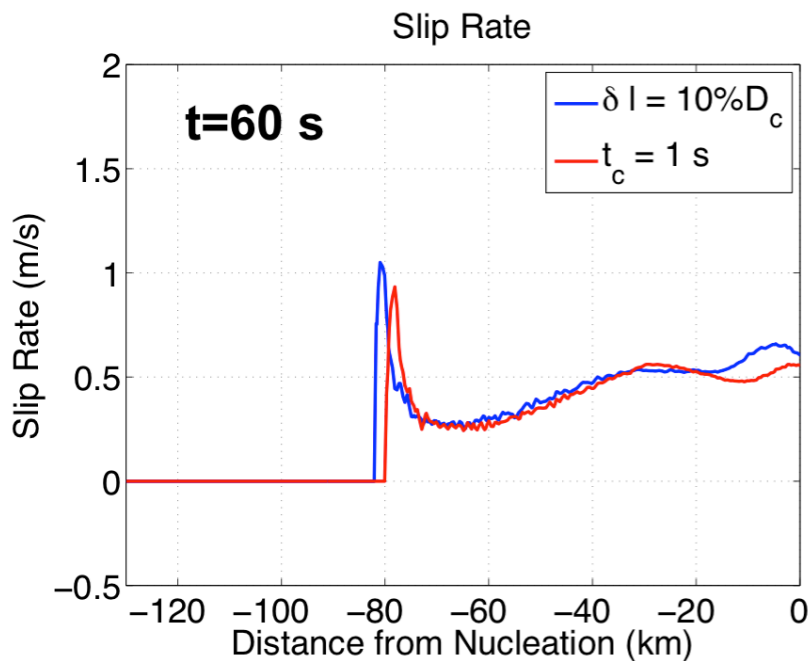


Figure 4.16 Slip rate profiles during downward propagation at  $t = 60s$ , comparison between the dynamic time scale of relaxation and the constant time scale with  $t_c = 1s$

Figure 4.17a shows that when a shorter time scale is used ( $t_c = 0.1s$ ) the solutions can be considered convergent for longer distance propagation (Figure 4.17a). Nevertheless, when the slip rate rapidly increases the two solutions differ more and more and the slip velocity deriving from constant time scale is delayed in terms of

position of crack front and less sharp in terms of maximum amplitude in the vicinity of the crack front (Figure 4.17b). Moreover within the crack, where the slip rate is very low ( $\delta v < 0.5 m/s$ ), the slip rate shows spurious oscillations due to the fastest relaxation scale introduced by the constant time scale.

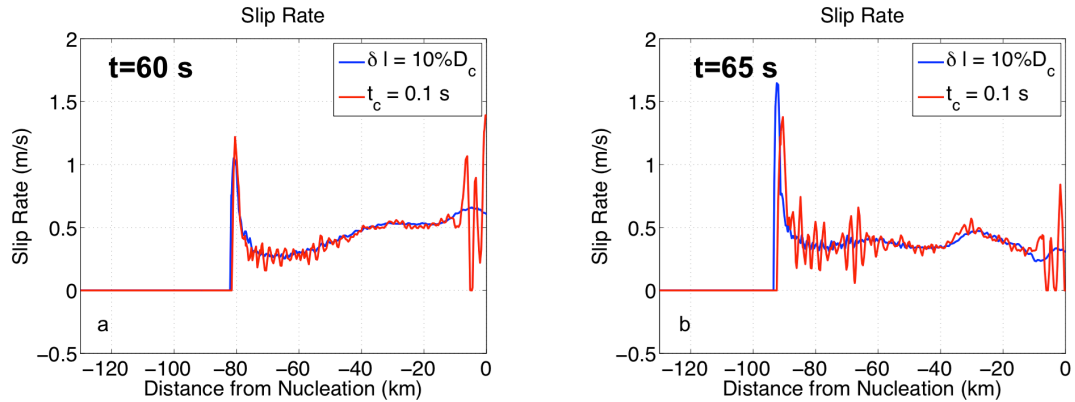


Figure 4.17 Comparison of slip rate for dynamic time scale and constant time scale ( $t_c = 0.1s$ ) at the same time of Figure 4.16 (a) and few seconds later. The constant time scale still provides delayed acceleration and it also shows spurious oscillations within the crack.

Finally smaller constant time scales were considered:  $t_c = 0.05s$  ( $\delta l = 10\%D_c = 0.1m$  and  $\delta v^* = 2m/s$ ) and  $t_c = 0.017s$  ( $\delta l = 10\%D_c = 0.1m$  and  $\delta v^* = 6m/s$ ). The results of these simulations were compared with the results obtained for dynamic time scale in terms of emitted radiation .

Two receivers are considered, one around the trench and one on the coast in the vicinity of the station MYG011, that is the closest station to the hypocentre of the Kik-NET, which recorded the Tohoku event. The position of both receivers is indicated in Figure 4.18.

Figure 4.19a shows the synthetic seismograms recorded at MYG011 filtered between 0.2 and 2 Hz for the dynamic time scale and the two considered constant time scales. Those velocity traces show that the dynamic time scale presents only one high-frequency packet: this signal recorded at  $t \sim 90s$  comes from the strong acceleration of the rupture at the geometrical discontinuity within the mantle. Conversely, the traces, obtained for the two constant time scales, contain much more energy in the considered frequency range and these high frequency signals come from bursts all along the fault plane (also in the vicinity of the trench). Figure 4.19a

showing the synthetic velocigrams recorded in the vicinity of the trench in the same frequency range, exhibits a similar pattern for the three considered simulations and the high-frequency content of synthetic seismograms increases as the regularization constant time scale decreases.

Figure 4.20 shows the synthetic velocigrams recorded at a station located in the vicinity of the trench in a lower frequency range ( $0.005 - 0.1 Hz$ ). This frequency range is less influenced by the chosen regularization and the frequency content of the radiation emitted in the shallower part is several orders of magnitude lower than the radiation emitted in the deepest part.

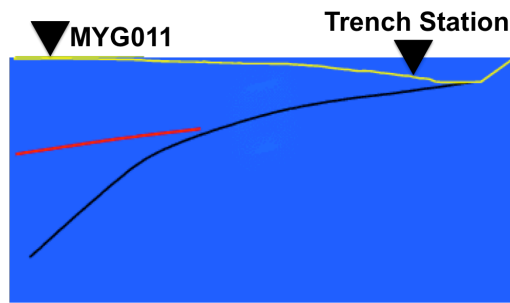


Figure 4.18 Position of the stations used to produce the synthetic seismograms

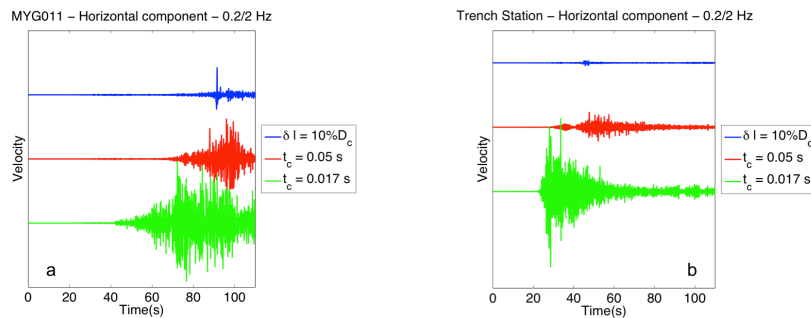


Figure 4.19 Synthetic velocigrams (in the frequency range  $0.2 - 2 Hz$ ) recorded at the stations indicated in Figure 4.18 when a regularization dynamic time scale is used (blue) and for two different regularization constant time scales (red and green). In both figures the horizontal components are plotted

Trench Station – Horizontal component – 0.005/0.1 Hz

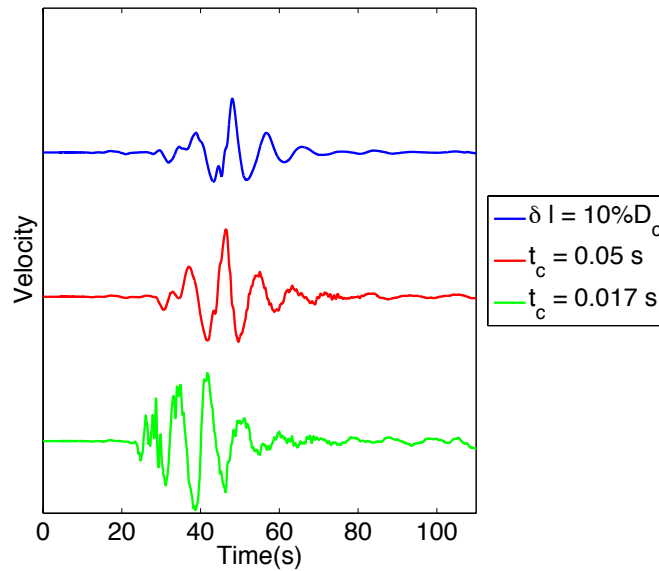


Figure 4.20 Synthetic velocigrams (in the frequency range 0.005 – 0.1 Hz ) recorded at the trench station indicated in Figure 4.18, when a regularization dynamic time scale is used (blue) and for two different regularization constant time scales (red and green). In the figure, the horizontal components are plotted

In conclusion, when a dynamic time scale is used the simulations produce convergent solutions in terms of acceleration in the deepest part and the high-frequency content recorded at the coastal stations only comes from the acceleration of the rupture downwards. Moreover the signals coming from the patch of large slip in the shallow part are totally depleted in high frequencies as also evidenced in all source inversion models (Maercklin *et al.*, 2012; Satriano *et al.*, 2014 etc.). Conversely when a constant time scale is used the solutions never converge for variation of  $t_c$  : when a larger  $t_c$  is considered the deep acceleration of the rupture is damped, on the other hand when a smaller  $t_c$  is taken into account, spurious high-frequency oscillations are generated around the trench and this noise totally pollutes the dynamics of rupture and the radiation.

#### 4.6 Small asperities in the deepest part

As already mentioned, the high-frequency radiation, recorded during Tohoku earthquake, was ascribed to 3/4 sub-events (Lee *et al.*, 2011; Suzuki *et al.*, 2011), associated with asperities in the deeper part of the fault (Asano & Iwata, 2012; Kurahashi & Irikura, 2013). Huang *et al.*, (2012) proposed a bi-dimensional dynamic

model of Tohoku earthquake to explain the frequency dependent distribution of slip along the dip direction including in the deepest area a few asperities to mimic the inhomogeneous distribution of remote shear stress associated with the recent seismic activity in the area.

Real seismograms recorded at MYG011 show two clear high-frequency bursts in the range  $0.2 - 2\text{ Hz}$  during the first 100s of rupture propagation (Figure 4.21). The origin of these bursts was located coastward from the hypocentre in all works using back-projection and other similar techniques (Honda *et al.*, 2011; Ishii, 2011; Meng *et al.*, 2011; Wang & Mori, 2011; Maercklin *et al.*, 2012, Satriano *et al.*, 2014).

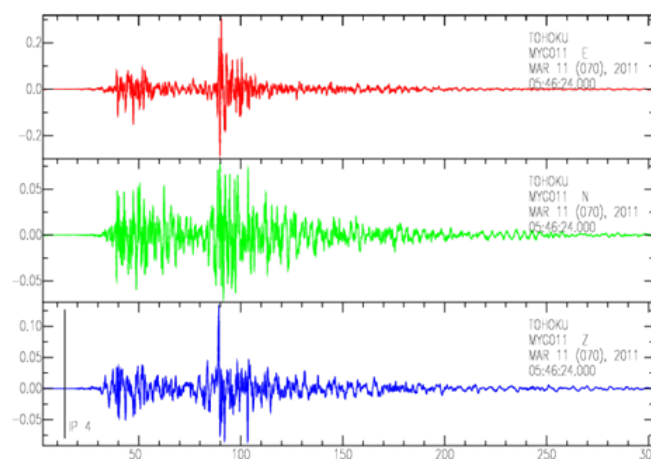


Figure 4.21 Real seismograms for Tohoku event recorded at MYG011. The blue signal represent the vertical component, whereas the green and red ones are the horizontal component.

In our simulations, when a dynamic time scale is used to regularize the bimaterial problem, we have evidenced only one high-frequency burst derived from the strong acceleration of rupture due to the geometrical discontinuity within the continental mantle part of the subduction slab. By analogy with the dynamic models of Huang *et al.*, (2012) we have included two asperities with a larger remote shear stress (just below the failure threshold in the area) to mimic the inhomogeneous distribution of the stress in the area, where recently moderate to large magnitude events occurred. In particular these asperities were placed in correspondence of the two accelerations of the rupture propagating downward: at the entrance of mantle and at the kink within the mantle itself. The position of the asperities is shown in Figure 4.22.

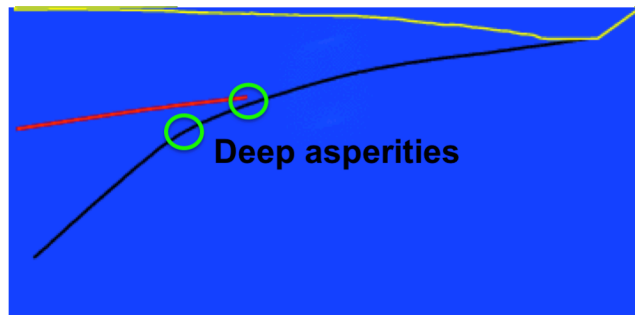


Figure 4.22 Position of deep asperities: the first at the entrance of the mantle, the second at the geometrical discontinuity.

Figure 4.23a-b shows respectively the horizontal and vertical components of synthetic seismograms recorded at the station MYG011 indicated in Figure 4.18. Red signals represent the traces recorded when no asperities are considered along the fault, while the blue traces were obtained including the two asperities of Figure 4.22. The high-frequency burst, due to the kink within the mantle wedge, shows clearly stronger amplitude due to the larger stress drop. Additionally of a strongest acceleration occurs in advance due to the first asperity at the entrance in the mantle wedge. Nevertheless even in this model only one high-frequency packet is evidenced.

In conclusion one of the high-frequency burst can be explained by considering a small asperity downwards. The second one, not evidenced in our bidimensional solutions, could be ascribed to 3-D effects as the reactivation of the slip during the along-strike propagation (Galvez *et al.*, 2014; Galvez *et al.*, 2016).

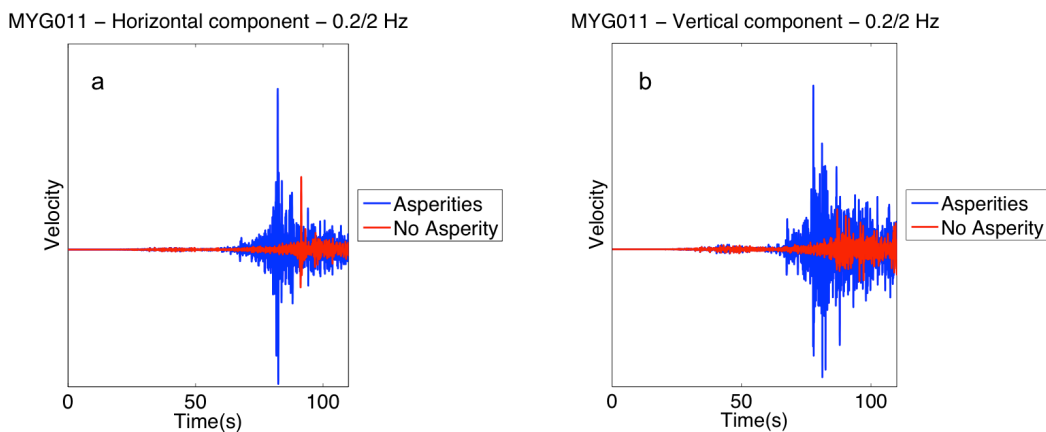


Figure 4.23 Synthetic velocigrams at station MYG011 of Figure 4.18 for horizontal (a) and vertical component (b) when a continuous initial remote shear stress is considered (red) and when the two asperities of Figure 4.22 are included in the initial model.

## 4.7 Dynamic models for tsunami hazard

As widely accepted the large amount of slip located in the vicinity of the trench is the main responsible for the huge tsunami waves generated during the Tohoku event.

The computation of probabilistic tsunami hazard requires the development of a large number of tsunami scenarios starting from the same number of inhomogeneous slip distributions in tsunamigenic areas. As a workaround, suites of likely earthquake slip are produced using stochastic slip distributions, which are based on general features observed across a wide range of geological and tectonic settings (Geist & Oglesby, 2014; Andrews, 1980). They are not site specific, and therefore do not account for systematic variations in the immediate environment of the fault, e.g. change in lithology or seismic wave/rupture interaction due to free surface/fault geometry which could influence the slip distribution over the fault plane as shown in this work of thesis.

In this part of the work a new technique is developed in order to create modified stochastic slip distributions, which take into account the structural and geometrical features of the tsunamigenic area as derived from 2D dynamic simulations. The aim is to obtain slip scenarios allowing to compute site-specific probabilistic tsunami hazard. The Tohoku earthquake will be used as a case-study and the results here presented are contained in Murphy *et al.*, (2016) paper, recently submitted.

The stochastic probability density function (SPDF) for the slip was obtained from 500 stochastic slip distributions without tapering the edge related to the free surface in order to take into account the possibility to have a large slip around the shallow part of the fault plane. This PDF, shown in Figure 4.24, is computed with the formula:

$$\Delta^K(x,y) = \frac{1}{N} \sum_{i=1}^N \left( \frac{\delta u_i^K(x,y)}{\iint_A \delta u_i^K(x,y) dA} \right) \quad (4.3)$$

Where the superscript  $\{ \}^K$  indicate the stochastic slip distribution,  $N$  is the number of models and  $A$  is the whole fault plane.

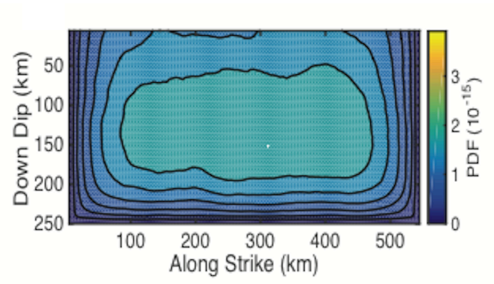


Figure 4.24 Stochastic PDF created in order to take into account largest slip in the shallow part

This SPDF, widely used in the computation of tsunami scenarios, once averaged along the strike has to be compared with another PDF obtained from the slip maps deriving from the along-dip dynamic simulations.

500 dynamic rupture simulations were performed with a stochastic initial stress distribution implemented as input. The location of nucleation is chosen randomly, a linear slip weakening friction law was used and the material properties are assumed as homogeneous ( $C_p = 6.3 \text{ km/s}$ ,  $C_s = 3.2 \text{ km/s}$ ,  $\rho = 3000 \text{ kg/m}^3$ ). In the vicinity of the trench (depth  $< 1 \text{ km}$ ), a low shear stress is considered to mimic the presence of a stable aseismic area. The effective normal stress,  $\sigma^n$ , varies as a function of depth based on the difference between the hydrostatic and lithostatic pressure starting from a value of  $5 \text{ MPa}$  in the trench zone. At  $25 \text{ MPa}$  we assume that the pore pressure tracks the increasing normal stress and the effective normal stress remains constant with depth as previously described (see section 4.4). This choice of frictional parameters produces a  $5 \text{ MPa}$  stress drop in the deep section of the fault (assuming slip is greater than the weakening distance,  $D_c$ ). The geometry is fixed as well as for the models presented before.

For dynamic simulations, the large variability of slip distributions, due to the different nucleation position and initial shear stress, can lead to a wide range of earthquakes with different seismic moment. The slip profiles on the 1D fault are converted to seismic moment by assuming that the effective along-strike length  $L$  scales with the mean slip and width using the following empirical relationship (Shaw, 2013):

$$L = \frac{7}{3} \left[ \frac{\Delta\sigma}{\mu\bar{\delta}} - \frac{1 - \left(\frac{C_s}{C_p}\right)^2}{W} \right]^{-1} \quad (4.4)$$

with  $\bar{\delta}$  representing the average slip,  $\Delta\sigma$  the average stress drop, and  $W$  is the width that is set to the rupture size in the individual simulations.

Using this scaling relationship the numerical slip distributions cover a range between  $M_w$  7.8 – 9.6. Very small events (i.e.  $M_w < 4$ ) have been omitted as the nucleation patch predominantly controls their slip distribution. Ignoring these small events leaves us with 320 slip distributions.

The events were grouped in 0.2 -width magnitude bins and for each bin a dynamic probability density function was computed with the equation (4.3).

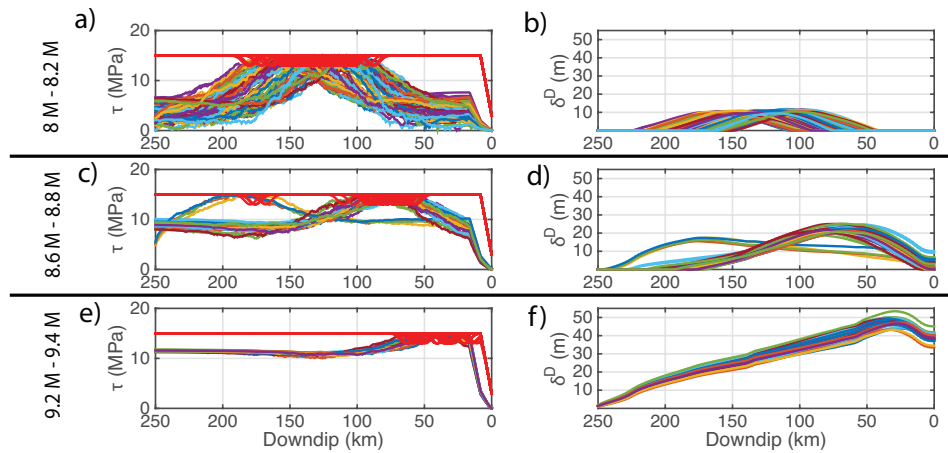


Figure 4.25 (a)-(c)-(e): Initial shear stress conditions for three magnitude bins (indicated on the left). The red curves represent the initial normal stress and the anomaly tracks the nucleation area. (b)-(d)-(f): for the initial conditions besides the slip maps are reported as a function of distance from the trench

Verification for this subdivision is demonstrated in Figure 4.25 where the large variation between slip distributions collapses when viewed by magnitude. In Figure 4.25, the location of the maximum slip systematically shifts from the centre of the fault, where it occurs for relatively small earthquakes to shallower depths for the largest events. Figure 4.25 provides a sample of the shear stress (left pictures) and slip distributions (right pictures) for three magnitude bins (the red curves in the left pictures represent the normal stress and the patch of lower normal stress track the nucleation area for each simulation); the slip distributions of earthquakes with

moment magnitude between 8.6 and 8.8 are bi-modal with the slip distribution peaking at depth (i.e. > 150km down dip) or near the surface (< 100 km down dip). For  $M_w > 8.8$ , and for events in the same magnitude bin, slip is always larger near the surface (Figure 4.25d). Figure 4.26 also demonstrates how earthquakes with magnitudes lower than 8.2 feature slip concentrated in the centre of the fault while for  $M_w > 9.0$  maximum slip is only found near the surface (i.e. roughly 30 km down dip from the surface).

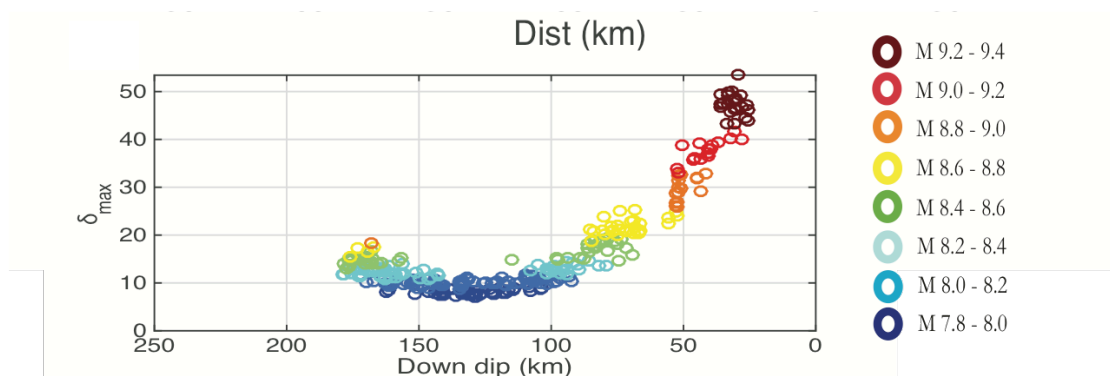


Figure 4.26: Position of maximum slip for each magnitude bin

To compare the 8 dynamically derived SPDFs with the stochastic source model, the 2D SPDF in Figure 4.24 was taken and averaged along strike to produce a 1D depth dependent stochastic SPDF. The shape of the stochastic SPDF is assumed to be similar over all magnitude ranges (i.e. near uniform across the fault). Comparing the different SPDFs (from stochastic slip distribution and from dynamic simulations in each bin of magnitude) (Figure 4.27a), there is clearly a relationship between the SPDF magnitude and the amplitude: the smaller the magnitude, the larger the SPDF maximum amplitude. This variation is due to the denominator in equation (4.3) that has the effect of equalising the magnitude between the different SPDFs. As a result, smaller events produce higher concentrations of probable slip in smaller areas in order to produce a similar seismic moment to the larger events, which cover a wider section of the fault.

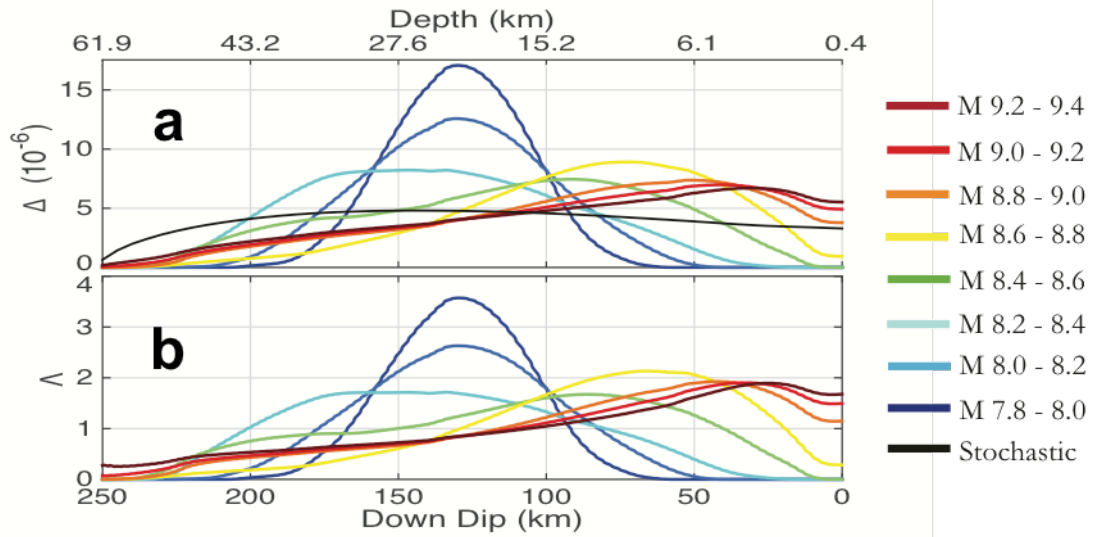


Figure 4.27 (a) SPDF (grouped for magnitude) deriving from the dynamic simulations are compared with the SPDF deriving from stochastic slip distribution (black line). (b)  $\Lambda(x)$  obtained for each magnitude bin.

Comparing the dynamic SPDFs with the stochastic source model (black line) Figure 4.27 demonstrates that the stochastic models systematically over represent slip near the surface (i.e.  $< 50$  km down dip) for  $M_w < 8.6$  but underrepresent slip in the same area for  $M_w > 8.6$ . This bifurcation is related to the point at which the fault is producing ruptures that can penetrate the low shear stress zone near the surface (Kozdon & Dunham, 2014) and the increased normal stress due to the reflection of seismic waves onto the fault. Simulations start to reach the surface for events greater than  $M_w 8.4$  which is consistent with the general idea that large energetic rupture may break into less coupled / aseismic shallow zones, as it might have been the case for the 2011 Tohoku earthquake featuring significant slip reaching to the trench. The spatial segregation of the larger and smaller events compliments the concept of depth dependent failure domains where relatively small asperities dominate the fault plane at depth (i.e. 35 to 55 km deep) with large slip occurring at shallower depths and may propagate up to the trench.

In order to produce a stochastic source model that better represents the systematic dynamic features depicted in Figure 4.27 the stochastic methodology requires some modification. We introduce a depth dependent transfer function,  $\Lambda(x)$ , representing the differences between the average stochastic and dynamic SPDFs:

$$\Lambda(x) = \frac{\Delta^D(x)}{\Delta^K(x)} \quad (4.5)$$

Where  $\Delta^K(x)$  is given by equation (4.3) and  $\Delta^D(x)$  is computed with the same formula (4.3) using the slip distributions obtained from dynamic simulations in each magnitude bin.

Considering the  $\Lambda(x)$  obtained for a particular magnitude bin a 2-D modified stochastic slip distribution can be obtained as:

$$\Delta^D(x,y) = \Lambda(x)\Delta^K(x,y) \quad (4.6)$$

with the reasonable hypothesis that the geometrical and structural variations along the strike direction are less important for the dynamic characteristics of the rupture.

$\Lambda(x)$  is magnitude dependent as shown in Figure 4.27b, requiring the function to be changed based on the size of the earthquake. An example of the application of the 1D  $\Lambda(x)$  as a depth dependent function to a 2D stochastic model is provided in Figure 4.28 where the effect of the function  $\Lambda(x)$  clearly amplifies the maximum slip and shifts it closer to the surface.

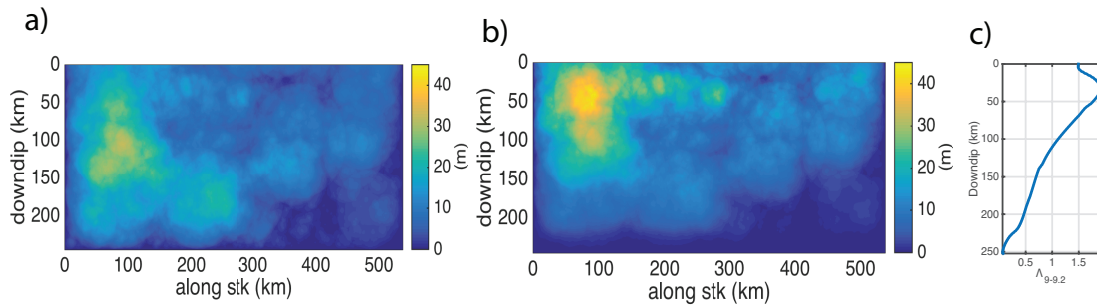


Figure 4.28 (a)-(b) slip distribution respectively from a stochastic model and a modified stochastic model. To obtain the latter the function  $\Lambda(x)$  for magnitude bin 9.0-9.2 (depicted in figure c) is used.

The ‘traditional’ stochastic source models were produced using the same method that generated the SPDF displayed in Figure 4.24 (i.e. not tapering the slip at the surface). The stochastic slip distributions were then multiplied, as indicated in equation (4.6), by the transfer function  $\Lambda(x)$  generated using dynamic simulations in the 9.0 - 9.2 magnitude range (represented by the red curve in Figure 4.27b) as in Figure 4.28. 500 magnitude 9.0 slip distributions were generated using the

‘traditional’ stochastic source model and 500 using the modified stochastic source model. The importance of applying such a correction to the traditional slip distribution is shown by the SPDF on the Tohoku fault plane (Figure 4.29), constructed by considering the slip distribution of the corrected models. This SPDF clearly shows an increase of probability for slip at shallow depths. This correlates with the  $\Lambda(x)$  function which amplifies slip between 0 km – 75 km down-dip of the surface (red line Figure 4.27b). With the traditional stochastic source model the maximum slip in each simulation in the ensemble ranges between 13 - 30 *m* with a mean of 20 *m* while the application of the transfer function raises this range to 17 – 52 *m* with a mean maximum slip of 29 *m*; in the ensemble of modified models, very large slip is observed in a limited number of cases: 14.4% show slip > 40 *m*, and 0.2% slip > 50 *m*. These values appear reasonable given that estimates for maximum slip for the Tohoku 2011 earthquake which ranged from 30m to > 80 m (Brown *et al.*, 2015).

For each slip distribution, the static ground displacement and the respective sea surface displacement were computed (Kajiura 1963) and the tsunami was propagated to the coastline using HySEA (De La Asunciòn *et al.*, 2013; Castro *et al.*, 2015) on the SRTM30+ (Becker *et al.*, 2009) digital elevation model and from each of the 500 magnitude 9.0 slip distributions the tsunami was simulated for both stochastic and corrected model types. Figure 4.29b-c display the probability of exceedance of  $H_{\max}$  at each receiver for both ensembles. The computation was performed by the Tsunami group at IGTV Roma. In those pictures, the logarithmic colour scale is the same (within Figure 4.29a) and the grey solid lines indicate the maximum and minimum  $H_{\max}$  obtained at each receiver. Blue diamonds are maximum tsunami wave height observed during the 2011 Mw 9 earthquake (Mori *et al.*, 2011). For assessing SPTHA, these probabilities should be combined with those of the earthquake occurrence (Lorito *et al.*, 2015). The modified stochastic model produced more extreme  $H_{\max}$  values between 35° – 40°N. This difference is clearly due to the shallow slip amplification introduced by the SPDF for large events shown in Figure 4.29a. The inset of Figure 4.29a, which represents the probability of exceedance for a wave height between 36° and 41° latitude based on the original (red line) and modified (black line) stochastic models also shows how the hazard curves (aggregated for the whole coastline) differ if using traditional or corrected stochastic models, with the former resulting in an underestimation of the hazard for large intensities. Therefore, it

is the correction with  $\Lambda(x)$  which is producing the large, more extreme  $H_{\max}$  values, which are missed in generic stochastic source models.

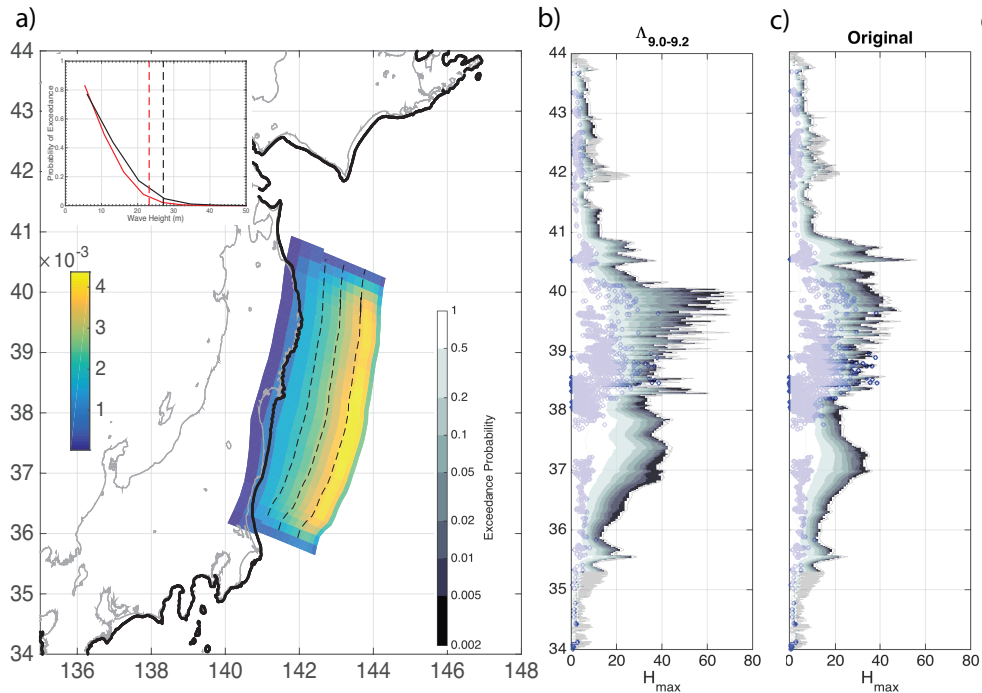


Figure 4.29: (a) Location of the fault (the subduction zone interface) relative to the Japanese coastline and receiver locations (denoted by black dots). Colours on the fault plane are the SPDF for the modified stochastic source model. Dashed lines across the fault plane mark 50 km, 100 km, 150 km down dip distance from the top of the fault. Bold black line denotes tsunami receiver locations (see Methods). Inset figure is the probability of exceedance for a wave height between  $36^\circ$  and  $41^\circ$  latitude based on the original (red line) and modified (black line) stochastic models. (b) Probability of exceedance of maximum wave height along latitude, for the modified source model; and (c) original stochastic source model. The logarithmic colour scale is the same for both plots. The grey solid lines indicate the maximum and minimum  $H_{\max}$  obtained at each receiver. Blue diamonds are maximum tsunami wave height observed during the 2011  $M_w$  9 earthquake.

The results presented in this section clearly show as the stochastic not site-specific slip distribution, generally used as input for the computation of tsunami scenarios, can be rapidly modified by performing bi-dimensional dynamic simulations, which take into account the main geometrical and structural features of the investigation area and thus the site-specific effects deriving from the expected normal/shear coupling. The comparison between the two slip probability distribution functions leads to the computation of a transfer function, which contains all site-specific features of a rupture. The inclusion of dynamic features for the case-study of Tohoku has shown the influence of shallow low normal traction coupled with interaction with the free

surface in the amplification of probability of exceedance of maximum wave height expected for a tsunamigenic event and this can help to compute more reliable tsunami scenarios for each subduction zone on the Earth and therefore leads to a more accurate estimate of the probabilistic tsunami hazard.

## 4.8 Conclusions

The Tohoku earthquake, occurred on March 11, 2011, off the northeast coast of Japan and it was one of the biggest event recorded on the Earth's surface. It also generated a huge tsunami wave, which caused several damages and casualties. The rupture of that earthquake was confined for a long time ( $\sim 100s$ ) in a small stripe of the fault surface along the dip direction before propagating for several kilometres along the strike direction originating the large moment magnitude ( $M_w = 9.0$ ). Most of the inversions obtained from the large amount of data (seismic, teleseismic, geodetic, tsunami etc.) recorded during the event, evidenced the complexities of the rupture as a function of depth and the most important feature can be considered the large amount of slip in the shallow portion of the plate associated with low frequency radiation. High-frequency radiators evidenced in the deep part of the subduction slab are related to smaller amount of coseismic slip. According to those works (e.g. Satriano *et al.*, 2014) the broadband characteristics of this rupture can be interpreted as the signature of segmentation and segment interactions, resulting from thermal and petrophysical structure, plate geometry and mechanical variations along the plate boundary interface, which seem to be more important along-dip as evidenced from tomographic studies and from the different features of the past events as a function of depth. For all these reasons bi-dimensional numerical simulations can be considered as a useful tool to investigate the initial stage of the rupture analysing the influence of the segmentation of the fault without an expensive computational cost.

In this work several 2D dynamic simulations for the Tohoku earthquake were performed with particular attention to the coupling between the shear stress and the normal stress perturbations induced mainly by bimaterial propagation and free surface interaction. A complex velocity model as well as realistic geometrical discontinuities were taken into account and they were considered as fixed in all the numerical models, while exploring the initial stress and the friction conditions.

In spite of the simplicity of these dynamic models, they were able to address the main features of the Tohoku along-dip rupture.

First of all, if uniform regional stresses are taken into account the high level of normal stress close to the almost horizontal trench can arrest the rupture not allowing the rupture itself to reach the trench. Nevertheless even when the remote shear stress is below the initial dynamic level given by  $\mu_d \sigma^n$  the rupture may reach the trench as the normal stress is dynamically decreased by the interaction with the reflected waves coming from the surface.

When a normal stress increasing with depth is considered as the effect of the lower lithostatic load in the vicinity of the trench and of the pore pressure in shallow part, the rupture was shown to propagate faster upward in the initial stage. Actually, during the initial phase of the earthquake the favoured direction, for the bimaterial interface oceanic/continental crust, is downward. Nevertheless, the low normal traction, coupled with the free-surface, accelerates more the rupture trenchward. Moreover the rupture produces large patches of slip around the trench with values of about  $\sim 30m$ .

When a low-velocity layer just above the trench is included in the initial model, to mimic the presence of the accretionary prism, a large compact patch of slip with maximum value of about  $30m$  is evidenced at the trench.

It is worth to note that the selection of the regularization algorithm can influence the results of the simulations. When a dynamic time scale is used to model the shear/normal stress coupling along the bimaterial subduction interface convergent solutions can be found as expected from the numerical analysis performed in Chapter 2. Moreover, only when a dynamic time scale is used the signal coming from the trench, where the largest slip is found, is depleted in high-frequency as expected from back-projection analysis.

For what concerns the downward propagation the rupture is very slow in the initial stage and it accelerates first at the structural discontinuity (the entrance in the mantle), where the contrast of impedance becomes higher and then at the geometrical discontinuity within the continental mantle wedge. Only when a dynamic time scale is selected these accelerations can be considered physically well-posed in the sense of the convergence described in Chapter 2.

In this area, small values of stress drop have to be imposed ( $< 5 MPa$ ) to avoid the emerging of supershear effects in the deepest part of subduction plate; the second

acceleration behaves as a high-frequency radiator that generates the sole high-frequency signal clearly visible in the synthetic seismograms.

To mimic the inhomogeneous remote shear stress distribution around the location of recent deep events we have considered two small asperities in correspondence of the two above described positions . The first asperity is shown to be able to further accelerate the rupture , whereas the second one significantly increases the amplitude of the high-frequency emitted at the geometrical discontinuity. It can be considered as one of the several high-frequency burst evidenced in most inversion works.

Finally, using simple homogeneous Tohoku models, with a realistic geometry of the subduction plate a new technique was developed to include the site-specific informations deriving from dynamic simulations in the stochastic slip models generally used to produce tsunami scenarios.

The large number of dynamic simulations showed as the maximum slip location is related to the magnitude and how largest events can produce largest slip close to the trench as the effect of the interaction between the propagating rupture and the reflected waves coming from the free surface. The difference between the classical stochastic slip distribution (averaged along strike) and the probability slip function distribution derived from a set of bi-dimensional dynamic simulations allows to define a transfer function, which contains the site-specific information for each magnitude. From this transfer function a modified stochastic slip distribution can be obtained for a particular geometry and initial conditions expected for the case of Tohoku. From these slip distribution an estimate of the probability of exceedance of maximum tsunami wave height was computed showing how the geometrical and initial stress conditions of the Tohoku earthquake may have boosted the rupture until the trench and they have originated the huge tsunami waves .

# Conclusions

In this work of thesis, we aimed to properly model the main features of the rupture dynamics along subduction zones. We mainly investigated the shear/normal stress coupling when geometrical discontinuities and/or realistic velocity models induce large normal traction perturbations on the fault surface.

The Spectral Element Method (SEM) was shown to be a powerful numerical tool to perform dynamic simulations for subduction earthquakes due to its geometrical flexibility and to the easy implementation of classical seismological boundary conditions (such as the free surface).

Sharp variations of normal stress are induced when a rupture propagates between materials presenting dissimilar elastic properties. Performing dynamic simulations along these bimaterial interfaces, we showed how the Coulomb friction law leads to unstable solutions due to a missing time/length scale related to the shear/normal coupling. We also show how the shear stress response has to be properly delayed to provide stable physical reliable solutions and how this delay can allow to define a length, comparable with the dissipation zone, which can be interpreted as the length of coupling. The characteristic time/length of the coupling for a bimaterial rupture propagation has to dynamically change during the crack growth as the slip rate at crack front increases and the size of the dissipation zone shrinks. We showed that a dynamic regularization allows to filter the high-frequency contribution to the coupling without damping the physical time scale of the normal stress variation around the crack front. This time scale was in turn shown to be comparable with the weakening time process in the framework of slip weakening constitutive law.

Free surface interaction was shown to generate a break of symmetry in the shallow part of dipping faults. In particular we evidenced larger ground motion on the hanging wall and thus larger coseismic slip, increasing as the dip angle decreases. Due to the fault/free surface interaction this slip is shown to be generally associated with low-frequency radiation.

Finally, exploiting these results some simplified 2D dynamic models of Tohoku earthquake are presented. In spite of the simplicity of these models, the main source

features of that event can be addressed in terms of influence of geometry and structure and thus of shear/normal coupling. Along dip we found a bilateral rupture faster trenchward where the largest coseismic slip is measured. This larger slip can be indeed ascribed to the interaction between the free surface and the fault that reaches the free surface in the vicinity of the Japan trench. When the bimaterial interface along the dip for Tohoku earthquake is properly modelled and the bimaterial coupling is driven by a dynamic time scale decreasing as the dissipative zone shrinks the emitted radiation was shown to be dominated by the wavelength of fault/free surface interaction and the larger coseismic slip at the trench is associated with low-frequency radiation ( $0.005 - 0.1\text{Hz}$ ). Strong rupture acceleration due to geometrical and velocity discontinuities implies high-frequency sub-sources ( $0.2 - 2\text{Hz}$ ) in the deep part of the subduction zone. Even to achieve physical convergent models describing this abrupt acceleration a dynamic time scale is needed to regularize the bimaterial rupture propagation at the interface between the slab and the continental mantle wedge.

Furthermore performing several bi-dimensional Tohoku-like simulations from stochastic pre-stress we showed as the location of larger slip along subduction zone changes as a function of the increasing magnitude. Only larger events ( $M_w > 8.6$ ) can penetrate the seismic stable area around the trench and in that case the coseismic slip in the shallow part of the fault dominates the slip profile with significant dislocation values between 30 m and 60m .

We finally showed how, taking into account these site-specific dynamic features, the tsunami scenarios for the Tohoku earthquake lead to higher estimates for tsunami hazard in terms of probability of exceedance of maximum wave height on the coast.

# References

Achenbach, J. D. & Epstein, H. L., 1967. Dynamic interaction of a layer and a half-space, *J. Eng. Mech. Division*, Vol. EM5, PP. 27-42.

Adams, G. G., 1995. Self-excited oscillations of two elastic half-spaces sliding with a constant coefficient of friction, *J. Appl. Mech.*, Vol. 62, 867-872.

Adams, G.G., 1998. Steady sliding of two elastic half-spaces with friction reduction due to interface stick-slip. *ASME J. Appl. Mech.*, Vol. 65, pp. 470–475.

Adda-Bedia M., Ben Amar M., 2003. Self-sustained slip pulses of finite size between dissimilar materials, *J. Mech. Phys. Solids*, Vol. 51, pp. 1849–1861.

Agrawal, A. & Karlsson, A. M., 2006. Obtaining mode mixity for a bimaterial interface crack using the Virtual Crack Closure Technique, *Int. J. Fract.*, Vol. 141(1-2), pp. 75-98.

Ampuero, J.-P., Ben-Zion, Y., 2008. Cracks, pulses and macroscopic asymmetry of dynamic rupture on a bimaterial interface with velocity-weakening friction, *Geophys. J. Int.*, Vol. 173(2), 674-692.

Andrews, D., 1980. A stochastic fault model 1. Static Case, *J. Geophys. Res.* Vol. 85, pp. 3867–3877

Andrews, D. J., 1985. Dynamic plane-strain shear rupture with a slip-weakening friction law calculated by a boundary integral method, *Bull. Seisin. Soc. Am.*, Vol. 75, pp. 1-21.

Andrews, D. J. & Ben-Zion Y., 1997. Wrinkle-like slip pulse on a fault between different materials, *J. Geophys. Res.*, Vol. 102, pp. 553-571.

Archuleta, R. J. & Frazier, G. A., 1987. Three-dimensional numerical simulations of dynamic faulting in a half-space, *Bull. Seisin. Soc. Am.*, Vol. 68(3), pp. 541-572.

Asano, K. & Iwata, T., 2012. Source model for strong ground motion generation in 0.1-10 Hz during the 2011 Tohoku earthquake. *Earth Planets Space*, Vol. 64, pp. 1111-1123.

Becker, J. J. *et al.*, Global Bathymetry and Elevation Data at 30 Arc Seconds Resolution: SRTM30\_PLUS. *Marine Geodesy*, Vol. 32, pp. 355–371,

Ben Zion Y. & Andrews, D. J., 1998. Properties and implications of dynamic rupture along a material interface. *Bull. Seism. Soc. Am.*, Vol. 88, pp. 1085-1094.

Bizzarri, A. & Cocco M., 2003. Slip-weakening behavior during the propagation of dynamic ruptures obeying rate-and state-dependent friction laws, *J. Geophys. Res.: Solid Earth*, Vol. 108(B8).

Broberg, K. B. (1989) The near-tip field at high crack velocities. *Znt. J. Fract.*, Vol. 39(1-2), pp. 1-13.

Brown, L., Wang, K. & Sun, T., 2015. Static stress drop in the Mw 9 Tohoku-oki earthquake: Heterogeneous distribution and low average value. *Geophys. Res. Lett.*, Vol. 42, Issues 24, pp. 10,513–10,960

Burridge, R. and Halliday, G. S., 1978. Dynamic shear cracks with friction as models for shallow earthquake, *Geophys. J. R. Astron. Soc.*, Vol. 25, pp. 261-283.

Burridge, R., 1973. Admissible speeds for plane-strain self-similar shear cracks with friction but lacking cohesion, *Geophys. J. R. Astr. Soc.*, Vol. 35, pp. 439-455.

Castro, M. J., González-Viday, J., Macías, S., Ortega, S. & De la Asunción, M. 2015. Efficient GPU implementation of a two waves TVD-WAF method for the two-dimensional one layer Shallow Water system and its validation for tsunami forecasting. *Proceedings of the XXIV Congress on Differential Equations and Applications / XIV Congress on Applied Mathematics – Cádiz*, June 8-12.

Chadwick P., 1999. *Continuum Mechanics Concise Theory and Problem*, Courier corporation.

Chambon, G., Schmittbuhl J., Corfidir., A, 2002. Laboratory gouge friction: Seismic-like slip weakening and secondary rate- and state-effects, *Geophys. Res. Lett.*, Vol. 29 (10).

Cherepanov, G. P., 1962, The stress state in heterogeneous plate with slits in Russian, *Izvestia AN SSSR, OTN, Mekhan. i Mashin.*, Vol. 1, pp. 131-137

Cochard, A. & Rice, J. R., 2000. Fault rupture ill-posedness between dissimilar materials: Ill-posedness, regularization, and slip-pulse response, *J. Geophys. Res.*, Vol. 105, pp. 25,891-25,907.

Comninou, M. & Schmueser, D., 1979. The interface crack in a combined tension-compression and shear field, *J. Appl. Mech.*, Vol. 60, 183-189.

De la Asunción, M. Castro-Diaz M., J., Fernandez-Nieto, E. D., Mantas, J. M., Ortega Acosta, S., Gonzalez-Vida, J. M., 2013. Efficient GPU implementation of a two waves TVD-WAF method for the two-dimensional one layer shallow water system on structured meshes, *Comput. Fluids*, Vol. 80, pp. 441-452.

Deng, X., 1993a. General crack tip fields for stationary and steadily growing interface cracks in anisotropic bimetals, *J. Appl. Mech.*, Vol. 60, 183-189.

Deng, X., 1993b. On stationary and moving interface cracks with frictionless contact in anisotropic bimetals, *Proc. R. Soc. Lond.*, Vol. A443, 563-572.

Deng, X., 1994. An asymptotic analysis of stationary and moving cracks with frictional contact along bimaterial interfaces and in homogeneous solids. *Int. J. Solids Structures*, Vol. 31 (17), pp. 2407-2429.

Dietrich, J. H., 1979a. Modelling of rock friction. I: Experimental results and constitutive equations, *J. Geophys. Res.*, Vol. 84, pp. 2161-2168.

Dietrich, J. H., 1979b. Modelling of rock friction. II: Simulations of preseismic slip, *J. Geophys. Res.*, Vol. 84, pp. 2169-2175.

Dietrich, J. H. & Kilgore B. D., 1994. Direct observation of frictional contacts; new insights fro state-dependent properties, *PAGEOPH*, Vol. 143, pp. 283-302.

Dor, O., Yildirim, C., Rockwell T. K., Emre O., Ben-Zion Y., Sisk M., & Duman T., 2005. Asymmetric structural properties across the 1943 rupture zone of Anatolian fault: A possible indication for a preferred rupture direction, *Eos Trans, AGU*, Vol. 86 (52), Fall meet. Suppl., Abstract S31B-07

Dor, O., Rockwell T. K., Ben-Zion Y., 2006. Geological observations of damage asymmetry in the structure of the San Jacinto, San Andreas and Puchbowl faults in southern California: A possible indicator for preferred rupture propagation distance, *Pure Appl. Geophys*, Vol. 163, pp. 301-349.

England, A. H., 1965. A crack between dissimilar media, *J. Appl. Mech.*, Vol. 32, pp. 400-402

Erdogan, F., 1965. Stress distribution in bonded dissimilar materials with cracks, *Bull. Seism. Soc. Am.*, Vol. 32, pp. 403-410

Eshelby, J.D., Read W.T., & Shockley, W. (1953). Anisotropic elasticity with applications to dislocation theory. *Acta Metall.*, Vol. 1, pp.251-259.

Festa, G., 2004. *Slip imaging by isochrones back projection and source dynamics with spectral element methods*, PhD Thesis, Università degli Studi di Bologna “Alma Mater Studiorum”, Bologna (Italy) & Università degli Studi di Napoli “Federico II”, Napoli (Italy)

Festa, G. & Nielsen, S. B., 2003. PML absorbing boundaries, *Bull. Seism. Soc. Am.*, Vol. 93(2), pp. 891-903.

Festa, G. & Vilotte, J.-P., 2006. Influence of rupture initiation on the intersonic transition: crack-like versus pulse like modes, *Geophys. Res. Lett.*, Vol. 33(15), L15320.

Freund, L. B. (1990) *Dynamic Fracture Mechanics*. Cambridge University Press, Cambridge.

Galvez, P., Ampuero, J.-P., Dalguer L. A., Somala S. N., & Nissen-Meyer T. (2014). Dynamic earthquake rupture modelled with an unstructured 3-D spectral element method applied to the 2011 M9 Tohoku earthquake, *Geophys. J. Int.*, Vol. 198, no. 2, 1222–1240.

Galvez P., Dalguer L. A., Ampuero J.-P., & Giardini D., 2016. Rupture reactivation during the 2011 Mw 9.0 Tohoku earthquake: Dynamic rupture and ground motion simulations. *Bull. Seism. Soc. Am.*, Submitted

Gautesen, A. K., & Dundurs, J., 1988. The interface crack under combined loading, *J. Appl. Mech.*, Vol. 55, pp. 580-586.

Geist, E. L. & Oglesby, D. D., 2014. In *Encyclopedia of Earthquake Engineering* 1–17, Springer Berlin Heidelberg.

Geubelle, P. H. & Rice, J. R., 1995. A spectral method for three-dimensional elastodynamic fracture problems, *J. Mech. Phys. Solids*, Vol. 43, pp. 1791-1824.

Gutenberg, B., 1955. Magnitude determination for larger Kern County shocks, 1952: effects of station azimuth and calculation methods. In: *Earthquakes in Kern County, California during 1952*, Bull. 171, US Division of Mines.

Harris R. A. & Day, S. M., 1993. Dynamics of fault interaction: parallel strike-slip faults, *J. Geophys. Res.*, Vol. 98, pp. 4461-4472.

Harris, R. A. & Day, S. M., 1997. Effects of a low-velocity zone on a dynamic rupture. *Bull. Seism. Soc. Am.*, Vol. 87, pp. 1267-1280

Harris, R.A. & Day, S. M., 2005. Material contrast does not predict earthquake rupture propagation direction, *Geophys. Res. Lett.*, Vol. 32, L23301.

Honda, R., Yukutake, Y., Ito, H., Harada, M., Aketagawa, T., Yoshida, A., Sakai, S., Nakagawa, S., Hirata, N. & Obara, K., 2011. A complex rupture image of the 2011 off the Pacific coast of Tohoku Earthquake revealed by the Me-SO-net. *Earth Planets Space*, Vol. 63(7), pp. 583-588.

Huang, Z., Zhao, D., Wang, L., 2011. Seismic heterogeneity and anisotropy of the Honshu arc from Japan Trench to the Japan Sea, *Geophys. J. Int.*, Vol. 184, pp. 1428-1444.

Ida, Y., 1972. Cohesive force across the tip of a longitudinal-shear crack and Griffiths specific surface energy, *J. Geophys. Res.*, Vol. 77, pp. 3796-3805.

Ide, S., Baltay, A. & Beroza, G. C., 2011. Shallow dynamic overshoot and energetic deppe rupture in the 2011 Mw 9.0 Tohoku-Oki earthquake, *Science*, Vol. 332 (6036), pp. 1426-1429.

Irwin, G. R., 1957. Analysis of stresses and strains near the end of a crack traversing a plate, *J. Appl. Mech.*, Vol. 24, pp. 361-364.

Ishii, M., 2011. High-frequency rupture properties of the Mw 9.0 off the Pacific coast of Tohoku earthquake. *Earth Planets Space.*, Vol. 63(7), pp. 609-614.

Kajiura, K., 1963. The Leading Wave of a Tsunami. *B. Earthq. Res. I. Tokyo*, Vol. 41, pp. 535-571.

Kammer, D. S., Yartebov, V. A., Anciaux, G. & Molinari, J.-F., 2014b. The existence of a critical length scale in regularised friction, *J. Mechan. Phys. Solids*, Vol. 63, pp. 40-50.

Kaneko Y. & Lapusta, N., 2010. Supershear transition due to a free surface in 3-D simulations of spontaneous dynamic rupture on vertical strike-slip faults, *Tectonophysics*, Vol., 493, pp. 272-284.

Komatitsch, D. & Tromp, J., 2002b. Spectral-element simulations of global seismic wave propagation – I. Validation, *Geophys. J. Int.*, Vol. 149, 390-412.

Komatitsch, D. & Tromp, J., 2002a. Spectral-element simulations of global seismic wave propagation – II. Three dimensional models, oceans, rotation and self-gravitation, *Geophys. J. Int.*, Vol. 150, 303-318.

Komatitsch, D. & Vilotte, J.-P., 1998. The spectral element method: an efficient tool to simulate the seismic response of 2D and 3D geological structures, *Bull. Seism. Soc. Am.*, Vol. 88, pp. 368-392.

Komatitsch, D., Vilotte, J.-P., Vai, J., Castillo-Covarrubias, J. M. & Sanchez-Sesma, F. J., 1998. The spectral element method for elastic wave equations: applications to 2D and 3D seismic problems.

Kozdon, J. E., & Dunham, E. M., 2013. Rupture to the trench: dynamic rupture simulations of the 11 March 2011 Tohoku earthquake. *Bull. Seismol. Soc. Am.*, Vol. 103, pp. 1275-1289

Kozdon, J. E. & Dunham, E. M. 2014. Constraining shallow slip and tsunami excitation in megathrust ruptures using seismic and ocean acoustic waves recorded on ocean-bottom sensor networks. *Earth Planet. Sci Lett.*, Vol. 396, p. 56–65.

Kurahashi, S. & Irikura, K., 2013. Short-period source model of the 2011 Mw 9.0 off the Pacific coast of Tohoku, *Bull. Seismol. Soc. Am.*, Vol. 103, pp. 1373-1393

Langer, S., Olsen-Kettle, L. & Weatherley, D., 2012. Identification of supershear transition mechanisms due to material contrast at bimaterial faults, *Geophys. J. Int.*, Vol. 190, pp. 1169-1180.

Lee, S.-J., Huang, B.-S., Ando, M., Chiu, H.-C., Wang, J.-H., 2011. Evidence of large scale repeating slip during the 2011 Tohoku-Oki earthquake. *Geophys. Res. Lett.*, Vol. 38.,

Liu, C., Lambros J. & Rosakis A. J., 1993. Highly transient elastodynamic crack growth in a bimaterial interface: higher order asymptotic analysis and optical experiments, *J. Mechan. Phys. Solids*. Vol. 41(12), pp. 77-90.

Lorito, S. *et al.*, 2015. Probabilistic hazard for seismically induced tsunamis: accuracy and feasibility of inundation maps. *Geophys. J. Int.*, Vol. 200, pp. 574–588,

Ludwig, W. J., Nafe, J. E. & Drake, C. L. 1971. Seismic refraction, in: *The Sea*, Vol. 4 pp. 54-84, ed. Maxwell, A.E., Wiley-Interscience, New York, USA.

Maday, Y. & Patera, A. T., 1989. Spectral element methods for incompressible Navier-Stokes equations, in *State of the art survey in computational mechanics*, pp. 71-143.

Maercklin, N., Festa, G., Colombelli, S., Zollo A., 2012. Twin ruptures grew to build up the giant 2011 Tohoku, Japan, earthquake. *Sci. Rep.*, Vol. 2.

Martins, J. A. C., Guimaraes, J. & Faria, L. O., 1995. Dynamic surface solutions in linear elasticity and visco-elasticity with frictional boundary conditions. *Journal of Vibrations and Acoustic*, Trans. ASME, Vol. 117, 445-451.

Martins, J. A. C. & Simões, F. M. F., 1995. On some sources of instability/ill-posedness in elasticity problems with Coulomb friction. In: Raous, M., Jean, M., Moreau, J.J. (Eds.), *Contact Mechanics*. Plenum Press, New York, pp. 95-106.

Meng, L., Inbal, A. & Ampuero J.-P., 2011. A window into the complexity of the dynamic rupture of the 2011 Mw 9 Tohoku-Oki earthquake. *Geophys. Res. Lett.*, Vol. 38.

Mori, N., Takahashi, T., Yasuda, T. & Yanagisawa, H., 2011. Survey of 2011 Tohoku earthquake tsunami inundation and run-up. *Geophys. Res. Lett.*, Vol. 38.

Murphy S., Scala A., Herrero A., Lorito S., Festa G., Trasatti E., Tonini R., Romano F., Molinari I. & S. Nielsen, 2016. Shallow slip amplification and enhanced tsunami hazard unravelled by dynamic simulations of mega-thrust earthquakes, *Sci. Rep.*, Submitted.

Muskhelishvili, N. I. 1953. *Some basic problems of the mathematical theory of elasticity*. Groningen, Holland: P. Noordhoff Ltd.

Muskhelishvili, N. I. 1953b. *Singular integral equations*. Groningen, Holland: P. Noordhoff Ltd.

Nielsen, S. B., 1998. Free surface effects on the propagation of dynamic rupture, *Geophys. Res. Lett.*, Vol. 25 (1), pp. 125-128.

Nielsen, S. B., Carlson J. M. & Olsen K. B., 2000. Influence of friction and fault geometry on earthquake rupture, *J. Geophys. Res.*, Vol. 105, 6069-6088.

Nikolic, R. & Djokovic, J. M., 2009. An approach to analysis of dynamic crack growth at bimaterial interface, *Thoeret. Appl. Mech.*, Vol. 36 (4), pp. 299-237.

Oglesby, D.D., Archuleta R.J. & Nielsen S. B., 1998. Earthquakes on Dipping Faults: The Effects of Broken Symmetry, *Science*, Vol. 280, Issue 5366, pp. 1055-1059.

Ozawa, S., Nishimura, T., Suito, H., Kobayashi, T., Tobita, M. & Imakiire, T., 2011. Co-seismic and postseismic slip of the 2011 magnitude-9 Tohoku-Oki earthquake, *Nature*, Vol. 475 (7536), pp. 373-376.

Patera, A. T., 1984. A spectral element method for fluid dynamics: laminar flow in a channel expansion, *J. Comput Phys.*, Vol. 54, pp. 468-488.

Prakash, V. & Clifton, R. J., 1993. Time resolved dynamic friction measurements in pressure-shear. In: Ramesh, K. T., *Experimental techniques in the dynamics of deformable solids*, AMD-Vol. 165. ASME, New York, pp. 33-48.

Prakash, V., 1998. Frictional response of sliding interfaces subjected to time varying normal pressures, *Journal of Tribology*, Trans. ASME, Vol. 120, pp.97-102.

Ranjith, K. & Rice, J. K., 2001. Slip dynamics at an interface between dissimilar materials, *J. Mech. Phys. Sol.*, Vol. 49, pp. 341-361.

Renardy, M., 1992. Ill-posedness at the boundary at the boundary for elastic solids sliding under Coulomb friction, *Journal of Elasticity*, Vol. 27, pp. 281-287.

Rice, J.R., 1988. Elastic fracture mechanics concepts for interfacial cracks, *J. Appl. Mech.*, Vol. 55, pp. 98-103

Rice, J. R. & Sih, G. C., 1965. Plane problems of cracks in dissimilar media, *J. Appl. Mech.*, Vol. 32, pp. 418-423.

Rice, J.R., 1997. Slip pulse at low driving stress along a frictional fault between dissimilar media. *EOS Trans. Am. Geophys. Union*, Vol. 78, F464.

Romano A., 2007. *Meccanica Analitica*, Apogeo

Rubin, A. M., Ampuero, J.-P., 2007. Aftershock asymmetry on a bimaterial interface, *J. Geophys. Res.*, Vol. 112, B05307.

Rudnicki, J. W. & Wu, M. 1995. Mechanics of dip-slip faulting in an elastic half-space. *J. Geophys. Res.*, Vol. 100, Issue B11, pp. 22173–22186

Ruina, A., 1983. Slip instability and state variable friction laws, *J. Geophys. Res.*, Vol. 88, pp. 10,359-10,370.

Sato, M., Ishikawa, T., Ujihara, N., Yoshida, S., Fujita, M., Mochizuki, M. & Asada, A., 2011. Displacement above the hypocentre of the 2011 Tohoku-Oki earthquake, *Science*, Vol. 332 (6036), 1395.

Satriano, C., Dionicio, V., Miyake, H., Uchida N., Vilotte, J.-P. & Bernard, P., 2014. Structural and thermal control of seismic activity and megathrust rupture dynamics in subduction zones: Lessons from the Mw 9.0, 2011 Tohoku earthquake, *Earth Plan. Sci. Lett.*, Vol. 403, pp. 287-298.

Simões, F. M. F. & Martins, J. A. C., 1998. Instability and ill-posedness in some friction problems, *Int. J. Eng. Sci.*, Vol. 36, pp. 1265-1293.

Simons, M., Minson, S. E., Sladen, A., Ortega, F., Jiang, J., Owen, S. E., Meng, L., Ampuero, J.-P., Wei, S., Chu, R., Helmberger, D.V., Kanamori, H., Hetland, E., Moore, A.W. & Webb, F.H., 2011. The 2011 magnitude 9.0 Tohoku-Oki earthquake: mosaicking the megathrust from seconds to centuries, *Science*, Vol.332(6036), pp. 1421–1425

Scholz, C. H., 1990. *The Mechanics of Earthquakes and Faulting*, Cambridge University Press

Schwab, C., 1998. *p- and hp-finite element methods. Theory and applications in solid and fluid mechanics*, Oxford Science Publications.

Shaw, B. E., 2013. Earthquake surface slip-length data is fit by constant stress drop and is useful for seismic hazard analysis. *Bull. Seismol. Soc. Am.*, Vol. 103, pp. 876–893.

Smirnov, V. I., 1964. *A course of higher mathematics*, Pergamon Press, Vol. 3, part 2.

Stroh, A. N., 1958. Dislocations and cracks in anisotropic elasticity, *Phil. Mag*, Vol. 3, pp. 625-646

Stroh, A. N., 1962. Steady state problems in anisotropic elasticity, *J. Math. Phys*, Vol. 41, 77-103.

Suo, Z. 1990. Singularities, interfaces and cracks in dissimilar anisotropic media, *Proc. R. Soc. Lond.*, Vol. A427, pp. 331-358.

Suzuki, W., Aoi, S., Sekiguchi, H. & Kunugi, T., 2011. Rupture process of the 2011 Tohoku-Oki mega-thrust earthquake (M9.0) inverted from strong-motion data. *Geophys. Res. Lett.*, Vol. 38.

Tada, T. & Yamashita, T., 1997. Non-hypersingular boundary integral equations for two dimensional non-planar crack analysis, *Geophys. J. Int.*, Vol. 130, pp. 269-282.

Takahashi N., Kodaira S., Tsuru T., Park, J.-O., Kaneda, Y., Suyehiro, K., Kinoshita H., Abe, S., Nishino, M. & Hino R., 2004. Seismic structure and seismogenesis off Sanriku region, northeastern Japan, *Geophys. J. Int.*, Vol. 159, pp. 129-145.

Uenishi, K. & Rice, J. R., 2003. Universal nucleation length for slip-weakening rupture instability under nonuniform fault loading, *J. Geophys. Res.*, Vol. 108(B1), 2042.

Virieux, J., 1984. SH wave propagation in heterogeneous media: velocity-stress finite difference method, *Geophysics*, Vol. 49, 1933-1957.

Virieux, J., 1986. P-SV wave propagation in heterogeneous media: velocity-stress finite difference method, *Geophysics*, Vol. 51, 889-900.

Wang, D. & Mori, J., 2011. Rupture process of the 2011 off the Pacific coast of Tohoku Earthquake (Mw 9.0) as imaged with back-projection of teleseismic P-waves. *Earth Planets Space*, Vol. 63, pp. 603-607.

Weertman, J., 1963. Dislocations moving uniformly on the interface between isotropic media of different elastic properties. *J. Mech. Phys. Solids*. Vol. 11, pp. 197-204.

Weertman, J., 1980. Unstable slippage across a fault that separates elastic media of different elastic constants, *J. Geophys. Res.*, Vol. 85, 1445-1461.

Williams, M. L., 1959. The stresses around a fault or crack in dissimilar media, *Bull. Seism. Soc. Am.*, Vol. 49, pp. 199-204

Willis, J. R., 1972. The penny-shaped crack on an interface, *Q. J. Mech. Appl. Math.*, Vol. 25, 367-385.

Xia, K., Rosakis, A. J. & Kanamori, H., 2004. Laboratory earthquakes: the sub-Rayleigh-to-supershear rupture transition, *Science*, Vol. 303, pp. 1859-1861.

Xia, K., Rosakis, A. J. & Kanamori, H., 2005a. Supershear and SubRayleigh-Intersonic Transition Observed in Laboratory Earthquake Experiments, *Experimental Techniques*, Vol. 29 (3), pp. 63-66

Xia, K., Rosakis, A. J., Kanamori, H. & Rice, J. R., 2005b. Laboratory earthquakes along inhomogeneous faults: directionality and supershear, *Science*, Vol. 308, pp. 681-684

Xu, S., Fukuyama, E., Ben-Zion Y. & Ampuero J.-P., 2015. Dynamic Rupture Activation of Backthrust Fault Branching, *Tectonophysics*, Vol. 644–645, pp. 161–183

Yamada, N. & Iwata T., (2005) Long-period ground motion simulation in the Kinki area during the MJ 7.1 foreshock of the 2004 off the Kii peninsula earthquakes, *Earth Planets Space*, Vol. 57, pp. 197-202.

Yang, W., Suo, Z., Shih, C. F., 1991. Mechanics of dynamic debonding, *Proc.: Math. and Phys. Sc.*, Vol. 433, pp. 679-697

Ziekiewicz, O. C. & Taylor R. L., 2000. *Finite element method*, 5th edn, Vol. 3, Butterworth-Heinemann.